

AD\_\_\_\_\_

Award Number: DAMD17-00-1-0596

**TITLE:** Real-Time Palpation Imaging for Improved Detection and Discrimination of Breast Abnormalities

**PRINCIPAL INVESTIGATOR:** Timothy J. Hall, Ph.D.

**CONTRACTING ORGANIZATION:** University of Kansas Medical Center  
Kansas City, KS 66160

**REPORT DATE:** July 2005

**TYPE OF REPORT:** Final

**PREPARED FOR:** U.S. Army Medical Research and Materiel Command  
Fort Detrick, Maryland 21702-5012

**DISTRIBUTION STATEMENT:** Approved for Public Release;  
Distribution Unlimited

The views, opinions and/or findings contained in this report are those of the author(s) and should not be construed as an official Department of the Army position, policy or decision unless so designated by other documentation.

# REPORT DOCUMENTATION PAGE

Form Approved  
OMB No. 0704-0188

Public reporting burden for this collection of information is estimated to average 1 hour per response, including the time for reviewing instructions, searching existing data sources, gathering and maintaining the data needed, and completing and reviewing this collection of information. Send comments regarding this burden estimate or any other aspect of this collection of information, including suggestions for reducing this burden to Department of Defense, Washington Headquarters Services, Directorate for Information Operations and Reports (0704-0188), 1215 Jefferson Davis Highway, Suite 1204, Arlington, VA 22202-4302. Respondents should be aware that notwithstanding any other provision of law, no person shall be subject to any penalty for failing to comply with a collection of information if it does not display a currently valid OMB control number. PLEASE DO NOT RETURN YOUR FORM TO THE ABOVE ADDRESS.

1. REPORT DATE (DD-MM-YYYY) 01-07-2005	2. REPORT TYPE Final	3. DATES COVERED (From - To) 15 Sep 2000 - 15 Jun 2005		
4. TITLE AND SUBTITLE Real-Time Palpation Imaging for Improved Detection and Discrimination of Breast Abnormalities		5a. CONTRACT NUMBER		
		5b. GRANT NUMBER DAMD17-00-1-0596		
		5c. PROGRAM ELEMENT NUMBER		
6. AUTHOR(S) Timothy J. Hall, Ph.D.  E-Mail: <a href="mailto:tjhall@wisc.edu">tjhall@wisc.edu</a>		5d. PROJECT NUMBER		
		5e. TASK NUMBER		
		5f. WORK UNIT NUMBER		
7. PERFORMING ORGANIZATION NAME(S) AND ADDRESS(ES)  University of Kansas Medical Center Kansas City, KS 66160		8. PERFORMING ORGANIZATION REPORT NUMBER		
9. SPONSORING / MONITORING AGENCY NAME(S) AND ADDRESS(ES)  U.S. Army Medical Research and Materiel Command Fort Detrick, Maryland 21702-5012		10. SPONSOR/MONITOR'S ACRONYM(S)		
		11. SPONSOR/MONITOR'S REPORT NUMBER(S)		
12. DISTRIBUTION / AVAILABILITY STATEMENT Approved for Public Release; Distribution Unlimited				
13. SUPPLEMENTARY NOTES				
14. ABSTRACT: The purpose of our work is to develop and test a new kind of imaging system we call "palpation imaging". We have demonstrated that palpation imaging can be a useful tool for improving the discrimination between benign and malignant breast tumors. We implemented our algorithm for imaging tissue elasticity on a commercial ultrasound imaging system and tested that new imaging system on phantoms and in vivo breasts. Palpation images are produced at substantially real-time frames rates with normal ultrasound B-mode and strain images displayed side-by-side. The algorithms are fully integrated into the commercial system and require no system modifications. Breast exams performed on volunteers have shown that palpation imaging techniques are almost identical to the standard clinical breast ultrasound exam. ROC analysis of elasticity image information demonstrates that the diagnostic confidence of breast radiologists is improved when elasticity information is added to standard ultrasound images. Further increases in observer performance will come through improved training, observer tools (automated segmentation) and image quality improvements.				
15. SUBJECT TERMS Breast Cancer, Mammography, Pendent Mammography				
16. SECURITY CLASSIFICATION OF:  a. REPORT U		17. LIMITATION OF ABSTRACT UU	18. NUMBER OF PAGES 210	19a. NAME OF RESPONSIBLE PERSON USAMRMC
b. ABSTRACT U				19b. TELEPHONE NUMBER (include area code)
c. THIS PAGE U				

## Table of Contents

<b>Cover.....</b>	
<b>SF 298.....</b>	<b>2</b>
<b>Introduction.....</b>	<b>4</b>
<b>Body.....</b>	<b>4</b>
<b>Key Research Accomplishments.....</b>	<b>13</b>
<b>Reportable Outcomes.....</b>	<b>14</b>
<b>Conclusions.....</b>	<b>22</b>
<b>References.....</b>	<b>23</b>
<b>Appendices.....</b>	<b>24</b>

## INTRODUCTION

The central hypothesis of this proposal was that a real-time side-by-side display of sonographic and elastographic images would significantly improve breast abnormality detection and discrimination. The goal of this study was to develop a real-time ‘palpation imaging’ system to test that hypothesis. We anticipated that high contrast-to-noise ratio images of mechanical strain (relative tissue deformation, “palpation images”) could be formed without the use of fixtures to control motion, and thus hand-held transducers would be sufficient. We also anticipated that real-time feedback would be essential for creating the appropriate boundary conditions to obtain high quality data that lacks significant elevational motion. We expected that with real-time “palpation imaging” it would be possible to detect lesions that are less than 5mm diameter at any location in the breast regardless of breast composition or size. This project included a broad spectrum of disciplines including scientists, engineers, and clinicians. Our research plan involved using tissue-mimicking test objects with known physical properties and included Phase I clinical trials on approximately 60 patients (funded by this proposal) supplemented with similar trials at two other institutions for a total of 477 human subjects. Our results demonstrate that elasticity imaging does improve diagnostic confidence in characterizing benign versus malignant lesions and has great potential for affecting the decision to biopsy.

## BODY

A sequence of six specific aim (‘Tasks’) were proposed to accomplish the goal of creating and testing a real-time elasticity imaging system. The results of this project will be reported for each task on a year by year basis.

### Task 1.

*Implement real-time palpation imaging on a commercial sonography system:*

1. *Program the imaging system digital signal processors to estimate strain from consecutive image frames.*
2. *Develop a user interface for controlling the data acquisition and processing parameters.*
3. *Test the system using existing phantoms and laboratory fixtures with motorized motion control to determine the penalty for using fixed-point versus floating point calculations.*

### Task 1. Year 1

One of the Co-Investigators in our effort (Dr. Yanning Zhu) spent three months at Siemens Medical Systems Ultrasound Group (SMSUG) (Issaquah, WA) learning to program their system and has modified our algorithms to efficiently execute on their SONOLINE Elegra Image Processor subsystem. We are grateful to SMSUG for their technical assistance in this effort. The software developed in year-1 was fully functional, but was still under development. Among the major accomplishments were that the system acquired ultrasound quadrature echo data, processed the normal ultrasound B-mode image and an image of mechanical strain, and displayed these images side-by-side at about eight frames per second. We found that frame rate to be sufficiently fast to provide feedback to the hand-eye coordination system to allow manipulating the conditions of tissue compression to consistently obtain high-quality strain images. We tested that system throughout its development and found no difference in the variance of time-delay (tissue

displacement) estimates for either floating-point or integer computations (assuming the integer computations are implemented to maximize the available bit depth), as reported in year-1. The algorithm was implemented both on-line using the Siemens SONOLINE Elegra with two Texas Instruments TMS320C80 MVP (TI C80) processors (integer computation) and off-line using MATLAB and both integer (an implementation identical to that on the TI C80) and floating point computation. Most of the development in Task 1 was completed during year-1.

### **Task 1. Year 2**

With additional testing and some minor development we significantly improved the computational efficiency of the software. The second prototype version of our software produced images for a 1 cm wide by 2 cm deep region of interest at about eight frames per second ( $16 \text{ cm}^2/\text{sec}$ ). The final version of the real-time (acquisition) software on the Siemens Elegra displays 3 cm wide by 3.5 cm deep image pairs at about seven frames per second ( $73.5 \text{ cm}^2/\text{sec}$ ). That frame rate is sufficiently fast to provide feedback to the hand-eye coordination system to allow manipulating the conditions of tissue compression to consistently obtain high-quality strain images. These results were published in (1).

### **Task 2.**

*Develop data acquisition techniques that provide high-quality palpation images without the use of fixtures:*

1. *Implement techniques that mimic those used for phantom imaging including small hand-held fixtures to restrict motion perpendicular to the image plane.*
2. *Test those techniques in phantoms and compare target contrast-to-noise ratio for laboratory (large motorized fixtures, controlled motion) versus clinical (small hand-held fixtures, restricted motion) systems.*
3. *Test the clinical systems (real-time palpation imaging with small fixtures) using anthropomorphic breast phantoms.*
4. *Test the clinical systems on volunteer patients with palpable breast abnormalities.*
5. *Modify the data acquisition techniques to eliminate the need for fixtures to restrict motion while maintaining image quality.*
6. *Measure conspicuity of breast lesions to assess the relative merit of different data acquisition techniques.*

### **Task 2. Year 1**

A great deal of the initial effort on this project was devoted to this Task. As described in the proposal and in the year-1 report, we began with simple rectangular block phantoms and compared motorized versus freehand scanning. These tests used fixtures that allowed us to restrict out-of-plane (elevation) motion of the phantom material as the block was deformed in the axial direction (parallel to the acoustic beam). We found that the small fixture used for freehand scanning (hereafter called the “fixture”) minimized elevation motion, just as the larger fixture used in the laboratory motorized compression system, but it was cumbersome to use. Freehand scanning of phantoms for strain imaging without fixtures was far easier than we

had anticipated. We skipped the step of using fixtures on breast-shaped phantoms and went directly to freehand scanning of these objects and found this to also be trivially easy. The leap to scanning *in vivo* breasts was more difficult. In this case, the use of the freehand scanning fixture for minimizing elevation motion was little, if any, help. We found that breast tissue is so heterogeneous, particularly with tissue boundaries sliding across each other, that the fixture did little to limit elevation motion and was more trouble than it was worth. The most significant improvement in ease of scanning came from modifications to obtain significantly higher elasticity image frame rate. When the frame rate hit about four frames per second we had sufficiently frequent frame update to provide the hand-eye coordination system enough information to control the conditions of tissue compression and obtain high-quality strain images *in vivo*. Iterating between what we learned with freehand scanning of phantoms, then *in vivo* breasts, and back to phantoms, we found that the key to obtaining sequences of high-quality strain images (high contrast-to-noise and high similarity from frame to frame) is high frame rate. The current frame rate is fast enough to allow us to manipulate the compression conditions while scanning, and this is essential for obtaining low noise strain image data. Results in the year-1 report show that the variance in our displacement estimates (the fundamental information in strain images) is comparable for freehand and motorized compression of a uniform block phantom. Displacement variance for *in vivo* breast scans were included for comparison and showed that the variance for *in vivo* displacement estimates is somewhat higher than that for homogeneous phantom materials with simple geometry. This shows that the penalty in image quality due to freehand scanning is small, especially considering the huge benefit in flexibility in scanning procedure and future clinical acceptability.

The research results from Tasks 1 and 2 during year-1 were summarized in conference proceedings (2; 3), a peer-reviewed manuscript (1) and a patent (listed below).

## **Task 2. Year 2**

Year-2 efforts on this Task were spent iterating between what we learned with freehand scanning of phantoms, then *in vivo* breasts, and back to phantoms, knowing that the key to obtaining sequences of high-quality strain images (high contrast-to-noise and high similarity from frame to frame) with freehand scanning is high frame rate. Within that effort we were developing improved scanning techniques for *in vivo* breast elasticity imaging. The scanning technique for breast palpation imaging is nearly identical to that used in typical breast sonography with compression. The subject lies on her back with her arm behind her head and the ultrasound transducer is pressed, by hand, toward the chest wall. The real-time image feedback allow manipulation of the compression conditions while scanning. This manipulation is essential for obtaining long sequences of low noise strain image data (often 100 image frames).

## **Task 3.**

*Implement high-quality palpation imaging algorithm on a commercial sonography system and perform preliminary tests of image quality:*

1. *Program the commercial sonography system to calculate a high-resolution, low-noise palpation images as quickly as possible over a large region of interest.*
2. *Develop a user interface that allows manipulation of the image formation algorithm for the trade-off between spatial resolution and image noise.*

3. *Test the high-quality algorithm on (geometrically) simple and anthropomorphic phantoms using the modified data acquisition techniques (Task 2.5).*
4. *Use the real-time palpation imaging technique to locate the desired region of interest and obtain sonographic data with the appropriate pre- and post-compression for volunteer patients with palpable breast abnormalities.*

### **Task 3. Year 1**

We implemented three displacement and strain algorithms on the Elegra, as described in the year-1 report. The simplest of these is the algorithm that runs in real-time for data acquisition. This uses an adaptive search strategy to predict the deformation based on previous displacement estimates. This adaptive search reduces the computational load for strain estimation by more than two orders of magnitude. The algorithm also decimates the data, thereby reducing the number of displacement estimates in a given region of interest. This algorithm is used primarily for data acquisition during freehand scanning and is a compromise between frame rate and image quality. To halt data acquisition the system 'freeze' button is pressed, just as in normal sonography, and the echo data are available for on-line post-processing. This same (real-time) strain imaging algorithm can be used to reprocess that data as the user scrolls through image memory, or one of the other algorithms can be used. The second algorithm is identical to the first except that the data is not decimated. Estimating displacement with higher data density reduces the displacement variance in the adaptive search strategy resulting in a slight improvement in image quality. The third algorithm operates on the full data field (no decimation) and does not use the adaptive search strategy, instead using a full 2-D search. This approach is much more computationally intensive, requiring about one second per strain image frame, but produces images that lack the displacement error accumulation that can result from the adaptive search strategy. Several image examples from our current algorithms were included in the year-1 report. There is a significant penalty in the printed version of these images. A CD-ROM was also included in the year-1 report that provided significantly higher quality images and 'movie loops' of strain image sequences to illustrate what is seen on the monitor of the Elegra.

By the end of year-1 we had scanned 42 volunteers. Among these there were 25 cysts, 18 fibroadenomas, and 6 invasive ductal carcinomas. Some of these patients had multiple lesions, and some were scanned on repeat occasions. We found that the high negative strain contrast for most fibroadenomas, with low pre-compression, decreases as the lesion is compressed. This implies that the tissue surrounding the lesion has a stress-strain relationship that is more nonlinear than that for the fibroadenoma. This behavior appears to be unique to fibroadenomas.

We found, as did Garra, et al., (4), that the width and height of benign lesions tend to be about the same size in B-mode and strain images and carcinomas are larger in strain images than B-mode, but the separation between benign and carcinoma is much larger when we use the lesion area (measurements performed by the PI). Those early results were very encouraging, and from this work we were confident that we were following a solid research plan. However, our enthusiasm had to be tempered with the fact that we had relatively small numbers of samples of each lesion type so far, the data included only one type of carcinoma (invasive ductal carcinoma), and the carcinomas were 'highly suspicious' based on mammography and sonography. The year-1 report provided images and included a CD-ROM with example images and 'movie loops' demonstrating these observations.

### **Task 3. Year 2**

The iteration of minor changes in elasticity image formation algorithm, tests in phantoms and scanning in limited *in vivo* breast lesions continued in the second year of support. We found, as described in the year-1 report, we could estimate displacement and strain accurately in inhomogeneous media (breast tissue) with greater success than originally anticipated. The key to this success is real-time imaging of strain that guides manipulation of the conditions of compression.

By the end of year-2 we had scanned 56 volunteers. Some of these patients had multiple lesions, and some were scanned on repeat occasions (perpendicular image planes, repeat visits, different transducers, etc.). The result was the experience of over 200 patient-scans. As detailed in the year-1 report, these images are very reproducible both within an acquisition sequence and on repeat visits.

Support for the observation that strain image contrast in fibroadenomas changes as the surface pressure increases, and that behavior appeared unique to fibroadenomas, continued to build in year-2. The frame-to-frame variability of strain images for cysts, reported in year-1, shifted our emphasis in data acquisition to solid lesions for year-2 and beyond. We also provided evidence in the year-1 report describing the frame-to-frame similarity in strain images of invasive ductal carcinomas and evidence demonstrating that the apparent size of a carcinoma in strain images is larger than that seen in the B-mode images. Aspects of these results were reported in a conference proceedings (5) and a peer-reviewed manuscript (6).

To begin designing the experiments for Tasks 4 and 5, we asked five observers (the PI and four ultrasound clinicians) to view each sequence of side-by-side B-mode and strain images from the KUMC data. From each sequence, each observer had to choose an image pair that represented the typical view of the lesion in both B-mode and strain images. That image pair was then displayed and the observer had to trace the lesion boundary in the B-mode image and measure the lesion height and width. The image pair was then re-displayed and the observer traced the lesion in the strain image and measure the lesion height and width. The combined average results for lesion measurements were shown in the year-2 report. A receiver operating characteristic (ROC) analysis of those measurements resulted in an overly-optimistic diagnostic accuracy of  $0.983 \pm 0.028$ —nearly perfect performance. Although these were very encouraging results, they could not be generalized to “average performance” for several reasons including the small size of the patient pool, correlations among the data (multiple lesions in a single patient included in the study), and the limited variety of lesion types (invasive ductal carcinomas, fibroadenomas and cysts). Results of this study were presented as a poster at the Radiological Society of North America meeting in November 2002.

That work demonstrated that we were following a solid research plan. By increasing the size of the study population, and comparing the change in diagnostic accuracy when using standard sonography versus sonography plus palpation imaging, we planned to test the utility of palpation imaging as a diagnostic tool with ROC analysis and multi-observer measurements.

### **Task 3. Year 3**

A total of 64 volunteer subjects had their breasts scanned with ‘palpation imaging’ at KUMC. Some of these patients had multiple lesions, and some were scanned on repeat occasions (perpendicular image planes, repeat visits, different transducers, etc.). As previously reported, the excitement from the potential for palpation imaging and the delay at KUMC in obtaining a sufficient number of patients to adequately test this technology resulted in Siemens contracting with two other institutions to test our technology (Charing Cross Hospital in London, UK and

Mayo Clinic, Rochester, MN). Those sites were quite productive in their trials. By the end of year-3 the Charing Cross group had scanned over 200 breast patients and the Mayo group had scanned over 100 patients. Each found that they became proficient in their scanning technique within 10–15 patients, and found that palpation imaging adds, on average, about five additional minutes to the normal breast ultrasound examination. The key to strain imaging, as in standard sonography, is training. With real-time feedback of the current strain images being acquired, the key is interpreting the data and making corrections to the technique, if necessary. In summary, the tools are adequate, the key to success is training.

Our plans at the end of year-3 were unchanged from those in the proposal and initial protocol, except for the change of institution and the use of data from outside this funded project. We were well prepared at that point to complete the final two tasks of the study (Tasks 4 and 5).

#### **Task 4.**

*Acquire sonograms, elastograms, and mammograms on patients with suspicious lesions that are either palpable or detectable with sonography or mammography.*

#### **Task 4. Year 4**

As noted in the year-3 report, the research performed in the prior years positioned us well to begin the Phase I clinical trial of “palpation imaging”. Unfortunately, the errors by administration employees at the University of Kansas in the grant transfer to the University of Wisconsin resulted in a loss of approximately \$64,000 (total funds). Our response was to eliminate the additional human subject scanning from our work and rely, with IRB and HSRRB approval, on the data that had been acquired by our colleagues at the Mayo Clinic (Rochester, MN) and Charing Cross Hospital (London, UK).

More specifically, the human subject population for the observer study (Task 5) came from the data acquired at Charing Cross Hospital in London, England and the Mayo Clinic in Rochester, Minnesota. Eligible patients were those women undergoing sonographically guided percutaneous breast biopsy. We excluded patients who had technically inadequate strain images or who did not undergo biopsy for pathologic outcome. Charing Cross enrolled 259 female patients between 2/22/2002 and 4/8/2004 imaging 259 lesions. Eleven lesions were excluded for technical reasons and 11 were excluded because biopsy was not performed. The Mayo Clinic enrolled 156 patients between 2/4/2002 to 5/25/2004 imaging 186 lesions of which 17 lesions were excluded for technical reasons and 3 were excluded because biopsy was not performed. In total, strain imaging was performed prospectively on 445 breast masses of which 42 were discarded based on our exclusion criteria leaving 403 (157 malignant-39.0%; 246 benign-61.0%) lesions as candidates for our reader study. Pathologic results determined by percutaneous or excisional biopsy were considered our reference standard in this study. Imaging-histologic concordance was documented for each lesion to minimize the chance for sampling error.

#### **Task 5.**

*Compare diagnosis of breast lesions with and without the use of palpation imaging. (using images obtained in Task 4).*

## Task 5. Year 4

The Mayo group, not directly under this project, performed an observer study based on strain image data they acquired. They recorded the RF echo signals and created strain images off-line using an algorithm we developed and provided to them. They tested whether lesion size ratio results we had observed in data from KUMC and Charing Cross were supported with their data. A significant limitation of their study was that the most highly trained observers attempted to perform the study during the normal workflow of a very busy radiology department. Worse, one of their observers was not trained in breast ultrasound imaging. As a result, the performance of their observers, as measured by the area under the ROC curve (AUC) for observer's lesion area ratios ranged from 0.92 (comparable to our results) down to 0.67 for an untrained observer. A detailed report of their results was published in a peer-reviewed manuscript (7).

A more careful study with a larger pool of data was performed within this project. Two parameters were used to select the abnormalities for the reader study: the distribution of pathologic diagnoses and image quality. First, in order to optimally represent the entire pathologic spectrum of solid breast abnormalities seen in clinical breast imaging practice, we determined the distribution of pathologic diagnoses in our collected cases. Next, we selected the 50 highest-quality malignant and the 50 highest-quality benign abnormalities on strain images while preserving this same distribution of pathologic diagnoses in the malignant and benign categories respectively. We also made sure that only one lesion per patient was included in the reader study to preserve independence of cases for statistical analysis.

Three radiologists were included in this study. All of the radiologists who participated were board certified (by the American Board of Radiology) and fulfilled the MQSA requirements in terms of volume of studies read per year and continuing medical education. All three radiologists are fellowship trained in breast imaging and spend at least 30% of their clinical time in breast imaging practice (years of experience range from 5 to 13 years).

The three observers (designated A-C) individually completed a training module containing 56 instructional PowerPoint® slides and 40 sample cases. The introductory slides provided didactic instruction on: 1) the physics of strain imaging; 2) characteristic appearance of strain imaging in benign and malignant masses; 3) the significance of size ratio differences between B-mode and strain imaging and 4) methods to evaluate the quality of strain imaging using ten of the 40 sample cases (5 benign, 5 malignant). The additional 30 sample cases contained 14 benign and 16 malignant solid masses shown as unknowns with illustrations of significant findings and relevant measurements available when desired. Once the training session was complete to the radiologist's satisfaction, test cases were presented in random order.

The observers were first presented the B-mode images as a movie clip which the radiologist assessed with BI-RADS descriptors, BI-RADS categories, and a probability of malignancy. The radiologist also selected a frame from the cine loop on which to make measurements on the B-mode image. The radiologist traced the lesion boundary and measured the largest linear dimension and the largest perpendicular dimension. Strain images were then made available and were presented as side-by-side B-mode and strain images in a movie clip. The radiologist first assessed the quality of the strain images on a 10 point scale. Then they selected a frame on which to trace the lesion boundary and measure the largest linear dimension and the largest perpendicular dimension on the strain image. Note that the frame used for strain image measurements was not necessarily the same as that used for B-mode measurements. The radiologist then viewed the ratio of the lesion area in the strain image to that in the B-mode image prior to re-assessment of the probability of malignancy. Probability assessment correlations between readers were calculated in a pair-wise fashion. Probability assessments were also used

to construct ROC curves to measure performance. The AUC without and with strain imaging were compared. Sensitivity and specificity were measured at a threshold of 2% probability of malignancy without and with strain and were compared. We also compared difference in AUC, sensitivity, and specificity between pairs of readers for B-mode and strain imaging.

The AUC values for the three radiologists and the group as a whole without and with strain images are shown in Table 1. While each radiologist improved in the assessment of the risk of malignancy when strain imaging was available, only Reader 1 demonstrated a statistically significant improvement. The improvement of the average AUC with strain imaging for the group as a whole also was statistically significant ( $P < 0.012$ ). A detailed report of this work is nearly complete and should be submitted by late May 2006 for publication in Radiology (8) (draft attached).

Table 1: Area under the receiver operating characteristic curves for rating the confidence that a breast lesion is malignant (risk = 0 for absolute confidence the lesion is benign; risk = 100 for absolute confidence the lesion is malignant)

	<b>B-mode</b>	<b>95% Confidence</b>	<b>B-mode &amp; Strain</b>	<b>95% Confidence</b>	<b>P-value</b>
Reader A	0.779	0.691–0.867	0.830	0.752–0.908	0.011
Reader B	0.916	0.859–0.972	0.929	0.878–0.980	0.51
Reader C	0.923	0.872–0.974	0.949	0.912–0.986	0.11
Average	0.872	0.837–0.907	0.903	0.870–0.936	0.021

## Task 6.

*Investigate the use of novel techniques, such as harmonic imaging and spatial quadrature, for improved information content in palpation images.*

### Task 6.Year 2

We continued to improve the image quality in a sequence of strain images. Viewing a sequence of strain images, instead of a single stationary image, illustrates the frame-to-frame variability in strain image noise. When attempting to choose a representative frame of data from a sequence and trace the lesion boundary, strain image noise reduces the observer's performance. Several sources of strain image noise were described in our contribution to the 2002 IEEE Ultrasonics Symposium Proceedings (9). Example images of the same data with and without these noise reduction strategies were provided in the year-2 report.

### Task 6.Year 3

As a result of the continued effort to further improve image quality, described in the year-2 report, it became clear that subjective visual assessment of image 'quality' and lesion conspicuity were not sufficient to quantify differences among motion tracking algorithms. Therefore, we began working on a quantitative method for measuring the accuracy of motion tracking in tissues in addition to the estimates of displacement estimate error variance that are commonly reported. That work was very early in development during year-3. The approach showed great promise for comparing the relative performance of various motion tracking algorithms

and parameter selection for a specific algorithm. Some of the concepts we were investigating for improving strain image quality were reported in a conference proceedings (10).

### Task 6. Year 4

When simulating data or experimentally imaging phantoms it is easy to know when the ‘correct’ image is being formed and displayed. That is not the case when viewing elasticity images of in vivo tissue. There is a natural bias toward accepting elasticity images as being ‘good’ when they share features with B-mode images, but this might be misguided. In addition, high-quality elasticity images can be formed that share none of the features of B-mode images. However, our experience in real-time elasticity imaging and in viewing numerous versions of post-processed elasticity image sequences strongly suggested that similarity among consecutive elasticity images in a long sequence suggests that reasonably high quality images are being displayed. That is, it is unlikely that significant stochastic errors in elasticity images would appear stable among a sequence of images since displacement estimate errors are random in nature.

That observation guided the development of a quantitative measure of elasticity image quality (actually a displacement estimate quality measure or DQM) described initially in the year-3 report. There are two components to the combined DQM. The first is a measure of the accuracy of motion tracking. The second is a measure of the similarity of consecutive strain images.

Recall that elasticity (strain) images are formed by tracking relative motion between the acquisition of two radiofrequency (RF) data fields (a reference field and a post-deformation field). The strain image typically displayed is the gradient of that 2-D displacement field in the direction of the acoustic beam. That same 2-D displacement field can be used to warp the post-deformation field to compensate for motion. The normalized cross correlation between the reference and motion-compensated post-deformation RF fields,  $\rho_{RF}$ , is a quantitative measure of motion tracking accuracy. If motion tracking is perfect, the warping is perfect and the cross correlation between the two RF fields is unity.

Similarly, the 2-D displacement field for deformation between the acquisition of two strain images can be used to warp one strain image into the coordinate system of the other. Then the normalized cross correlation between these consecutive strain images,  $\rho_S$ , is an objective measure of their similarity.

The product of these normalized cross correlations,  $DQM = \rho_{RF} \rho_S$ , is an objective measure of the accuracy of motion tracking and the similarity of consecutive strain images. More details of this measure of strain image quality and the results of an observer study to measure the correlation between this objective measure of strain image quality and the subjective assessment of image quality by three trained observers is provided in (11).

Other developments in elasticity image formation included investigations into elastic modulus estimation and image formation. Strain images are images of relative tissue properties—just as ultrasound B-mode images and mammograms are. Strain images of the same tissue can change when different “boundary conditions”, such as external forces, are applied. Estimates and images of absolute properties of tissue are more attractive and likely more specific to tissue type. Initial work in this area was based on rewriting the typical finite element analysis equations where the modulus distribution became the unknown instead of the known parameter. Applying measured displacement estimates from the ‘palpation imaging’ data and additional measurements of the applied surface force at the ultrasound transducer allowed solving that equation system for the modulus distribution. If the noise in displacement estimates and force measurements are sufficiently small, very accurate modulus images can be achieved as reported

in (12) and (13).

A comparison of our (then) current strain image formation algorithm applied to data acquired with a high-end ultrasound imaging system was compared to images obtained with a simple strain image formation algorithm applied to data from a lower-end imaging system. An obvious difference in image quality and target detectability was demonstrated (14).

The experience gained through this research effort led to the realization that many of the methods for estimating quantitative ultrasound parameters that we had derived and measured in phantoms and tissue over the years could be programmed into a clinical imaging system for real-time display. A report describing strategies for accomplishing these goals was reported in a conference proceedings (15).

## KEY RESEARCH ACCOMPLISHMENTS

- The motion tracking algorithm has been implemented on the Siemens SONOLINE Elegra and displays B-mode and strain images side-by-side at about eight frames per second.
- We found that the key to obtaining high-quality *in vivo* strain images of the breast is to form the images in “real-time,” that is, fast enough to provide the hand-eye coordination system sufficient feedback to control the conditions of tissue deformation. The minimum frame rate appears to be about four frames per second, but higher frame rates (currently about eight frames per second) make palpation imaging easier.
- There is no significant difference between the displacement variance (strain image noise) for freehand scanning versus motorized compression for strain imaging.
- We have found that the frame-to-frame strain patterns from various breast abnormalities appears to be unique to the abnormality. For example, the fluid within cysts appears to be ‘stirred’ when deformed in palpation imaging, and that ‘stirring’ causes the RF echo signal, and therefore the strain image, to decorrelate rapidly with time. We have also found that the strain contrast for fibroadenomas is not constant with compression; at very low pre-loading fibroadenomas are stiffer than their surroundings and provide high negative contrast. With increased compression that contrast is often significantly reduced; Invasive ductal carcinomas maintain a high negative contrast at all pre-load compressions.
- We have found that by comparing the area of a lesion measured on the standard ultrasound B-mode image with area measured on a strain image, benign lesions have nearly equal area on both modalities but most carcinomas are significantly larger on the strain image than in B-mode.
- The area under the receiver operating characteristic curve (AUC for an ROC curve), which is a measure of diagnostic accuracy, increased when a group of radiologists interpreted strain images side-by-side with ultrasound B-mode images over that for B-mode images alone (0.872 versus 0.902), and the increased performance is statistically significant ( $P = 0.012$ )
- Using a threshold of 2% probability of malignancy, as a group, specificity with strain improved significantly over B-mode alone (0.140 versus 0.191,  $P < 0.0001$ ) while achieving high sensitivity (0.986 versus 0.993,  $P = 0.32$ )

- Statistically significant inter-observer variability was observed ( $p < 0.001$ ) in a multi-reader study of elasticity imaging (both for B-mode image interpretation and strain image interpretation)

## REPORTABLE OUTCOMES

### Peer-reviewed articles in scientific journals—Attached in order as Appendices

1. Zhu Y and Hall TJ. A modified block matching method for real-time freehand strain imaging, *Ultrasonic Imaging* 24(3): 161-176, 2002
2. Hall TJ, Zhu Y, and Spalding CS. In vivo real-time freehand palpation imaging, *Ultrasound Med Biol* 29(3): 427-35, 2003
3. Zhu Y, Hall TJ, and Jiang J. A finite element approach for Young's modulus reconstruction. *IEEE Trans Med Imaging* 22(7): 890-901, 2003
4. Hall TJ. AAPM/RSNA physics tutorial for residents: topics in US: Beyond the basics: elasticity imaging with ultrasound, *Radiographics* 23(6): 1657-71, 2003
5. Madsen EL, Frank GR, Hobson MA, Shi H, Jiang J, Varghese T, Hall TJ, Spherical lesion phantoms for testing the performance of elastographic systems, *Phys Med Biol* 50(24):5983-5995, 2005
6. Regner DM, Hesley GK, Hangiandreou NJ, Morton MJ, Nordland MR, Meixner DD, Hall TJ, Farrell MA, Mandrekar JN, Harmsen WS, Charboneau JW, Ultrasound Strain Imaging for the Evaluation of Breast Lesions: Clinical Experience of Multiple Observers, *Radiology* 238(2): 425-437, 2006
7. Jiang J, Hall TJ, Sommer AM. A novel performance descriptor for ultrasonic strain imaging: A preliminary study, accepted in *IEEE Trans Ultrason, Ferroelec, Freq Contr (UFFC)* 2005
8. Burnside ES, Hall TJ, Sommer AM, Hesley GK, Sisney GA, Svensson WE, Hangiandreou NJ. Using Ultrasound Strain Imaging to Improve the Decision to Biopsy Solid Breast Masses, to be submitted to *Radiology* May 2006.

### Conference Proceedings—Attached in order as Appendices

1. Hall TJ, Zhu Y, Spalding CS, Cook LT. In vivo results of real-time freehand elasticity imaging. 2001 Ultrasonics Symposium Proceedings 01CH37263: 1653-1657, 2001
2. Hall TJ, Zhu Y, Spalding CS, Cook LT. In vivo real-time freehand elasticity imaging. 2002 International Symposium on Biomedical Imaging, CD-ROM 2002
3. Hall TJ, Jaing JF, Zhu Y, Cook LT. Noise Reduction Strategies in Freehand elasticity Imaging. 2002 Ultrasonics Symposium Proceedings 02CH37388C 1877-1880, 2002
4. Hall TJ, Svensson W, Behren PV, Zhu Y, Malin J, Spalding C, Connors A, Chopra D, Lowery C. Lesion size ratio for differentiating breast masses. 2003 IEEE Ultrasonics Symposium Proceedings 1247-1250, 2003

5. Hall TJ and Jiang J. Motion tracking for palpation imaging, IEEE International Symposium on Biomedical Imaging: Macro to Nano, 2004, 45-48, 2004
6. Jiang, J and Hall TJ. Computational aspects of Young's modulus reconstruction from ultrasonic freehand scanning. 2004 IEEE Ultrasonics Symposium Proceedings 1517-1520, 2004
7. Zagzebski, JA, Gerig A, Chen Q, Tu H, Liu W, Varghese T, Hall TJ. Parametric imaging using a clinical scanner, 2004 IEEE Ultrasonics Symposium Proceedings 2165 - 2168, 2004

## Book Chapters

1. Hall TJ "The Physics of Elasticity Imaging: A New Option on the Latest Ultrasound Systems." 2004 RSNA Syllabus in Diagnostic Radiology Physics: Advances in Breast Imaging

## Abstracts

1. Zhu Y, Hall, TJ, Cook LT. A new technique for real-time freehand ultrasonic elasticity imaging, *J Acoust Soc Am* 109(5, Pt. 2): 2361-2362, 2001
2. Hall TJ, Zhu Y, Spalding C, Cook LT. Experimental results of real-time freehand elasticity imaging, *J Acoust Soc Am* 109(5, Pt. 2): 2362, 2001
3. Zhu Y, Hall TJ. A new system for real-time freehand imaging of tissue elasticity, *Radiology* 221(P): 692, 2001
4. Hall TJ, Zhu Y, Spalding CS, Von Behren P, Cox GG, Brecheisen MA. Ultrasound palpation imaging as a tool for improved differentiation among breast abnormalities," , *Radiology* 221(P): 697, 2001
5. Zhu Y, Hall TJ, Cook LT. Real-time freehand elasticity imaging, *Ultrasonic Imaging* 23(3): 190-191, 2001
6. Zhu Y, Hall TJ, Cook LT. A new method for Young's modulus reconstruction, *Ultrasonic Imaging* 23(3): 191, 2001
7. Hall TJ, Zhu Y, Cook LT. Results of real-time in vivo elasticity imaging in breasts, *Ultrasonic Imaging* 23(3): 191-192, 2001
8. Rosenthal SJ, Hall TJ, Zhu Y, Spalding CS, Brecheisen MA. Real-time palpation breast imaging, *J Ultrasound Med* 21(3S): 17-18, 2002
9. Hall TJ, Zhu Y, Cook LT. A new system for real-time freehand imaging of tissue elasticity, *J Ultrasound Med* 21(3S): 77-78, 2002
10. Hall TJ "Phantoms for elasticity imaging. Proceedings of the First International Conference on the Ultrasonic Measurement and Imaging of Tissue Elasticity 49, 2002
11. Hall TJ and Zhu Y, "Real-time freehand elasticity imaging," Proceedings of the First International Conference on the Ultrasonic Measurement and Imaging of Tissue Elasticity 60, 2002

12. Hall TJ, Zhu Y, Spalding C, Von Behren P. Lesion size measurement in palpation imaging, *Radiology* 225(P): 185, 2002
13. Cook LT, Zhu Y, Hall TJ. The effect of kernel size on ultrasonic displacement estimation, *Ultrasonic Imaging* 25:56-57, 2003
14. Zhu Y, Hall TJ, Cook LT, Jiang J. Young's modulus reconstruction using ultrasound, *Ultrasonic Imaging* 25:64-65, 2003
15. Hangiandreou NJ, Meixner DM, Hesley GK, Farrell MA, Morton MJ, Charboneau JW, Hall TJ, Zhu Y, Spalding C. Ultrasound strain image data obtained in breast masses: preliminary quantitative analysis, *Ultrasound in Med and Biol* 29: S178, 2003
16. Hall TJ, Svensson WA, Von Behren P, Zhu Y, Malin J, Spalding C, Connors A, Chandra D, Lowery C, "Lesion size ratio for differentiating among breast lesions. Proceedings of the Second International Conference on the Ultrasonic Measurement and Imaging of Tissue Elasticity 44, 2003
17. Hall TJ, Cook LT, Zhu Y. The statistics of motion tracking with large deformation, *Proceedings of the Second International Conference on the Ultrasonic Measurement and Imaging of Tissue Elasticity* 64, 2003
18. DM Regner, Hesley GK, Hangiandreou NJ, Nordland MR, Meixner DD, Morton MJ, Meixner DD, Hall TJ, Farrell MA, Charboneau JW. Initial clinical experience with ultrasound strain imaging for the evaluation of breast masses," *Radiology* 229(P): 213, 2003
19. Hesley GK, Nordland MR, Regner DM, Hangiandreou NJ, Morton MJ, Meixner DD. Visual Interpretation of Strain Images for the Evaluation of Breast Masses, *Am J Roentgenology* 182(S):83-84, 2004
20. Hesley GK, Nordland MR, Hangiandreou NJ, Morton MJ, Meixner DD, Charboneau JW, Hall TJ, Farrell MA. Subjective visual evaluation of real-time ultrasound strain images for differentiation of breast lesions, *J Ultrasound Med* 23:S105, 2004
21. Svensson WE, Hall TJ, Zhu Y, Malin J, Rattansingh A, Lowery C, Shousha S, Chopra D. Elasticity imaging may improve pre-treatment staging of breast cancers, *Proceedings of the Third International Conference on the Ultrasonic Measurement and Imaging of Tissue Elasticity* 39, 2004
22. Jiang J, Hall TJ, Madsen EL. Absolute modulus imaging using ultrasonic freehand scanning and pressure sensory data, *Proceedings of the Third International Conference on the Ultrasonic Measurement and Imaging of Tissue Elasticity* 47, 2004
23. Madsen EL, Frank G, Hobson MA, Shi H, Varghese T, Jiang J, Hall TJ, Krouskop TA, Ophir J, Weaver J, Doyley MM. Tissue-mimicking spherical lesion phantoms for elastography with and without ultrasound refraction effects," *Proceedings of the Third International Conference on the Ultrasonic Measurement and Imaging of Tissue Elasticity* 102, 2004
24. Madsen EL, Frank G, Hobson MA, Shi H, Varghese T, Jiang J, Hall TJ, Krouskop TA, Ophir J, Weaver J, Doyley MM. Tissue-mimicking anthropomorphic breast phantoms for ultrasound and MR elastography, *Proceedings of the Third International Conference on the Ultrasonic Measurement and Imaging of Tissue Elasticity* 103, 2004

25. Zagzebski JA, Brunke S, Pelissier L, Hall TJ, Wilson T. The ultrasound research interface: A new tool for biomedical investigations, *Med Phys* 32(6): 2119-2119, 2005
26. Hesley GK, Nordland MR, Morton MJ, Hangiandreou NJ, Meizner DD, Hall TJ, Lucas JM, McNamara JM, Ryan-O'Neill RF, Higgins RL, Cropp JT, Champa SR. Performance of visual interpretation of lesion conspicuity in ultrasound strain image sequences for diagnosis of malignant and benign breast lesions, *Am J Roentg* 184(4): 27-27 Suppl. S, 2005
27. Jiang J and Hall TJ. Regularization issues in Young's modulus reconstruction, *Ultrasonic Imaging* 26: 261, 2005
28. Hall TJ, Zagzebski JA, Jiang J, Tu H, Varghese T. Parametric imaging on a clinical imaging system, *J Ultrasound Med* 24:S37-S38, 2005

## Oral Presentations

1. Real-Time Palpation Imaging by Hall TJ, Presented at The Conference for Ultrasonics in Biophysics and Bioengineering, Allerton Park, University of Illinois at Urbana-Champaign, May, 2001. (Invited)
2. A New Technique for Real-Time Freehand Ultrasonic Elasticity Imaging by Zhu Y, Hall, TJ, Cook LT. Presented at the Annual Meeting of the Acoustical Society of America, June, 2001
3. Experimental Results of Real-Time Freehand Elasticity Imaging by Hall TJ, Zhu Y, Spalding C, Cook LT. Presented at the Annual Meeting of the Acoustical Society of America, June, 2001
4. Imaging the Visco-Elastic Properties of Tissues by Hall TJ. Presented at the University of Wisconsin-Madison Medical Physics Seminar, September, 2001
5. In Vivo Results of Real-Time Freehand Elasticity Imaging by Hall TJ, Zhu Y, Spalding CS, Cook LT. Presented at the 2001 IEEE Ultrasonics Symposium, Atlanta, Georgia, October, 2001
6. Imaging the Viscoelastic Properties of Tissue Using Ultrasound by Hall TJ. Presented at the Mayo Radiology Department, November, 2001
7. Palpation Imaging: Imaging the Viscoelastic Properties of Tissue Using Ultrasound by Hall TJ. Presented at the Joint Department of Physics, Institute for Cancer Research, The Royal Marsden Hospital, London, UK, March 2002
8. Real-Time Palpation Breast Imaging by Rosenthal SJ, Hall TJ, Zhu Y, Spalding CS, Brecheisen MA. Presented at the American Institute of Ultrasound in Medicine Annual Convention, Nashville Tennessee, March 2002
9. A New System for Real-Time Freehand Imaging of Tissue Elasticity by Hall TJ, Zhu Y, Cook LT. Presented at the American Institute of Ultrasound in Medicine Annual Convention, Nashville Tennessee, March 2002

10. Real-Time Freehand Elasticity Imaging by Zhu Y, Hall TJ, Cook LT. Presented at the 27th International Symposium on Ultrasonic Imaging and Tissue Characterization, Arlington, Virginia, June 2002
11. A New Method for Young's Modulus Reconstruction by Zhu Y, Hall TJ, Cook LT. Presented at the 27th International Symposium on Ultrasonic Imaging and Tissue Characterization, Arlington, Virginia, June 2002
12. Results of Real-Time In Vivo Elasticity Imaging in Breasts by Hall TJ, Zhu Y, Cook LT. Presented at the 27th International Symposium on Ultrasonic Imaging and Tissue Characterization, Arlington, Virginia, June 2002
13. In vivo results of real-time freehand elasticity imaging by Hall TJ, Zhu Y, Spalding CS, Cook LT. Presented at the First International Symposium on Biomedical Imaging, Washington, DC, July 2002
14. Noise Reduction Strategies in Freehand elasticity Imaging by Hall TJ, Jaing JF, Zhu Y, Cook LT. Presented at the 2002 IEEE Ultrasonics Symposium, Munich, Germany, October 2002
15. Phantoms for elasticity imaging by Hall TJ. Presented at the First International Conference on the Ultrasonic Measurement and Imaging of Tissue Elasticity Niagra Falls, Ontario CA, October, 2002
16. Real-time freehand elasticity imaging by Hall TJ and Zhu Y. Presented at the First International Conference on the Ultrasonic Measurement and Imaging of Tissue Elasticity Niagra Falls, Ontario CA, October, 2002
17. Lesion size measurement in palpation imaging by Hall TJ, Zhu Y, Spalding C, Von Behren. Presented at the 88th Scientific Assembly and Annual Meeting of the Radiological Society of North American, Chicago, Illinois, November 2002
18. The effect of kernel size on ultrasonic displacement estimation by Cook LT, Zhu Y, Hall TJ. Presented at the 28th International Symposium on Ultrasonic Imaging and Tissue Characterization, Arlington, Virginia, June 2003
19. Young's modulus reconstruction using ultrasound by Zhu Y, Hall TJ, Cook LT, Jiang J. Presented at the 28th International Symposium on Ultrasonic Imaging and Tissue Characterization, Arlington, Virginia, June 2003
20. Ultrasound strain image data obtained in breast masses: preliminary quantitative analysis by NJ Hangiandreou, Meixner DM, Hesley GK, Farrell MA, Morton MJ, Charboneau JW, Hall TJ, Zhu Y, Spalding C. Presented at the American Institute of Ultrasound in Medicine Annual Convention, Montreal, CA, June 2003
21. Subjective visual evaluation of real-time ultrasound strain images for differentiation of breast lesions by Hesley GK, Nordland MR, Hangiandreou NJ, Morton MJ, Meixner DD, Charboneau JW, Hall TJ, Farrell MA. Presented at the American Institute of Ultrasound in Medicine Annual Convention, Montreal, CA, June 2003
22. Lesion size ratio for differentiating among breast lesions by Hall TJ, Svensson WA, Von Behren P, Zhu Y, Malin J, Spalding C, Connors A, Chandra D, Lowery C. Presented

at the Second International Conference on the Ultrasonic Measurement and Imaging of Tissue Elasticity, Corpus Christi, TX, October, 2003

23. The statistics of motion tracking with large deformation by Hall TJ, Cook LT, Zhu Y. Presented at the Second International Conference on the Ultrasonic Measurement and Imaging of Tissue Elasticity, Corpus Christi, TX, October, 2003
24. Palpation Imaging in Ultrasound by Hall TJ. Presented at the Focus on Ultrasound meeting, Madison, WI October, 2004. (Invited)
25. Elasticity imaging may improve pre-treatment staging of breast cancers by Svensson WE, Hall TJ, Zhu Y, Malin J, Rattansingh A, Lowery C, Shousha S, Chopra D. Presented at the Third International Conference on the Ultrasonic Measurement and Imaging of Tissue Elasticity Lake Windermere, Cumbria UK, October, 2004
26. Absolute modulus imaging using ultrasonic freehand scanning and pressure sensory data by Jiang J, Hall TJ, Madsen EL. Presented at the Third International Conference on the Ultrasonic Measurement and Imaging of Tissue Elasticity Lake Windermere, Cumbria UK, October, 2004
27. Tissue-mimicking spherical lesion phantoms for elastography with and without ultrasound refraction effects by Madsen EL, Frank G, Hobson MA, Shi H, Varghese T, Jiang J, Hall TJ, Krouskop TA, Ophir J, Weaver J, Doyley MM. Presented at the Third International Conference on the Ultrasonic Measurement and Imaging of Tissue Elasticity Lake Windermere, Cumbria UK, October, 2004
28. Tissue-mimicking anthropomorphic breast phantoms for ultrasound and MR elastography by Madsen EL, Frank G, Hobson MA, Shi H, Varghese T, Jiang J, Hall TJ, Krouskop TA, Ophir J, Weaver J, Doyley MM. Presented at the Third International Conference on the Ultrasonic Measurement and Imaging of Tissue Elasticity Lake Windermere, Cumbria UK, October, 2004
29. Development of a Real-Time Elasticity Imaging System by Hall TJ Presented at the Biomedical Engineering Seminar, UW-Madison, November 2004. (Invited)
30. Young's modulus reconstruction with freehand scanning - a feasibility study by J. Jiang, T. J. Hall. Presented at the 3rd International Conference on the Ultrasonic Measurement and Imaging of Tissue Elasticity, October, 2004, Windermere, UK
31. Tissue-mimicking spherical lesion phantoms for elastography with and without ultrasound refraction effects by E. Madsen, G. Frank, M. Honson, H. Shi, T. Varghese, J. Jiang, T. Hall, T. Krouskop, J. Ophir, J. Weaver and M. Doyley. Presented at the 3rd International Conference on the Ultrasonic Measurement and Imaging of Tissue Elasticity , Windermere, UK, October, 2004
32. Tissue-mimicking anthropomorphic breast phantoms for ultrasound and MR elastography by E. Madsen, G. Frank, M. Honson, H. Shi, T. Varghese, J. Jiang, T. Hall, T. Krouskop, J. Ophir, J. Weaver and M. Doyley. Presented at the 3rd International Conference on the Ultrasonic Measurement and Imaging of Tissue Elasticity , Windermere, UK, October, 2004

33. Physics of Elasticity Imaging: A New Option on the Latest US Systems by Hall TJ. Presented at the 90th Scientific Assembly and Annual Meeting of the Radiological Society of North American, Chicago, Illinois, November 2004
34. The ultrasound research interface: A new tool for biomedical investigations by Zagzebski JA, Brunke S, Pelissier L, Hall TJ, Wilson T., Presented at the Annual Meeting of the American Association of Physicists in Medicine, Seattle, WA July, 2005
35. Performance of visual interpretation of lesion conspicuity in ultrasound strain image sequences for diagnosis of malignant and benign breast lesions by Hesley GK, Nordland MR, Morton MJ, Hangiandreou NJ, Meizner DD, Hall TJ, Lucas JM, McNamara JM, Ryan-O'Neill RF, Higgins RL, Cropp JT, Champa SR. Presented at the American Roentgen Ray Society Meeting New Orleans, LA, May, 2005
36. Regularization issues in Young's modulus reconstruction Jiang J and Hall TJ. Presented at the 30th International Symposium on Ultrasonic Imaging and Tissue Characterization, Arlington, Virginia, May 2005
37. Parametric imaging on a clinical imaging system by Hall TJ, Zagzebski JA, Jiang J, Tu H, Varghese T. Presented at the American Institute of Ultrasound in Medicine Annual Convention, Orlando, FL, June 2005
38. Regularization issues in Young's modulus reconstruction by Jiang J and Hall TJ. Presented at the Fourth International Conference on the Ultrasonic Measurement and Imaging of Tissue Elasticity 29, 2005

## Poster Presentations

1. A new system for real-time freehand imaging of tissue elasticity by Zhu Y, Hall TJ. Presented at the 87th Scientific Assembly and Annual Meeting of the Radiological Society of North America, Chicago, Illinois, November 2001. **Certificate of Merit**
2. Ultrasound palpation imaging as a tool for improved differentiation among breast abnormalities by Hall TJ, Zhu Y, Spalding CS, Von Behren P, Cox GG, Brecheisen MA. Presented at the 87th Scientific Assembly and Annual Meeting of the Radiological Society of North America, Chicago, Illinois, November 2001
3. Palpation imaging: Real-time freehand imaging of tissue elasticity by Hall TJ, Zhu Y, Spalding Cs, Von Berhren P, Chen J-F, Fan L, Rosenthal SJ. Presented at the European Congress of Radiology, Vienna, Austria, February 2002
4. Lesion size measurement in palpation imaging Hall TJ, Spalding C, Hall M, Von Behren P, Zhu Y, Mayo M, Cook LT. Presented at the 88th Scientific Assembly and Annual Meeting of the Radiological Society of North America, Chicago, Illinois, December 2002
5. Initial clinical experience with ultrasound strain imaging for the evaluation of breast masses by DM Regner, Hesley GK, Hangiandreou NJ, Nordland MR, Meixner DD, Morton MJ, Meixner DD, Hall TJ, Farrell MA, Charboneau JW. Presented at the 89th Scientific Assembly and Annual Meeting of the Radiological Society of North America, Chicago, Illinois, December 2003

6. Visual Interpretation of Strain Images for the Evaluation of Breast Masses by Hesley GK, Nordland MR, Regner DM, Hangiandreou NJ, Morton MJ, Meixner DD. Presented at the 104th Annual Meeting of the American Roentgen Ray Society, 2004
7. Accuracy of Motion Compensation in Elasticity Imaging by A. Sommer, T. J. Hall and J. Jiang. Presented at the 90th scientific assembly and annual meeting, RSNA, Chicago, UK, December, 2004
8. A feasibility study of Young's modulus reconstruction using ultrasonic freehand scanning by J. Jiang, T. J. Hall. Presented at the 90th scientific assembly and annual meeting, RSNA, Chicago, UK, December, 2004
9. Surface Pressure-dependant Strain Image Contrast in Breast Tissue by L. Kiessel, T. J. Hall, J. Jiang and W. Liu. Presented at the 90th scientific assembly and annual meeting, RSNA, Chicago, UK, December, 2004

## Patents and Licenses

1. Ultrasound Elasticity Imaging by Zhu Y and Hall TJ US Patent 6,508,768, Sept 17, 2001

## Degrees obtained

1. Jingfeng Jiang, Masters in Electrical and Computer Engineering, University of Kansas
2. Amy M. Sommer, Masters in Physics, University of Wisconsin-Madison
3. Amy M. Sommer, Masters in Medical Physics, University of Wisconsin-Madison (Ph.D. candidate)

## Funding applied for

Table 2: Funding awarded or applied for based, in part, on the successes of this project

Title	PI	Agency	Status
Palpation Imaging	TJ Hall	NIH/NCI	R01CA100373 (active)
Normal and Shear Strain from Angled US Acquisition	T Varghese	NIH/NIBIB	R21EB003853 (active)
Palpation Imaging Supplement	TJ Hall	NIH/NCI	R01CA100373-S1 (pending)
Ultrasound imaging technology for cancer detection and diagnosis	WD O'Brien (UIUC) TJ Hall (UW)	NIH/NCI	R01CA111289 (pending)

## **Employment or research opportunities**

1. The PI for this project was recruited for an Endowed Professorship at the University of Rochester in the Department of Biomedical Engineering (Rochester, NY)
2. The PI for this project was recruited for and accepted a position as a tenured Professor of Medical Physics at the University of Wisconsin-Madison (Madison, WI)

## **Personnel receiving pay from the research effort**

1. Timothy J. Hall, Ph.D. (PI, KUMC and UW)
2. Yanning Zhu, Ph.D. (KUMC electrical engineer)
3. Larry T. Cook, Ph.D. (KUMC mathematician)
4. Glendon G. Cox, MD (KUMC radiologist)
5. Lisa Stenho-Bittel, Ph.D. (KUMC physiologist, biomechanics)
6. Carol Fabian, MD (KUMC oncologist)
7. Carol Connor, MD (KUMC breast surgeon)
8. Jingfeng Jiang, Ph.D. (UW mechanical engineer)
9. James A. Zagzebski, Ph.D. (UW medical physicist)
10. Elizabeth S. Burnside Rollins, MD (UW radiologist)
11. Jason Fine, Ph.D. (UW biostatistician)
12. Amy M. Sommer, MS (UW Research Assistant)

## **CONCLUSION**

We find that ultrasound strain imaging has potential to aid radiologists in the differentiation of malignant and benign solid breast masses and, therefore, has the potential to improve the decision to perform breast biopsy. Such decisions have a high impact on the efficacy of breast cancer screening programs in terms of cost and quality. Our work also demonstrates that further research will be important to understand how image quality and interobserver variability attenuate the contribution of strain imaging to performance. This work also demonstrates the need for improvements in strain image quality and better tools to aid radiologists in interpreting strain images. Prospective trials are now necessary to confirm that strain imaging is a promising tool for radiologists in the accurate diagnosis of breast cancer.

The promise for this technology is possibly most convincingly demonstrated by the fact that at least one clinical ultrasound system manufacturer (Hitachi) is marketing elasticity imaging for breast tumor diagnosis on their latest system. Other manufacturers are actively working on elasticity imaging systems. Phase II clinical trials will be necessary to determine the merit of elasticity imaging for any particular clinical application. But, the results of this study are encouraging and can be used to help design those Phase II clinical trials of breast elasticity imaging.

## References

- [1] Zhu Y, Hall TJ. A Modified Block Matching Method for Real-Time Freehand Strain Imaging. *Ultrasonic Imaging*. 2002;24(3):161–176.
- [2] Hall TJ, Zhu Y, Spalding CS, Cook LT. In vivo results of real-time freehand elasticity imaging. In: *IEEE Ultrason. Symp. Proc.*; 2001. p. 1653–1657.
- [3] Hall TJ, Zhu Y, Spalding CS, Cook LT. In vivo results of real-time freehand elasticity imaging. In: *Int Symp Biomed Imag Proc.*; 2002. p. 805–808.
- [4] Garra BS, Céspedes I, Ophir J, Spratt SR, Zuurbier RA, Magnant CM, et al. Elastography of the breast: Initial clinical results. *Radiology*. 1997;202:79–86.
- [5] Hall TJ, Svensson W, Behren PV, Zhu Y, Malin J, Spalding C, et al. Lesion Size Ratio for Differentiating Breast Masses. In: *Proc. 2003 IEEE Ultrasonics Symposium*; 2003. .
- [6] Hall TJ, Zhu Y, Spalding CS. In Vivo Real-Time Freehand Palpation Imaging. *Ultrasound Med Biol*. 2002;29(3):427–435.
- [7] Regner DM, Hesley GK, Hangiandreou NJ, Morton MJ, Nordland MR, Meixner DD, et al. Ultrasound Strain Imaging for the Evaluation of Breast Lesions: Clinical Experience of Multiple Observers. *Radiology*. 2006;238(2):425–437.
- [8] Burnside ES, Hall TJ, Sommer AM, Hesley GK, Sisney GA, Svensson WE, et al. Ultrasound Strain Imaging to Improve the Decision to Biopsy Solid Breast Masses. *Radiology*. to be submitted;.
- [9] Hall TJ, Jiang J, Zhu Y, Cook LT. Noise reduction strategies in freehand elasticity imaging. In: *IEEE Ultrason. Symp. Proc.*; 2002. p. 1877–1880.
- [10] Hall TJ, Zhu Y, Spalding CS, Cook LT. Motion tracking for palpation imaging. In: *Int Symp Biomed Imag Proc.*; 2004. p. 45–48.
- [11] Jiang J, Hall TJ, Sommer AM. A novel performance descriptor for ultrasonic strain imaging: A preliminary study. *IEEE Trans Ultrason, Ferroelec, Freq Cont*. accepted 2006;.
- [12] Zhu Y, Hall TJ, Jiang J. A finite element approach for Young's modulus reconstruction. *IEEE Trans Med Imag*. 2003;22(7):890–901.
- [13] Jiang J, Hall TJ. Computational aspects of Young's modulus reconstruction from ultrasonic freehand scanning. In: *IEEE Ultrason. Symp. Proc.*; 2004. p. 1517–1520.
- [14] Madsen EL, Frank GR, Hobson MA, Shi H, Jiang J, Varghese T, et al. Spherical lesion phantoms for testing the performance of elastographic systems. 2005;50(24):5983–5995.
- [15] Zagzebski JA, Gerig A, Chen Q, Tu H, Liu W, Varghese T, et al. Parametric imaging using a clinical scanner. In: *IEEE Ultrason. Symp. Proc.*; 2004. p. 2165–2168.

## A Modified Block Matching Method for Real-Time Freehand Strain Imaging

YANNING ZHU AND TIMOTHY J. HALL

*Department of Radiology  
University of Kansas City Medical Center  
3901 Rainbow Boulevard  
Kansas City, KS 66216-7234  
yzhu@kumc.edu*

This manuscript reports a technical innovation that has been developed for real-time, freehand strain imaging. This work is based on a well-known block-matching algorithm with two significant modifications. First, since displacements are estimated row-by-row, displacement estimates from the previous row are used to predict the displacement estimates in the current row, thereby drastically reducing the search-region size and increasing computational efficiency. Second, a displacement error detection and correction method is developed to overcome the local tracking errors that may be more severe with freehand scanning and thereby improve the robustness of the algorithm. This algorithm has been implemented on a clinical ultrasound imaging system, and with real-time imaging feedback, long sequences of high quality strain images are observed using freehand compression. Displacement estimation errors with this method are experimentally measured and compared with results from simulation. We report only a specific implementation, with no comparison to other displacement estimators in the literature and no optimization of this specific technique. Images of tissue-mimicking phantoms with small spherical targets are used to test the ability to detect small lesions using the strain imaging technique. *In vivo* strain images of breast and thyroid are also shown.

KEY WORDS: Elasticity; elastography; palpation; tissue characterization; ultrasound.

### 1. INTRODUCTION

Ultrasonic strain imaging<sup>1-9</sup> is expected to have great potential for improving soft tissue diagnosis. The vast majority of the strain imaging work in the literature has focused on proof of concept and algorithm development. However, two major advances need to occur to make ultrasonic strain imaging a clinically useful tool. First, there is a need to acquire rf (or equivalent) echo data under clinically acceptable conditions with high patient throughput and low rescanning rates. Second, there is a need to further develop the clinical interpretation and significance of these results. In this work, we concentrate our effort on the first issue.

A skilled sonographer can acquire B-mode images with relative ease. Low noise strain images are more difficult to produce. Deformation of heterogeneous tissue can result in complex motion and echo signal decorrelation between the pre- and postcompression rf echo frame pair. Echo signal decorrelation leads to large strain estimation errors. Most strain imaging techniques in the literature produce strain images in two steps. First, the rf echo data is acquired by either digitizing the output from a modified clinical ultrasound system or directly downloading the rf data from the system if it is available. Second, the stored rf echo frames are processed off-line to produce strain images. With off-line processing, it is difficult to know, while scanning, whether the acquired echo frame pairs are coherent enough for strain estimation. Hence, off-line data processing is not as efficient for clinical utilization as real-time imaging.

A more clinically desirable system would be capable of displaying B-mode images and strain images side-by-side in real-time. Real-time strain imaging can help clinicians determine whether satisfactory strain images are being acquired and can also help clinicians improve their freehand compression techniques. With real-time feedback, clinicians can adjust the compression speed and angle to compensate for irregular motion (large-scale rotation or lateral or elevational translation). Hence, real-time strain imaging increases data acquisition efficiency.

Another important aspect for clinical utilization of strain imaging is the technique used to deform the soft tissue. Most phantom experiments in the literature used motorized compression fixtures. These devices are cumbersome, limit the locations that strain imaging can be applied, and are time consuming to incorporate.<sup>8</sup> Thus freehand scanning is desirable. Doley et al have shown that, compared with motorized compression, the penalty for freehand scanning is small with tissue mimicking phantoms.<sup>6</sup> Hiltawsky et al have shown that strain imaging of breast tissues with freehand compression is feasible.<sup>7</sup>

Lorenz et al have developed a real-time freehand strain imaging system that is external to the ultrasound imaging platform.<sup>9</sup> Some encouraging results are obtained for prostate applications using the system. In their system, a modified 1-D cross-correlation algorithm is used for displacement estimation. It performs well with small strains (much less than 1%) since the motion is tracked only in one dimension. It is well-known in the literature that the contrast-to-noise ratio in strain images increases with the applied strain (below about 5%).<sup>5,10</sup> Hence, larger single step compression is desirable.

In our work, strain-imaging software is implemented within a high-end commercial ultrasonic imaging platform (SONOLINE Elegra, Siemens Medical Solutions, Ultrasound Group). The strain images are displayed in real-time, side-by-side with the regular B-mode images. For the purpose of estimating displacement with relatively large applied strain (1~2% for *in vivo* tissue and up to 5% for tissue mimicking phantoms), a modified 2-D block matching algorithm was selected. Block matching (template matching) algorithms are widely used in image processing applications for tracking motion. The most notable application is video compression standards such as MPEG. Its utilization in ultrasonic imaging was first reported by Trahey et al for blood flow estimation.<sup>11</sup>

The purpose of this paper is to report our work in developing a real-time freehand strain imaging technique. We report only a specific implementation with no comparison to other displacement estimators in the literature and no optimization of this specific technique.

In the next section, we will introduce our displacement and strain estimation algorithms. In the results section, we provide performance measures of this algorithm in the form of displacement estimation error and spatial resolution with tissue-mimicking phantoms. We also provide examples of *in vivo* strain images obtained from this system. The conclusion section summarizes this work.

## METHODS

### 1. Standard block matching

The 2-D block matching algorithm computes a sum-squared difference (SSD) between pre- and postcompression rf frames for a rectangular kernel over a search region as follows:

$$SSD(u, v) = \sum_{i=-(K_1-1)/2}^{(K_1-1)/2} \sum_{j=-(K_2-1)/2}^{(K_2-1)/2} [r_1(I+i, J+j) - r_2(I+i+u, J+j+v)]^2 \quad (1)$$

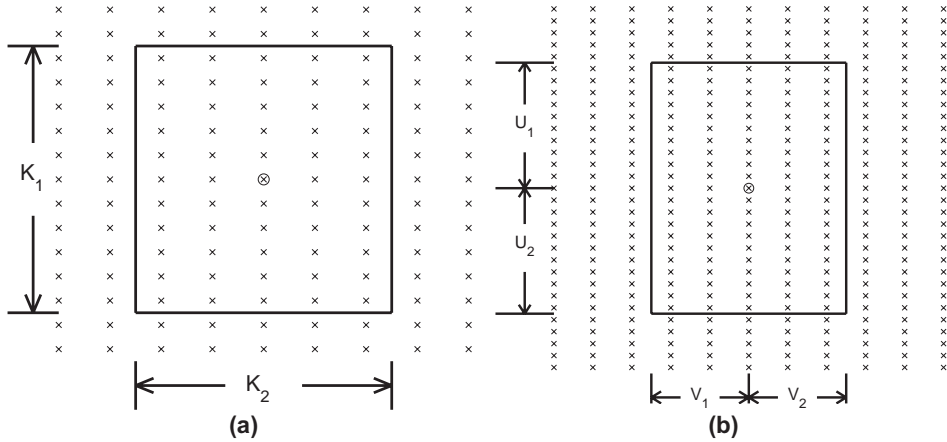


**FIG. 1** Illustration of a kernel and search region. (a) Illustration of a kernel. (b) The search region defining the range of locations of kernel centers. Each 'x' represents an rf data sample. A kernel is composed of several adjacent rf A-lines (5 in our implementation) with several rf samples (11 in our implementation) per line in the pre-compression rf field. The search region defines the range of possible locations of the center of the kernel in the postcompression rf field.

where  $r_1$  and  $r_2$  are pre- and postcompression rf echo fields, respectively;  $I$  and  $J$  are axial and lateral rf sample indices for the location where the displacement is estimated;  $u$  and  $v$  define search locations in a search region; and  $K_1$  and  $K_2$  are kernel height and width, respectively. The kernel size is empirically chosen to be 11 axial samples by 5 A-lines ( $K_1 = 11$  and  $K_2 = 5$ ) for a 7.5MHz transducer, or approximately half the area of the pulse-echo point-spread function. A pictorial illustration of the kernel and search region is shown in figure 1. For each location  $(I, J)$  at which the displacement is estimated, the SSD function is computed for every rf sample location that is within the search region (range of kernel centers) defined by  $-U_1 = u = U_2$  and  $-V_1 = v = V_2$ , where  $U_1$ ,  $U_2$ ,  $V_1$ , and  $V_2$  represent search up, down, left and right distances, respectively, as shown in figure 1. The search-region height and width are  $U = U_1 + U_2 + 1$  and  $V = V_1 + V_2 + 1$ , respectively. The displacement distribution usually does not need to be estimated as finely as rf samples. We use  $k$  and  $l$  as axial and lateral indices of displacement estimates. The location,  $(u_{\min}, v_{\min}) = (d_1(k, l), d_2(k, l))$ , at which the minimum SSD is found is considered to be the displaced position of the kernel. Hence,  $d_1(k, l)$  and  $d_2(k, l)$  are axial and lateral displacement estimates, respectively.

The computational cost of the block-matching algorithm to produce one displacement estimate is mainly determined by the kernel and the search-region sizes. In fact, to estimate one displacement vector, the subtraction-square-accumulation operation defined in Eq. (1) needs to be performed  $K_1 K_2 U V$  times. The computed SSD values are then compared  $UV$  times to find the minimum. Since the kernel size is usually predefined and fixed, the task of reducing the computational cost of the block matching algorithm is to find a way to minimize  $U$  and  $V$ .

It is straightforward to estimate the computational load of the typical implementation of SSD-based block matching. In this case,  $U$  and  $V$  are selected to be sufficiently large to guarantee that the displacement vector is enclosed by the search region. Assume the size of each rf echo field is 40 mm by 40 mm (typical in our experiments) and the maximum applied strain is 5%. The associated axial displacement magnitude is then  $0.05 \times 40 \text{ mm} = 2 \text{ mm}$ . The axial sampling frequency for our study is 36 MHz, so the maximum axial displacement magnitude is about 94 samples. Assuming uniaxial compression of an incompressible medium, the to-

tal lateral strain is at most 5% (assuming no elevational expansion). However, it is difficult to accurately estimate the maximum lateral displacement magnitude since we do not know the location of the center of the compression (location where lateral displacement is zero). If we assume the center of the compression occurs at the middle of the data field, the maximum lateral displacement magnitude is  $0.05 \times 20 \text{ mm} = 1 \text{ mm}$ . Given that the rf echo field usually consists of 200 A-lines, the maximum lateral displacement magnitude is about 5 A-lines. With these assumptions, the search-region size can be chosen as  $94 \times 2+1$  by  $5 \times 2+1$  or  $UV=189 \times 11=2079$ .

## 2. Search region reduction

The size of the search region can be minimized by using prior knowledge. The axial and lateral strain are defined by the following partial differential equations

$$s_1(k, l) = \frac{\partial d_1(k, l)}{\partial x_1}, \quad (2)$$

$$s_2(k, l) = \frac{\partial d_2(k, l)}{\partial x_2}.$$

In the sampled space, the axial and lateral strain can usually be approximated by the following difference equations

$$s_1(k, l) = \frac{d_1(k, l) - d_1(k-1, l)}{x_1(k, l) - x_1(k-1, l)}, \quad (3)$$

$$s_2(k, l) = \frac{d_2(k, l) - d_2(k, l-1)}{x_2(k, l) - x_2(k, l-1)},$$

where  $x_1(k, l)$  and  $x_2(k, l)$  are the axial and lateral coordinates of the location of the displacement estimate  $(k, l)$ , respectively;  $k-1$  and  $l-1$  represent the indices of adjacent displacement estimates relative to  $k$  and  $l$ . The following inequalities can be derived from Eq. (3)

$$|d_1(k, l) - d_1(k-1, l)| \leq S_1 |x_1(k, l) - x_1(k-1, l)|, \quad (4)$$

$$|d_2(k, l) - d_2(k, l-1)| \leq S_2 |x_2(k, l) - x_2(k, l-1)|,$$

where  $S_1$  and  $S_2$  are the maximum (allowed) local strain magnitudes in the axial and lateral directions, respectively. The spatial separations of displacement estimates are  $x_1(k, l) - x_1(k-1, l)$  and  $x_2(k, l) - x_2(k, l-1)$ , respectively. For real-time strain imaging, the axial separation is 16 samples and the lateral is 2 A-lines. Experiments in phantoms have demonstrated that displacement can be estimated when the applied strain is greater than 5%. However, strain contrast-to-noise ratio decreases rapidly for applied strain in excess of 5%.<sup>10</sup> Our *in vivo* experiments have shown that the displacement can be successfully estimated for applied strain up to about 2%. Noise dominates in the displacement estimates when the applied strain is more than 2% for *in vivo* tissues. We can use this as prior knowledge to limit the ex-

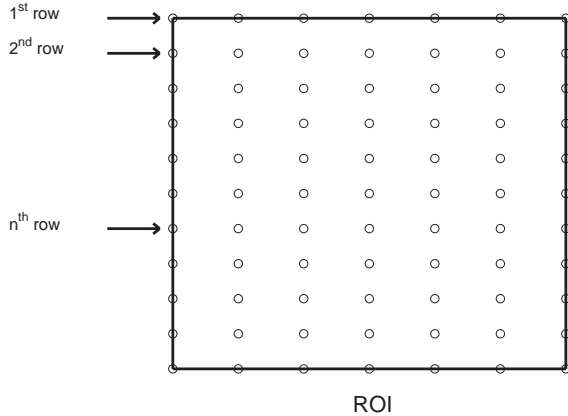


**FIG. 2** Illustration of an ROI. Grid points (circles) are locations at which the displacement distribution is estimated. Each grid point coincides with an rf sample location, but the displacement distribution is less densely sampled than the rf echo signals. In our real-time implementation, grid point separations are 16 samples in the axial direction and 2 A-lines in the lateral direction.

tent of the search region. Note that if the displacement difference between adjacent estimates is 1 sample in the axial direction and 1 A-line in the lateral direction, then Inequalities (4) give us

$$\begin{aligned} S_1 &\leq 6.25\%, \\ S_2 &\leq 50\%. \end{aligned} \tag{5}$$

The maximum local strain we intend to estimate is less than 6.25%. If we estimate displacement in the order of increasing  $k$  and  $l$  (row by row and from left to right), then the displacement that is currently being estimated is within a 3 sample by 3 sample block centered at the location predicted by the previously estimated displacement (one sample in each direction away from our best guess). In other words, we can reduce the search-region size to 3 by 3 if we use the previous estimates to predict where to search for adjacent estimates. Note that we allow larger local strain than the total strain since the strain distribution is not uniform. With the search region reduction,  $UV=3\times 3=9$ . Compared to typical block matching, the new method reduces the computational load by a factor of  $2079/9 = 231$ .

In implementing the reduced search-region block-matching strategy, we first manually select a region of interest (ROI) which is a subregion of the field of view. For example, in breast imaging, we select an ROI that excludes undesired echo regions. The locations at which the displacement is estimated are determined by grid points with equal spacing starting at the upper-left corner of the ROI, as shown in figure 2. The displacement is then estimated in two stages. In the first stage, the displacement of the first row of grid points, as shown in figure 2, is estimated using Eq. (1). Since there is no prior knowledge of the displacement distribution, a large search region is used. The size of the search region at this stage is determined by the following equations.

$$\begin{aligned} U_1 = U_2 &= \text{CEIL}(S_1 x_1(0,0)), \\ V_1 = V_2 &= \text{CEIL}(S_1 A), \end{aligned} \tag{6}$$

where  $CEIL$  is the function that rounds to the next larger integer;  $x_1(0,0)$  is the depth of the top of the ROI;  $A$  is the number of A-lines in the field of view. The search region created by Eq. (6) is large enough to enclose the true displacements as long as the applied strain does not exceed  $S_1$ .

In the second stage, the displacement is estimated from the top of the ROI to the bottom, row by row. Displacement estimates obtained in the first row are used to predict displacements in lower rows, and the search region in this stage is reduced to 3 rf samples by 3 A-lines using the equation

$$SSD(u, v) = \sum_{i=-(K_1-1)/2}^{(K_1-1)/2} \sum_{j=-(K_2-1)/2}^{(K_2-1)/2} [r_1(I+i, J+j) - r_2(I+d_1(k-1, l)+i+u, J+d_2(k-1, l)+j+v)]^2. \quad (7)$$

In Eq. (7), a search center,  $(I+d_1(k-1, l), J+d_2(k-1, l))$ , is used to guide the search. In other words, when we do not have any knowledge of the displacement distribution, the search center is  $(I, J)$ . After a row (or rows) of the displacement distribution is estimated, that information can be used to guide the search at neighboring locations and allows the use of a small search region. Note from Inequalities 4 that it is logical to set the search-region center to be  $(I+d_1(k-1, l), J+d_2(k, l-1))$ . However, since the difference between  $d_2(k-1, l)$  and  $d_2(k, l-1)$  is small, the search-region center is selected as  $(I+d_1(k-1, l), J+d_2(k-1, l))$  to simplify the algorithm.

The computational load can be further reduced by performing the 2-D (3 by 3 search region) search sparsely. Lateral displacement does not need to be estimated as densely as axial displacement because lateral sample spacing is much greater than axial. For real-time imaging, we can apply 3 by 3 search regions every 5 rows and use the lateral displacement estimates to guide the next 4 rows of displacement estimation. These 4 rows of displacement estimates are obtained using a 3 by 1 search region (1-D search). An even more aggressive strategy is to only estimate the lateral displacement for the first row and use this to predict the lateral displacement for the remaining rows and limit the 2-D search to the first row only.

### 3. Displacement error detection and correction

Two types of displacement estimation errors can occur. It is common for large errors to appear in the first row. This is due to the inherent pre- and postcompression rf waveform decorrelation and periodic ambiguities ('false-peak errors') associated with large search regions. Figure 3 shows an example of this type of error.

The second type of error results from correlations in displacement estimates when using predicted displacements to reduce the search-region size. Errors in displacement estimates propagate if they are large enough that the defined search regions do not enclose true displacements. When tissue is compressed, large and irregular local deformation can occur. This may cause local decorrelation in the recorded rf frame pair. Figure 4 shows an example of this type of error. The displacement estimation errors tend to accumulate when estimating displacement near those local regions.

A segmentation method that can detect and correct large errors is needed to overcome these problems. Each row of the displacement estimates is checked for errors in three steps. In the first step, from left to right within a row, the displacement estimates are segmented. Segmentation occurs if the difference between adjacent displacement estimates is larger than 2 samples. The result of this step for the displacement curve shown in figure 3 (row

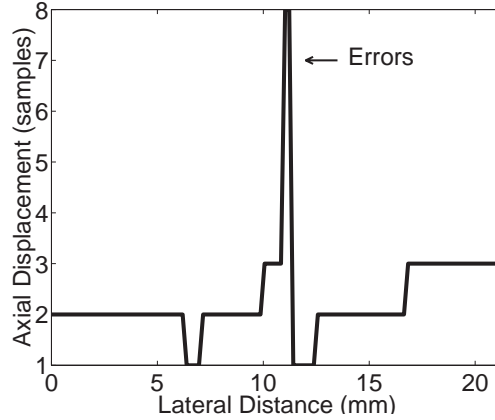


FIG. 3 Example of errors in the first row displacement estimates.

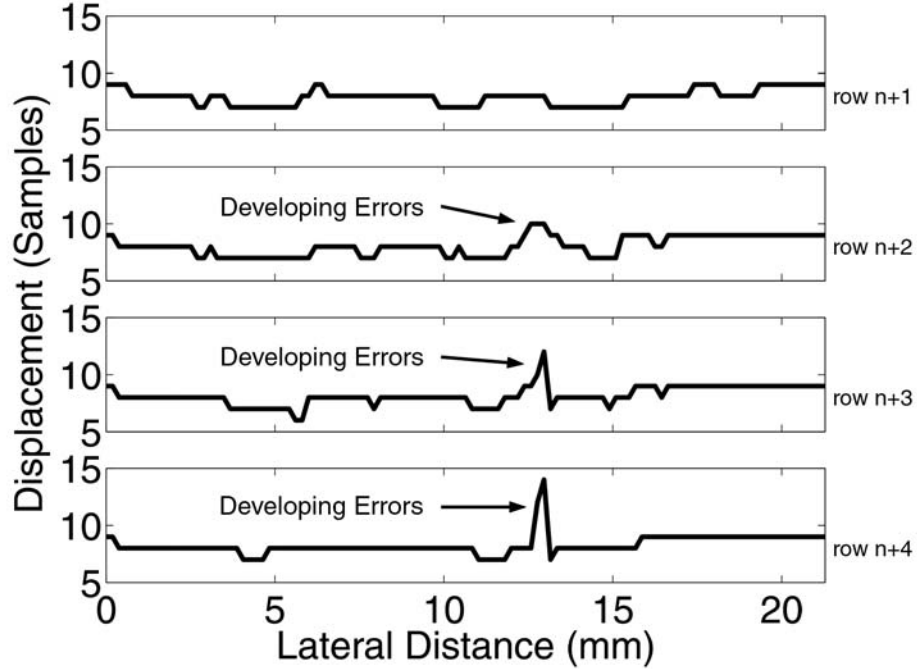
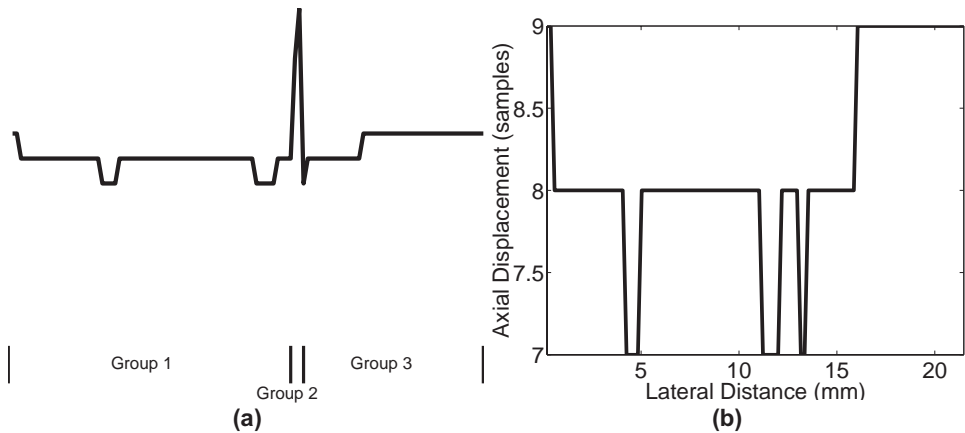
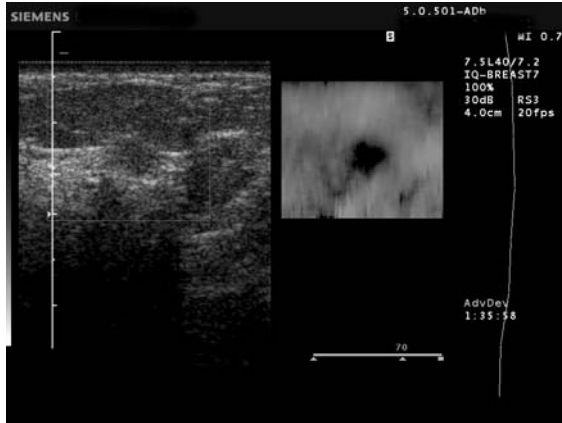


FIG. 4 Example of errors in consecutive rows with a 3x3 search region.

$n+4$ ) is shown in figure 5(a) where the displacement estimates are segmented into three groups. In the second step, groups that are not adjacent are merged if the difference of displacement estimates between two nearest end points of the two groups is smaller than a threshold (3 samples in this case). For the example displacement curve, group 3 is merged into group 1. In the last step, the group that has the largest number of displacement estimates ('members', group 1 in this example) is marked as the 'correct' group of displacement estimates and all remaining groups are marked as errors. In the error correction stage, the displacement values of the error groups are then discarded and replaced by linearly interpolating values from the correct group. Figure 5(b) shows the displacement curve after error correction.



**FIG. 5** Demonstration of error detection and correction. (a) Groups that are generated after initial segmentation. This displacement curve is the same as row  $n+4$  in figure 4. (b) Displacement curve after error correction with the segmentation method.



**FIG. 6** Example of B-mode and strain images displayed side-by-side on an Elegra monitor during patient scanning.

Tests with *in vivo* data have shown that the error detection and correction process does not need to be applied to every row of displacement estimates. Displacement errors build up gradually since the small search region prevents large displacement deviations between adjacent rows. Errors are more apparent and easier to detect after the displacement estimation process progresses several rows. With this observation, we apply the error detection and correction process once every 5 rows. For each detected error, all 5 displacement estimates are replaced by the interpolated values.

#### 4. Subsample accuracy displacement estimation

The displacement distribution that is estimated using this modified block matching algorithm has integer sample accuracy. With 36 MHz sampling and the strain estimation method described below, we find in phantom experiments that when the total applied strain is larger than 2%, this accuracy is adequate for creating low noise strain images. However, when the total applied strain is smaller than 2%, obvious strain artifacts can be seen in the image.<sup>12,13</sup> There are two ways of alleviating this problem. One way is to interpolate recorded rf frames



**FIG. 7** Photograph of a transducer with the compressor plate mounted.

to higher sampling frequencies. This will increase the computational cost tremendously since interpolation requires computation and the kernel and search-region sizes must be increased. The alternative method, used in our implementation, is to quadratically interpolate the SSD values around the minimum to obtain sub-sample accuracy in displacement estimates. With this added processing, the strain artifacts are not severe when the applied strain is more than 0.2%.

### 5. Strain estimation

The axial strain is defined as the spatial derivative of the axial displacement, and there are several methods to estimate this derivative. The simplest methods are forward, backward, and center differences where only two data points are used. Estimating derivatives using only two data points requires low noise in displacement estimates. Since a relatively small kernel is used to estimate displacement, the noise in the displacement is too high to use these methods. However, axial strain can be estimated using a low order polynomial curve fitting method,<sup>14</sup> and we have implemented a linear regression strain estimator. In addition, this method provides the ability to trade off spatial resolution for increased smoothness of strain images. The strain images have better spatial resolution, but more noise, if shorter segments of displacement estimates are used in linear regression. The strain images are visually well balanced in smoothness and spatial resolution if the linear window length is set between 2-3 mm for a 7.5 MHz transducer.

## IMPLEMENTATION

We have implemented the modified block matching algorithm on the Siemens Sonoline Elegra. The strain imaging software is an application that resides in the Elegra. The real-time beamformed I-Q (analytical representation of the rf signal<sup>15</sup>) frames are passed to a digital signal processor subsystem. That subsystem houses two Texas Instruments TMS-320C80 MVP processors that execute the software. An I-Q frame pair is used for displacement and strain estimation. The first frame is also envelope detected and a B-mode image is formed. Then, both B-mode and strain images are displayed side-by-side on the Elegra's monitor as shown in figure 6. The strain image corresponds to a region of interest (ROI) marked by the white-outlined rectangular subregion on the B-mode image. A user interface

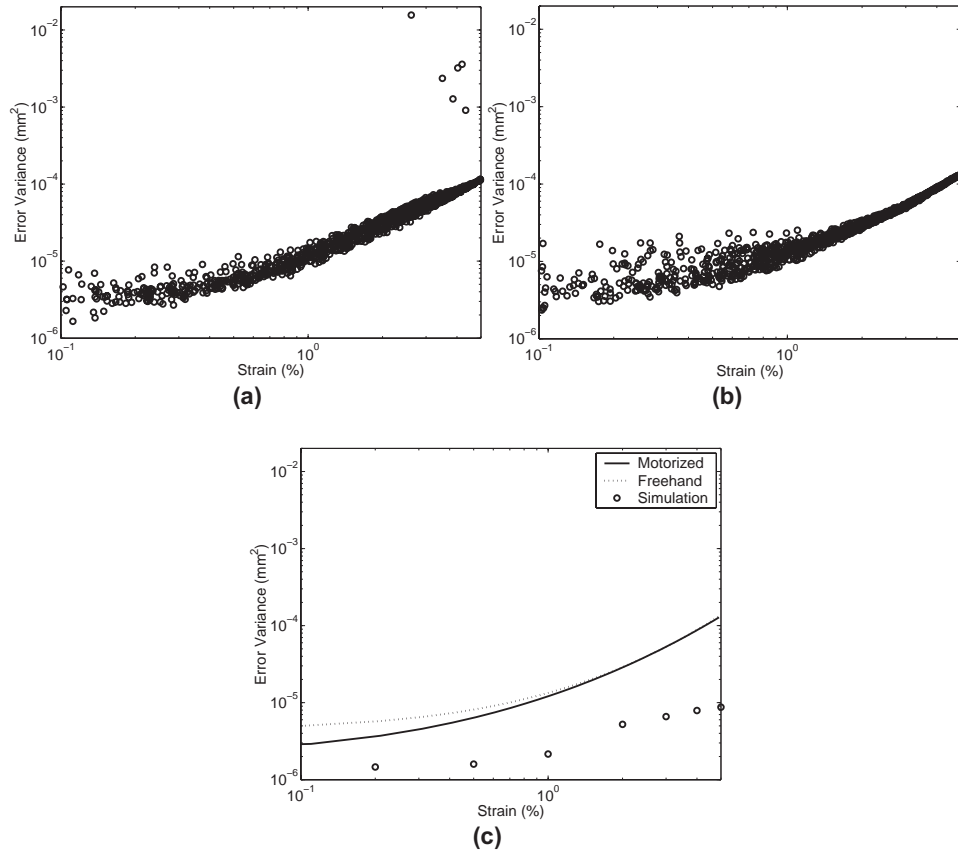


**FIG. 8** Plots of the variance in displacement estimate errors for experimental and simulated data. (a) Motorized compression. (b) Freehand compression. (c) Curve-fits for experimental data with simulated data. In (c), the solid and dotted curves represent results obtained from motorized and freehand compression, respectively; circles are data obtained from simulation.

allows the adjustment of the size and location of the ROI, the separation (in the data stream) between I-Q frames used to estimate strain, and some of the strain visualization parameters such as strain to gray-scale mapping, etc. This software is capable of displaying the side-by-side images at about 7 frames/second.

With this system, strain imaging is performed in three stages. In the setup stage, the sonographer locates the lesion and selects the ROI in which the strain is estimated and displayed. Then, by pushing a button, the software enters the real-time side-by-side display mode. The user starts the compress-release cycle. If the user finds an image sequence that is of interest, she can freeze the data acquisition. A cine-mode allows the user to browse each frame or loop through a selected set of frames for a more careful study of the acquired data.

Tissue deformation is generated by cyclic motion of the transducer (i.e., compressing and releasing the body surface). A small (4.5 cm x 9 cm) compressor plate can be mounted to the face of the transducer to enlarge the compression surface and produce a more uniform stress field<sup>16</sup>. A picture of the transducer with a mounted compressor plate is shown in figure 7. Krouskop et al<sup>17</sup> have shown that if the cyclic motion is approximately 1Hz, then the breast tissue components behave as elastic materials (i.e., the viscous effects are negligible). Hence, during data acquisition, cyclic deformation of about 1Hz is attempted.

Experiments have shown that 7/s frame rate is sufficient for a sonographer to scan freehand and control the compression motion of the transducer to compensate for undesirable lateral and elevational motion. No additional motion restricting device is necessary. However, successfully acquiring strain image data is not trivial. The sonographer needs to understand that the information being extracted is mechanical in nature and that the major challenge in strain image scanning is to minimize the rf waveform decorrelation.

Note that most of the parameters involved in the processing that generates strain estimates have not been optimized. These parameters include the kernel size used in the block-matching algorithm and the window length used in the moving linear regression algorithm that estimates strain from the displacement distribution. The optimization will be performed in our future work.

## RESULTS

All data sets shown in this section were acquired using the system described above. A 7.5L40 linear array transducer (pulsed at 7.2MHz) was used in our data acquisition. The field of view was 40 mm x 40 mm. The system performance is studied in terms of basic image quality parameters. Reported here are representative measurements of noise and resolution. More detailed investigations into these topics will follow in future work after the processing parameters are optimized.

### 1. Displacement estimation error

The variance of the error in the displacement estimates was measured using a uniform gelatin phantom to produce a predictable displacement distribution. Both motorized compression and freehand compression were used in order to compare the variance of displacement errors with each of these methods. The motorized compression (a laboratory system<sup>10</sup>) used a large compression plate that covered the entire upper surface of the free-standing gelatin block (10 cm x 10 cm x 7 cm (WxDxH), no additional fixtures). The motor was programmed to produce a sinusoidal compression of 20% at 0.4 Hz. Freehand scanning was performed with the compressor plate shown in figure 7 and the compression was intended to replicate that of motorized compression. The separation between I-Q frame pairs, called the skip number and used for strain image formation, was adjusted to achieve a wide range of frame-average strains from these data sets.

The acquired data sets were processed off-line using an algorithm identical to that programmed on the Elegra. Since the phantom had uniform stiffness, the displacement curve along the compression direction should be a straight line (strain is constant over the entire field of view). Linear regression was applied to the estimated displacement curve along each A-line in the region of interest to generate the best-fit displacement curve. This line was then considered to be the true displacement. The displacement error was calculated as the difference between estimates and the fitted lines. The corresponding strain was calculated by averaging over strain estimates for all A-lines in the ROI.

We also simulated rf frame pairs for the medium with uniform stiffness.<sup>5</sup> The scanning pulse, sampled at 36 MHz, had 7.2 MHz center frequency, a -6 dB bandwidth of 40% and a Gaussian lateral profile with -6 dB beam-width of 400  $\mu$ m and beam spacing of 200  $\mu$ m. These parameters closely simulated the beam profile produced by the Elegra 7.5L40 probe. The simulated compressions resulted in applied strains of 0.2, 0.5, 1, 2, 3, 4 and 5%. For each compression, 30 rf frame pairs were generated and the modified block-matching algorithm

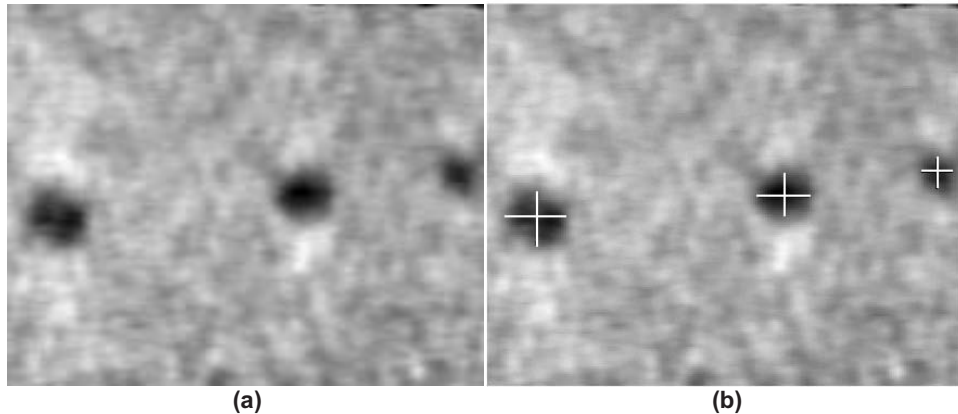


**FIG. 9** Strain image (a) of a phantom with spherical targets. The average strain is 2.5%. The size measurements, shown in (b), are accurate, as detailed in table 1.

was used for displacement estimation. The displacement estimates were compared with the known true displacements to calculate the variance of the displacement estimation error.

Figure 8 shows the variance of the displacement estimation error versus the estimated applied strain. In figure 8(a) and (b) (motorized and freehand compression, respectively) the first 50 frames in the collected rf data sequences were used as precompression data fields. The skip number was varied from 1 to 15 for motorized compression and from 1 to 25 for freehand compression to achieve strains ranging from 0.1% to 5%. There were a total of 725 strain and variance measurements for motorized compression and 1250 measurements for freehand compression. In figure 8(a), there are 6 measurements with high displacement estimation error at relatively high strain. These are the cases where the error detection and correction method failed due to excessive noise in the first row displacement estimates.

Displacement error variance estimates for motorized and freehand compression were fit to a second degree polynomial in log-log space to generate representative curves for each data set and those curves were plotted in figure 8(c). Note that the 6 measurements for motorized compression with high error variance were excluded when curve fitting. The circles in figure 8(c) are displacement error variance measurements obtained from the simulation. The standard deviations of the error variance measurements for simulation are so small that they are not plotted (they would not be visible if plotted).

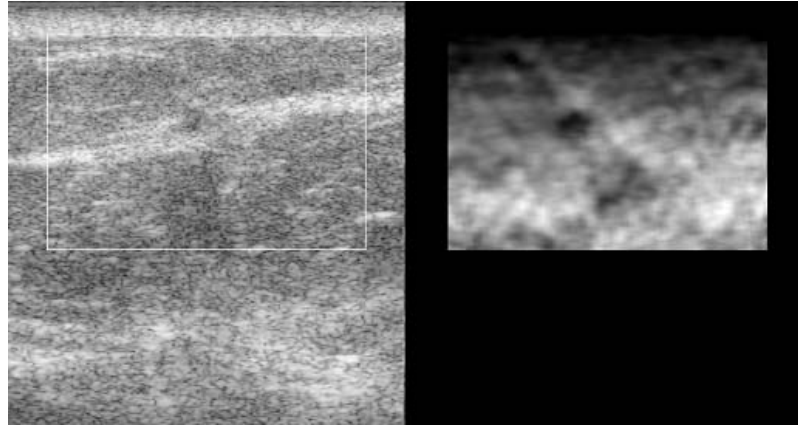
As seen in figure 8(c), the displacement error variance curve is relatively flat for strain less than 1%. This is likely due to the fixed displacement error produced by the quadratic interpolation.<sup>13</sup> The displacement estimate error variance for experimental data increases with the applied strain faster than the results obtained from simulation. This is likely due to elevational motion resulting from compressing the free-standing gel block (plane stress conditions), whereas the simulated data employed plane strain conditions (no elevational motion). Comparable performance is observed with motorized and freehand compression. Although motorized compression generally has slightly lower displacement errors, the benefit associated with freehand scanning offsets the small improvement in displacement estimate errors.

## 2. Small lesion detection

Gelatin phantoms with spherical targets that were three times stiffer than the background<sup>18</sup> were used to test the strain imaging system performance with small targets. The strain image (acquired with 2.5% compression) shown in figure 9(a) contains three targets (4.0 mm, 3.2

TABLE 1 Measured target size in millimeters.

	Leftmost target	Middle target	Rightmost target
<b>Height (axial)</b>	4.1	3.1	2.3
<b>Width (lateral)</b>	4.0	3.4	2.3
<b>Actual diameter</b>	4.0	3.2	2.4

**FIG. 10** Strain image of a 3 mm x 3 mm *in vivo* cyst in breast.

mm and 2.4 mm diameter, respectively). The apparent size of these targets was measured in the strain image in both axial and lateral directions. Figure 9(b) shows line segments that correspond to the width and height for each target and table 1 shows the measured sizes. These results suggest that spherical targets as small as 2.4 mm diameter can be accurately measured in both the lateral and axial dimensions.

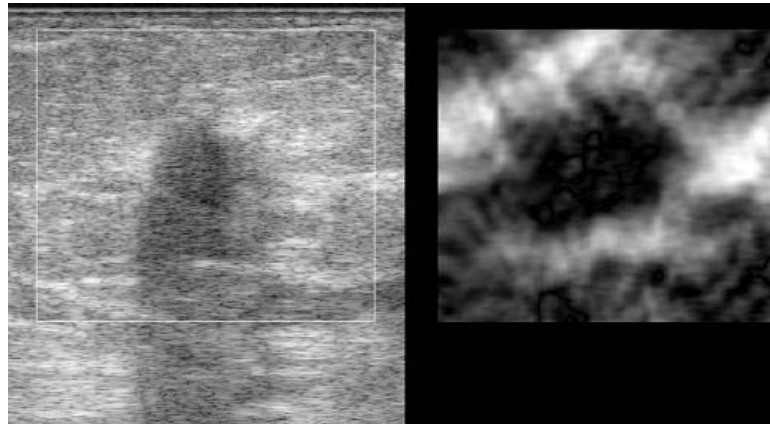
### 3. *In vivo* strain images

Real-time freehand strain imaging has also been performed on *in vivo* tissues. The images, shown below, demonstrate that these strain images have reasonably low noise and high contrast.

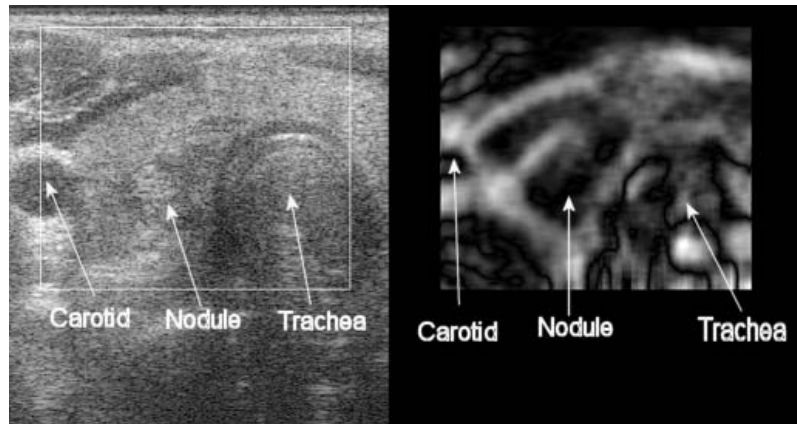
Figure 10 shows an *in vivo* breast cyst that is about 3 mm x 3 mm. The visibility of the cyst in the strain image confirms our phantom results that lesions of a few millimeters in diameter can be detected in the strain images. The exact reason that the fluid filled cyst appears stiffer than the background is unknown. A reasonable hypothesis is that the cyst fluid is bounded by a distended capsule and appears stiff much like an air-filled balloon feels stiff.

Figure 11 shows an *in vivo* breast carcinoma. The apparent size of the tumor is much larger in the strain image (about twice as big) than in the B-mode image. This is consistent with the findings of Garra et al.<sup>8</sup>

Figure 12 shows an *in vivo* thyroid strain image. There is a nodule inside the thyroid, seen in both B-mode and strain images. The tissue structures and therefore the boundary conditions around the thyroid are very different from the breast, and in both cases compression induced motion is complex. However, with real-time feedback, the sonographer can manipulate the compression technique and obtain strain images. A problem in strain imaging of the thyroid is that the trachea and major blood vessels are often included in the field of view. Since



**FIG. 11** Strain image of an *in vivo* breast carcinoma.



**FIG. 12** Strain image of an *in vivo* thyroid with a nodule. Flow in the carotid and echo noise in the trachea cause errors in motion tracking and strain estimation.

there are no echo signals from the trachea, displacement estimates in this region are at best misleading. The blood flow in the carotid is perpendicular to the image plane and introduces elevational motion that causes echo signal decorrelation and motion tracking errors. The observer must consider these factors for correct strain image interpretation in this case.

## CONCLUSION

A computationally efficient displacement estimation algorithm has been developed for real-time, freehand ultrasonic strain imaging. The proposed method is based on a block-matching algorithm that is widely used for motion detection in digital image processing. Major modifications increase the computational efficiency and robustness of the typical block matching algorithm. The algorithm is implemented on the Siemens SONOLINE Elegra as an add-on software application.

With real-time feedback of strain images, sonographers can adjust their compression/scanning technique to consistently form strain images. Strain images with acceptable quality are observed in both breast and thyroid scanning, which require different scanning tech-

niques and where the motion is much more complex than in phantoms. Since the algorithm is implemented on a commercially available clinical imaging system, data can be efficiently acquired from a large number of patients, enabling clinical evaluation of strain imaging in soft tissue diagnosis.

## ACKNOWLEDGEMENTS

We are grateful for the technical assistant provided by Siemens Medical Solutions Ultrasound Group. Without their help this work would not have been accomplished. All *in vivo* scanning was done by Candace S. Spalding. We greatly appreciate her help. We are also grateful for the financial support of USAMRAA DAMD17-00-1-0596 and NSF BES-9708221. The U.S. Army Medical Research Acquisition Activity, 820 Chandler Street, Fort Detrick MD 21702-5014 is the awarding and administering acquisition office for DAMD17-00-1-0596. The information reported here does not necessarily reflect the position or policy of the U.S. Government, and no official endorsement should be inferred.

## REFERENCES

1. Tristam, M., Barbosa, D.C., Cosgrove, D.O., Nassiri, D.K., Bamber, J.C. and Hill, C.R., Ultrasonic study of *in vivo* kinetic characteristics of human tissues, *Ultrasound Med. Biol.* 12, 927-937 (1986).
2. Krouskop, T.A., Dougherty, D.R. and Vinson, S.F., A pulsed Doppler ultrasonic system for making non-invasive measurements of the mechanical properties of soft tissues, *J. Rehab. Res. Dev.* 24, 1-8 (1987).
3. Ophir, J., Céspedes, I., Ponnekanti, H., Vazdi, Y., and Li, X., Elastography: a quantitative method for imaging the elasticity of biological tissues, *Ultrasonic Imaging* 13, 111-134 (1991).
4. O'Donnell, M., Skovoroda, A.R., Shapo, B., and Emelianov, S., Internal displacement and strain imaging using ultrasonic speckle tracking, *IEEE Trans. Ultrason. Ferroelec. Freq. Contr.* 41, 314-325 (1994).
5. Chaturvedi, P., Insana, M.F. and Hall, T.J., 2-d companding for noise reduction in strain imaging, *IEEE Trans. Ultrason. Ferroelec. Freq. Contr.* 45, 179-191 (1998).
6. Doyley, M.M., Bamber, J.C., Fuechsel, F. and Bush, N.L., A freehand elastographic imaging approach for clinical breast imaging: system development and performance evaluation, *Ultrasound Med. Biol.* 27, 1347-1357 (2001).
7. Hiltawsky, K., Kruger, M., Starke, C., Heuser, L., Ermert, H., and Jensen, A., Freehand ultrasound elastography of breast lesions: clinical results, *Ultrasound Med. Biol.* 27, 1461-1469 (2001).
8. Garra, B.S., Céspedes, I., Ophir, J., Spratt, S.R., Zuurbier, R.A., Magnant, C.M. and Pennanen, M.F., Elastography of breast lesions: initial clinical results, *Radiology* 202, 79-86 (1997).
9. Lorenz, A., Sommerfeld, H.J., Garcia-Schurmann, M., Philippou, S., Senge, T. and Ermert, H., A new system for the acquisition of ultrasonic multicompression strain images of the human prostate *in vivo*, *IEEE Trans. Ultrason. Ferroelec. Freq. Contr.* 46, 1147-1154 (1999).
10. Chaturvedi, P., Insana, M.F., and Hall, T.J., Testing the limitations of 2-D local companding in strain imaging using phantoms, *IEEE Trans. Ultrason. Ferroelec. Freq. Contr.* 45, 1022-1031 (1998).
11. Trahey, G.E., Allison, J. W. and von Ramm, O.T., Angle independent ultrasonic detection of blood flow, *IEEE Trans. Biomed. Eng.* 34, 965-967 (1987).
12. Varghese, T. and Ophir, J., Characterization of elastographic noise using the envelope of echo signals, *Ultrasound Med. Biol.* 24, 543-555 (1998).
13. Alam, S.K. and Ophir, J., The effects of nonlinear signal transformations on bias errors in elastography, *IEEE Trans. Ultrason. Ferroelec. Freq. Contr.* 47, 297-303 (2000).
14. Kallel, F. and Ophir, J., A least-squares strain estimator for elastography, *Ultrasonic Imaging* 10, 195-208 (1997).
15. Urkowitz, H., *Signal Theory and Random Processes* (Artech House, Inc., Norwood, MA, 1983).

16. Konofagou, E., Dutta, P., Ophir, J. and Céspedes, I., Reduction of stress nonuniformities by apodization of compressor displacement in elastography, *Ultrasound Med. Biol.* 22, 1229-1236 (1996).
17. Krouskop, T.A., Wheeler, T.M., Kallel, F., Garra, B.S. and Hall, T.J., Elastic moduli of breast and prostate tissues under compression, *Ultrasonic Imaging* 20, 260-274 (1998).
18. Hall, T.J., Bilgen, M., Insana, M.F., and Krouskop, T.A., Phantom materials for elastography, *IEEE Trans Ultrason, Ferroelec. Freq Contr.* 44, 1355-1365 (1997).

● *Original Contribution*

## IN VIVO REAL-TIME FREEHAND PALPATION IMAGING

TIMOTHY J. HALL, YANNING ZHU and CANDACE S. SPALDING

Department of Radiology, University of Kansas Medical Center, Kansas City, KS, USA

(Received 26 February 2002; in final form 23 October 2002)

**Abstract**—Previous experience with laboratory fixtures and off-line processing of elasticity data showed that problems occurring in data acquisition often resulted in poor elasticity image quality. A system for real-time estimation and display of tissue elastic properties using a clinical ultrasonic imaging system has been developed. A brief description of that system and the initial clinical tests of that system are reported. Experience with real-time freehand elasticity imaging shows that images with high contrast-to-noise ratios are consistently obtained. Images of breast lesions were acquired with freehand palpation using standard linear-array ultrasound (US) transducers. Results in volunteer patients show that high-quality elasticity images are easily obtained from *in vivo* breast studies. The key element to successful scanning is real-time visual feedback of B-mode and strain images that guide the patient positioning and compression direction. Results show that individual images of axial strain in tissues can be quite misleading, and that a “movie loop” of side-by-side B-mode and strain images provides significantly more information. Our preliminary data suggest that the strain image sequences for various breast pathologies are unique. For example, strain images of fibroadenomas lose contrast with increasing precompression, but those of invasive ductal carcinoma have high negative contrast (dark relative to “normal” tissue) for a wide range of precompression. In addition, a comparison of the lesion area measured in B-mode vs. strain images, for a representative image from the sequence, appears to be a sensitive criterion for separating invasive ductal carcinoma from cyst and fibroadenoma. (E-mail: thall@wisc.edu) © 2003 World Federation for Ultrasound in Medicine & Biology.

**Key Words:** Ultrasound, Tissue characterization, Elasticity, Palpation, Elastography.

## INTRODUCTION

The potential for improving the qualitative nature of palpation by imaging quantitative measures of tissue viscoelasticity has generated a great deal of interest world-wide. Our initial efforts focused on modeling displacement and strain, developing algorithms for displacement and strain estimation, and testing those techniques in phantoms and in kidneys *in vitro* (see, for example, Chaturvedi et al. 1998a, 1998b; Hall et al. 1997; Insana et al. 1997; Zhu et al. 1998). Significant effort was expended on developing high-order motion estimators for tracking fine-scale motion. However, little data were available to investigate the need or utility of the high-order motion-estimation techniques for *in vivo* imaging of tissues.

The first report testing the utility of strain imaging in breast lesion imaging (Garra et al. 1997) clearly demonstrated that strain imaging had merit in breast lesion

discrimination. The data-acquisition system employed a modified mammography compression paddle and, therefore, was limited in the lesion locations that could be studied. Also, only (nonreal-time) static strain images were available. In that report, Garra et al. (1997) described a set of criteria applied to evaluate strain imaging combined with normal B-mode imaging. Among those criteria were lesion visibility, relative brightness, lesion margin regularity, lesion margin definition, lesion size (lateral and axial) and B-mode image measurements relative to strain image and pathology measurements. Among their findings, they noted that benign lesions have about the same width on B-mode and strain images, but that the height measurement had lower confidence due to axial blurring in strain image formation and difficulty in determining lesion boundaries with shadows due to high attenuation. Fibroadenomas typically had heterogeneous stiffness; cancers were uniformly stiffer than their surroundings in all but one case.

The purpose of the present study was to test the utility of performing strain imaging in real-time on a commercial ultrasound (US) imaging system and to test

Address correspondence to: Timothy J. Hall, Medical Physics Department, 1530MSC, 1300 University Ave, Madison, WI 53706 USA. E-mail: tjhall@wisc.edu

one of the strain image criteria described by Garra et al. (1997) with data acquired from this new system. Results demonstrate the value in real-time side-by-side display of B-mode and strain images for guiding data acquisition and data interpretation. Comparisons among various lesion types studied *in vivo* show a significant difference in the strain image sequence for fibroadenomas, cysts and carcinoma, and help to explain some of the difficulties in data interpretation described by Garra et al. (1997). Our results are generally consistent with those found by Garra and colleagues, but the differences we found in carcinoma size in B-mode and strain images are greater, and all lesions found in sonography or mammography, whether palpable or not, were visible with our techniques. These results will help to guide future strain-imaging data acquisition and provide further evidence for the potential of elasticity imaging in breast lesion discrimination.

## MATERIALS AND METHODS

The motion-tracking algorithm, its implementation on the commercial clinical US, imaging system and performance measurements in experiments with phantoms are reported elsewhere (Zhu and Hall 2002). The essential details are included here for the convenience of the reader.

### *Strain image formation*

A 2-D block-matching algorithm, based on the sum-squared difference (SSD) method, was used for motion tracking in our implementation. With this method, motion is tracked by searching for a kernel of data from the precompression radio frequency (RF) echo data in a 2-D search region of the postcompression RF echo field. A fixed kernel size (five A-lines by 11 RF samples) was used with both the 7.5L40 (with and without tissue harmonic imaging, THI) and the VFX13-5 linear arrays for the system employed (Siemens SONOLINE Elegra, Issaquah, WA). The data are temporally sampled at 36 MHz with a lateral beam spacing of 200  $\mu\text{m}$ . Therefore, the kernel size corresponds to about one half the area of the 2-D pulse-echo US point spread function for the 7.5L40 array pulsed at 7.2 MHz. A small kernel was chosen because the assumption of rigid body motion is increasingly accurate as the size of the kernel is decreased, and because spatial resolution is expected to improve with smaller kernels. No attempt to optimize the kernel size was pursued in this study. Kernel size optimization will likely be task-dependent and will be addressed in future work.

Data were processed on the image processor subsystem of the Elegra. This subsystem hosts two Texas Instruments TMS320C80 processors. To reduce the com-

putational load (required to achieve real-time frame rates), an adaptive search strategy was developed that reduces the size of the required search region in performing the SSD block matching. Displacements are estimated (for real-time imaging) with kernels that are separated by 16 RF samples center-to-center (no spatial overlap of displacement estimates). Displacements are estimated row-by-row, and the prior row of estimates are used to predict displacements in the current row, allowing the search region to be reduced to within one RF sample in each direction of the predicted displacements. The use of predicted displacements results in correlated displacement errors, and an error detection and correction scheme was also implemented. Strain is estimated from the displacement data using a linear regression technique similar to that described by Kallel and Ophir (1997). For real-time imaging, linear regression is performed with a 24-sample window (about 4 mm) that is incremented one displacement sample for each strain estimate. The resulting algorithm displays streaming B-mode and strain images side-by-side at about seven frames per second and stores the full sequence of I-Q (analytic form of the RF) echo data at full system bus speed. The stored data, which were acquired at a higher frame rate than the real-time display, can then be online postprocessed with the same displacement algorithm or other algorithms (not reported here), the size and location of the subregion-of-interest (SROI) can be adjusted, the grey-scale mapping can be modified, etc., and the results displayed frame-by-frame or as a cine loop.

Although the additional degrees of freedom of motion allowed with freehand compression, compared with motorized compression, were expected to result in an increase in displacement estimate error variance, that variance is only slightly higher for freehand compression (Zhu and Hall 2002). Given that the contrast and resolution of the strain-imaging system do not depend on the method of tissue deformation, displacement estimate error variance (resulting in strain image noise) is the dominant image quality parameter that will differ with the two methods of tissue deformation. With equal applied strain, motorized and freehand compression have comparable strain image noise. However, the frame-to-frame strain is not constant with freehand compression (as described below). This results in frame-to-frame variability in strain image quality with freehand scanning.

Small (*e.g.*, 2.4-mm diameter) isoechoic spherical targets in a phantom are considerably easier to locate and scan freehand than with motorized compression. The size of spherical targets measured from the resulting strain images is very close to their true dimensions (both height and width, see Zhu and Hall 2002), so both linear and area measurements in strain images *in vivo* should be accurate.

The grey-scale mapping of these strain images conforms with the *de facto* standard of mapping pixels, representing small strains dark and large strains bright. Typically, a sinusoidal (freehand) compress/release cyclic deformation was used and the acquired data contained one or more complete cycles. At the top and bottom of the stroke, there is little motion and, occasionally, there were brief hesitations during the motion. A consequence of freehand scanning is that the frame-to-frame strain is not constant. To compensate for that variability in average strain, the grey-scale for individual strain images (in the sequence of B-mode and strain images) was automatically adjusted to minimize brightness flicker. With this scaling, strain images that had an average strain of less than 0.15% were set to black. These frames rarely occur, but are most common at the top and bottom of the cyclic compression. Frames with greater than 0.15% compression were encoded as follows:

$$s_e(k, l) = \text{round} \left( \frac{s(k, l) - s_{\min}}{s_{\max} - 0.05 \frac{s_{\max}}{s_{\min}}} \right), \quad (1)$$

where  $s_e(k, l)$  is the encoded strain value at position  $(k, l)$ , and  $s_{\max}$  and  $s_{\min}$  are the maximum and minimum strain values in the frame, and  $\text{round}()$  is a function that rounds to the nearest integer. After scaling, the results are encoded into an 8-bit display range. This simple scaling provides a reasonably constant strain image brightness through the compression cycle, in the absence of significant displacement estimation errors. Large displacement estimation errors sometimes occur and this automatic grey-scale mapping can be dominated by erroneous displacement estimates.

#### Patient scanning

All patients provided informed consent consistent with the protocol approved by the Human Subjects Committee (Institutional Review Board) at The University of Kansas Medical Center. Patient scans were performed in a manner consistent with a normal breast US examination; the breast was scanned with the patient (typically) in the supine position with her ipsilateral arm behind her head. When the breast lesion was located, SROI was chosen that would avoid inappropriate data (lungs, areas of lost transducer contact, etc.) and the transducer was pressed toward the chest wall at a steady rate in an effort to achieve about 1–1.5% compression frame-to-frame. Subregion selection also typically excluded the retro-mammary fat layer and the chest wall. The soft fat, the stiff muscle and the slipping boundary between these layers can also dominate the dynamic grey-scale mapping. In some cases, for example, when scanning lateral

lesions in large (D-cup) breasts, the patient was rolled slightly to her contralateral side so that gravity would flatten the breast tissue in the region to be scanned. A small plate (approximately 45-mm wide, 90-mm long) was sometimes attached to the transducer body to extend the compression surface in an effort to provide a more uniform stress field and to control motion perpendicular to the image plane. The compress/release cycle was repeated for relatively large ( $> 10\%$ ) compression range, while watching the B-mode image. The compression motion was adjusted by changing the compression direction or patient position until there was nearly uniaxial compression with minimal elevation motion. With this achieved, the strain-imaging software was enabled to evaluate the quality of the sequence of strain images. If a large sequence ( $\geq 30$  frames) of strain images had good image quality (relatively high contrast-to-noise ratio) and high frame-to-frame similarity, the data acquisition was frozen, the image sequence stored, and the cine feature of this software was used to review, post-process and select images to record. If the compression rate was too slow, resulting in low frame-average strain, the interframe skip was adjusted to increase the strain between frame pairs used in displacement and strain estimation, as suggested by Lubinski *et al.* (1999). Representative results obtained when scanning a 3-mm cyst are shown in Fig. 1. The average strain per frame (Fig. 1b) suggests nearly ideal compression rate in this case. Consecutive frames were paired for displacement estimation when analyzing this sequence of data. The cumulative strain in the sequence (Fig. 1c), obtained by summing the strain in consecutive frames, demonstrates that about an 18% compression range was achieved in this study. The initial value on the ordinate axis in each plot was set to zero and (the frame-average) strain was accumulated (Fig. 1c) from that starting point. If, for example, there was a net compression of the tissue in the first frame pair, the initial average strain was negative and the first value on the cumulative frame plot was negative. Data acquisition was frozen by the operator when an acceptable image sequence was acquired. The starting and ending points of that sequence could be at any point in the cyclic motion. Therefore, the precompression at the starting point is a random value between the minimum and maximum precompression.

## RESULTS

One of the most promising uses of strain imaging is differentiation among breast lesions. To date, we have successfully scanned 39 patients with over 175 patient scans (multiple lesions per patient, repeat visits, perpendicular scan planes, different transducers and THI). Data from only 29 of these patients are included in this study

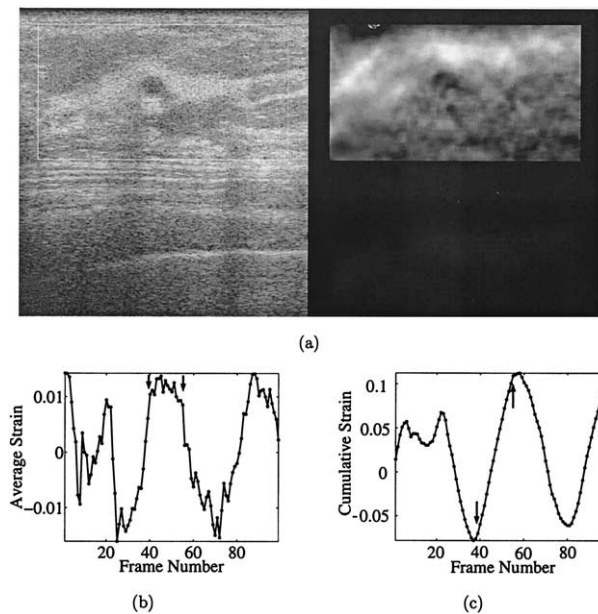


Fig. 1. Data obtained by freehand scanning of a breast cyst *in vivo*. (a) A B-mode and strain image pair obtained for frame 51 in the sequence. The white box in the B-mode image defines the ROI for strain imaging. (b) The average strain in the ROI; (c) the cumulative strain in the ROI. The arrows in (b) and (c) indicate that a sequence of frames was acquired with nearly equal average strain in each frame but with varying cumulative strain (precompression).

(data from patients with surgical scars or closely spaced lesions were excluded, as described below). Among these 29 patients, 19 fibroadenomas, 29 cysts and 7 carcinomas were included in this study. Ten of the fibroadenomas, at least five of the cysts and four of the carcinomas were palpable. All fibroadenomas were either pathologically proven or had been stable under radiological investigation for more than 1 year. All carcinomas were pathologically proven. Both simple and complex (hemorrhagic) cysts were included. Fibroadenomas, cysts and invasive ductal carcinomas have distinctive behavior in their strain image under cyclic compression, as detailed below.

One of the key tests was to show that strain images are reproducible, both within an image sequence and on repeat acquisitions. The question of reproducibility within an image sequence is addressed for each lesion type (fibroadenoma, cyst and invasive ductal carcinoma) below. Figure 2 shows results of repeating the freehand *in vivo* elasticity imaging on the same patient. A skilled sonographer can acquire a sufficiently similar B-mode image of an ROI with repeat scanning. However, obtaining a similar strain image requires that the ROI be found, and the direction of compression/release relative to the lesion and chest wall be the same in the two studies. No

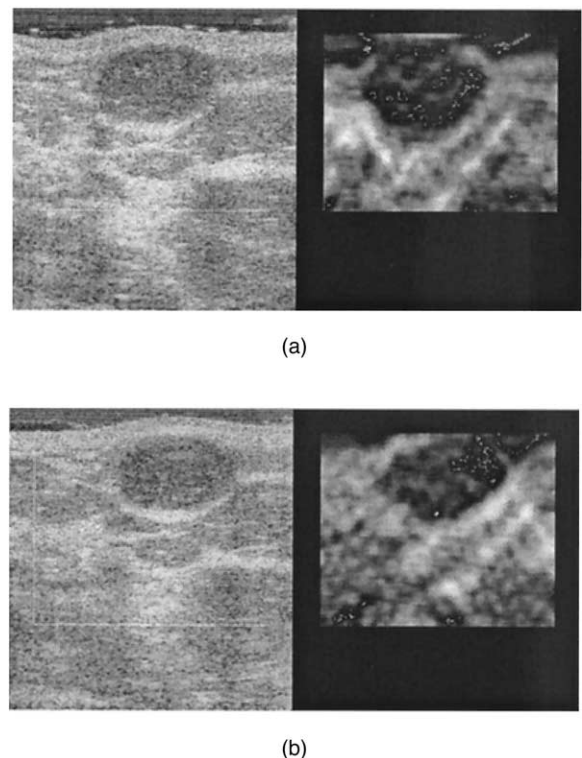


Fig. 2. Two image pairs from the same patient on repeat visits. The patient has a palpable fibroadenoma that measures about 16 mm  $\times$  11 mm. (a) The strain image acquired with the VFX13-5 array during the first visit, which is very similar to (b) that acquired with the 7.5L40 array 2 weeks later.

special effort was used to obtain similar images, but Fig. 2 demonstrates that the strain patterns in these images are very similar.

Too few independent samples of each lesion type have been observed to make strong statistical statements regarding each criterion described by Garra et al. (1997). The following descriptions state our qualitative observations to date, in the hope of guiding the scanning and image-evaluation techniques used by others in future studies. In particular, the automatic scaling of grey-scale values precludes quantitative statements of (and homogeneity of) relative stiffness.

A total of 37 B-mode and strain image sequences were acquired from 19 unique fibroadenomas among 9 patients. One of our most significant findings is that there was an obvious (subjective, visual) loss in strain image contrast for 14 of these 19 fibroadenomas (27 of 37 image sequences, 6 of 9 patients, average age 44 years). Fibroadenomas typically have negative contrast (are more stiff than their surroundings) at low precompression and lose contrast (stiffness becomes more like their surroundings) as they are compressed. An example of this is illustrated in Fig. 3. The largest negative contrast

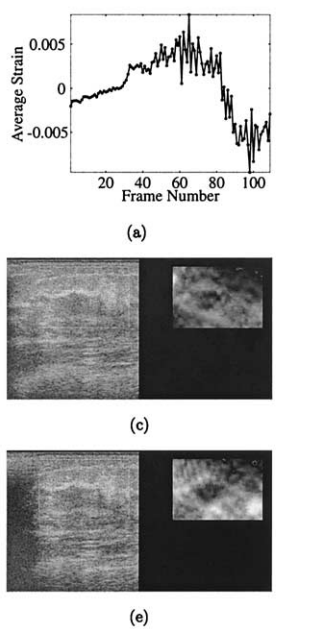


Fig. 3. Data obtained by freehand scanning of a fibroadenoma *in vivo*. (a) The average strain in the ROI for each frame suggests a slow compression rate. The interframe skip was increased to pair every fourth frame in analyzing this sequence of data. (b) The cumulative strain in the sequence shows that a 20% compression range was achieved. Images of fibroadenomas acquired with equivalent precompression [equivalent cumulative strain, frames (c) 75 and (e) 90, (d) 52 and (f) 106] are similar, but, because of the nonlinear stress-strain relationship of tissue, strain images acquired at different precompression can have significantly different contrast.

occurs with minimal precompression. Figure 3c and e shows that the transducer is barely in contact with the skin surface at this precompression. Comparing these with Fig. 3d and f demonstrates that images of fibroadenomas acquired within a sequence at equivalent precompression are very similar. However, as precompression changes, strain contrast changes (comparing Fig. 3c or e with d or f).

Both simple and complex cysts were included in this study, to investigate the possibility that fluid-filled cysts, regardless of "echogenicity," have a common behavior in cyclic strain images. The hope was that strain images might help to differentiate complex cysts from solid lesions that lack evidence of blood flow.

The frame-to-frame variability of strain images of cysts is more complicated than that observed with fibroadenomas. A total of 39 B-mode and strain image sequences were acquired from 29 unique cysts among 15 patients. A very soft bottom layer in the interior of the cyst was observed in 7 of 29 cysts (11 of 12 image sequences of those cysts). That layer might be due to a sediment inside the cystic fluid. Repositioning the patient

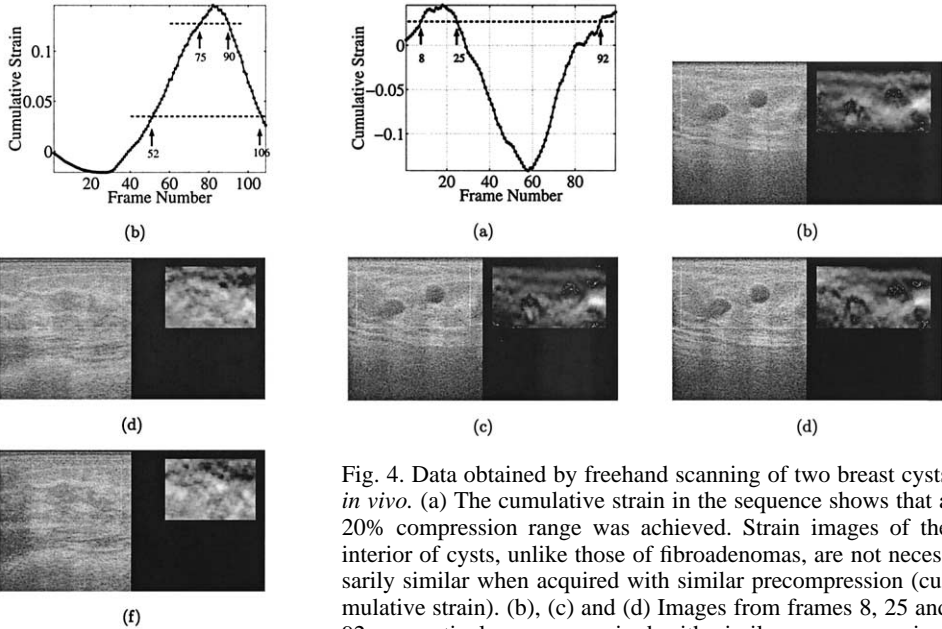


Fig. 4. Data obtained by freehand scanning of two breast cysts *in vivo*. (a) The cumulative strain in the sequence shows that a 20% compression range was achieved. Strain images of the interior of cysts, unlike those of fibroadenomas, are not necessarily similar when acquired with similar precompression (cumulative strain). (b), (c) and (d) Images from frames 8, 25 and 92, respectively, were acquired with similar precompression. Although strain images can vary smoothly from frame to frame, decorrelation of the signals within the cysts results in strain images that vary significantly over the compression cycle.

might have allowed us to confirm that conjecture, but that test was not performed. The interior echoes within the cysts rapidly decorrelate with compression. As a result, the apparent strain in the lesions varies with compression, but that compression-dependent strain image contrast is very different from that observed for fibroadenomas. If the incremental average strain from one strain image to the next is small ( $< 0.5\%$ ), the strain image brightness (on a pixel-by-pixel basis) changes gradually, regardless of precompression. If the incremental average strain is not small ( $\geq 1\%$ ), then the local brightness within the cyst varies rapidly and (seemingly) unpredictably. The typical behavior of the strain pattern in cysts is demonstrated (as well as can be with static images) in Fig. 4. Unlike the behavior observed with fibroadenomas, frames with equivalent precompression might have very different apparent strain within the cyst. Overall, a cyst can be either relatively stiff, as if it were a distended balloon, or relatively soft.

A total of 21 B-mode and strain image sequences were acquired from 7 unique carcinomas among 6 patients. All carcinomas studied so far were invasive ductal carcinomas and all but one were highly suspicious of carcinoma, based on mammogram and sonogram results. This is by far the most commonly diagnosed breast cancer. Relatively small lesions ( $\leq 2$  cm) have high negative contrast (stiff) in a background of "normal" breast tissue, regardless of precompression. An example of this is shown in Fig. 5. The exception to this occurs for

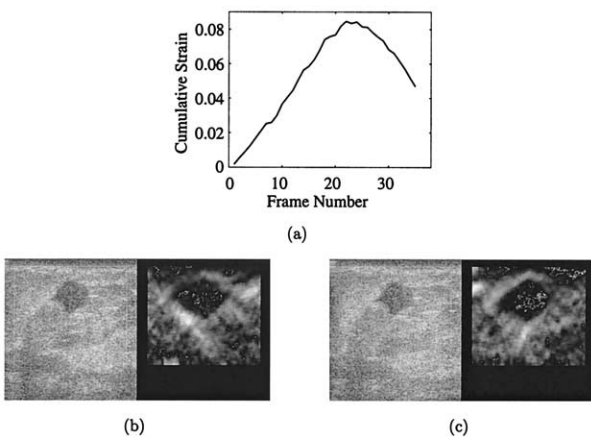


Fig. 5. Data obtained by freehand scanning of invasive ductal carcinoma *in vivo*. (a) The cumulative strain in the sequence shows that a 8% compression range was achieved. (b) Images in frame 4 acquired at low precompression, are very similar to (c) those in frame 18 acquired at much higher precompression. Some differences in the strain in "normal" surrounding tissue are seen, but vary smoothly from frame to frame.

very large lesions where little, if any, healthy tissue is included in the strain image.

One of the criteria that Garra et al. (1997) found to be most useful in differentiating between benign and malignant lesions was the relative size of the lesion in B-mode vs. strain images. To compare lesion size in the two imaging modalities, we transferred the I-Q echo data to an off-line computer for further analysis. The strain images were reprocessed using the same displacement estimation algorithm as that implemented on the Elegra. Off-line processing used a 16-sample (< 3 mm) window for strain estimation instead of the 24-sample window used on the Elegra (higher axial resolution). Movie loops of the side-by-side B-mode and strain image pairs (avi files) were created to view the motion of the lesion in the B-mode image and the resulting strain image. A representative frame was selected that showed the "typical" strain image for that lesion and the B-mode image was displayed, allowing the lesion boundary to be traced. The boundary in the B-mode image excluded the capsule of the lesion. The lesion width (and height) were estimated, based on the traced lesion perimeter, as the maximum dimension perpendicular (and parallel) to the acoustic beam. The tracing and measurement process was then repeated with the strain image from that same frame. The boundary traced in the strain image was the location of the steepest (visual) gradient in strain. High negative-contrast images were chosen for fibroadenomas. All tracings were performed by the first author, and most boundaries were very easily identified. In some cases, for example, in the atypical fibroadenoma shown in Fig. 3,

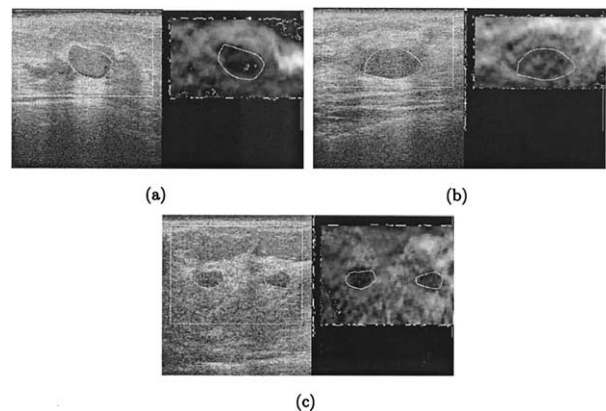


Fig. 6. B-mode and strain images of fibroadenomas with their perimeter traced in the B-mode image; that tracing also in the strain image for comparison. A fibroadenoma measuring (a) 71.4 mm<sup>2</sup> in B-mode and 75.0 mm<sup>2</sup> in strain, (b) 88.7 mm<sup>2</sup> in B-mode and 102 mm<sup>2</sup> in strain, (c) 27.2 mm<sup>2</sup> and 21.5 mm<sup>2</sup> in B-mode and 26.8 mm<sup>2</sup> and 21.7 mm<sup>2</sup> in strain, respectively. The B-mode tracing is a reasonably good approximation to that on the strain image.

an experienced clinician assisted in tracing the boundary. Example images for a fibroadenoma, cysts and an invasive ductal carcinoma are shown in Figs. 6, 7 and 8.

It is intriguing to examine the relative size of these lesions, comparing their width, height and area as measured in B-mode and strain images. Figure 9a and b shows plots of the width and height of these three lesion types as measured in B-mode and strain images. Figure 9c shows plots of a similar comparison of the total area

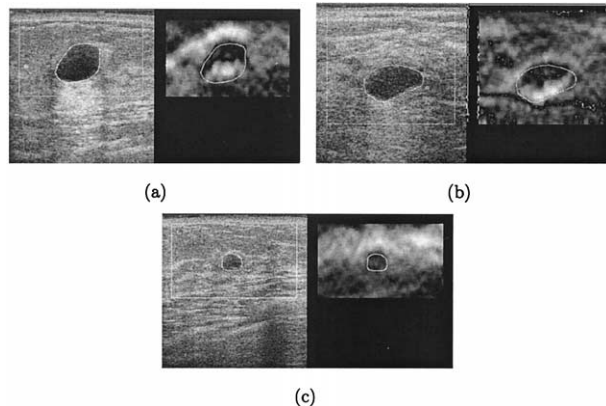


Fig. 7. B-mode and strain images of cysts with their perimeter traced in the B-mode image; that tracing also in the strain image for comparison. A cyst measuring (a) 139 mm<sup>2</sup> in B-mode and 145 mm<sup>2</sup> in strain, (b) 102 mm<sup>2</sup> in B-mode and 84.1 mm<sup>2</sup> in strain, (c) 30.3 mm<sup>2</sup> in B-mode and 32.5 mm<sup>2</sup> in strain. The B-mode tracing is a good approximation to that on the strain image, if the soft region at the bottom of the cyst, (a) and (b), were included.

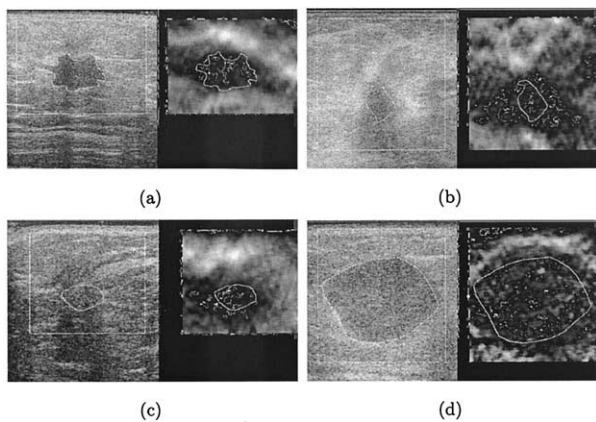


Fig. 8. B-mode and strain images of invasive ductal carcinomas with their perimeter traced in the B-mode image; that tracing also in the strain image for comparison. An invasive ductal carcinoma measuring (a)  $96.1 \text{ mm}^2$  in B-mode and  $170 \text{ mm}^2$  in strain, (b)  $22.8 \text{ mm}^2$  in B-mode and  $319 \text{ mm}^2$  in strain, (c)  $48.7 \text{ mm}^2$  in B-mode and  $170 \text{ mm}^2$  in strain, (d)  $465 \text{ mm}^2$  in B-mode and at least  $768 \text{ mm}^2$  in strain. The B-mode tracing is not representative of what would likely have been drawn on any of these strain images.

of the lesion in the two imaging modes. Table 1 shows that the width and height of benign lesions tend to be about the same size in B-mode and strain images and carcinomas are larger in strain images than in B-mode, as

observed by Garra *et al.* (1997), but the separation between benign lesion and carcinoma is larger when we use the lesion area.

In each of these examples, the study was performed on an isolated lesion. Although some data sets contained more than one lesion, those lesions were separated by at least one diameter of the largest lesion in the image. Measurements of individual lesions in clusters of lesions, most frequently observed in clusters of breast cysts, proved problematic in obtaining high-quality strain image sequences and in interpreting the motion. An example of this, shown in Fig. 10, shows that it might be more reasonable to study the cluster as a group instead of as individual lesions. When lesions are closely spaced, particularly when they share a common boundary, the motion due to compression can be quite complex, as observed in the B-mode image sequence, and the block-matching algorithm fails to track motion adequately. The block-matching algorithm assumes rigid body motion and does not accurately track significant rotation or shear motion. Further, our current system acquires data (effectively) in a plane, and significant motion perpendicular to the image plane is lost. A 3-D acquisition system would be required to track significant elevation motion. A higher-order algorithm, such as the deformable mesh (Zhu *et al.*, 1998), would be required to track rotation and shear motion accurately. At this stage of strain image processing and interpretation, it is likely best to restrict the study to individual isolated lesions.

## DISCUSSION

Real-time display of side-by-side B-mode and strain images is essential for guiding the manipulation of boundary conditions for the mechanics experiment that is strain imaging. Real-time feedback to the hand-eye co-ordination system allows the sonographer to manipulate the compression direction, force and rate to obtain high-quality sequences of strain images. The system employs standard linear-array transducers and requires no additional fixtures or remote data-acquisition or signal-processing hardware. It is fully integrated into the Elegra system. A small plate  $9 \text{ cm} \times 4.5 \text{ cm}$  is sometimes attached to the face of the transducer to extend the compression surface. This was most useful when scanning benign lesions that tended to move in elevation when compressed.

Our results show significantly different strain-image sequences for each lesion type studied. Although the three lesion types reported here do not include all those found in breasts, they represent the most common clinically observed breast lesions. It was found that, to appreciate the differences among lesion types, and to determine the “typical” strain image for a given lesion, it

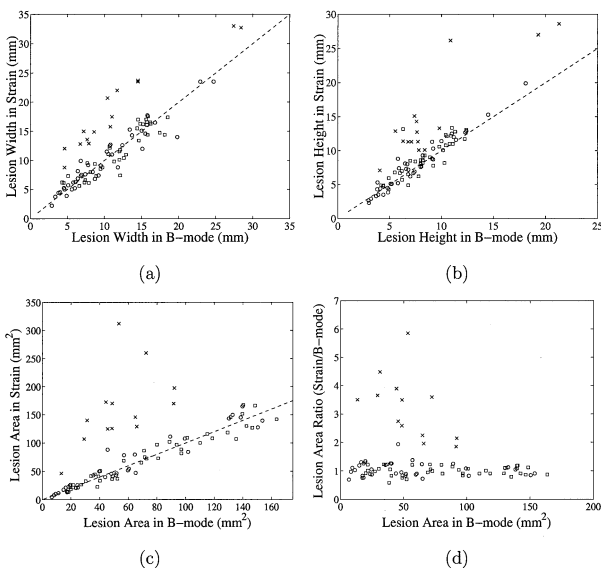


Fig. 9. Plots comparing the size of a lesion traced in the B-mode image vs. the same lesion traced in a representative strain image for (○) cysts, (□) fibroadenomas and (x) invasive ductal carcinomas. (a) The width and (b) height comparisons. (c) The areas for lesions less than 20-mm wide (in B-mode) are compared, and (d) the area ratio. The dashed line in (a)–(c) represents equal size measurement in both images.

Table 1. Results of measurements of the size of lesions in B-mode and strain images and the ratio of their size (strain/B-mode)

	Lesion type		
	Cyst	Fibroadenoma	IDC
<b>B-mode</b>			
Width (mm)	9.8 ± 5.3	11.8 ± 4.1	11.7 ± 7.2
Height (mm)	7.2 ± 3.4	8.4 ± 2.4	9.2 ± 4.8
Area (mm <sup>2</sup> )	69.3 ± 72.2	81.9 ± 44.4	104 ± 135
<b>Strain</b>			
Width (mm)	9.8 ± 5.1	11.6 ± 4.1	18.6 ± 7.3
Height (mm)	7.6 ± 3.8	8.8 ± 2.7	14.8 ± 6.7
Area (mm <sup>2</sup> )	72.8 ± 77.8	81.2 ± 44.6	236 ± 206
<b>Ratio (strain/B-mode)</b>			
Width	1.02 ± 0.16	1.00 ± 0.18	1.74 ± 0.36
Height	1.04 ± 0.16	1.07 ± 0.21	1.68 ± 0.36
Area	1.05 ± 0.24	1.00 ± 0.17	3.02 ± 1.19

Tabulated values are the mean ± the SD of the group. The size ratio for benign lesions is near unity, showing that these lesions typically have the same size in both imaging modalities. However, invasive ductal carcinomas (IDC) typically are 2 to 3 times as large in strain images than in B-mode images.

was necessary to observe a sequence of B-mode and strain images displayed side-by-side. With that sequence, a very reproducible determination of the lesion boundary could be obtained. Measurements of lesion dimension were then made and the results for lesion width are

consistent with those reported by Garra et al. (1997). That report stated a lack of confidence in their measurements of lesion height. Our results with spherical targets in phantoms show that we can accurately measure lesion dimension in both height and width (Zhu and Hall 2002) and, therefore, we use lesion area as the criterion for comparing lesion size in B-mode and strain images.

The significant, but monotonic, change in strain contrast as a function of precompression appears to be unique to fibroadenomas so far in our experience. This contrast variation suggests that the stress-strain relationship for fibroadenoma does not parallel that of the surrounding tissue. Fibroadenomas that vary in strain contrast appear dark (stiffer) at low precompression and lose contrast (become relatively softer) at higher precompression. One possible explanation is that the stress-strain relationship for the surrounding tissue is more nonlinear than that of the fibroadenoma over the range that each are compressed in this technique. The average age of the women with fibroadenomas in this study was 44 years, and their dominant breast tissue type was subjectively judged to be fibroglandular from B-mode images. The data reported by Krouskop et al. (1998), demonstrate that both glandular tissue and (primarily) fibrous tissue, such as fibroadenoma, have nonlinear stress-strain relationships. When preloaded to 5% strain, fibrous tissue is about 3 times more stiff than glandular tissue. However, the appropriate comparison for our application is when both tissues have minimal preload and when glandular tissue is preloaded about 15% and fibrous tissue is preloaded some small fraction of that (because the less stiff tissues strain more when they are treated as a composite), and that composite is strained an average of about 1% for

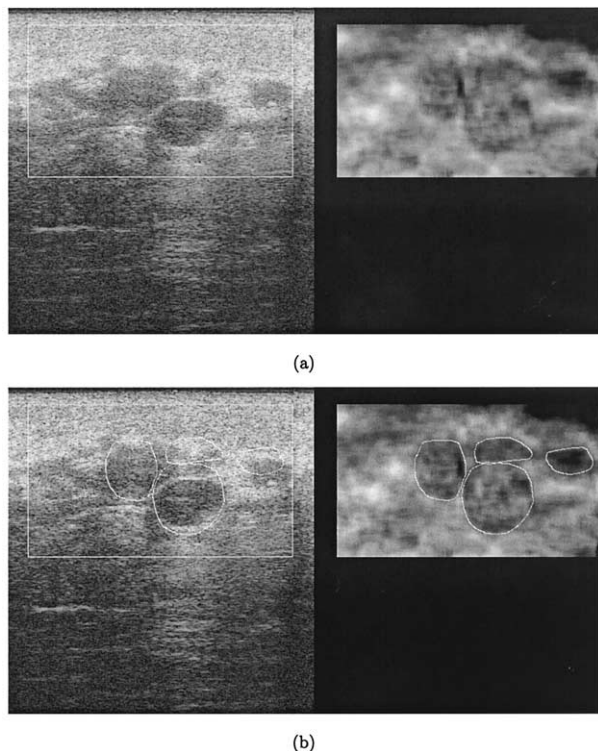


Fig. 10. B-mode and strain images of a cluster of breast cysts with their perimeter traced in the strain image; that tracing also in the B-mode image for comparison.

data acquisition. Krouskop and colleagues did not report those results.

Garra *et al.* (1997) tested numerous criteria for discriminating benign from malignant breast lesions. The criterion that provided the greatest discrimination in their study was the comparison of lesion width measured in B-mode and strain images. They attributed that size difference to the desmoplasia that surrounds most malignant breast tumors (Tavassoli 1999). Desmoplasia is the excessive growth of fibrous connective tissue in the stroma surrounding the malignancy. That growth appears gray-white and feels very hard in gross pathology (Tavassoli 1999). Our study tested this criterion and extended the observation to a comparison of lesion area. The sequence of B-mode and strain image pairs allows the sonographer to select images representative of the "typical" strain image for a lesion. This ability, along with better determination of lesion boundary available by viewing a sequence of images, has likely improved the ability to measure true lesion size in strain imaging compared with the results reported by Garra *et al.* (1997). A study to estimate the intraobserver and interobserver variability in choosing the "typical" strain image and measuring lesion size is underway. That study is an essential part of determining the value of the relative size of lesions in B-mode and strain image pairs as a diagnostic criterion. The utility of elasticity imaging in differentiating (from benign growths) malignancies that lack desmoplasia has not been tested.

Garra *et al.* (1997) also found the brightness of the lesion in strain images to be a useful parameter, but our observation of the changing contrast with compression in fibroadenomas provides an improved description of the contrast of solid lesions in strain imaging. The change in strain image contrast with applied compression (*e.g.*, Fig. 3) demonstrates that observing only a single B-mode and strain image pair at an unknown precompression could be very misleading in the interpretation of the strain image data. A sequence of side-by-side B-mode and strain image pairs greatly adds to the ability to interpret strain images.

Numerous other criteria were tested by Garra *et al.* (1997), but demonstrated limited utility. As with their study, the current study is limited by the small number of patients and lesions included, and by the fact only one observer was involved in each report. A larger cohort of patients and a larger number of observers are needed to

improve the statistical analysis of this technique. That effort will be the subject of a future report.

## CONCLUSIONS

A new system for real-time imaging of tissue strain *in vivo* using freehand scanning is described and some of the results obtained with this system are reported. The new system provides real-time feedback, allowing the user to manipulate the conditions of tissue compression resulting in the ability to successfully scan all patients for which the technique was attempted. The strain images for various lesion types are unique, and the relative size of the lesions appears to be a useful criterion for discriminating benign from cancerous lesions. However, further testing will be needed to support this observation.

**Acknowledgments**—The authors are grateful for the financial support of USAMRAA (DAMD17-00-1-0596) and NSF (BES-9708221) and technical support from Siemens Medical Systems Ultrasound Group. We thank Stanton J. Rosenthal, M.D., for his assistance in tracing lesions and valuable discussions. We also thank Pat Von Behren for numerous helpful discussions. The U.S. Army Medical Research Acquisition Activity, 820 Chandler Street, Fort Detrick MD 21702-5014 is the awarding and administering acquisition office for DAMD17-00-1-0596. The information reported here does not necessarily reflect the position or policy of the U.S. Government, and no official endorsement should be inferred.

## REFERENCES

- Chaturvedi P, Insana MF, Hall TJ. 2-D companding for noise reduction in strain imaging. *IEEE Trans Ultrason Ferroelec Freq Cont* 1998a; 45(1):179-191.
- Chaturvedi P, Insana MF, Hall TJ. Testing the limitations of 2-D companding for strain imaging using phantoms. *IEEE Trans Ultrason Ferroelec Freq Cont* 1998b;45(4):1022-1031.
- Garra BS, Céspedes I, Ophir J, *et al.* Elastography of the breast: Initial clinical results. *Radiology* 1997;202:79-86.
- Hall TJ, Bilgen M, Insana MF, Krouskop TA. Phantom materials for elastography. *IEEE Trans Ultrason Ferroelec Freq Cont* 1997; 44(6):1355-1365.
- Insana MF, Chaturvedi P, Hall TJ, Bilgen M. 3-D companding using linear arrays for improved strain imaging. *Proc IEEE Ultrason Symp* 97CH36118. 1997;1435-1438.
- Kallel F, Ophir J. A least-squares strain estimator for elastography. *Ultrason Imaging* 1997;10:195-208.
- Krouskop TA, Wheeler TM, Kallel F, Garra BS, Hall TJ. The elastic moduli of breast and prostate tissues under compression. *Ultrason Imaging* 1998;20:260-274.
- Lubinski MA, Emelianov SY, O'Donnell M. Adaptive strain estimation using retrospective processing. *IEEE Trans Ultrason Ferroelec Freq Cont* 1999;46(1):97-107.
- Tavassoli FA. *Pathology of the breast*. New York: McGraw-Hill, 1999.
- Zhu Y, Chaturvedi P, Insana M. Strain imaging with a deformable mesh. *Ultrason Imaging* 1998;21:127-146.
- Zhu Y, Hall TJ. A modified block matching method for real-time freehand strain imaging. *Ultrason Imaging* 2002;24:161-176.

# A Finite-Element Approach for Young's Modulus Reconstruction

Yanning Zhu\*, Timothy J. Hall, and Jingfeng Jiang

**Abstract**—Modulus imaging has great potential in soft-tissue characterization since it reveals intrinsic mechanical properties. A novel Young's modulus reconstruction algorithm that is based on finite-element analysis is reported here. This new method overcomes some limitations in other Young's modulus reconstruction methods. Specifically, it relaxes the force boundary condition requirements so that only the force distribution at the compression surface is necessary, thus making the new method more practical. The validity of the new method is demonstrated and the performance of the algorithm with noise in the input data is tested using numerical simulations. Details of how to apply this method under clinical conditions is also discussed.

**Index Terms**—Tissue characterization, tissue elasticity.

## I. INTRODUCTION

THE ELASTIC properties of biological tissues are usually modified by disease. Surgeons often describe the “feel” of excised abnormal tissues. As a result, a quantitative measure of the elastic properties of tissue should be useful in diagnosing abnormalities. The physical quantities that describe tissue elastic properties are stress, strain, and elastic moduli, and methods have been developed to estimate each of these. Palpation, which has been used for more than 4000 years, utilizes tissue surface stress information to detect tissue abnormalities. Palpation remains an effective diagnostic tool. In fact, the majority of breast tumors are discovered with palpation [1]. However, palpation is qualitative and lacks sensitivity to small deep abnormalities. Quantitative methods similar to palpation have been developed to visualize surface pressure [2], [3]. Other recent developments in bioelasticity imaging techniques involve accurately and noninvasively measuring the tissue strain distribution during external compression. Studies have shown that these techniques show promise in diagnosing and monitoring diseases of the breast [4]–[7], kidney [8]–[11], and blood vessels [12], [13].

Mapping stress or strain distributions provides only relative information about tissue elasticity. Using either stress or strain information alone, one can only identify a region of tissue that is stiff (or soft) relative to its surroundings. Elastic moduli provide

an absolute measure of tissue elasticity that is intrinsic to the material. The stress or strain distributions alone lacks a one-to-one relationship with the elastic moduli distribution. Images of the stress or strain distribution may also include misleading artifacts that could lead to uncertainties in diagnosing tissue abnormalities. Therefore, it is desirable to measure elastic moduli in bioelasticity imaging techniques. However, measuring the distribution of elastic moduli is more difficult than either the stress or strain distribution.

The theory of mechanics shows that to describe the complete elastic properties of a material requires a tensor that has 81 components [14]. Clearly, it is impractical to measure all these components. Assumptions can be made to simplify the problem and reduce the number of unique tensor elements. If a material is assumed to be continuous, incompressible, and isotropic, then its elasticity can be completely described by one elastic modulus, either Young's modulus  $E$  or shear modulus  $\mu$ . Strictly speaking, none of the above assumptions are valid for biological tissues, but most biological tissues closely approximate continuous and incompressible materials. Some tissues, such as muscle, are anisotropic in their structure, function, and mechanical properties. For this paper, however, we will assume tissue to be continuous, incompressible, and isotropic as a first approximation.

Currently, ultrasonic-based techniques for measuring the elastic modulus of tissue fall into two categories. First, dynamic compression techniques [15]–[18], such as sonoelasticity, use a vibrator to propagate low-frequency “pumping” waves into tissue. In the most promising of these approaches, shear wave velocity or wavelength are estimated, and from these the shear modulus can be estimated. However, problems associated with this technique are high image noise, low spatial resolution, and difficulty in propagating the shear wave energy across tissue boundaries.

The other category is referred to as (quasi)static compression techniques. In static compression techniques, the tissue Young's modulus distribution is estimated from the tissue deformation and boundary pressure measurements. The methods to estimate tissue deformation have been extensively discussed in ultrasound based elastography [19]–[28]. The tissue is deformed either by an external force or an internal force. The RF echo waveforms before and after an incremental deformation are recorded, and the tissue displacement distribution is estimated by comparing these RF waveforms. Tissue internal displacement can be also obtained using magnetic resonance imaging [29]–[31] and optical elastography [32] techniques. Young's modulus estimation can be performed utilizing the tissue deformation information obtained with the strain imaging

Manuscript received September 18, 2002; revised January 17, 2003. The Associate Editor responsible for coordinating the review of this paper and recommending its publication was G. Wang. Asterisk indicates corresponding author.

\*Y. Zhu is with the Department of Radiology, The University of Kansas Medical Center, 3901 Rainbow Blvd., Kansas City, KS 66160-7234 USA (e-mail: yzhu@kumc.edu).

T. J. Hall and J. Jiang are with the Department of Radiology, The University of Kansas Medical Center, Kansas City, KS 66160-7234 USA.

Digital Object Identifier 10.1109/TMI.2003.815065

techniques. In addition to the displacement distribution, some Young's modulus estimation methods also require knowledge of the pressure or force boundary conditions.

There are four methods in the literature for reconstructing the Young's modulus distribution based on static compression techniques for displacement estimation. The first method estimates Young's modulus by numerically solving a second-order partial differential equation that describes a linear, isotropic, incompressible medium under static deformation [33]. That method requires significant spatial smoothing of the displacement estimates to obtain second-order partial differentials that are also smooth. Hence, with noisy displacement estimates, that method inherently has low spatial resolution. Another problem associated with that method is that for a two-dimensional (2-D) analysis, the force boundary condition of the medium must be known on all sides. However, in practice, the force distribution can only be (easily) measured on one side (the compression surface) of the medium.

The second method uses an iterative technique to reconstruct the modulus distribution [34], [35]. That method uses finite-element analysis (FEA) to solve the forward elasticity problem. The input to the FEA algorithm is the measured displacement field, the assumed boundary conditions, and an initial guess of the modulus distribution. The output of the FEA algorithm is an estimate of the displacement distribution. The difference between the measured displacement distribution and the FEA prediction is used to adjust the modulus distribution from its initial guess. By repeating the process multiple times, one can obtain a modulus distribution that minimizes the displacement distribution difference in a least squares sense. The advantage of that approach is that it does not require knowledge of the pressure boundary conditions. However, without knowing the boundary pressure, only relative modulus estimates can be obtained. In other words, the ratio of the modulus between different locations can be determined. Although that method can reduce the artifacts in strain images, it does not provide absolute measurement of the tissue modulus distribution which can be useful in tumor discrimination as suggested in [36], and an incorrect initial modulus guess may result in convergence to an incorrect modulus distribution. For media, such as tissue, that have a complicated modulus distribution, a good initial guess for the modulus distribution is difficult to obtain.

In the third modulus reconstruction method, a finite-difference approach is used to describe the elasticity problem in a medium [37]. That approach rearranges linear equations that describe the forward problem so that the modulus distribution becomes unknown variables in these equations. The modulus distribution can then be solved. However, that method also requires knowledge of the boundary conditions on all sides of the object.

The fourth approach uses a variational method to formulate the forward solution [38]. Then the terms with unknowns are rearranged to derive a matrix equation similar to ours. However, the boundary force condition was not utilized in their treatment. Hence, this method can only reconstruct the ratio between the Lame constants and tissue mass density.

In our approach, FEA is used to construct a set of linear equations that describes the elastic behavior of a 2-D object. Similar

to the third method mentioned above, we rewrite the linear equation set so that the Young's modulus distribution are explicit variables which can be solved. The solution does not require an initial guess or iteration of the modulus distribution solution, and it provides absolute, not relative, modulus estimates. Unlike the equation set for solving forward elasticity problems, where the number of equations equals the number of unknown variables, the equation set for our inverse solution usually involves more equations than unknowns. This allows us to simplify the force boundary conditions so that only one (surface) force distribution is necessary to solve for the modulus distribution.

The details of our modulus estimation method are described in Section II. The validity of this method is tested with simulations and results are shown in Section III. The discussion of how this technique can be implemented for ultrasonic imaging systems is provided in Section IV.

## II. METHOD

Three integral parts of the proposed modulus estimation method are described in this section, one subsection each. Section II-A provides the information necessary for solving a forward elasticity problem of 2-D continua using FEA. Although the content of this subsection is well known in the literature, it is briefly reviewed here to provide sufficient background, terminology, and notation for the development of Section II-B. In Section II-B, the FEA-based modulus estimation technique (inverse problem) is described in detail. Section II-C addresses issues of how to apply the proposed method under practical constraints.

### A. The FEA Method for Solving a Forward Problem of 2-D Continua

The FEA procedure for solving a forward elasticity problem of 2-D continua can be summarized as follows [39]–[41].

- 1) Select an element type and derive the element stiffness matrix.
- 2) Form a mesh using the selected element to cover the region of interest (ROI) for which the elasticity problem is solved.
- 3) Generate the global stiffness matrix by assembling element stiffness matrices.
- 4) Apply the boundary conditions to solve the global matrix equations for the solution.

The details of these steps are provided below.

*Step 1:* For 2-D problems, the common choices for element type are triangles or quadrilaterals. In other words, each element has either three or four nodes. The element matrix equations for elasticity problems have the form

$$K^{(e)}\delta^{(e)} = f^{(e)} \quad (1)$$

where  $K^{(e)}$ ,  $\delta^{(e)}$ , and  $f^{(e)}$  are, respectively, the element stiffness matrix, the element nodal displacement vector, and the element nodal force vector for element  $e$ . In this paper, rectangular elements, as shown in Fig. 1, are used. Details of how to compute the element stiffness matrix is provided in Appendix I.

*Step 2:* For problems that can be described by partial differential equations but do not have closed form solutions, FEA has

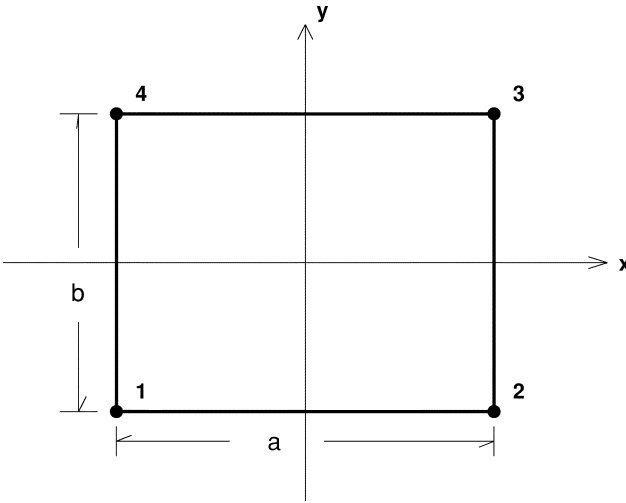


Fig. 1. The rectangular mesh element. Nodal numbers start from the bottom left corner and increase on the clockwise direction.

been developed to find approximate numerical solutions on discretized problem domains. These solutions can then be interpolated to form continuous solution spaces using shape functions. The discretization process is performed by creating a mesh that covers the ROI in the object.

A mesh is composed of elements that cover a contiguous area in the problem domain. In this paper, all elements in the ROI are rectangles of the same size. A nine-element mesh is illustrated in Fig. 2. The numbers in the center of the rectangular elements are element numbers and numbers close to nodes (intersection points) are nodal numbers.

The mesh configuration can be represented by a connectivity matrix,  $C$ . The number of rows of  $C$  equals the number of elements,  $N_e$ . For four-node elements (rectangles),  $C$  has four columns. The  $i$ th row of  $C$  records nodes associated with the  $i$ th element. For the mesh shown in Fig. 2, the first two rows of  $C$  are

$$\begin{pmatrix} 1 & 2 & 6 & 5 \\ 2 & 3 & 7 & 6 \end{pmatrix}. \quad (2)$$

*Step 3:* The matrix equation for a meshed system (for example, the system described in Fig. 2) has the form

$$K\delta = f, \quad (3)$$

where  $K$  is the global stiffness matrix;  $\delta$  is the global nodal displacement vector; and  $f$  is the global nodal force vector. The global displacement vector has the form

$$\delta = (\delta_{1x} \ \delta_{1y} \ \delta_{2x} \ \delta_{2y} \ \dots)^T \quad (4)$$

where  $\delta_{1x}$  and  $\delta_{1y}$  are the displacements in the  $x$  and  $y$  directions for node 1, and so on. The global nodal force vector has the form

$$f = (f_{1x} \ f_{1y} \ f_{2x} \ f_{2y} \ \dots)^T \quad (5)$$

where  $f_{1x}$  and  $f_{1y}$  are the net force exerted on node 1 in  $x$  and  $y$  directions, and so on. The global stiffness matrix  $K$  is assembled from element stiffness matrices. The assembly process can be found in Appendix II.

*Step 4:* Displacement boundary conditions are usually specified for the elasticity problems in our applications, and a penalty

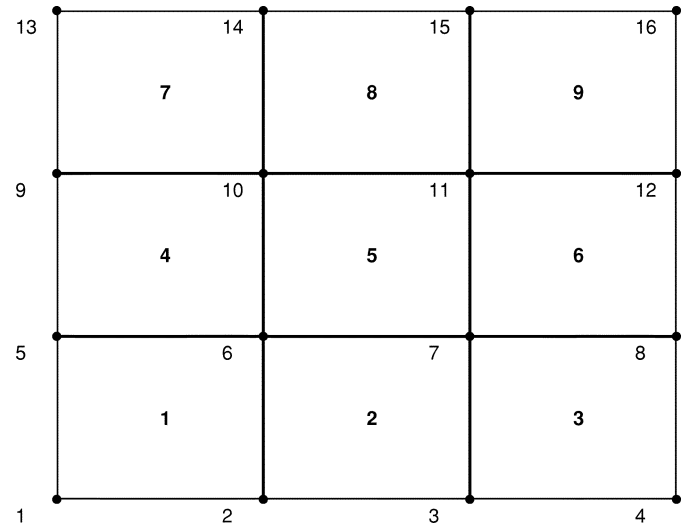


Fig. 2. A nine-element mesh composed of rectangular elements with uniform size. Numbers in the center of the rectangular elements are the element numbers and numbers close to nodes (intersection points) are the global nodal numbers.

approach [41] can be used to solve (3). The details of the penalty approach is provided in Appendix III.

#### B. The FEA Approach for Solving an Inverse Problem of 2-D Continua

Soft tissues can generally be considered as incompressible media [33]. Hence, the Possion's ratio can be assumed to be a constant that is close to 0.5 (0.49, for instance) throughout the ROI. With this assumption, matrix  $\tilde{K}$  in (24) is same for every element if all elements have the same aspect ratio (which is true in this paper since the mesh is composed of the elements with same size).

In the element-to-global stiffness matrix assembly procedure described in Section II-A, each component of  $K^{(e)}$  (i.e., the product of the element Young's modulus and a constant) is accumulated onto the global stiffness matrix. Hence, each component of the global stiffness matrix is a linear combination of the Young's modulus of each element. In other words, the global stiffness matrix can be written as

$$K = [K_{ij}] \quad i = 1, \dots, N, j = 1, \dots, N, \quad (6)$$

$$K_{ij} = \sum_{e=1}^{N_e} c_e^{ij} E^{(e)} \quad (7)$$

where  $c_e^{ij}$  are constants.

From (3), the left-hand side of the system matrix equation is  $K\delta$ . In Young's modulus reconstruction, the displacement distribution is estimated with tissue motion tracking techniques. In other words,  $\delta$  is a "known" vector. Performing the matrix-vector multiplication

$$K\delta = \begin{bmatrix} \sum_{j=1}^N \delta_j K_{1j} \\ \vdots \\ \sum_{j=1}^N \delta_j K_{ij} \\ \vdots \\ \sum_{j=1}^N \delta_j K_{Nj} \end{bmatrix}. \quad (8)$$

Since  $K_{ij}$  is a linear combination of  $E^{(e)}$  [see (7)], each component of the resulting vector on the right-hand side of (8) is also a linear combination of  $E^{(e)}$ . Or

$$K\delta = \begin{bmatrix} \sum_{j=1}^{N_e} D_{1j} E^{(j)} \\ \vdots \\ \sum_{j=1}^{N_e} D_{ij} E^{(j)} \\ \vdots \\ \sum_{j=1}^{N_e} D_{Nj} E^{(j)} \end{bmatrix}. \quad (9)$$

The right-hand side of (9) can be written as a product of a matrix and a vector. Or

$$K\delta = DE \quad (10)$$

where  $D$  is a  $N$ -by- $N_e$  matrix;  $E = (E^{(1)} \dots E^{(j)} \dots E^{(N_e)})^T$  is the Young's modulus vector. Now, (3) can be rewritten as

$$DE = f. \quad (11)$$

Recall from the global stiffness matrix assembly procedure, provided in Section II-B, that the component  $K_{ij}^{(e)} = E^{(e)} \tilde{K}_{ij}$  of the local stiffness matrix of element  $e$  is accumulated to the  $C_i^{(e)}$ th row and  $C_j^{(e)}$ th column of the global stiffness matrix, or  $K_{C_i^{(e)} C_j^{(e)}}$ . When performing the multiplication of  $K\delta$  [see (8)],  $E^{(e)} \tilde{K}_{ij}$  is multiplied with  $\delta_{C_j^{(e)}}$ . The product is then accumulated to the  $C_i^{(e)}$ th component of the resulting vector. Hence,  $\tilde{K}_{ij} \delta_{C_j^{(e)}}$  is a summand of the  $C_i^{(e)}$ th row and  $e$ th column component of the matrix  $D$ . Based on this observation, the matrix  $D$  can be assembled from the element stiffness matrix using the following procedure.

- 1) Initialize a  $N$ -by- $N_e$  null matrix.
- 2) For element  $e$ , generate a local variable number to global variable number conversion index vector  $I^{(e)}$  defined in (26).
- 3) Accumulate  $\tilde{K}_{ij} \delta_{I_j^{(e)}}$  to  $D_{I_i^{(e)} e}$  for  $i = 1, \dots, 8$  and  $j = 1, \dots, 8$ .
- 4) Iterate 2 and 3 for all elements.

Similar to solving forward elasticity problems with (3), the Young's modulus reconstruction problem can be solved from (11) were  $D$  is an  $N$ -by- $N_e$  matrix. Usually,  $N > N_e$  and (11) defines an over-determined set of equations. The common technique for solving an over-determined linear equation set is to convert it to a least-square problem [42]. The conversion can be done by multiplying both sides of (11) by  $D^T$

$$(D^T D)E = D^T f. \quad (12)$$

Since  $(D^T D)$  is an  $N_e$ -by- $N_e$  matrix,  $E$  can be solved by the following equation

$$E = (D^T D)^{-1} D^T f. \quad (13)$$

The application of this method under practical constraints is provided in the next subsection.

### C. Practical Concerns

1) *Necessary Measurements*: Equation (3) implies that there is an unstressed state to which the object returns when all external forces are removed from the object. Then, the external

forces (e.g., gravitational force, atmospherical pressure, and compressional force) are exerted on the object. The displacement is measured between the unstressed state and the state with external load. In reality, however, the geometrical distribution of the object in the unstressed state is unknown. Hence, (11) [which is derived from (3)] cannot be used directly to solve the inverse problem. Fortunately, if the object is assumed to be a linear elastic body for small incremental deformations, then this problem can be solved.

Assume there are two loading states of the object  $S_1$  and  $S_2$ . In  $S_1$ , the object can be described by

$$K\delta^{(S_1)} = f^{(S_1)} \quad (14)$$

where  $\delta^{(S_1)}$  is the object displacement between the natural state and  $S_1$ ;  $f^{(S_1)}$  is the compressional load measured in  $S_1$ . In  $S_2$ , the object can be described by

$$K\delta^{(S_2)} = f^{(S_2)}. \quad (15)$$

Note that  $K$  is state independent given the linear elastic body assumption.

Subtracting (15) from (14), we find

$$K\Delta\delta = \Delta f \quad (16)$$

where  $\Delta\delta = \delta^{(S_1)} - \delta^{(S_2)}$  and  $\Delta f = f^{(S_1)} - f^{(S_2)}$ . Replacing (3) with (16), the derivation introduced in Section II-B still holds. (16) states that three measurements, namely,  $\Delta\delta$ ,  $f^{(S_1)}$ , and  $f^{(S_2)}$ , are necessary for Young's modulus reconstruction.

2) *Young's Modulus Reconstruction With Partial Boundary Conditions*: Recall that (11) defines an over-determined set of linear equations. This means that only a subset of (11) are needed for inverse solution. Let  $D_s$  be a matrix that is formed from a subset of rows from  $D$ , and  $f_s$  be the force vector formed from the corresponding subset of  $f$ . As long as  $(D_s^T D_s)$  is invertible, a unique inverse solution can be obtained from

$$E = (D_s^T D_s)^{-1} D_s^T f_s. \quad (17)$$

This property can be used to relax the force boundary conditions for the inverse problem.

Under typical conditions a subregion of the tissue under study is observed. A mesh can be created to cover an ROI which is a subset of the field of view. Only one side (the surface of the tissue) of the boundary force distribution can be measured with ease with a force sensor array. With the example shown in Fig. 2, let us assume that the compressional force can be measured along the top side (nodes {13, 14, 15, 16}).  $D_s$  and  $f_s$  are determined by the following rule: *select all equations from (11) involving all interior nodes of the mesh and all nodes except the outer most two for which the force measurements are made*. With the example shown in Fig. 2, the selected nodes are {6, 7, 10, 11, 14, 15}. The related subset of the matrix equations include rows {11, 12, 13, 14, 19, 20, 21, 22, 27, 28, 29, 30} of (11).

It is difficult to mathematically prove that the equation selection rule described above always provides invertible  $D_s^T D_s$ , however, it is easy to test whether  $D_s^T D_s$  is invertible given a mesh configuration. From the variety of mesh configurations that have been tested, the equation selection rule described above always provides invertible  $D_s^T D_s$ .

3) *The Size of D Matrix:* The size of the matrix  $D$  can be a problem if it is assembled as a dense matrix. For example, if the mesh has  $100 \times 100$  elements, then there are total of  $101 \times 101 = 10201$  nodes. The size of  $D$  is 20402-by-10000, or 204 020 000 components. Representing each component as double precision floating point numbers and storing this dense matrix requires about 1.52 GB of computer memory. With current computer technology, storing such a large matrix may not be a problem. However, calculating  $(D^T D)^{-1}$  is impractical.

Fortunately,  $D$  is a sparse matrix. Recall that each row of (3) describes the behavior of a node, and there are a maximum of four elements related to one node. Thus, the maximum nonzero components of a row in  $D$  is four.

The number of nonzero components of  $D$  for a 100-by-100 element mesh is in fact 80 000. Using the sparse matrix features provided by MATLAB, this can be stored with about 1MB of memory. Compared with dense matrix storage, this is a 1600:1 reduction in memory requirement. Using a 750-MHz Pentium III PC,  $(D^T D)^{-1}$  can be computed in about 20 s. Note that although the discussion is based on  $D$ , same conclusion can be drawn for  $D_s$ .

### III. RESULTS

#### A. Solving the Forward Problem With Ideal Input

First, we simulated an object for which the forward problem was solved. The dimension of the simulated object was  $40 \times 40 \times 2$  (width  $\times$  height  $\times$  thickness in millimeters). Young's modulus distribution of the object is shown in Fig. 3. The Young's modulus of the background was 15 kPa which approximates the stiffness of normal glandular breast tissue [36]. There were two 10-mm-diameter targets in the object that simulate lesions. The upper target was three times stiffer (45 kPa) than the background and the lower target was three times less stiff (5 kPa) than the background.

A mesh was created for this object with 160 elements in both horizontal and vertical directions. The total number of elements was  $160 \times 160 = 25600$ . The size of each element was 0.25 mm  $\times$  0.25 mm. To produce a realistic estimate of boundary force values, we assumed plain stress conditions for the compression. The Possion's ratio  $\nu$  of 0.49 was used (incompressible media). The displacement boundary conditions were assigned such that the displacement of bottom side of the object was zero and the top side of the object was 0.8 mm simulating a 2% compression of the object.

Using the forward FEA method introduced in Section II-A, we calculated the displacement distribution and the force distribution along top and the bottom sides of the object. Using the displacement distribution, strain in both the horizontal direction ( $s_{xx}$ ) and vertical direction ( $s_{yy}$ ) were calculated and shown in Fig. 4(a) and (b), respectively. With the plain stress assumption, the following relationship holds  $s_{xx}/s_{yy} = -\nu/2$ . The force distribution on the top and bottom sides of the object are shown in Fig. 5(a) and (b), respectively. Note that the forces on the top side are all negative since the direction of the applied force is pointing vertically down. As shown in Fig. 5, the magnitude of force on the outer most nodes are half of the magnitude of the

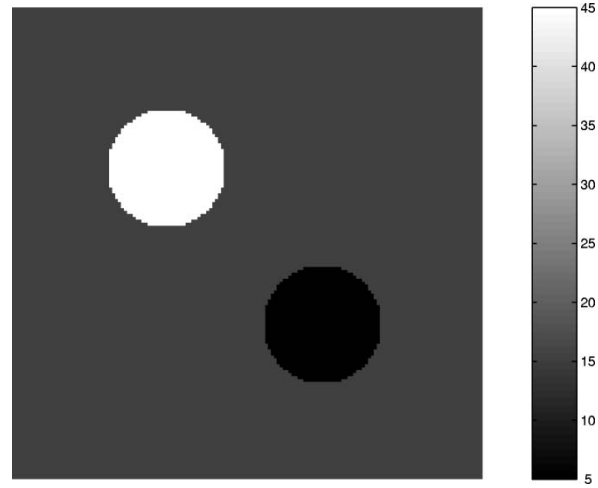


Fig. 3. The Young's modulus distribution for the simulated object. The units of the color bar are kPa.

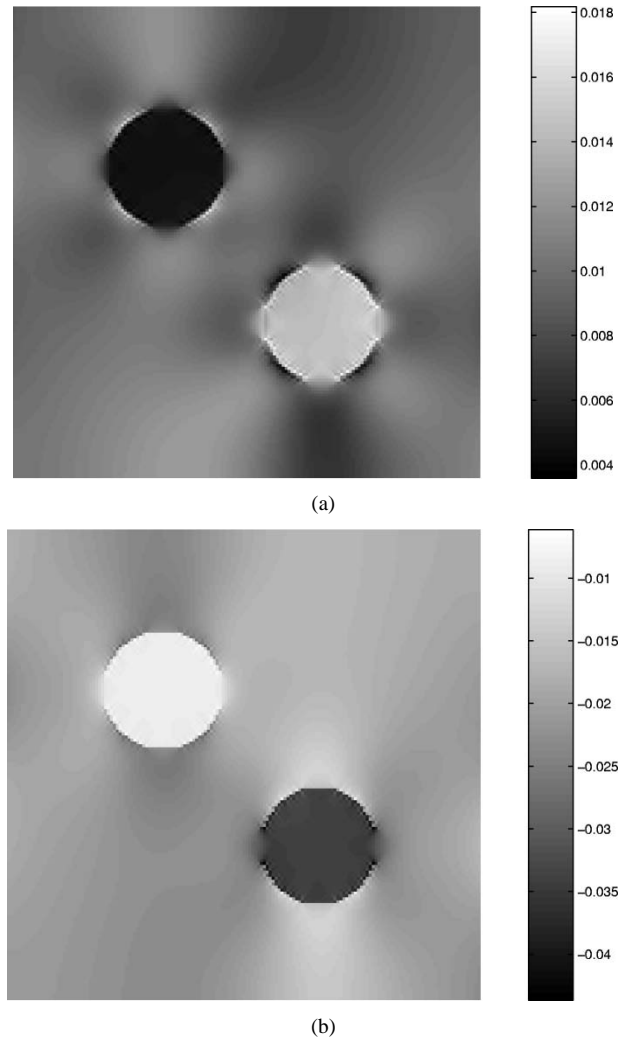


Fig. 4. Strain images obtained from the forward FEA calculation for the object illustrated in Fig. 3. (a) Horizontal strain  $s_{xx}$ . (b) Vertical strain  $s_{yy}$ .

force on their adjacent nodes since the area of support for the outer most nodes is half that of the inner nodes. With the same surface pressure is half the magnitude.

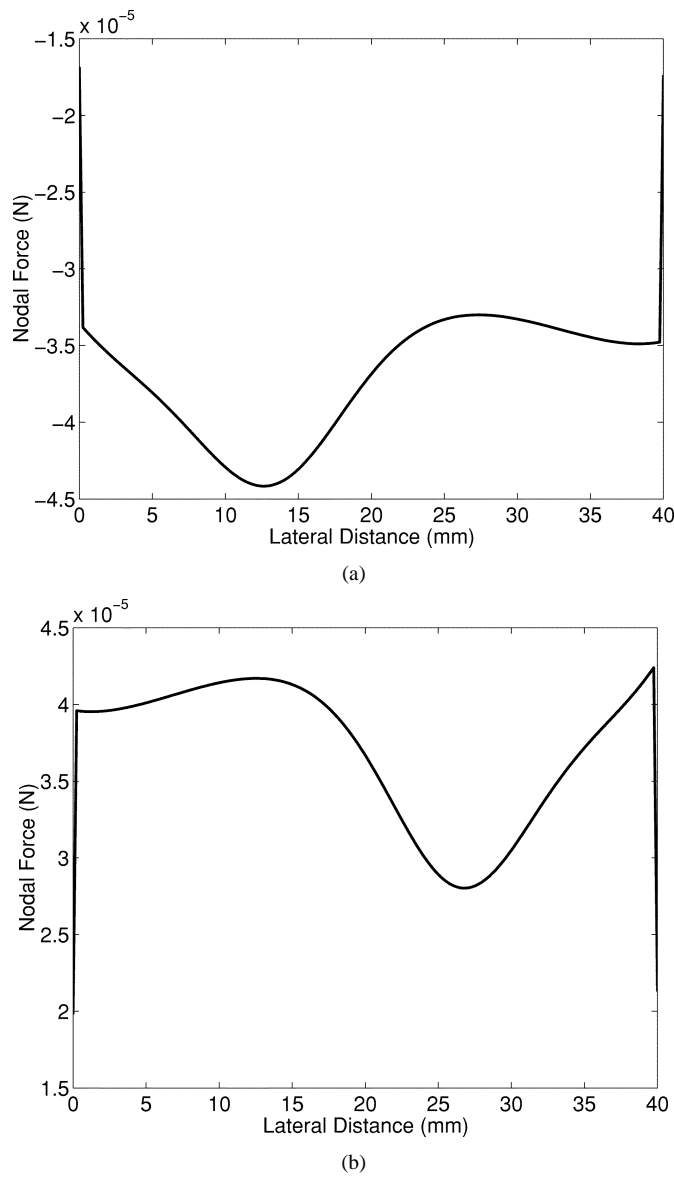


Fig. 5. The boundary force distribution obtained from the forward FEA calculation for the object illustrated in Fig. 3. (a) Force on the top side. (b) Force on the bottom side.

#### B. Solving the Inverse Problem With Ideal Input

To test the modulus reconstruction technique we used the results of the forward problem calculations, but, in effect, discarded nonessential information. The only input to the inverse (modulus distribution) computation were the ideal displacement distribution over a (sub-)ROI and the force distribution at the top (compression) surface generated by the forward solution. The sub-ROI was  $30 \text{ mm} \times 30 \text{ mm}$  and a new mesh was created to cover that area. An illustration of the meshed areas for the forward simulation and the inverse reconstruction is shown in Fig. 6.

Fig. 7 shows the result of the Young's modulus estimation. The standard deviation of the relative error in the reconstructed Young's modulus distribution is  $2.0 \times 10^{-5}\%$ —a nearly exact reconstruction is obtained. This result is encouraging since it shows that the Young's modulus estimation method introduced above is a valid approach and confirms that the “partial force”

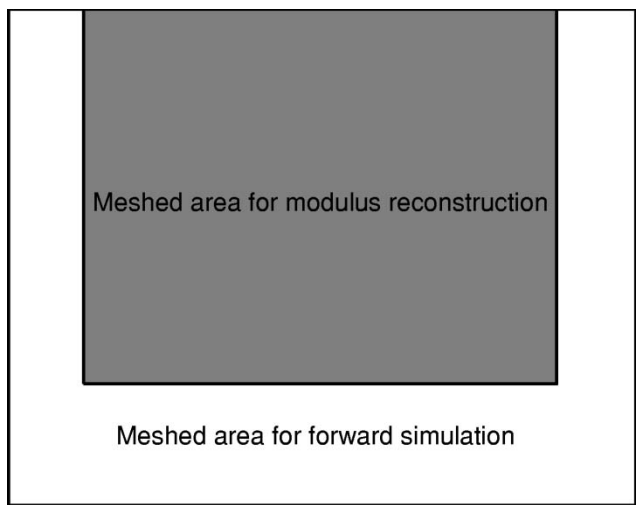


Fig. 6. An illustration of the meshed areas for the forward simulation and the Young's modulus reconstruction.

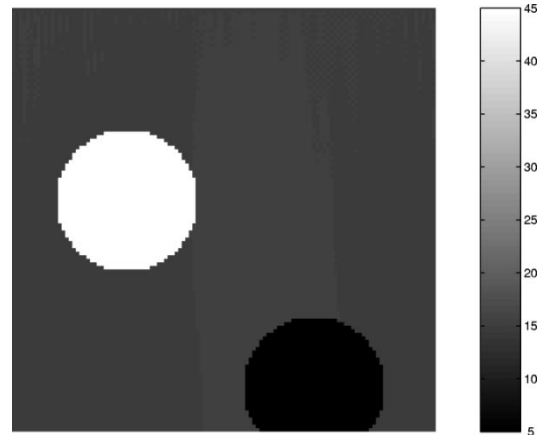


Fig. 7. The reconstructed Young's modulus image using the ideal (noise-free) displacement and force boundary conditions.

boundary condition is sufficient to estimate the modulus distribution.

In the above modulus estimation simulation, the size of the elements was the same as that used in the forward simulation. The small elements provide high spatial resolution. However, it is not likely that such high spatial resolution can be achieved under all practical conditions. In the next simulation, we increased the size of the elements to  $1 \text{ mm} \times 1 \text{ mm}$ . In other words, we blurred the spatial sampling by a factor of 4. Fig. 8(a) shows the “true” modulus image of the same object. The “true” modulus value of each element were calculated by averaging the 16 modulus values in the corresponding area of the finer meshed object. The inverse problem was solved using the exact displacement and force from the forward simulation results produced by the finer mesh. The result of the modulus estimation is shown in Fig. 8(b). The relative difference between Fig. 8(a) and (b) is shown in Fig. 8(c). The mean and standard deviation of the image shown in Fig. 8(c) are  $-1.25\%$  and  $17.8\%$ , respectively. The small mean value suggests that the modulus estimates are unbiased. However, the standard deviation value shows that the reconstructed modulus image using larger element size can be noisy. Since the modulus estimates are unbiased, a simple spatial averaging can improve the visual effect of the reconstructed

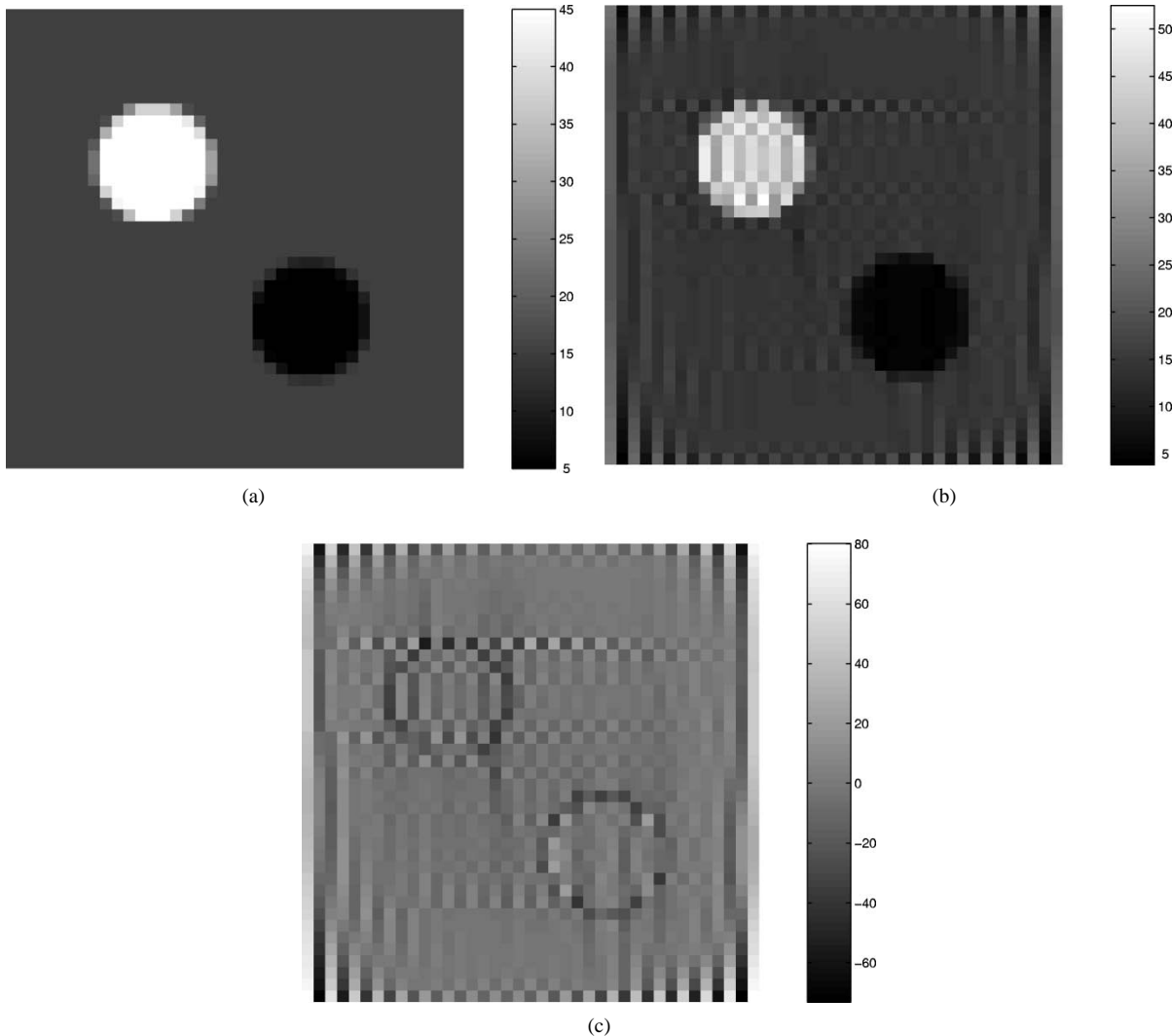


Fig. 8. Simulation results using the larger element size. (a) The ideal decimated modulus image. (b) The reconstructed modulus image using the larger element size. (c) The relative difference between (a) and (b) measured in percentage, mean =  $-1.25\%$ , std =  $17.8\%$ .

modulus images at the expense of further reducing the spatial resolution.

### C. Modulus Estimation With Noisy Displacement and Boundary Force Estimates

Inevitably, there is noise in the displacement and boundary force estimates that are used in modulus estimation. Hence, it is necessary to study the effect of noise in the input data on the resulting modulus estimates. To avoid the difficulty of analytically deriving the noise relationship between input data and final outcome, we rely on numerical simulation. The forward solution shown in Figs. 4 and 5 was used as the ideal displacement and boundary force distributions. The inverse simulation was based on the mesh configuration that produced the result shown in Fig. 8. Noise, modeled as zero mean white Gaussian random processes [43],<sup>1</sup> was added to

both the ideal displacement and boundary force distributions. A range of the standard deviations (noise) were used to study the relationship between noise power and the modulus estimation error. For each predetermined level of noise, 100 realizations of (noisy) displacement and force distributions were generated and the object modulus distributions were reconstructed.

The modulus estimation error is defined as the difference between the “true” modulus distribution [Fig. 8(a)] and the estimated modulus distribution with noise present in the input data (force boundary condition and displacement distribution). The relative mean and the relative standard deviation of the error were calculated from the outcome of all 100 realizations of noise fields. The simulation results are shown in Fig. 9. The standard deviation of the noise added to the boundary force distribution is 5% of the mean ideal force in Fig. 9(a) and (b) and 10% in Fig. 9(c) and (d). Fig. 9(a) and (c) shows the relationship between the standard deviation of the displacement error and the mean relative modulus estimation error. Fig. 9(b) and (d) shows the relationship between the standard deviation of the displacement error and the standard deviation of the relative modulus estimation error.

<sup>1</sup>Bilgen *et al* have shown through simulation that the noise in displacement estimates is Gaussian distributed. However, the spectrum of the noise is not shown in their work. The spectrum of noise is assumed to be white as an approximation.

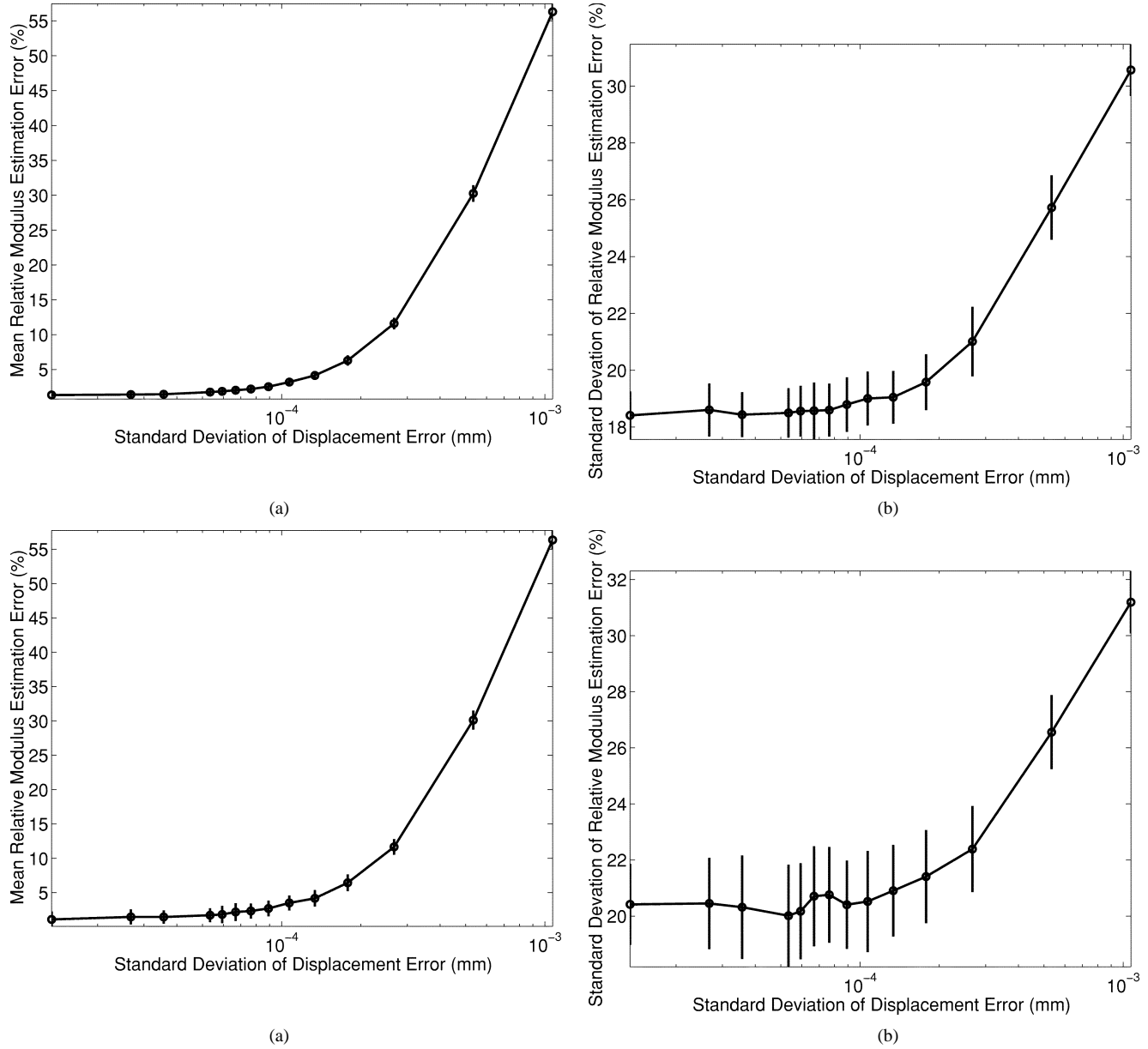


Fig. 9. Modulus estimation performance curves. (a) Standard deviation of the error in displacement versus the mean relative error in modulus estimates resulting from a 5% standard deviation in the “measured” force. (b) Standard deviation of the error in displacement versus standard deviation of the relative error in modulus estimates resulting from a 5% standard deviation in the “measured” force. (c) Standard deviation of the error in displacement versus the mean relative error in modulus estimates resulting from a 10% standard deviation in the “measured” force. (d) Standard deviation of the error in displacement versus standard deviation of the relative error in modulus estimates resulting from a 10% standard deviation in the “measured” force.

Comparing Fig. 9(a) with Fig. 9(c) and (d), we found that the modulus estimation error is not very sensitive to the errors in the boundary force measurements. However, it is very sensitive to errors in the displacement measurements. When the standard deviation of the displacement error exceeds  $10^{-4}$  mm, the modulus estimation becomes biased, as shown in Fig. 9(a) and (b), and the noise in modulus estimation starts to increase rapidly. Note that the units in the horizontal axis of all plots in Fig. 9 are mm. To make the results independent of the actual object dimension, we re-plotted results in Fig. 10. In Fig. 10 the horizontal axis is changed to standard deviation of relative strain error. From the plots shown in Fig. 10, we can see that when the noise in the displacement estimates causes more than 1% strain error, the quality of modulus estimates starts to degrade rapidly.

#### IV. DISCUSSION

The derivation in Section II-C2, shows that the boundary conditions for the inverse problem with the proposed method are less restrictive than those of the forward problem. In the forward simulation, boundary conditions that describe all sides of the meshed object are required to solve (3) for the displacement distribution and the boundary force distribution. In modulus reconstruction, however, only the sub-ROI of the object needs to be meshed, and only partial boundary force conditions need to be specified. This makes our approach more practical and far easier to implement (experimentally) than other methods.

In our method, the medium is assumed to be elastic. Possible tissue viscous behavior is not accounted for in our model. With

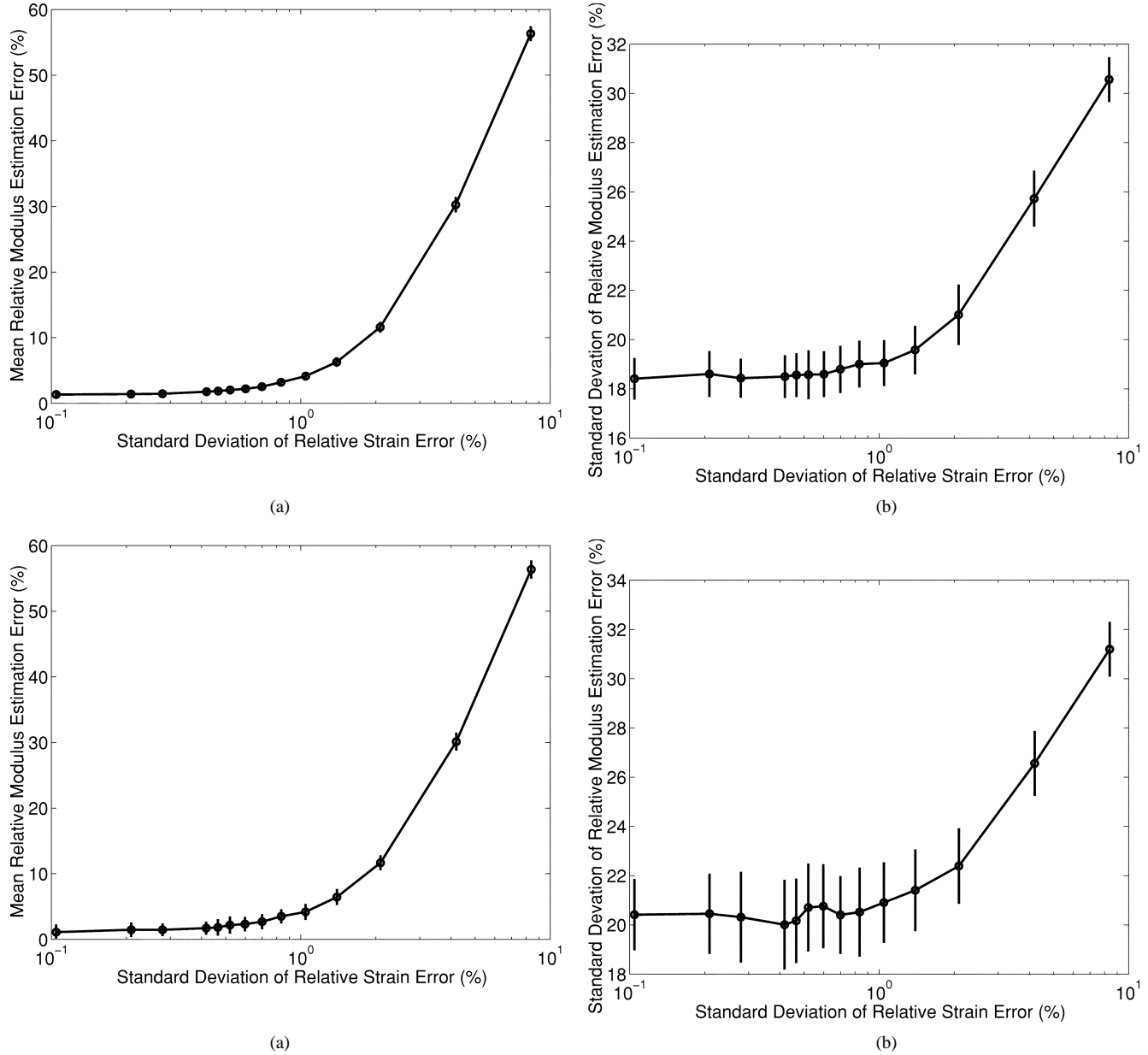


Fig. 10. Modulus estimation performance curves. (a) Standard deviation of the error in strain versus the mean relative error in modulus estimates resulting from a 5% standard deviation in the “measured” force. (b) Standard deviation of the error in strain versus standard deviation of the relative error in modulus estimates resulting from a 5% standard deviation in the “measured” force. (c) Standard deviation of the error in strain versus the mean relative error in modulus estimates resulting from a 10% standard deviation in the “measured” force. (d) Standard deviation of the error in strain versus standard deviation of the relative error in modulus estimates resulting from a 10% standard deviation in the “measured” force.

carefully designed methods for data acquisition, the viscous response to the external compression can be negligible [36].

In Section II-C1 we also assume the elastic behavior of the medium to be linear. This assumption only needs to be true between two states,  $S_1$  and  $S_2$ . Most human tissues have a nonlinear stress-strain relationship. Although the tissue can have significant nonlinear behavior, we can restrict our analysis to incremental deformations and forces as described in (16). Since the incremental deformation between  $S_1$  and  $S_2$  is usually small (less than 2%), the assumption of linear elasticity is reasonable.

For high accuracy FEA solutions to the forward elasticity problem, the object is usually meshed with nonuniform size and shape elements. The mesh has higher element density near curved interfaces where the modulus changes value, but

this requires knowledge of the object geometry. In modulus reconstruction, the internal geometry is unknown, so rectangular elements are used. One may argue that it is possible to first obtain a rough modulus reconstruction using uniform elements, then re-mesh the object with nonuniform elements and reconstruct modulus again for higher accuracy. To do so requires higher accuracy displacement estimates in the regions with higher element density. Since the displacement field is usually estimated with uniform accuracy, this approach is likely to fail.

To understand the effect of the noise in the measured displacement and force distribution, we conducted a number of numerical simulations. The results of these simulations, shown in Figs. 9 and 10, provide an estimate of the required accuracy in

input displacement and force data. We found that the method is less sensitive to noise in the force measurements than to noise in the displacement estimates. The size of mesh elements can be adjusted to change the sensitivity to displacement estimation errors. For a given displacement error, larger mesh elements result in smaller the strain error.

From Figs. 10(b) and (d), we observed that the modulus estimates obtained from noisy displacement and force estimates are also noisy (22% relative errors). However, since the modulus contrast between normal and cancerous tissues is usually large (greater than 100%) [36], the modulus image contrast-to-noise ratio for cancerous lesions will still be high.

We cannot prove that the inverse problem has a unique solution from physical principles. However, our method provides a unique solution algebraically. For the simulations that we have conducted, when there is no noise in the input data, the solution that we obtained is the same (within the numerical processing errors) as the Young's modulus distribution that we specified for the object (see Fig. 7 and Section III-B). With the added noise (to both surface force and the displacement distribution), our method generates solutions that are close to the true Young's modulus distribution (see Fig. 9 and Section III-C). This suggests that our method is stable and robust. Since we lack the necessary equipment to simultaneously measure surface force and the displacement distribution and, therefore, cannot test our method experimentally. This will be the subject of future effort.

FEA treats 2-D elasticity problems as special cases of a general three-dimensional (3-D) problem. The choice of these special cases are either plain strain (elevational strain is zero) or plain stress (elevational stress is zero). With the plain strain assumption, the external force is assumed to be exerted on a one-dimensional boundary, and it is difficult to relate such a load condition to reality. With the plain stress assumption, the object has finite thickness, and the calculated boundary force can be more easily related to actual measurements obtained on a 2-D surface.

Tissue deformation is 3-D in nature. However, we have found that *in vivo* breast, for example, can be deformed such that the motion perpendicular to the image plane is small. Thus, a 2-D description of motion provides a reasonable approximation to the plane strain condition. However, force measurements are more easily related to the plane stress condition, and with this assumption the resulting modulus estimates will have limited accuracy. To overcome this limitation, we need to extend our approach to 3-D. Extending 2-D modeling to 3-D is relatively straightforward with FEA methods.

The examples and discussion of displacement estimation techniques relate to our work in using ultrasound to track tissue motion. There is also a growing body of work where magnetic resonance techniques are used for estimating tissue elasticity [44], [45]. The modulus reconstruction technique should be applicable in that work as well.

## V. CONCLUSION

A new approach for estimating the modulus distribution from noninvasively determined force and displacement estimates is

reported. Simulations demonstrate that the modulus distribution for an ROI can be determined from force measurements on a single surface and displacement estimates within that ROI. The accuracy in force and displacement estimates required with this approach are also estimated with simulations. These results suggest that moduli of *in vivo* tissues can be estimated with reasonable accuracy with minor modification to current clinical imaging systems.

## APPENDIX I

In Fig. 1, nodes are locally numbered.<sup>2</sup> The element nodal displacement vector for the rectangular element has eight components and can be written as

$$\delta^{(e)} = (\delta_{1x}^{(e)} \ \delta_{1y}^{(e)} \ \delta_{2x}^{(e)} \ \delta_{2y}^{(e)} \ \delta_{3x}^{(e)} \ \delta_{3y}^{(e)} \ \delta_{4x}^{(e)} \ \delta_{4y}^{(e)})^T \quad (18)$$

where  $\delta_{1x}^{(e)}$  and  $\delta_{1y}^{(e)}$  are the displacement components in the  $x$  and  $y$  directions of the first node, and so on for the rest of the components;  $T$  is the matrix or vector transpose operator. The element nodal force vector also has eight components and can be written as

$$f^{(e)} = (f_{1x}^{(e)} \ f_{1y}^{(e)} \ f_{2x}^{(e)} \ f_{2y}^{(e)} \ f_{3x}^{(e)} \ f_{3y}^{(e)} \ f_{4x}^{(e)} \ f_{4y}^{(e)})^T. \quad (19)$$

The element stiffness matrix can be computed as [40]

$$K^{(e)} = \int_{-b/2}^{b/2} \int_{-a/2}^{a/2} t B^{(e)T} M^{(e)} B^{(e)} dx dy \quad (20)$$

where  $t$  is the element thickness,  $M$  is the material property matrix, and  $B$  is the displacement to strain mapping matrix. For example, with linear elasticity problems and assuming plain stress

$$M^{(e)} = E^{(e)} \frac{(1 - \nu^{(e)})}{(1 + \nu^{(e)}) (1 - 2\nu^{(e)})} \cdot \begin{bmatrix} 1 & \frac{\nu^{(e)}}{1 - \nu^{(e)}} & 0 \\ \frac{\nu^{(e)}}{1 - \nu^{(e)}} & 1 & 0 \\ 0 & 0 & \frac{1 - 2\nu^{(e)}}{2(1 - \nu^{(e)})} \end{bmatrix} \quad (21)$$

where  $E^{(e)}$  and  $\nu^{(e)}$  are the Young's modulus and Poisson's ratio of element  $e$ , and  $a$  and  $b$  are the element width and height. For rectangular elements, the displacement to strain mapping matrix is

$$B^{(e)} = \begin{bmatrix} \frac{\partial H_1}{\partial x} & 0 & \frac{\partial H_2}{\partial x} & 0 & \frac{\partial H_3}{\partial x} & 0 & \frac{\partial H_4}{\partial x} & 0 \\ 0 & \frac{\partial H_1}{\partial y} & 0 & \frac{\partial H_2}{\partial y} & 0 & \frac{\partial H_3}{\partial y} & 0 & \frac{\partial H_4}{\partial y} \\ \frac{\partial H_1}{\partial y} & \frac{\partial H_1}{\partial x} & \frac{\partial H_2}{\partial y} & \frac{\partial H_2}{\partial x} & \frac{\partial H_3}{\partial y} & \frac{\partial H_3}{\partial x} & \frac{\partial H_4}{\partial y} & \frac{\partial H_4}{\partial x} \end{bmatrix} \quad (22)$$

<sup>2</sup>The number starts from the lower left corner of the element and increases in the clockwise direction. Note that other numbering methods can also be selected as long as the connectivity matrix (introduced in Step 2) is created with the same numbering scheme for all elements.

where  $H_i, i = 1, \dots, 4$  are shape functions. The shape functions are usually selected to perform bilinear interpolations that have the form

$$\begin{aligned} H_1 &= \frac{1}{ab} \left( \frac{a}{2} - x \right) \left( \frac{b}{2} - y \right) \\ H_2 &= \frac{1}{ab} \left( \frac{a}{2} + x \right) \left( \frac{b}{2} - y \right) \\ H_3 &= \frac{1}{ab} \left( \frac{a}{2} + x \right) \left( \frac{b}{2} + y \right) \\ H_4 &= \frac{1}{ab} \left( \frac{a}{2} - x \right) \left( \frac{b}{2} + y \right). \end{aligned} \quad (23)$$

The representation of the element stiffness matrix (24) can be obtained by substituting (21)–(23) into (20) and performing the double definite integration. For convenience in deriving the inverse (modulus estimation) problem, the element stiffness matrix can be written as

$$K^{(e)} = E^{(e)} \tilde{K} \quad (24)$$

where  $\tilde{K}$  is an 8-by-8 matrix in which each component is a function of the aspect ratio ( $a/b$ ) and Possion's ratio of the rectangular element.

## APPENDIX II

Following is a description of the global stiffness matrix assembling process.

- 1) Initialize a  $N$ -by- $N$  null matrix (all zero entries), where  $N$  equals the total degrees of freedom of the system or

$$N = \text{number of nodes} \times \text{degrees of freedom per node.} \quad (25)$$

For the mesh shown in Fig. 2,  $N = 16 \times 2 = 32$ .

- 2) For element  $e$ , generate a local (element) variable number to global (system) variable number conversion index vector

$$I^{(e)} = \left( c_{e1}*2 - 1, c_{e1}*2, c_{e2}*2 - 1, c_{e2}*2, c_{e3}*2 - 1, c_{e3}*2, c_{e4}*2 - 1, c_{e4}*2 \right) \quad (26)$$

where  $c_{e1}$  is the  $e^{th}$  row and first column entry of the connectivity matrix  $C$ , and so on. For the system shown in Fig. 2, the index vector for the first element is

$$I^{(1)} = (1 \ 2 \ 3 \ 4 \ 11 \ 12 \ 9 \ 10). \quad (27)$$

- 3) Accumulate  $K_{ij}^{(e)}$  to  $K_{I_i^{(e)} I_j^{(e)}}$  for  $i = 1, \dots, 8$  and  $j = 1, \dots, 8$  ( $K_{ij}^{(e)}$  is the  $i^{th}$  row  $j^{th}$  column component of matrix  $K^{(e)}$ ;  $K_{I_i^{(e)} I_j^{(e)}}$  is the  $I_i^{(e)}$  row  $I_j^{(e)}$  column component of matrix  $K$ ;  $I_i^{(e)}$  is the  $i^{th}$  component of the index matrix).
- 4) Iterate 2 and 3 for all elements.

## APPENDIX III

The displacement boundary condition can be defined as  $\delta_{\text{sub}} = \delta_c$ , where  $\delta_{\text{sub}}$  is a vector that is composed of a subset

of the components of the global nodal displacement vector  $\delta$ ;  $\delta_c$  is a known constant vector that specifies the nodal boundary displacement. For example, a common displacement boundary condition for the object meshed by our 9-node example shown in Fig. 2 is to compress the top side downward 1% of the total height of the object while the bottom is fixed vertically. This example displacement boundary condition can be defined as  $\delta_{\text{sub}} = (\delta_2 \ \delta_4 \ \delta_6 \ \delta_8 \ \delta_{26} \ \delta_{28} \ \delta_{30} \ \delta_{32})^T$  and  $\delta_c = (0 \ 0 \ 0 \ 0 \ 0.01h \ 0.01h \ 0.01h \ 0.01h)^T$ , where  $h$  is the height of the object. The penalty approach can be expressed as the following seven steps.

- 1) Initialize the global force vector  $f$  as a null vector.
- 2) Select a large number  $L$  (a choice for  $L$  is  $L = \max|K| \times 10^4$  as suggested by Chandrupatla [41].
- 3) According to  $\delta_{\text{sub}}$ , set the corresponding  $f_{\text{sub}}$  to  $L \times \delta_c$  ( $f_{\text{sub}} = (f_2 \ f_4 \ f_6 \ f_8 \ f_{26} \ f_{28} \ f_{30} \ f_{32})^T$  for the given example).
- 4) According to  $\delta_{\text{sub}}$ , add  $L$  to the corresponding diagonal component of  $K$  (for our example, these diagonal components are  $K_{2,2}, K_{4,4}, K_{6,6}, K_{8,8}, K_{26,26}, K_{28,28}, K_{30,30}$ , and  $K_{32,32}$ ).
- 5) Solve  $K\delta = f$  for  $\delta$ .
- 6) Calculate reaction force  $f_{\text{sub}} = -L(\delta_{\text{sub}} - \delta_c)$ .
- 7) Replace  $\delta_{\text{sub}}$  with  $\delta_c$ .

## REFERENCES

- [1] C. P. McPherson, K. K. Swenson, G. Jolitz, and C. L. Murray, "Survival among women ages 40–49 years with breast carcinoma according to method of detection," *Cancer*, vol. 79, no. 10, pp. 1923–1932, 1997.
- [2] A. Sarvazyan, "Mechanical imaging: A new technology for medical diagnosis," *Int. J. Med. Inform.*, vol. 49, pp. 195–216, 1998.
- [3] P. S. Wellman, "Tactile imaging," Ph.D. dissertation, Dept. Eng. Sci., Harvard Univ., Cambridge, MA, 1999.
- [4] E. I. Cespedes, J. Ophir, H. Ponnekanti, and N. Maklad, "Elastography: Elasticity imaging using ultrasound with application to muscle and breast *in vivo*," *Ultrasound Imag.*, vol. 15, pp. 73–88, 1993.
- [5] E. Chen, R. Adler, P. Carson, W. Jenkins, and W. O'Brien, "Ultrasound tissue displacement imaging using ultrasound with application to muscle and breast cancer," *Ultrasound Med. Biol.*, vol. 21, pp. 1153–1162, 1995.
- [6] B. S. Garra, E. I. Cespedes, J. Ophir, S. R. Spratt, R. A. Zaubrier, C. M. Magnant, and M. F. Pennanen, "Elastography of breast lesions: Initial clinical results," *Radiology*, vol. 202, pp. 79–86, 1997.
- [7] T. J. Hall, Y. Zhu, and C. S. Splading, "In vivo real-time freehand palpation imaging," *Ultrasound Med. Biol.*, Oct. 2002.
- [8] S. Y. Emelianov, M. A. Lubinski, W. F. Weitzel, R. C. Wiggins, A. R. Skovoroda, and M. O'Donnell, "Elasticity imaging for early detection of renal pathology," *Ultrasound Med. Biol.*, vol. 21, pp. 871–883, 1995.
- [9] P. Chaturvedi, M. F. Insana, and T. J. Hall, "Acoustic and elastic imaging to model disease-induced changes in soft tissue structure," in *Lecture Notes in Computer Science*, A. Kuba and M. Samal, Eds. New York: Springer-Verlag, 1997, vol. 1230, pp. 1–14.
- [10] F. Kallel, J. Ophir, K. McGee, and T. Krouskop, "Elastographic imaging of low-contrast elastic modulus distributions in tissue," *Ultrasound Med. Biol.*, vol. 24, pp. 409–425, 1998.
- [11] T. J. Hall, H. A. Khant, M. F. Insana, J. G. Wood, Y. Zhu, D. Preston, and B. D. Cowley, "The utility of quantitative ultrasound for tracking the progression of polycystic kidney disease," *Proc. SPIE*, vol. 3982, pp. 161–171, 2000.
- [12] B. M. Shapo, J. R. Crowe, A. R. Skovoroda, M. J. Eberle, N. A. Cohn, and M. O'Donnell, "Displacement and strain imaging of coronary arteries with intraluminal ultrasound," *IEEE Trans. Ultrason., Ferroelect. Freq. Contr.*, vol. 43, pp. 234–246, Mar. 1996.
- [13] L. K. Ryan and F. S. Foster, "Ultrasonic measurement of differential displacement and strain in a vascular model," *Ultrason. Imag.*, vol. 19, pp. 19–38, 1997.
- [14] Y. C. Fung, *A First Course in Continuum Mechanics*. Englewood Cliffs, NJ: Prentice-Hall, 1994.

- [15] T. A. Krouskop, D. R. Dougherty, and F. S. Vinson, "A pulsed doppler ultrasonic system for making noninvasive measurement of the mechanical properties of soft tissue," *J. Rehab. Res. Dev.*, vol. 24, pp. 1-8, 1987.
- [16] R. M. Lerner, S. R. Huang, and K. J. Parker, "Sonoelasticity images derived from ultrasound signals in mechanically vibrated tissues," *Ultrasound Med. Biol.*, vol. 16, no. 3, pp. 231-239, 1990.
- [17] Y. Yamakoshi, J. Sato, and T. Sato, "Ultrasonic imaging of internal vibration of soft tissue under forced vibration," *IEEE Trans. Ultrason., Ferroelect. Freq. Contr.*, vol. 37, pp. 45-53, Mar 1990.
- [18] L. Sandrin, S. Catheline, M. Tanter, X. Hannequin, and M. Fink, "Time-resolved pulsed elastography with ultrafast ultrasonic imaging," *Ultras. Imag.*, vol. 21, no. 4, pp. 259-272, 1999.
- [19] R. J. Dickinson and C. R. Hill, "Measurement of soft tissue motion using correlation between a-scans," *Ultrasound Med. Biol.*, vol. 8, no. 3, pp. 263-271, 1982.
- [20] L. S. Wilson and D. E. Robinson, "Ultrasonic measurement of small displacements and deformations of tissue," *Ultras. Imag.*, vol. 4, pp. 71-82, 1982.
- [21] M. Tristam, D. C. Barbosa, D. O. Cosgrove, D. K. Nassiri, J. C. Bamber, and C. R. Hill, "Ultrasonic study of *in vivo* kinetic characteristics of human tissues," *Ultrasound Med. Biol.*, vol. 12, no. 12, pp. 927-937, 1986.
- [22] J. Ophir, I. Cespedes, H. Ponnekanti, Y. Yazdi, and X. Li, "Elastography: A quantitative method for imaging the elasticity of biological tissues," *Ultras. Imag.*, vol. 13, pp. 111-134, 1991.
- [23] M. O'Donnell, A. Skovoroda, B. Shapo, and S. Emelianov, "Internal displacement and strain imaging using ultrasonic speckle tracking," *IEEE Trans. Ultrason., Ferroelect. Freq. Contr.*, vol. 41, pp. 314-325, May 1994.
- [24] M. Bilgen and M. F. Insana, "Deformation models and correlation analysis in elastography," *J. Acoust. Soc. Amer.*, vol. 99, pp. 3212-3224, 1996.
- [25] K. A. Wear and R. L. Popp, "Theoretical analysis of a technique for the characterization of myocardium contraction based upon temporal correlation of ultrasound echoes," *IEEE Trans. Ultrason., Ferroelect. Freq. Contr.*, vol. UFFC-34, pp. 368-375, 1987.
- [26] R. Adler, J. Rubin, P. Bland, and P. Carson, "Quantitive tissue motion analysis of digitized m-mode images: Gestational differences of fetal lung," *Ultrasound Med. Biol.*, vol. 16, pp. 561-569, 1990.
- [27] P. DeJong, T. Arts, A. Hoeks, and R. Reneman, "Determination of tissue motion velocity by correlation interpolation of pulsed ultrasonic echo signals," *Ultras. Imag.*, vol. 12, pp. 84-98, 1990.
- [28] Y. Zhu and T. J. Hall, "A modified block matching method for realtime freehand strain imaging," *Ultras. Imag.*, Nov. 2002.
- [29] R. Muthupillai and R. L. Ehman, "Magnetic resonance elastography," *Nat. Med.*, vol. 2, no. 5, pp. 601-603, 1996.
- [30] A. M. T. E. Oliphant, M. A. Dresner, J. L. Mahowald, S. A. Kruse, E. Amromin, J. P. Felmlee, J. F. Greenleaf, and R. L. Ehman, "Magnetic resonance elastography: Non-invasive mapping of tissue elasticity," *Med. Image Anal.*, vol. 5, no. 4, pp. 237-254, 2001.
- [31] J. B. Weaver, E. E. V. Houten, M. I. Miga, F. E. Kennedy, and K. D. Paulsen, "Magnetic resonance elastography using 3D gradient echo measurements of steady-state motion," *Med. Phys.*, vol. 28, no. 8, pp. 1620-1628, 2001.
- [32] D. D. Duncan and S. J. Kirkpatrick, "Processing algorithms for tracking speckle shifts in optical elastography of biological tissues," *J. Biomed. Opt.*, vol. 6, no. 4, pp. 418-426, 2001.
- [33] A. R. Skovoroda, S. Y. Emelianov, and M. O'Donnell, "Tissue elasticity reconstruction based on ultrasonic displacement and strain images," *IEEE Trans. Ultrason., Ferroelect. Freq. Contr.*, vol. 42, pp. 747-765, July 1995.
- [34] F. Kallel and M. Bertrand, "Tissue elasticity reconstruction using linear perturbation method," *IEEE Trans. Med. Imag.*, vol. 15, pp. 299-313, June 1996.
- [35] M. M. Dooley, P. M. Meaney, and J. C. Bamber, "Evaluation of an iterative reconstruction method for quantitative elastography," *Phys. Med. Biol.*, vol. 45, pp. 1521-1540, 2000.
- [36] T. A. Krouskop, T. M. Wheeler, F. Kallerl, B. S. Garra, and T. J. Hall, "Elastic moduli of breast and prostate tissues under compression," *Ultras. Imag.*, vol. 20, pp. 260-274, 1998.
- [37] K. R. Raghavan and A. E. Yagle, "Forward and inverse problems in elasticity imaging of soft-tissue," *IEEE Trans. Nucl. Sci.*, vol. 41, pp. 1639-1648, Aug. 1994.
- [38] A. J. Romano, J. J. Shirron, and J. A. Bucaro, "On the noninvasive determination of material parameters from a knowledge of elastic displacements: Theory and numerical simulation," *IEEE Trans. Ultrason., Ferroelect. Freq. Contr.*, vol. 45, pp. 751-759, May 1998.
- [39] K. H. Huebner, E. A. Thornton, and T. G. Byrom, *The Finite Element Method for Engineers*, 3rd ed. New York: Wiley, 1995.
- [40] Y. W. Kwon and H. Bang, *The Finite Element Method Using MATLAB*, 2nd ed. New York: CRC, 2000.
- [41] T. R. Chandrupatla and A. D. Belegundu, *Introduction to Finite Elements in Engineering*, 2nd ed. Englewood Cliffs, NJ: Prentice-Hall, 1997.
- [42] W. H. Press, S. A. Teukolsky, W. T. Vetterling, and B. P. Flannery, "Numerical Recipes in C," in *The Art of Scientific Computing*, 2nd ed. Cambridge, MA: Cambridge Univ. Press, 1992.
- [43] M. Bilgen and M. F. Insana, "Covariance analysis of time delay estimates for strained signals," *IEEE Trans. Signal Processing*, vol. 46, pp. 2589-2600, Oct. 1998.
- [44] E. E. V. Houten, K. D. Paulsen, M. I. Miga, F. E. Kennedy, and J. B. Weaver, "An overlapping subzone technique for MR-based elastic property reconstruction," *Magn. Reson. Med.*, vol. 42, no. 4, pp. 779-786, 1999.
- [45] T. Wu, J. P. Felmlee, J. F. Greenleaf, S. J. Riederer, and R. L. Ehman, "Assessment of thermal tissue ablation with MR elastography," *Magn. Reson. Med.*, vol. 45, no. 1, pp. 80-87, 2001.

# AAPM/RSNA Physics Tutorial for Residents: Topics in US

## Beyond the Basics: Elasticity Imaging with US<sup>1</sup>

*Timothy J. Hall, PhD*

**Editor's Note.**—

Although this article is based on information presented as part of the AAPM/RSNA Physics Tutorial for Residents at the 2002 RSNA scientific assembly, as the title suggests, it discusses a new technology not found in clinical practice and not typically covered in physics courses for residents. However, since this technology is very likely to be in clinical use in the near future, many readers should find this article interesting and timely.

A new mode of imaging with ultrasonography (US) is under development in several laboratories around the world. This technique allows estimation of some measure of the viscoelastic properties of tissue. The information displayed in the images is a surrogate for that obtained with manual palpation. Fundamental concepts in elasticity imaging include stress, strain, and the elastic modulus; strain imaging has received the most attention from researchers. A system for elasticity imaging is under development that produces images of mechanical strain in real time by means of a freehand scanning technique. This system is integrated into a clinical US system without any external equipment and involves software changes only. Data obtained with this system demonstrate that the relative stiffness of many fibroadenomas changes as they and the surrounding tissue are deformed. At elasticity imaging of *in vivo* breast lesions, invasive ductal carcinomas appear, on average, more than twice as large on the elasticity image than on the B-mode image, but fibroadenomas and cysts are nearly equal in size on the two image types. The usefulness of this technology and the new information it provides suggest that it might soon be available on commercial US systems.

©RSNA, 2003

**Abbreviations:** RF = radiofrequency, 1D = one-dimensional, 2D = two-dimensional, 3D = three-dimensional

**Index terms:** Breast neoplasms, diagnosis, 00.30 • Physics • Ultrasound (US), elastography, 00.12989 • Ultrasound (US), tissue characterization, 00.12989

**RadioGraphics 2003; 23:1657–1671 • Published online 10.1148/rg.236035163**

<sup>1</sup>From the Department of Medical Physics, University of Wisconsin, 1530 Medical Sciences Center, 1300 University Ave, Madison, WI 53706-1532. From the AAPM/RSNA Physics Tutorial at the 2002 RSNA scientific assembly. Received July 11, 2003; revision requested July 30 and received August 7; accepted August 14. Supported by grant DAMD17-00-1-0596 from the U.S. Army Medical Research and Materiel Command; supported in part by a research agreement with Siemens Medical Solutions, Ultrasound Group (Issaquah, Wash). **Address correspondence to** the author (e-mail: *tjhall@wisc.edu*).

## Introduction

It is the experience of many that palpation, pressing on the surface of soft tissue in an effort to "feel" abnormalities, is a commonly used diagnostic tool. This tool has been used for thousands of years and is the primary diagnostic tool for some diseases. Examples include breast self-examination for sensing breast "lumps" and digital rectal examination for prostate cancer. Palpation is known to be subjective, and it lacks sensitivity to small abnormalities that are deep beneath the skin surface.

Improving sensitivity and reducing the subjectivity of palpation could have a significant impact on breast cancer prognosis. Breast cancer is the second-leading cause of cancer deaths in women. Over 200,000 new cases of invasive breast cancer are expected in the United States this year alone. It is anticipated that approximately 40,000 women in the United States will die of breast cancer in 2003. The prognosis for breast cancer patients is best when the disease is detected at an early stage. Specifically, 5- and 10-year survival statistics are best when cancer is noninvasive (1) and is less than 1 cm in diameter (2). Improvements in mammography have resulted in improved detection of breast lesions, and mammography can allow detection of smaller tumors in young women than either breast self-examination or clinical breast examination (3). However, mammography is not infallible. Approximately 15% of palpable breast cancers are not detectable with mammography, and this number is likely higher in younger women (4). A combination of clinical palpation with either mammography or ultrasonography (US) has been shown to significantly increase the sensitivity and specificity of breast cancer detection (5).

One of the greatest difficulties in mammography is imaging the radiographically dense breast. Unfortunately, women with mammographically dense breasts have a risk of breast cancer that is

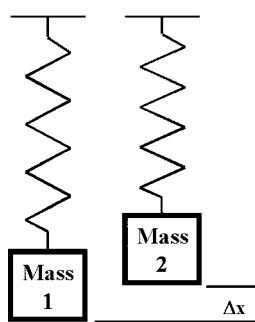
1.8–6.0 times greater than that of women the same age with little or no mammographic density (6). Small lesions become much more difficult to detect when obscured by dense connective tissues and ducts. Several recent studies have demonstrated that US has higher sensitivity for breast cancer detection than mammography alone (7), mammography combined with physical examination (7,8), or mammoscintigraphy (9). Furthermore, the sensitivity of mammography decreases significantly with increasing mammographic density (7,10). Hormone replacement therapy reduces the sensitivity of x-ray mammography (11) and increases the need for alternate diagnostic tools.

In an effort to improve the sensitivity of palpation and provide quantitative measures of "palpable," research groups around the world are actively working toward imaging technologies that display quantitative maps of "tissue stiffness." This article reviews the physics of palpation and uses that information to describe the limitations of palpation. That basic physical understanding is then used to describe the various approaches to these imaging technologies. The emphasis then turns to elasticity imaging systems and the development of an elasticity imaging system that is implemented on a commercial US system and displays real-time elasticity images with freehand scanning. Results of preliminary tests of the usefulness of that system for diagnosing breast abnormalities are then described.

Previous reviews of elasticity imaging with US are available (12,13). This article updates those prior reviews and emphasizes a specific real-time elasticity imaging system and results obtained with that system.

## Physics of Palpation

An understanding of how palpation works can be obtained by examining the basic physics of applying an external deformation to an object. Begin with a simple model of forces and deformation. A standard concept presented in introductory physics is the elastic deformation of a simple spring (a one-dimensional [1D] object) due to a known



$$\mathbf{F} = m \mathbf{a}$$

$$\Delta \mathbf{F} = k \Delta \mathbf{x}$$

Spring Constant  $k$

**Figure 1.** Introductory mechanics describes the behavior of a spring supporting different masses. Diagram shows how one spring would be stretched to two different lengths by two different masses. Hooke's law describes this behavior and can be used to characterize the spring under small deformations. Newton's second law equates a force,  $F$ , with a mass,  $m$ , and an acceleration,  $a$ . A known mass suspended from a spring exerts a known force due to the acceleration of gravity. Hooke's law relates the difference in the stretch of the spring,  $\Delta x$ , due to the change of force,  $\Delta F$ , resulting from suspending different masses. The proportionality constant,  $k$ , characterizes the stiffness of the spring.

applied force. Figure 1 illustrates the typical simple experiment to study elasticity. A known mass suspended from a simple spring results in a measurable elongation of that spring. Suspending a different known mass results in a different elongation of the spring. Each mass in the standard gravitational field of the earth places a known force on the spring. The difference in these forces and the difference in the elongations of the spring due to those forces can be combined by using Hooke's law to estimate the spring constant,  $k$ , which is characteristic of the spring and quantifies its "stiffness."

To extend the concept of force and deformation to a three-dimensional (3D) object, consider separately the forces and resulting displacements. The analysis will be simplified by assuming that the material is homogeneous and isotropic (meaning that the material properties are uniform in composition without any directional dependence in elasticity). Ignore the class of forces, called *body forces*, that act on all volume elements of the material (such as gravity and inertia). The class of forces to consider are called *surface forces* because they have units of force per unit area and can be viewed as acting on a surface element of

the object. That surface element is not necessarily on the exterior boundary of the object, but can be a surface of an arbitrary interior volume element.

The orientation of that surface is described by a vector that is perpendicular to the surface element (a normal vector); thus, a 3D coordinate system ( $x_i$ ,  $i = 1, 2, 3$  or  $x_1, x_2, x_3$ ) is required to describe the normal vector. A force acting on that surface element has a magnitude and direction (force is a vector quantity), and the direction of that force is not necessarily perpendicular to the surface element. Thus, to describe the direction of the force vector also requires a 3D coordinate system ( $y_j$ ,  $j = 1, 2, 3$ ). To maintain generality and simplicity (to obtain principle components) in the description of the surface force, two separate 3D coordinate systems are used ( $x_i$  and  $y_j$ ). Collapsing the arbitrary surface element to a point, we obtain a "stress tensor." A tensor is a generalization of the concept of a vector; tensor calculus is used to study the derivatives of vector fields. The stress tensor,  $\sigma_{ij}$ , is a  $3 \times 3$  matrix corresponding to the nine combinations available by combining the two independent 3D coordinate systems of the force and the surface element on which it acts.

Similarly, consider the displacement of a volume element acted on by an external force. If the motion does not involve a change of volume or shape of the object, the motion is termed *rigid body motion*. On the other hand, if the object is deformed (changes shape or volume) as a result of the external force, the description of motion is again more complex. A 3D coordinate system is required to describe the motion in space. To maintain generality and simplicity (to obtain principle components) in the description of the gradients (spatial rate of change) of that deformation (strain is the spatial rate of change of displacement), another 3D coordinate system is required. The strain tensor,  $\epsilon_{kl}$ , is thus another  $3 \times 3$  matrix corresponding to the nine combinations available by combining these two independent 3D coordinate systems.

An equation to relate the nine-component stress tensor to the nine-component strain tensor is called a *constitutive equation*. The form of the constitutive equation depends on whether a material is a fluid (an ideal fluid with no viscosity or a

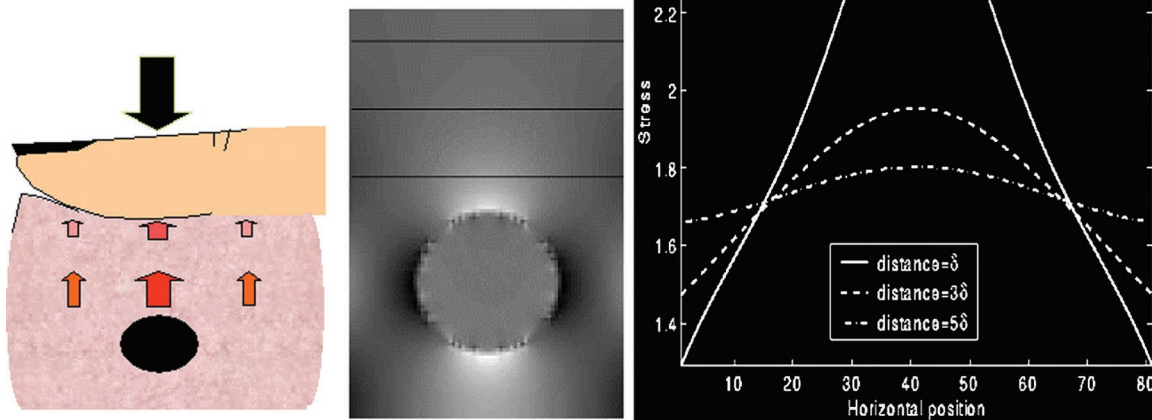


**Figure 2.** Palpation can be approximated with a simulation tool (finite element analysis). Left: Drawing shows uniform displacement of the top surface of a block containing a spherical object. Center: Image shows the axial stress distribution resulting from the displacement. Right: Plot shows profiles of the stress distribution across the lines in the center image. A large variation in the stress profile is seen for the profile close to the spherical object. This situation simulates location of the sphere near the surface of the block. As the profile moves further away from the sphere, the variation in stress across the profile decreases, suggesting that the sphere would be more difficult to palpate as it is placed deeper in the block.

Newtonian viscous fluid), purely elastic (eg, an idealized solid), or viscoelastic (neither purely viscous nor purely elastic). In a purely elastic (lossless) deformation, the stress is dependent only on the strain:  $\sigma_{ij} = C_{ijkl} \epsilon_{kl}$ . This equation is analogous to Hooke's law for the 1D spring, but it accounts for forces and deformations in all three directions.

The quantity  $C_{ijkl}$  is the "modulus tensor" of elastic coefficients and is the equivalent of the spring constant,  $k$ , used to describe the deformation of a spring. The four subscripts indicate that four sets of 3D coordinate systems are required for a general description of the relationship between the stress and strain tensors, and thus,  $C_{ijkl}$  has (3<sup>4</sup>) 81 components. The stress and strain tensors are symmetric and therefore each contains at most six independent components. Therefore, the modulus tensor for infinitesimal elastic deformations is also symmetric and contains at most 36 independent components. By assuming a material to be completely isotropic, it can be shown (14) that the number of independent elastic coefficients is reduced to two (called the *Lamé constants*). A more detailed description of stress and strain can be found in any text on continuum mechanics (eg, reference 15).

The elastic coefficients that describe the behavior of a material are absolute measures of intrinsic properties of the material. Estimating these quantities requires measurements of stresses and strains under well-characterized experimental conditions. For example, the viscoelastic properties of many soft tissues under cyclic uniaxial loading are found to depend on the strain range, strain rate, measurement temperature, and so on (16). It is often easier to simplify the experiment and measure only components of the surface stress distribution or the internal strain distribution. The drawback is that stress or strain alone is a relative quantity and not intrinsic to the material under study.

The basic physics of elasticity (stress and strain) can be used to understand the limitations of palpation. Engineers often use a computational tool called *finite element analysis* to study the behavior of objects under external forces or deformations. Finite element analysis was used to simulate the stress and strain involved when deforming a uniform block containing a spherical inclusion (Fig 2). The upper surface of the block is uniformly displaced by 1% of the total height. The lower surface is allowed to move freely laterally, and the sides have unrestricted motion. Figure 2 shows the distribution of stress and profiles of that stress distribution. In palpation, the fingers press on the tissue to deform it and then sense the

### Elastic Moduli of in Vitro Breast Tissue at Two Different Strain Ranges and Strain Rates

Type of Breast Tissue	Elastic Moduli by Strain Range and Strain Rate	
	5% Precompression, 10%/sec Strain Rate	20% Precompression, 20%/sec Strain Rate
Normal fat	19 ± 7	20 ± 6
Normal glandular tissue	33 ± 11	57 ± 19
Fibrous tissue	107 ± 32	233 ± 59
Ductal carcinoma in situ	25 ± 4	301 ± 58
Invasive ductal carcinoma	93 ± 33	490 ± 112

Note.—Ductal carcinoma demonstrates the largest difference between modulus measurements under these two conditions. This result suggests that it has the most nonlinear stress-strain relationship among the tissues studied.

stress distribution that results. The simulation shows that as the sphere moves further away from the surface (profile further from the sphere), the variation in stress across the profile decreases, suggesting that the sphere would be more difficult to palpate (less stress contrast available to the fingers to sense) as it is placed deeper in the block.

### In Vitro Tissue Studies

The most common approach to studying the viscoelastic properties of soft tissues is to sinusoidally deform in vitro samples of tissue, measure the force required to induce the deformation, and study the phase relationship between force and displacement. In vitro studies of the viscoelastic properties of breast tissue (13,17) have demonstrated several findings that are significant to elasticity imaging (Table). First, for cyclic load-unload experiments, there is little phase delay between the sinusoidal deformation and response (strain and stress) for compression frequencies near 1 Hz. This shows that the energy required to deform the tissue is nearly completely recovered when the deforming force is released (nearly lossless deformation). Thus, in vitro breast tissue behaves as a nearly completely elastic medium at these strain rates, and the viscous component can be ignored. These deformation motion frequencies are typical of that used in clinical US breast examinations with compression.

Second, the stress-strain relationship for most breast tissues is nonlinear, and the degree of nonlinearity varies with tissue type. (Materials with linear stress-strain relationships exhibit stress that is directly proportional to strain; that is, they exhibit constant stiffness. Materials with nonlinear

stress-strain relationships change stiffness, most commonly getting stiffer, as they are deformed.) Third, the elastic moduli of breast tissue, obtained from the slope of the stress-strain curves, vary significantly among breast tissue types and strain range. In summary, breast tissue is mostly elastic for the strain rates likely encountered with freehand scanning, object contrast is likely high in strain and modulus images, contrast will likely be different for different lesion types, and contrast will likely change with increasing compression.

### Imaging the Elastic Properties of Tissue

Approaches to elasticity imaging can be classified by the modality of the signal source (primarily US or magnetic resonance [MR] imaging), the mechanical parameter estimated (eg, stress, strain, or modulus), or a descriptor of the experimental procedure ("dynamic" or "[quasi]-static" techniques). The mechanical properties estimated with these techniques are related. As described earlier, stress and strain are mutually responsive quantities, but they are not intrinsic material properties. Images of stress and strain are maps of a parameter relative to its surroundings (as a mammogram maps the relative x-ray attenuation, for example). Elastic moduli are intrinsic material properties generally described with a matrix (as described earlier), but for practicality experimental conditions are manipulated and material properties (such as incompressibility, homogeneity,

and isotropy) are assumed so that the size of this matrix is reduced to one or two parameters.

Several research groups are developing techniques for imaging the stress distribution. Most notable among the stress imaging techniques is the work from Wellman et al (18), who use a piezoresistive sensor array (Tekscan, Boston, Mass) coupled to a position-tracking system. This system closely mimics the mechanics of palpation and demonstrates a strong correlation between the size of the lesion measured with the tactile system and the lesion size measured following resection. The performance for small lesions ( $<10$  mm) that are relatively deep ( $>10$  mm) remains to be seen. Also noteworthy is the work of Sarvazyan (19), in which he attempts to solve the inverse problem of determining the 3D modulus distribution that causes the measured surface pressure distribution.

Strain imaging has received the most attention in elasticity imaging. The earliest implementations used M-mode acquisition and cross-correlation to track tissue motion and study tissue elasticity (20,21). In later studies, Doppler processing techniques were used to track differences in motion (22,23), and "sonoelasticity imaging" soon followed (24). The Doppler processing techniques were the first "dynamic techniques" and derived their data from US. "Static compression elastography" is the most common approach to strain imaging. Numerous groups are pursuing US-based strain imaging, with efforts in algorithm development (25-29), performance evaluation (30-32), and clinical testing (33,34) (representative citations).

The basic information derived in strain imaging techniques is the relative tissue displacement. An imaging system (typically US or MR imaging) acquires (predeformation) data corresponding to a map of tissue anatomy. A small deformation is applied, either through an external compressor or physiologic function (breathing, cardiac pressure variations, etc), and another (postdeformation) map of the anatomy is acquired. The displacement field in the deformed tissue is estimated by comparing these two maps of anatomy. Mechanical strain is estimated by calculating the gradient (the spatial rate of change) of the displacement field. In US, the displacement along the acoustic beam propagation (axial) direction can be estimated far more accurately and with higher precision than that in the lateral or elevational direction (32).

An important aspect for clinical acceptance of US strain imaging is the technique for deforming the soft tissue between image pairs. Most phantom experiments in the literature used motorized compression devices and extensive fixtures. These devices are not likely to gain clinical acceptance because they either limit the locations where strain imaging can be applied or are time-consuming to incorporate. Freehand scanning, in which tissue is deformed with the surface of the transducer, is desirable (33-35).

Developing a real-time strain imaging system that allows freehand scanning is essential for clinical usability. The strain imaging algorithm must be computationally efficient, be insensitive to motion irregularities, and track tissue motion in two dimensions (eventually three and four dimensions). Block-matching (template-matching) algorithms are widely used in image processing applications for tracking motion. The most notable application is movie image compression algorithms such as the Moving Picture Experts Group (MPEG) format. The use of block matching in US was initially reported by Trahey et al (36) for blood flow estimation. Block matching is a good candidate since it is simple in principle and is capable of tracking motion in two dimensions. However, for strain imaging, the algorithm needs to be modified to increase its computational efficiency and insensitivity to decorrelation noise (29). (Decorrelation is a measure of how similar two signals are. That similarity is measured with cross-correlation or surrogate measures of correlation. Echo signals decorrelate when there is high electronic noise or when there is large deformation of the tissue.)

There has been less attention focused toward strain imaging systems than toward strain imaging algorithms, data simulation, and performance testing. Doyley et al (35) have reported their progress in freehand elasticity imaging. Their system lacked real-time feedback in the data acquisition process; nevertheless, they found that it is possible to obtain good elasticity data with freehand scanning. Their rate of success was relatively low, and significant pre- and postprocessing were necessary to obtain accurate displacement estimates.

The system reported by Garra et al (33) used a modified mammography paddle with a hole cut out to provide an acoustic window. This allowed (relatively) easy correlation with the mammogram. However, the acoustic data acquisition system was crude. The system allowed scanning with only a 5-MHz transducer—lower than the standard of its day (7.5 MHz)—and had significantly

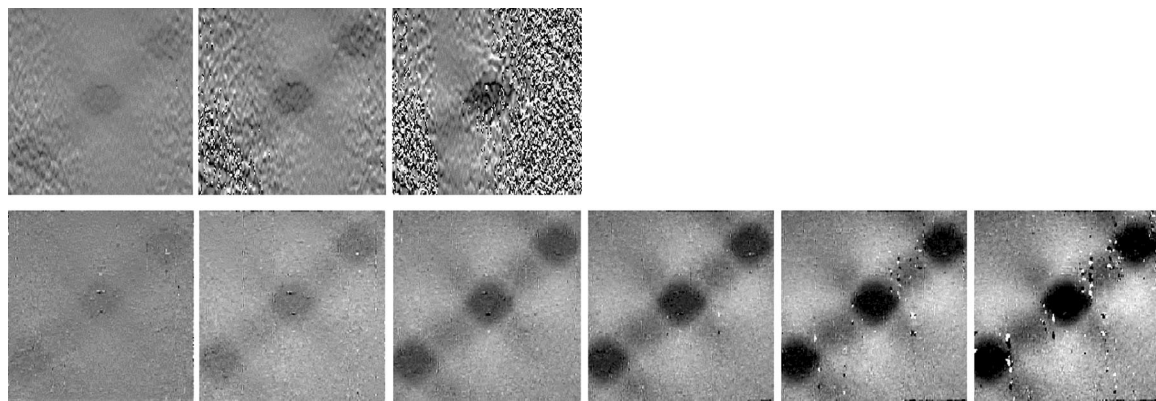


**Figure 3.** Images of the mechanical strain in the axial direction for a gelatin phantom with three cylinders that are three times stiffer than the background. Top row: Strain images obtained with 1D tracking by using cross-correlation. Bottom row: Strain images obtained with 2D companding (2D motion tracking). The applied deformation (top and bottom rows) from left to right is 0.6%, 1.2%, 2.4%, 3.6%, 4.8%, and 6.0% strain. With 1D tracking (top row), lateral expansion (bulging) occurring with axial compression causes the echo A-lines to not match and the echo signals to decorrelate. Two-dimensional tracking (bottom row) is able to track the lateral as well as axial motion to allow acquisition of strain images with a higher contrast-to-noise ratio.

poorer performance than current systems. In addition, the digitization was external to the US scanner, resulting in reduced electronic signal-to-noise ratio and increased timing jitter in the acquired echo signals. The increased jitter significantly reduces the performance of displacement estimates in strain imaging. The current system used by that group incorporates a midrange US scanner with a five-axis motor controlled compression system (37). The first real-time elasticity imaging system was developed for prostate imaging (38). Data were acquired in a sector-shaped scan from an endocavity transducer, and a 1D tracking method was used. As a result, elasticity image frame rates were quite high at the expense of image quality.

The *in vivo* studies of strain imaging reported by Garra et al (33) demonstrated that strain imaging has merit in differentiating among solid tumors in breasts. Their most significant finding was that invasive ductal carcinomas are significantly wider in strain images than in the corresponding B-mode image. This difference is likely due to the desmoplastic reaction that surrounds this tumor type.

Modulus imaging has also been investigated, and there are three primary approaches in the literature. The first approach estimates the shear wavelength in tissue and from this directly estimates the shear modulus of the tissue (39–41). The other techniques require simultaneous measurements of stress and strain and require assumptions regarding the boundary conditions of the experiment (42–46). Compared with strain

imaging, modulus imaging has lower spatial resolution and higher noise, and the assumptions regarding boundary conditions can result in biased estimates. However, estimating an intrinsic tissue parameter, instead of the relative parameters estimated in stress or strain images, makes this an attractive approach.

There are also methods under development that use acoustic radiation force to deform tissue and study tissue viscoelasticity (47–49) with promising results. Other novel approaches to describing the viscoelastic behavior of tissues, such as those reported by Fatemi et al (50,51), are also under investigation.

Early work in strain imaging demonstrated the limitations of tracking motion in one dimension and motivated the development of two-dimensional (2D) and 3D motion-tracking algorithms for elasticity imaging (27,28,52). Those studies demonstrated that 1D tracking failed to correctly track motion in a 3-cm-wide field of view with as little as 0.6% compression, and motion-tracking errors became increasingly worse with increased compression. However, by using 2D tracking algorithms that appropriately compensate for lateral motion, high contrast-to-noise images of mechanical strain could be obtained with compressions of more than 5% in phantoms (Fig 3). The basic approach, called *companding*, was to use 2D motion tracking to align (warp) either the pre- or postdeformation data field prior to 1D cross-correlation.

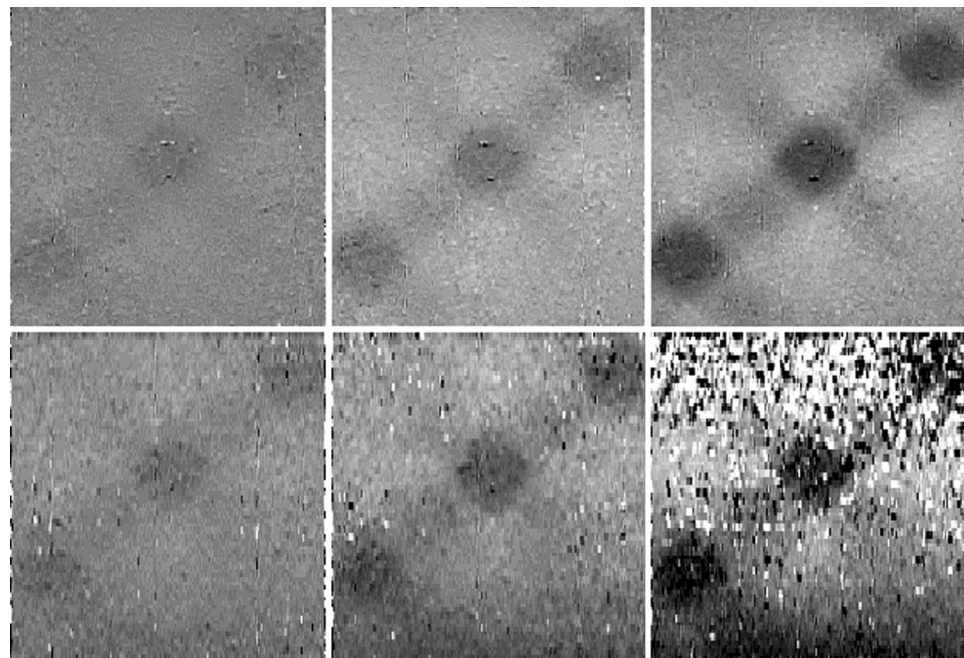


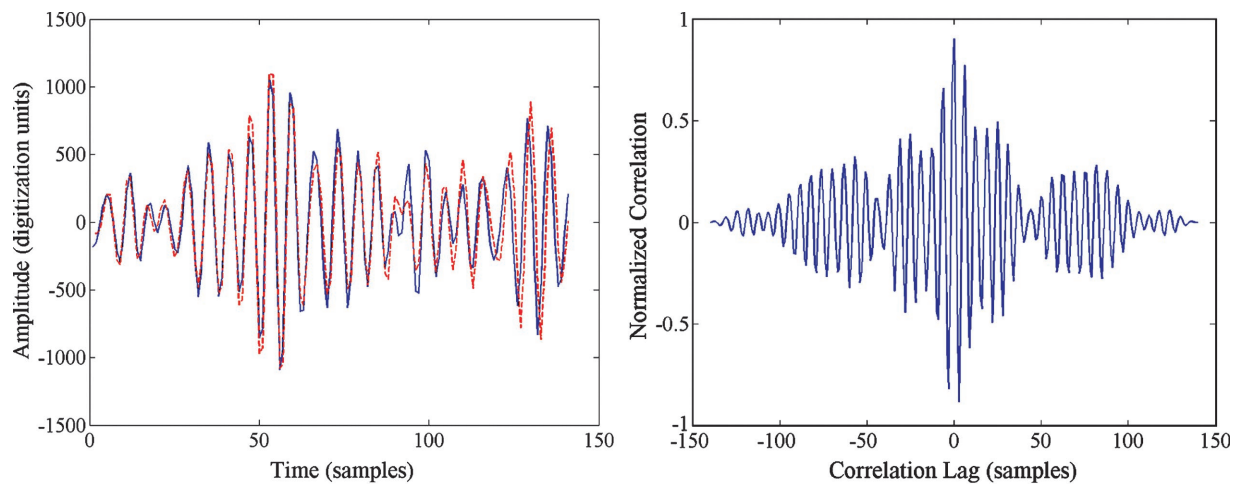
**Figure 4.** Images of a gelatin phantom with varying deformation (from left to right, 0.6%, 1.2%, and 2.4% axial strain). Top row: Images acquired with the top and bottom surfaces slipping freely and with minimal elevational motion, as in Figure 3. Bottom row: Images acquired near the edge (in elevation, perpendicular to the image plane) of the phantom, which was bound in elevation at the bottom and slid freely at the top. As the phantom was deformed, the top slid out of the image plane in elevation, resulting in decorrelation of the echo signals. Increasing the deformation caused greater decorrelation.

Other early work also demonstrated the need to control motion during elasticity imaging experiments. The images in Figure 4 demonstrate that it is essential to control the motion during deformation, especially with regard to elevation motion. A typical clinical US system acquires echo data, nominally, from a plane of tissue. Any out-of-plane motion of tissue will result in echo signal decorrelation and reduced elasticity image quality.

The key to obtaining high-quality elasticity images is the quality of the motion-tracking algorithm. Ultrasound radiofrequency (RF) echo signals, the same data used to form a B-mode image, are used as a map of anatomy. Those same signals are used to track the deformation of the anatomy. The task is to accurately track the anatomic deformation with minimal uncertainty (displacement estimate variance or covariance). A review

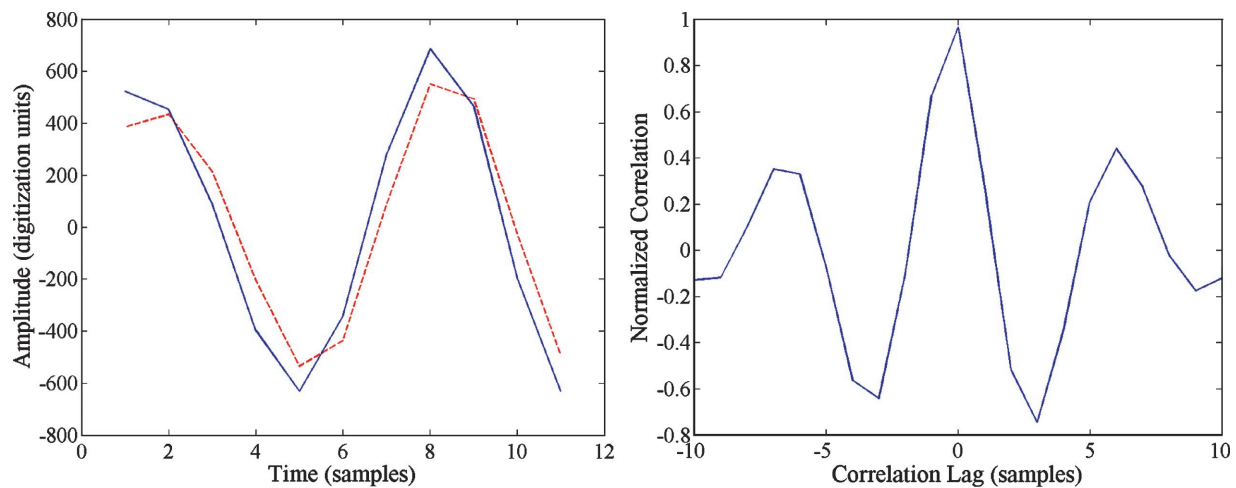
of many of the techniques used for tracking tissue motion with ultrasound can be found in reference 53. A tutorial on the general topic of waveform coherence and time-delay estimation can be found in reference 54.

A review of the assumptions used in signal correlation analysis can help one appreciate the difference between many motion-tracking algorithms. A typical assumption in motion tracking based on the time delay of ultrasound echo signals is that the deformation of the tissue is minimal (or recoverable) within the echo signal segment being tracked. Another common assumption is that the observation window (data segment length) is large compared to the time delay. Thus, a relatively long data segment is needed to avoid ambiguous displacement estimates (referred to as *peak hopping*). The plot in Figure 5 demonstrates that with an RF echo segment as short as 3 mm and with only 1.5% axial strain, there is obvious echo signal decorrelation between the pre- and postdeformation A-lines. However, the single



a.

**Figure 5.** (a) Plot of the predeformation (red dashed line) and postdeformation (solid blue line) data for a 3-mm segment (140 RF samples) of the echo signals from the center of a gelatin phantom under 1.5% axial strain. The postdeformation signal has been shifted in time to match the predeformation signal as closely as possible. The deformation has caused decorrelation in the echo signals, which reduces coherence (cross-correlation coefficient = 0.87). (b) Plot of the cross-correlation function comparing the predeformation and time-delayed postdeformation RF echo signals. The single large positive peak suggests that there is little ambiguity in the correct delay required to match these signals.



a.

**Figure 6.** (a) Plot of the predeformation (red dashed line) and postdeformation (solid blue line) data for a 0.24-mm segment (11 RF samples) of the echo signals from the center of a gelatin phantom under 1.5% axial strain. The postdeformation signal has been shifted in time to match the predeformation signal as closely as possible. Little decorrelation in the echo signals within this short echo segment results in high coherence (cross-correlation coefficient = 0.96). (b) Plot of the cross-correlation function comparing the predeformation and time-delayed postdeformation RF echo signals.

large peak in the cross-correlation function plotted in Figure 5 demonstrates that there is little ambiguity in the time delay required to match pre- and postdeformation signals.

Use of shorter RF echo segments in motion tracking reduces the decorrelation within the echo

signal segment and increases the waveform coherence (Fig 6). However, short data segments increase the likelihood of time-delay ambiguity (eg,

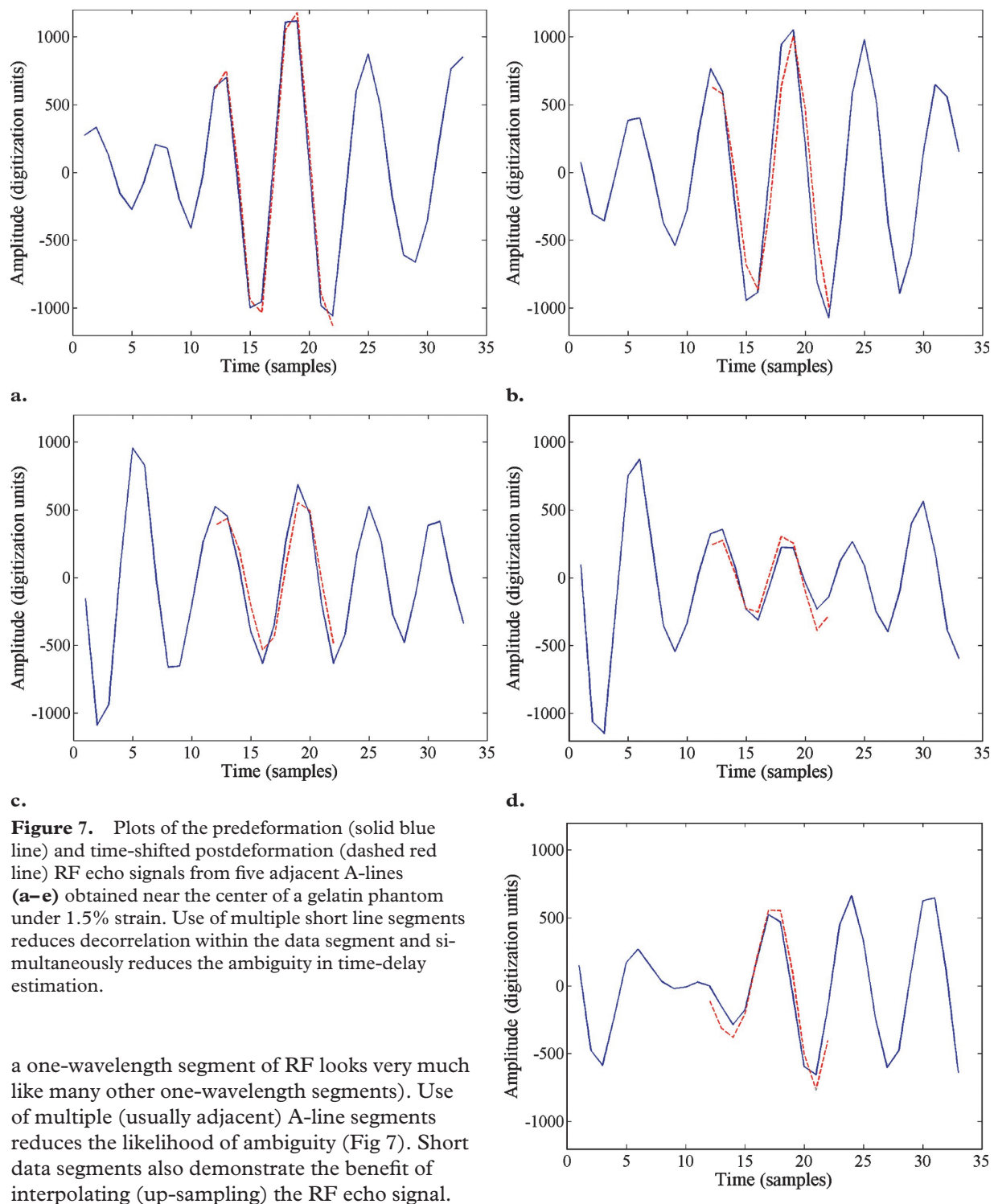
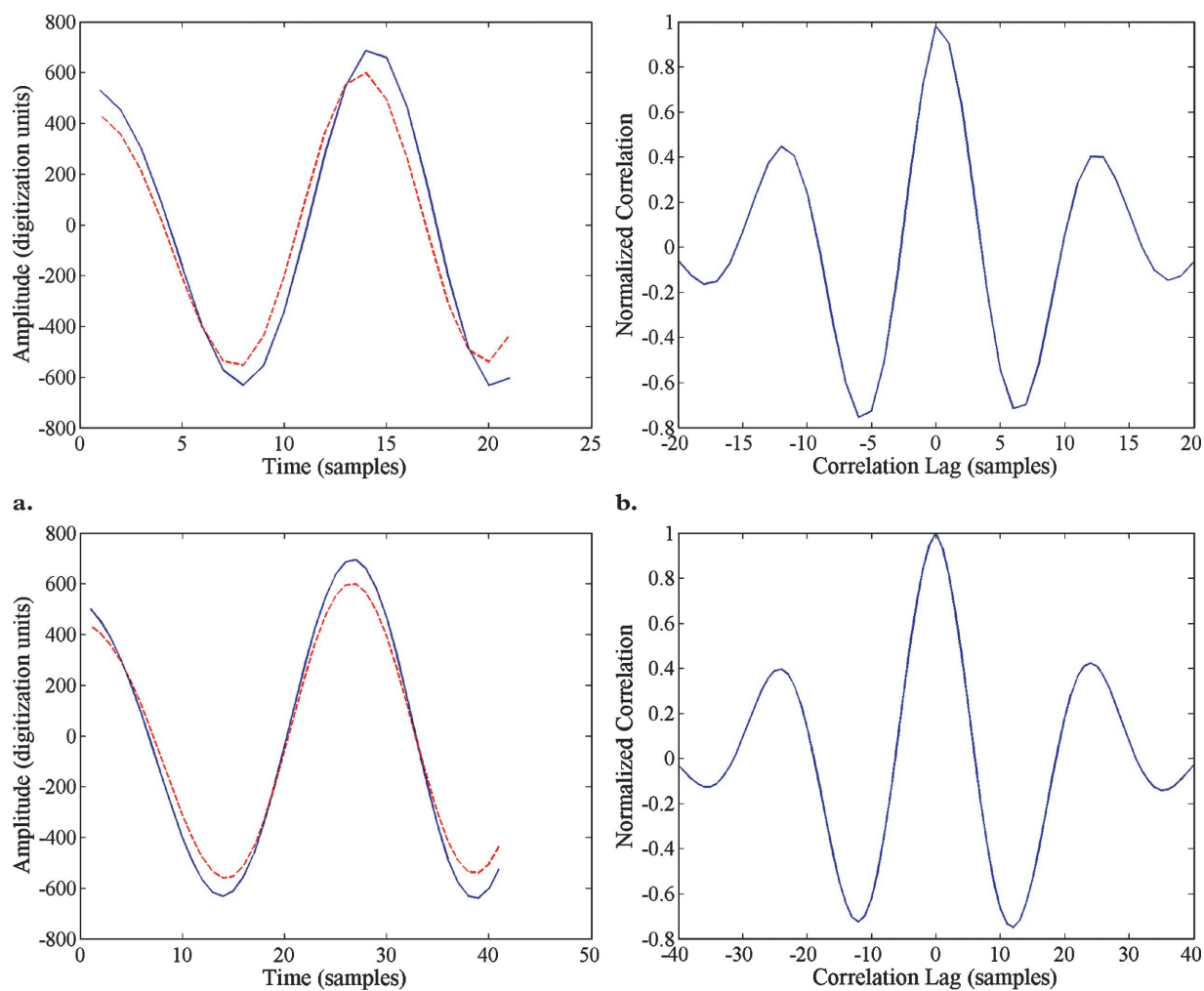


**Figure 7.** Plots of the predeformation (solid blue line) and time-shifted postdeformation (dashed red line) RF echo signals from five adjacent A-lines (a-e) obtained near the center of a gelatin phantom under 1.5% strain. Use of multiple short line segments reduces decorrelation within the data segment and simultaneously reduces the ambiguity in time-delay estimation.

a one-wavelength segment of RF looks very much like many other one-wavelength segments). Use of multiple (usually adjacent) A-line segments reduces the likelihood of ambiguity (Fig 7). Short data segments also demonstrate the benefit of interpolating (up-sampling) the RF echo signal. The waveforms shown in Figure 6 illustrate that waveform coherence would improve if time delays of less than one sample were available. An alternative is to interpolate the correlation function, but this requires a model for the functional form

of the cross-correlation function. If up-sampling the RF echo signal can be justified, it reduces the need for an accurate model of the cross-correlation function when interpolating subsample displacement estimates (Fig 8).



c.

**Figure 8.** Plots of the predeformation (red dashed line in **a** and **c**) and postdeformation (solid blue line in **a** and **c**) data for a 0.24-mm segment of the echo signals at 1.5% axial strain acquired at a 36-MHz sampling frequency upsampled to 72 MHz (**a**, **b**) and 144 MHz (**c**, **d**). The postdeformation signal has been shifted in time to match the predeformation signal as closely as possible. As the effective sampling interval is reduced, the integer time-delay error is also reduced, allowing greater waveform coherence. (Correlation coefficients of 0.965 [Fig 6], 0.978, and 0.998 were obtained with 36-MHz, 72-MHz, and 144-MHz sampling, respectively.)

### Development of a Real-Time Strain Imaging System

Experience in developing motion-tracking algorithms and experiments with phantoms and in vitro tissues suggest criteria for a clinically viable elasticity imaging system. First, the system must track tissue motion in two dimensions (or three dimensions, if available) for high contrast-to-noise images (27,28). Second, the system should use short 2D data segments (kernels) for motion tracking to minimize decorrelation within the data segments and to minimize time-delay ambiguity. Third, the system should provide real-time

elasticity images, as well as normal B-mode images, to allow the user to monitor the images being acquired and manipulate the transducer array with freehand scanning, thus ensuring that the tissue motion is suitable for forming high-quality elasticity images. In addition, the data acquisition technique should be similar to that currently used in US to increase the likelihood of clinical acceptance. A large deviation from standard clinical practice would likely receive a more skeptical assessment by potential users than a subtle modification to current practice.

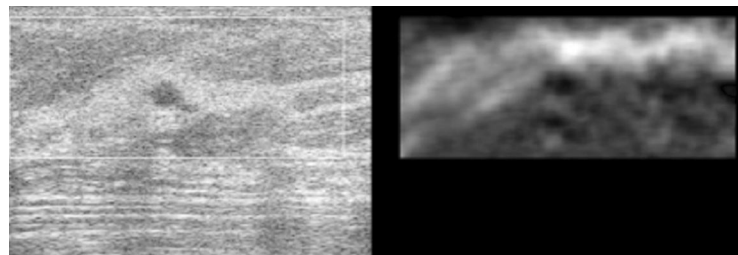
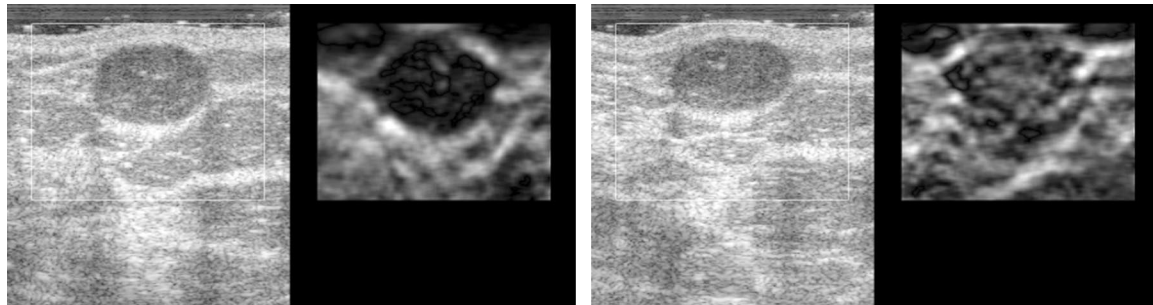


**Figure 9.** B-mode (left) and elasticity (mechanical strain) (right) images of an *in vivo* breast cyst 3 mm in diameter show that small *in vivo* structures are resolvable on strain images.



**a.**

**b.**

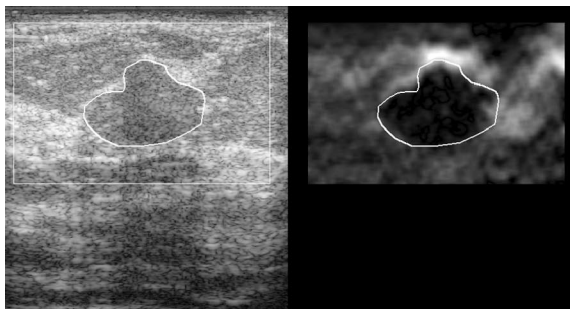
**Figure 10.** B-mode (left) and strain (right) images of a typical fibroadenoma under different amounts of preload (deformation): low preload (**a**) and increased preload (**b**). For both elasticity images, the average strain is about 1.2%. The images obtained at low preload (**a**) were acquired with the US transducer just barely in contact with the skin surface. At low preload, fibroadenomas are typically stiff relative to the surrounding glandular tissue. As the preload increases (**b**), the contrast of the fibroadenoma on the strain image decreases and the stiffness of the lesion appears nearly equal to that of the surrounding tissue.

A novel motion-tracking algorithm has been developed and implemented on a clinical US system (Sonoline Elegra; Siemens Medical Solutions, Issaquah, Wash) (29). Phase-sensitive (I-Q) echo data are processed internally in real time on this system to estimate displacement and strain. The system can use any of the linear-array transducers available on the Elegra and is compatible with tissue harmonic imaging on that system. The system displays B-mode and strain images side by side on the normal system display at about seven frames per second. A region of interest (ROI) is displayed in the B-mode image, and displacement and strain are estimated for tissue within that ROI. The size and location of the ROI can be manipulated with front panel controls. When scanning, the normal freeze and cine capabilities of the system are available. When a sequence of data is acquired and stored (frozen), online postprocessing capabilities allow the ROI location and size to be modified, and other common tools such as modifying the gray-scale mapping are available. Initial tests of the elasticity image noise and spatial resolution are found in reference 29. Spherical lesions as small as 2.4 mm in

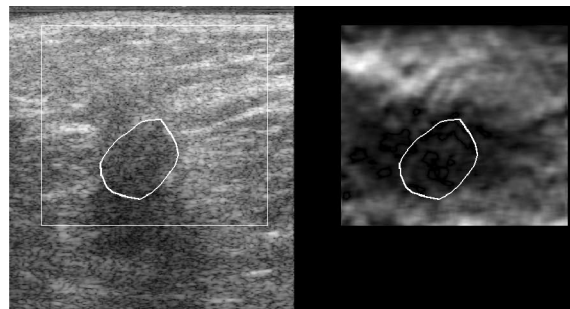
diameter that are three times stiffer than the background were easily displayed. The protocol for clinical testing of this system was approved by the Humans Subjects Committee at the University of Kansas Medical Center, where that initial work was performed.

A critical issue in the development and use of any imaging system is the achievable spatial resolution for a given task. The ability to image a 3-mm-diameter sphere in a phantom is encouraging. More important, those encouraging results are corroborated by the ability to image small structures *in vivo*. For example, images of an *in vivo* 3-mm cyst are shown in Figure 9. Although the ability to image small structures *in vivo* is clearly demonstrated, the required contrast to view objects of a specific size is unknown. Investigations are under way to evaluate this through contrast-detail analysis (55).

The ability to acquire and view long sequences of elasticity images has provided the opportunity to observe nonlinear elastic behavior of *in vivo* tissues. Nonlinearity in the stress-strain relationship of tissue was observed with *in vitro* breast tissues (17) and was therefore expected with *in vivo* tissues, but it was only recently observed with the availability of a real-time elasticity imaging system (34). Figure 10 shows an example of



11.



12.

**Figures 11, 12.** (11) B-mode (left) and strain (right) images of a fibroadenoma. The lesion is traced on the B-mode image, and that tracing is displayed on the strain image. The size and shape of the lesion on the two images are very similar. (12) B-mode (left) and strain (right) images of a scirrhouous invasive ductal carcinoma. The lesion is traced on the B-mode image, and that tracing is displayed on the strain image. The lesion is larger on the strain image (right) than on the B-mode image (left).

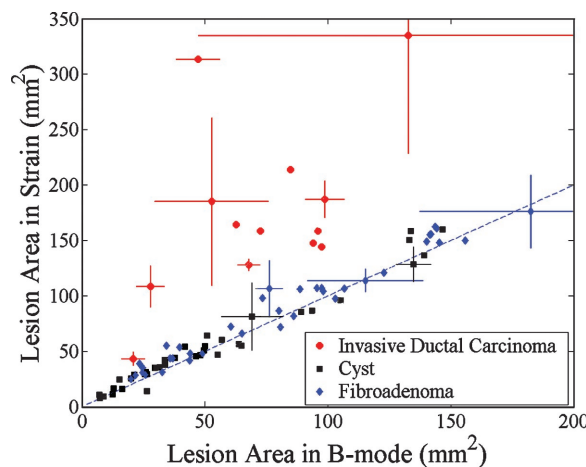


**Figure 13.** Plot of lesion area measured on strain images versus on corresponding B-mode images for cysts, fibroadenomas, and invasive ductal carcinomas. The average results of five observers are plotted. Dashed line = equal area on both image types, error bars = standard deviations of the measurements.

the implications of nonlinear elasticity in strain imaging. At low preload (transducer barely in contact with the skin surface and minimal pressure applied), the fibroadenoma appears dark in the strain image. As the preload is increased (pressure applied with the transducer increasing deformation), the strain image contrast of the fibroadenoma (its stiffness relative to the surrounding tissue) decreases. This behavior might explain why others have found that some fibroadenomas are not visible in single strain images (33).

One of the significant findings in prior clinical trials of in vivo elasticity imaging (33) was that the size of a breast lesion displayed in strain images, relative to its size in a normal B-mode image, appears to be a significant criterion for differentiating malignant from benign breast lesions. Figures 11 and 12 show examples of the B-mode

and strain image pairs for a fibroadenoma and an invasive ductal carcinoma, respectively. In each case, the lesion is traced in the B-mode image and that tracing is reproduced in the respective strain image. The lesion boundary traced for benign lesions has about the same size and shape in the two image types. However, the lesion boundary traced in B-mode images of invasive ductal carcinomas is much smaller than the lesion displayed in the respective strain image. On average, the area of these carcinomas displayed in strain images is three times larger than that in B-mode images (34). It is postulated (33,34) that the increased size of carcinomas in strain images is due to the desmoplasia that often surrounds invasive ductal carcinoma.

To test the usefulness of relative lesion size for differentiating between benign and malignant breast lesions, five observers individually viewed a set of image sequences from in vivo breast elasticity imaging. Each observer selected the image pair from a sequence (movie loop) that was most representative of the B-mode and strain image pair from that sequence. Each observer then traced the outline of the lesion in each image type and measured the width and height of the lesion in each image. This was repeated for data from 97 movie loops of 55 unique lesions in 29 patients. A plot of the average lesion area for each lesion measured by the group of observers is shown in Figure 13. These data are consistent with those reported by others (33) and suggest that elasticity imaging may be a helpful tool to improve the usefulness of breast US. If the ratio of lesion size in strain images versus in B-mode images proves to be a sensitive criterion for increasing confidence of a benign diagnosis, the fraction of biopsy specimens that prove to be benign tissue will likely be

reduced at significant savings in health care expense and trauma to patients and their families and friends.

## Conclusions

Elasticity imaging is a relatively new technique for studying the stiffness of tissue. The information acquired with these techniques is similar to that obtained with manual palpation, but elasticity imaging is more sensitive and less subjective than palpation. Further, the information is provided in an image format so that it can be compared with data from other image modalities and can more easily be documented and shared with others.

Several interesting approaches to elasticity imaging are currently being investigated by research groups around the world. Different approaches provide different information about the viscoelastic properties of tissue. Many of these approaches emphasize the elastic properties of tissue due to the techniques of data acquisition.

At least one method for elasticity imaging is under development that produces images of mechanical strain in real time by using a freehand scanning technique very similar to that of standard breast US examinations. The system is integrated into a clinical US system without any external equipment and involves software changes only. In vivo tests of this system have demonstrated the ability to image small breast lesions with confidence. It has also allowed visualization of the effects of nonlinear elasticity of in vivo breast tissues. Further investigations with this system suggest that benign breast lesions are about the same size and shape in B-mode and strain images, but invasive ductal carcinomas tend to be significantly larger in strain images than in the corresponding B-mode images. This fact suggests that elasticity imaging might increase the usefulness of breast US and might be offered in clinical US systems in the near future.

**Acknowledgments:** The author is grateful to many for their contribution to this effort. Significant contributions came from Yanning Zhu, PhD, in algorithm development and implementation, Candace Spalding, RT, RDMS, RVT, for clinical coordination and assistance in developing elasticity scanning techniques, and Patrick Von Behren, PhD, for technical assistance and the loan of the US system used in this research.

## References

1. Sariego J, Zrada S, Byrd M, Matsumoto T. Breast cancer in young patients. *Am J Surg* 1995; 170: 243–245.
2. Peer PG, Verbeek AL, Ravunac MM, et al. Prognosis of younger and older patients with early breast cancer. *Br J Cancer* 1996; 73:382–385.
3. McPherson CP, Swenson KK, Jolitz G, Murray CL. Survival among women ages 40–49 years with breast carcinoma according to method of detection. *Cancer* 1997; 79:1923–1932.
4. Costanza ME, Edmiston KL. Breast cancer screening: early recognition. *Compr Ther* 1997; 23:7–12.
5. Yang WT, Mok CO, King W, Tang A, Metreweli C. Role of high frequency ultrasonography in the evaluation of palpable breast masses in Chinese women: alternative to mammography? *J Ultrasound Med* 1996; 15:637–644.
6. Boyd NF, Dite GS, Stone J, et al. Heritability of mammographic density, a risk factor for breast cancer. *N Engl J Med* 2002; 347:886–894.
7. Hou MF, Chuang HY, Ou-Yang F, et al. Comparison of breast mammography, sonography and physical examination for screening women at high risk of breast cancer in Taiwan. *Ultrasound Med Biol* 2002; 28:415–420.
8. Kolb TM, Lichy J, Newhouse JH. Comparison of the performance of screening mammography, physical examination, and breast US and evaluation of factors that influence them: an analysis of 27,825 patient evaluations. *Radiology* 2002; 225: 165–175.
9. Wang HC, Chen DR, Kao CH, et al. Detecting breast cancer in mammographically dense breasts: comparing technetium-99m tetrofosmin mammoscintigraphy and ultrasonography. *Cancer Invest* 2002; 20:932–938.
10. Saarenmaa I, Salminen T, Geiger U, et al. The effect of age and density of the breast on the sensitivity of breast cancer diagnostic by mammography and ultrasonography. *Breast Cancer Res Treat* 2001; 67:117–123.
11. Laya MB, Larson EB, Taplin SH, et al. Effect of estrogen replacement therapy on the specificity and sensitivity of screening mammography. *J Natl Cancer Inst* 1996; 88:643–649.
12. Gao L, Parker KJ, Lerner RM, Levinson SF. Imaging of the elastic properties of tissue: a review. *Ultrasound Med Biol* 1996; 22:959–977.
13. Ophir J, Alam SK, Garra B, et al. Elastography: ultrasonic estimation and imaging of the elastic properties of tissues. *Proc Inst Mech Eng H* 1999; 213:203–233.
14. Tschoegl NW. The phenomenological theory of linear viscoelastic behavior: an introduction. New York, NY: Springer-Verlag, 1989.
15. Fung YC. A first course in continuum mechanics. Englewood Cliffs, NJ: Prentice Hall, 1994.
16. Fung YC. Biomechanics: mechanical properties of living tissues. 2nd ed. New York, NY: Springer-Verlag, 1993.
17. Krouskop TA, Wheeler TM, Kallel F, Garra BS, Hall T. Elastic moduli of breast and prostate tissues under compression. *Ultrason Imaging* 1998; 20:260–274.
18. Wellman PS, Dalton EP, Krag D, et al. Tactile imaging of breast masses: first clinical report. *Arch Surg* 2001; 136:204–208.
19. Sarvazyan A. Mechanical imaging: a new technology for medical diagnostics. *Int J Med Inf* 1998; 49:195–216.
20. Dickinson RJ, Hill CR. Measurement of soft tissue motion using correlation between A-scans. *Ultrasound Med Biol* 1982; 8:263–271.

21. Wilson LS, Robinson DE. Ultrasonic measurement of small displacements and deformations of tissue. *Ultrason Imaging* 1982; 4:71–82.
22. Krouskop TA, Dougherty DA, Vinson FS. A pulsed Doppler ultrasonic system for making non-invasive measurements of the mechanical properties of soft tissue. *J Rehabil Res Dev* 1987; 24:1–8.
23. Yamakoshi Y, Sato J, Sato T. Ultrasonic imaging of internal vibration of soft tissue under forced vibration. *IEEE Trans Ultrason Ferroelectr Freq Control* 1990; 37:45–53.
24. Lerner RM, Huang SR, Parker KJ. Sonoelasticity images derived from ultrasound signals in mechanically vibrated tissues. *Ultrasound Med Biol* 1990; 16:231–239.
25. Ophir J, Cespedes EI, Ponnekanti H, et al. Elastography: a quantitative method for imaging the elasticity of biological tissues. *Ultrason Imaging* 1991; 13:111–134.
26. O'Donnell M, Skovoroda A, Shapo B, Emelianov S. Internal displacement and strain imaging using ultrasonic speckle tracking. *IEEE Trans Ultrason Ferroelectr Freq Control* 1994; 41:314–325.
27. Chaturvedi P, Insana MF, Hall TJ. 2-D companding for noise reduction in strain imaging. *IEEE Trans Ultrason Ferroelectr Freq Control* 1998; 45:179–191.
28. Insana MF, Chaturvedi P, Hall TJ, Bilgen M. 3-D companding using linear arrays for improved strain imaging. In: *Proceedings of the 1997 IEEE Ultrasonics Symposium*. New York, NY: Institute of Electrical and Electronics Engineers, 1997; 1435–1438.
29. Zhu Y, Hall TJ. A modified block matching method for real-time freehand strain imaging. *Ultrason Imaging* 2002; 24:161–176.
30. Bilgen M, Insana MF. Elastostatics of a spherical inclusion in homogeneous biological media. *Phys Med Biol* 1998; 43:1–20.
31. Bilgen M, Insana MF. Deformation models and correlation analysis in elastography. *J Acoust Soc Am* 1996; 99:3212–3224.
32. Insana MF, Cook LT, Bilgen M, Chaturvedi P, Zhu Y. Maximum-likelihood approach to strain imaging using ultrasound. *J Acoust Soc Am* 2000; 107:1421–1434.
33. Garra BS, Cespedes EI, Ophir J, et al. Elastography of breast lesions: initial clinical results. *Radiology* 1997; 202:79–86.
34. Hall TJ, Zhu Y, Spalding CS. In vivo real-time freehand palpation imaging. *Ultrasound Med Biol* 2003; 29:427–435.
35. Dooley M, Bamber JC, Fuechsel F, Bush NL. A freehand elastographic imaging approach for clinical breast imaging: system development and performance evaluation. *Ultrasound Med Biol* 2001; 27:1347–1357.
36. Trahey GE, Allison JW, von Ramm OT. Angle independent ultrasonic detection of blood flow. *IEEE Trans Biomed Eng* 1987; 34:965–967.
37. Merritt CR, Forsberg F, Liu J, Kallel F. In vivo elastography in animal models: feasibility studies (abstr). *J Ultrasound Med* 2002; 21:S98.
38. Lorenz A, Sommerfeld HJ, Garcia-Schurmann M, et al. A new system for the acquisition of ultrasonic multicompression strain images of the human prostate in vivo. *IEEE Trans Ultrason Ferroelectr Freq Control* 1999; 46:1147–1154.
39. Dutt V, Kinnick RR, Muthupillai R, Oliphant TE, Ehman RL, Greenleaf JF. Acoustic shear-wave imaging using echo ultrasound compared to magnetic resonance elastography. *Ultrasound Med Biol* 2000; 26:397–403.
40. Sandrin L, Tanter M, Catheline S, Fink M. Shear modulus imaging with 2-D transient elastography. *IEEE Trans Ultrason Ferroelectr Freq Control* 2002; 49:426–435.
41. Sandrin L, Tanter M, Gennisson JL, Catheline S, Fink M. Shear elasticity probe for soft tissues with 1-D transient elastography. *IEEE Trans Ultrason Ferroelectr Freq Control* 2002; 49:436–446.
42. Skovoroda AR, Emelianov SY, O'Donnell M. Tissue elasticity reconstruction based on ultrasonic displacement and strain images. *IEEE Trans Ultrason Ferroelectr Freq Control* 1995; 42:747–765.
43. Sumi C, Suzuki A, Nakayama K. Estimation of shear modulus distribution in soft-tissue from strain distribution. *IEEE Trans Biomed Eng* 1995; 42:193–202.
44. Kallel F, Bertrand M. Tissue elasticity reconstruction using linear perturbation method. *IEEE Trans Med Imaging* 1996; 15:299–313.
45. Dooley M, Meaney PM, Bamber JC. Evaluation of an iterative reconstruction method for quantitative elastography. *Phys Med Biol* 2000; 45:1521–1540.
46. Zhu Y, Hall TJ, Jiang J. A finite-element approach for Young's modulus reconstruction. *IEEE Trans Med Imaging* 2003; 22:890–901.
47. Nightingale KR, Palmeri ML, Nightingale RW, Trahey GE. On the feasibility of remote palpation using acoustic radiation force. *J Acoust Soc Am* 2001; 110:625–634.
48. Fatemi M, Greenleaf JF. Application of radiation force in noncontact measurement of the elastic parameters. *Ultrason Imaging* 1999; 21:147–154.
49. Tanter M, Bercoff J, Sandrin L, Fink M. Ultrafast compound imaging for 2-D motion vector estimation: application to transient elastography. *IEEE Trans Ultrason Ferroelectr Freq Control* 2002; 49:1363–1374.
50. Fatemi M, Greenleaf JF. Ultrasound-stimulated vibro-acoustic spectrography. *Science* 1998; 280: 82–85.
51. Fatemi M, Wold LE, Alizad A, Greenleaf JF. Vibro-acoustic tissue mammography. *IEEE Trans Med Imaging* 2002; 21:1–8.
52. Chaturvedi P, Insana MF, Hall TJ. Testing the limitations of 2-D companding for strain imaging using phantoms. *IEEE Trans Ultrason Ferroelectr Freq Control* 1998; 45:1022–1031.
53. Hein IA, O'Brien WD. Current time-domain methods for assessing tissue motion by analysis from reflected ultrasound echoes: a review. *IEEE Trans Ultrason Ferroelectr Freq Control* 1993; 40:84–102.
54. Carter GC. Coherence and time-delay estimation: an applied tutorial for research, development, test, and evaluation engineers. New York, NY: IEEE Press, 1993.
55. Madsen EL, Frank FR, Krouskop TA, et al. Low-contrast spherical lesion phantoms for assessing elastography performance (abstr). *Ultrason Imaging* 2003; 25:61.

# Spherical lesion phantoms for testing the performance of elastography systems

Ernest L Madsen, Gary R Frank, Maritza A Hobson, Hairong Shi,  
Jingfeng Jiang, Tomy Varghese and Timothy J Hall

Department of Medical Physics, University of Wisconsin, 1300 University Avenue, Room 1530,  
Madison, WI, USA

E-mail: [elmadson@wisc.edu](mailto:elmadson@wisc.edu)

Received 15 June 2005, in final form 14 October 2005

Published 7 December 2005

Online at [stacks.iop.org/PMB/50/5983](http://stacks.iop.org/PMB/50/5983)

## Abstract

A set of three cubic one-litre phantoms containing spherical simulated lesions was produced for use in comparing lesion detection performance of different elastography systems. The materials employed are known to be stable in heterogeneous configurations regarding geometry and elastic contrast  $\equiv$  (storage modulus of lesion material)  $\div$  (storage modulus of background material), and regarding ultrasound and NMR properties. The materials mimic soft tissues in terms of elastic, ultrasound and NMR properties. Each phantom has only one value of elastic contrast (3.3, 4.6 or 5.5) and contains arrays of 1.6 mm, 2 mm, 3 mm and 4 mm diameter spherical simulated lesions. All the spheres of a given diameter are arranged in a regular array with coplanar centres. Elastograms of an array made with ultrasound allow determination of the depth range over which lesions of that diameter and elastic contrast can be detected. Two phantoms are made from agar-plus-gelatin-based materials, and one is made from oil-in-gelatin dispersions. The methods for producing the phantoms are described in detail. Lesion detection performances for two ultrasound systems, both operating at about 7.5 MHz and focused at about 5 cm, were quantified with distinctions between the two systems demonstrated. Neither system was capable of detecting any of the 1.6 mm lesions. Phantoms such as these should be useful in research labs that are refining hardware and/or software for elastography.

## 1. Introduction

Spherical lesion phantoms for use in testing the performance of *ultrasound* imagers have been reported (Kofler and Madsen 2001). The production methods described there for producing planar arrays of spheres have been adapted to produce the spherical lesion phantoms for elastography which are the subject of this report.

Two types of materials have been developed for producing temporally stable phantoms with inclusions having a Young's modulus that is different from that of the surrounding background (Madsen *et al* 2003, 2005a, 2005b). These materials have been used to produce a set of three phantoms, each containing arrays of spherical inclusions with diameters 1.6, 2, 3 and 4 mm. The elastic contrast has a single value for each phantom, and spheres of each diameter are coplanar and arranged in a regular array. (Elastic contrast equals the ratio of the storage modulus of the inclusion material to the storage modulus of the surrounding background material. The storage modulus is the real part of the complex Young's modulus.) The elastic, ultrasonic and NMR properties simulate soft tissues. The elastic contrasts of the three phantoms are 3.3, 4.6 and 5.5. These values are in the range of elastic contrasts determined for *in vitro* breast tissue specimens. Krouskop *et al* (1998) found, at 1 Hz and 5% pre-compression, that the elastic contrast of invasive and infiltrating ductal carcinoma relative to breast fat was  $106 \text{ kPa}/18 \text{ kPa} \approx 5.9$ , while relative to normal glandular tissue was  $106 \text{ kPa}/28 \text{ kPa} \approx 3.8$ ; the elastic contrast of breast fibrous tissue relative to breast fat was  $96 \text{ kPa}/18 \text{ kPa} \approx 5.3$  and relative to normal glandular tissue was  $96 \text{ kPa}/28 \text{ kPa} \approx 3.4$ . The phantom elastic contrasts are also in the range of elastic contrasts in terms of shear storage moduli for 85 Hz shear waves in *in vivo* MR breast elastography (Sinkus *et al* 2005), where elastic contrasts (ratio of shear storage modulus of a lesion to that of the surroundings) vary from about 2 through 5.5.

The primary purpose of this paper is to report the development of a novel type of phantom useful for assessing the performance of elasticity imaging systems. Production techniques are detailed and values of relevant physical parameters are given. The utility of the phantoms is illustrated by comparing the performances of two different ultrasound elastography systems based on simple human observer detectability of the spheres as a function of their diameter, elastic contrast and their distance from the transducer (depth). It is reasonable that the utility of such phantoms—perhaps with larger sphere diameters—could be extended to MR systems.

## 2. Materials

Two of the phantoms (1 and 2) were formed from mixtures of agar and gelatin, plus additives to adjust ultrasonic and NMR properties and to prevent bacterial invasion. All dry weight concentrations of components are uniform throughout each phantom except for the agar and microscopic glass beads. The latter provide increases in ultrasonic attenuation and backscatter. The greater the dry weight concentration of agar in the spheres relative to that in the background, the higher the elastic contrast. Formalin provides for formaldehyde cross-linking of the gelatin component resulting in thermal stability by raising the melting point to over 60 °C. Preserving is done with Germall-plus® (International Specialty products, Wayne, New Jersey, USA).

The compositions of phantoms 1 and 2 are given in detail in table 1. The method of production of the agar/gelatin materials has been described previously (Madsen *et al* 2005a).

The other type of material, used to make phantom 3, includes dispersions of different concentrations of microscopic oil droplets in a gelatin matrix. Preservation and thermal stability are again accomplished through the presence of Germall-plus® and formalin. However, the Young's modulus is determined by the presence or absence of a dispersion of microscopic safflower oil droplets (Hollywood brand, The Hain Celestial Group, Inc., Melville, New York, USA). The greater the concentration of oil, the lower the storage modulus (real part of the complex Young's modulus). The material forming the spherical inclusions contains no oil droplets, while 50% of the volume of the surrounding background consists of oil droplets. Also, there is a liquid surfactant (liquid Ultra Ivory®, Procter and Gamble

**Table 1.** Dry-weight per cents of the various components in the agar/gelatin phantoms (1 and 2). The weight per cent of  $18 \text{ M}\Omega \text{ cm}$  (doubly de-ionized) water is not shown since it just makes up the remainder. The gelatin concentrations in the background and spheres are the same in the agar/gelatin when glass beads are excluded; because of the significant difference in glass bead concentrations between background and spheres, the *weight per cent* of gelatin, e.g., gelatin is higher in the spheres than in the background. The purpose of the  $\text{CuCl}_2 \cdot 2\text{H}_2\text{O}$  and EDTA tetra-Na hydrate is to lower the NMR  $T_1$  to tissue-like values, and the purpose of the NaCl is to produce tissue-like coil loading for MR (Rice *et al* 1998).

Material	Agar	Gelatin	$\text{CuCl}_2 \cdot 2\text{H}_2\text{O}$	EDTA tetra-Na hydrate	NaCl	HCHO	Germall plus	Glass bead scatterers
Phantom 1 background	1.17	3.60	0.113	0.33	0.77	0.24	1.45	4.6
Phantom 1 spheres	3.60	3.77	0.119	0.34	0.79	0.25	1.49	0.7
Phantom 2 background	1.11	4.80	0.114	0.33	0.77	0.32	1.45	3.4
Phantom 2 spheres	3.44	4.92	0.116	0.34	0.79	0.33	1.49	0.75

**Table 2.** Weight per cents of components in the spheres of phantom 3 and in the gel matrix surrounding the microscopic safflower oil droplets when oil is present (background of phantom 3). When oil droplets are present, the volume of liquid surfactant equals approximately 1% of the volume of the gel matrix.

Gelatin	Germall plus	Formalin	Glass beads
12.77	1.24	0.735	0.083

Company, Cincinnati, Ohio, USA) present in the background material having a volume of surfactant equal to 1% of the volume of the matrix gel. The weight per cent of surfactant is not shown in table 2 because it is not known how the surfactant is distributed between the aqueous gel matrix and the oil droplets.

Details of the method of production of these oil-in-gelatin materials have been described elsewhere (Madsen *et al* 2003, 2005b).

To minimize changes in mechanical or geometric properties due to osmotic effects in a heterogeneous phantom such as a spherical lesion phantom, it is important that the composition of the spheres be the same as that of the gel matrix surrounding the microscopic oil droplets in the background material. Table 2 shows the composition of sphere and matrix materials.

### 3. Phantom geometry and production

All three of the phantoms have the geometry depicted in figures 1 and 2. The geometry is such that each sphere is at least four times its diameter from its nearest neighbour to minimize mechanical cross-talk<sup>1</sup>.

The procedure for producing a phantom has four overall steps. First, all spheres are made from a single batch of molten material. Two-part acrylic moulds with opposing equal diameter

<sup>1</sup> The ‘rule of thumb’ that mechanical cross-talk would be minimized when the distance to the nearest neighbour is at least four times the diameter was suggested to us by Professor Jonathan Ophir of the University of Texas at Houston. Except for 4 mm—or larger—diameter spheres, earlier elastography spherical lesion phantoms made in our lab also had nearest neighbour distances greater than four times the diameter of included spheres.

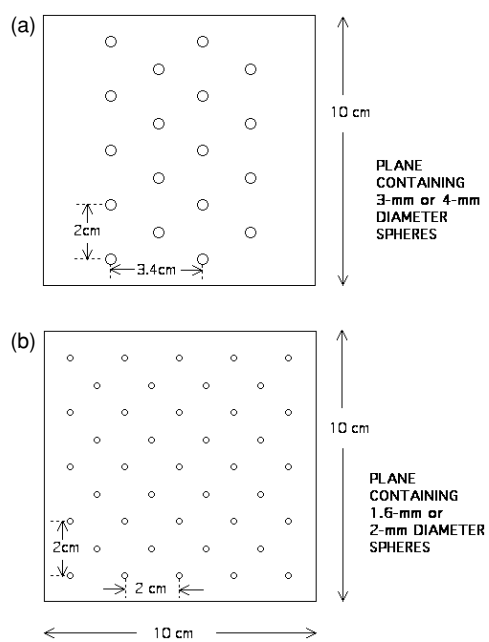


**Figure 1.** Diagrams showing the planar array of 3 mm and 4 mm diameter spheres (a) and of 1.6 mm and 2 mm diameter spheres in each phantom (b).

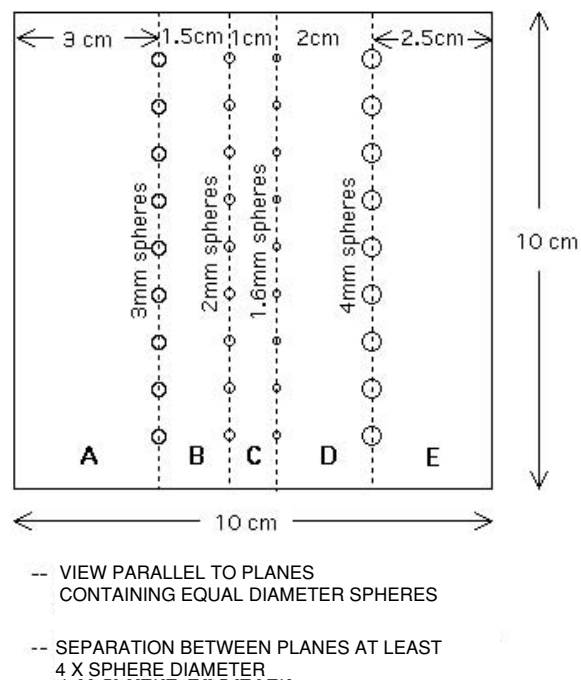


**Figure 2.** View of phantom with planes containing the centres of equal diameter spheres being perpendicular to the figure. In use, the ultrasound scan planed is superimposed on one of these planes.

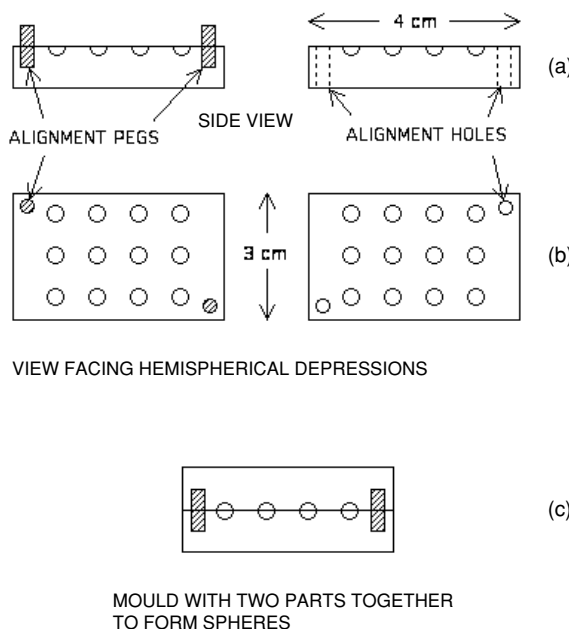


**Figure 3.** Diagrams of two-part moulds used to form twelve 4 mm diameter spherical inclusions: (a) side view; (b) view facing hemispherical depressions; (c) two parts of the mould pressed together to form 4 mm spheres.

hemispherical depressions are brought together after immersion in the molten material. Prior to immersion, a thin layer of petrolatum is applied to all surfaces to assure release of the spheres from the mould. One part of the mould has two alignment pegs projecting at opposite corners on the same side as the hemispherical depressions. The other side has receiving holes with the same diameter as the pegs. An example of these moulds is shown in figure 3.

The second step is to form sections A and E (figure 2) from one batch of the background material. The same procedure is used to form both sections A and E. The mould components for forming section A are depicted in figure 4. An acrylic plate with 3 mm diameter acrylic hemispheres projecting from one surface is shown in the figure. A frontal view of the plate is shown in figure 4(a) and a side view is shown in figure 4(b). Figure 4(c) shows the mould for forming a 3 cm × 10 cm × 10 cm background section of the phantom when the acrylic plate shown in (b) has been clamped onto its open side. The same clamp presses the constraining acrylic plate (d) against the 25 µm thick polyvinylidene chloride film (Saran Wrap®, The Dow Chemical Company, Midland, Michigan, USA) which has been epoxied to the bottom of the 3 cm deep square acrylic rim; the rim defines the lateral boundaries of section A. Acrylic and polyvinylidene chloride film surfaces that will contact the molten background material are coated with a thin layer of petrolatum. The 35 °C molten background material is poured through the filling syringe barrel, and a syringe piston is inserted without trapping air bubbles. (Note that the melting point of the petrolatum is about 45 °C.) A constant force is applied via rubber bands to the piston causing the molten material to be under positive gauge pressure during congealing. Then the clamped unit is rotated at 2 rpm around a horizontal axis until congealing has been completed. The rotation step assures that gravitational sedimentation of background components does not occur.

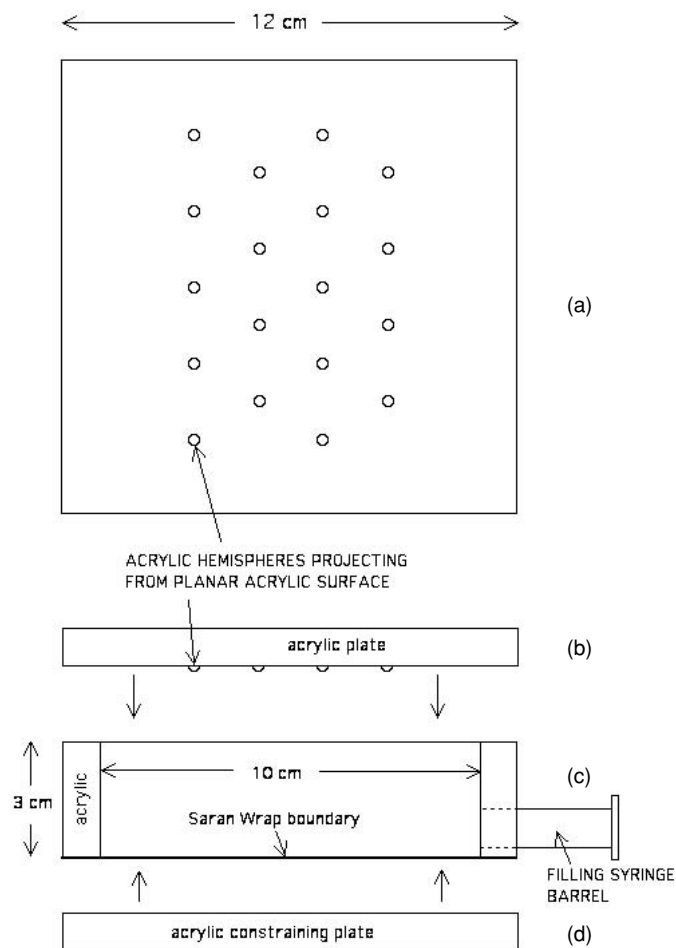


**Figure 4.** Mould parts for forming background section A (figure 2) of the phantom. A frontal view (a) and side view are shown of an acrylic plate with an array of equal diameter acrylic hemispheres projecting from one surface. A C-clamp is used to clamp that acrylic plate to the second part of the mould (c) along with bottom constraining plate (d) to define section A.

After congealing, the acrylic plate shown in figure 4(b) is removed leaving section A with sockets in the background material into which spherical inclusions can be inserted. To bond a sphere in a socket, a drop of molten background material is placed in the socket followed by immediate insertion of the sphere.

Next, background sections B and D are made in a way equivalent to forming sections A and E except that the polyvinylidene chloride film and constraining plate (figure 4(d)) are missing leaving the bottom of the mould open. The B and D moulds are temporarily glued with 5 min epoxy (Araldite 2012, Huntsman Advanced Materials Americas Inc., East Lansing, Michigan, USA) to the completed sections A and E, respectively. In figure 5 is shown the situation described for section B.

Then a second batch of molten background material is made and sections B and D are filled, the syringe is inserted under positive gauge pressure, and the entire mould system is clamped to a plate rotating at 2 rpm about a horizontal axis to allow congealing without gravitational sedimentation.

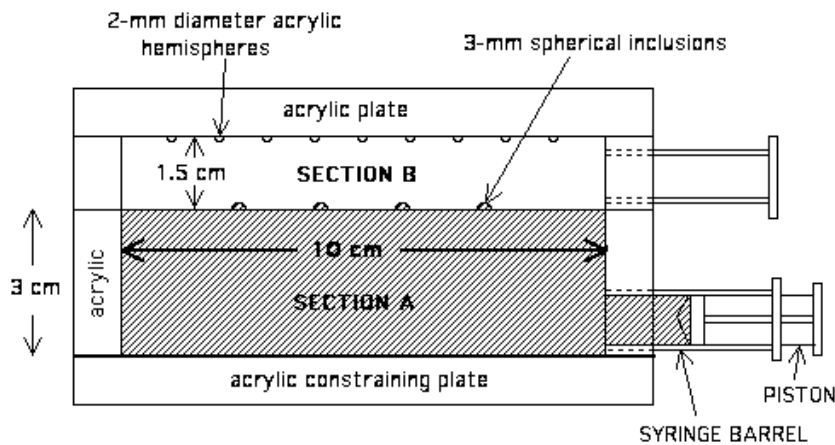


**Figure 5.** Moulds for production of background section B. Background section A has been completed and the 3 mm diameter spheres have been implanted in its sockets (cross-hatching). The upper bounding acrylic plate has 2 mm diameter acrylic hemispheres projecting downwards to form sockets for the 2 mm diameter spherical inclusions.

Next, the 2 mm and 1.6 mm diameter spheres are glued into their sockets with molten background material and background section C is produced. Sections A + B and D + E, in their respective containers, are 5 min epoxied to a 1 cm thick square acrylic bounding mould with their exposed background surfaces facing one another. Then a third component of molten background material is introduced with 2 rpm rotation, etc.

After about 24 h the completed phantom is removed from its final containing vessel as follows. The polyvinylidene chloride films are removed from sections A and E, and a knife blade is passed around the boundary of the phantom separating it from the acrylic walls and cutting the gel material projecting into the syringe barrels. Then the phantom is slid out of the acrylic walls, submerged in safflower oil in a sufficiently deep container, and the container is covered. The covering of the container will prevent long-term hardening of the safflower oil.

#### 4. Physical properties of the materials

At the time that each batch of molten gel material was made for a phantom, test samples were also produced for determination of storage moduli (real part of the complex Young's modulus), ultrasound propagation speed and attenuation and NMR relaxation times. Regarding determination of storage moduli in a phantom, however, the most reliable method is to employ test samples obtained by excising them from an auxiliary phantom having a cylindrical inclusion made at the same time and of the same materials as those in the spherical lesion phantom (Madsen *et al* 2005a, 2005b). Such cylinder inclusion phantoms were produced in the case of phantoms 2 and 3, but not in the case of phantom 1.

Complete descriptions of the test samples and methods of measurement of properties have been given previously (Madsen *et al* 1999, 2005a). The mechanical, ultrasound and NMR properties of the components of the phantoms are given in tables 3 and 4.

The reason that an auxiliary cylindrical inclusion was not made in the case of phantom 1 is that at the time phantom 1 was made, we did not expect that the elastic contrast found using isolated test samples might be different from that found using excised samples. Following is evidence (not proof) that the value for the elastic contrast of phantom 1 in table 4 is reasonably

**Table 3.** Mechanical, ultrasound and NMR properties at 22 °C of the materials composing the spheres and backgrounds of the phantoms. Storage moduli for phantom 1 were measured using small samples made at the time the phantom was produced. Storage moduli for phantoms 2 and 3 were measured using test samples excised from cylinder phantoms made at the same time and of the same materials as the corresponding spherical lesion phantom. Storage modulus uncertainties are standard errors (also called standard deviations of the mean) (Bevington 1969) unless a value is less than 3% of the mean; in the latter case the uncertainty is taken to be 3% which is approximately the day-to-day reproducibility for storage modulus determinations. Ultrasound uncertainties are instrumental and NMR relaxation time ‘uncertainties’ result from curve fitting.

Component identity	Storage modulus ± standard error (kPa)	Ultrasound properties		NMR relaxation times	
		Propagation speed (m s <sup>-1</sup> )	Attenuation coeff. ÷ frequency (dB cm <sup>-1</sup> MHz <sup>-1</sup> )	T1 (ms)	T2 (ms)
Phantom 1 background	19.6 ± 0.8	1524 ± 1	0.32 ± 0.02	480 ± 1	66 ± 2
Phantom 1 spheres	107.2 ± 3.2	1528 ± 1	0.32 ± 0.02	443 ± 1	45 ± 1
Phantom 2 background	24.4 ± 0.7	1518 ± 1	0.46 ± 0.02	396 ± 1	59 ± 1
Phantom 2 spheres	112.2 ± 3.4	1518 ± 1	0.18 ± 0.02	488 ± 1	53 ± 1
Phantom 3 background	51.0 ± 1.5	1498 ± 1	0.34 ± 0.02	340 ± 20	111 ± 1
Phantom 3 spheres	170 ± 15	1547 ± 1	0.14 ± 0.02	1350 ± 40	290 ± 3

**Table 4.** Elastic contrasts (storage modulus of inclusion material) ÷ (storage modulus of background material) for the three phantoms using the storage moduli in table 3. Uncertainties are propagated from uncertainties given in table 3.

Phantom 1	Phantom 2	Phantom 3
5.5 ± 0.3	4.6 ± 0.2	3.3 ± 0.3

accurate. One month before production of phantom 1, a cylindrical inclusion phantom was made using the same recipe for inclusion and background as in phantom 1 except that the glass bead concentration in the cylindrical inclusion was eight times that in the spheres of phantom 1. (The glass bead concentration was reduced in the phantom 1 spheres so that the spheres would be more easily detected on B-mode images for alignment purposes.) For the cylindrical inclusion phantom, the elastic contrast determined using isolated test samples differed by only 6% from that using samples excised from the phantom.

## 5. Apparatus providing for alignment of the ultrasound scan plane on a sphere plane and for precisely controlled axial compressions

To optimize the alignment of the scan plane (plane of symmetry of the scan slice) on one of the planes containing spheres of equal diameter and elastic contrast, the apparatus shown in figure 6 was employed. The phantom is placed on an acoustic absorbing pad in a tank containing safflower oil, the phantom being completely submerged in oil. A constraining plate with a 10 cm × 10 cm square opening is attached to the bottom of the tank, and the base

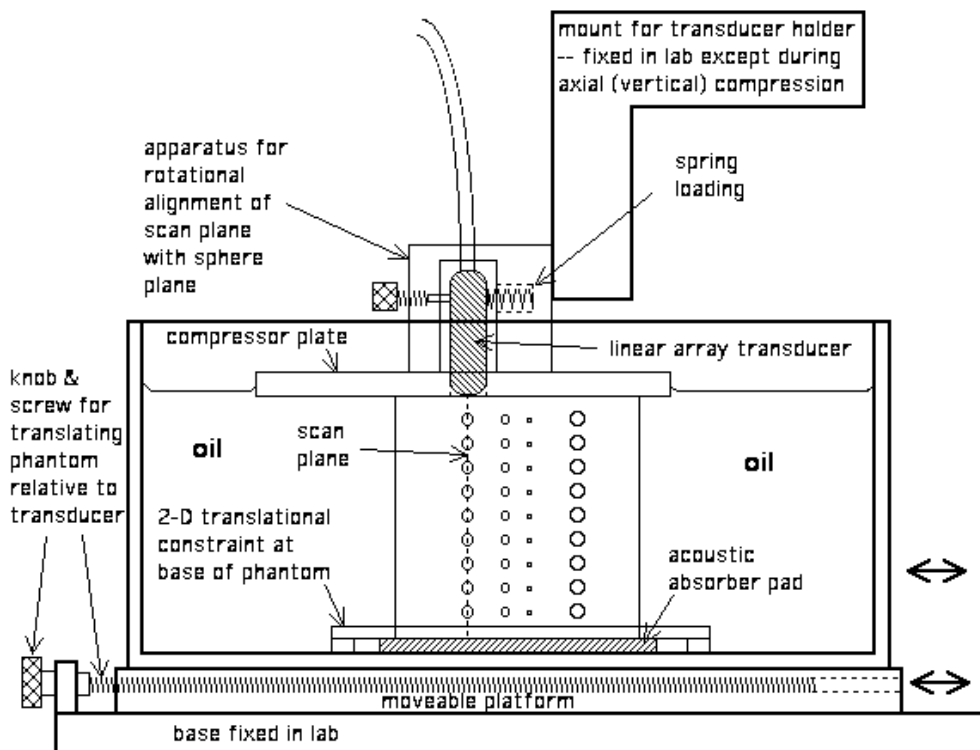


**Figure 6.** Apparatus used to align the ultrasound scan plane on a plane of spheres with equal diameter and equal elastic contrast and also to allow precisely controlled axial compressions for generating elastograms. See section 5 of the text for a detailed description of its use.

of the phantom is in the square opening, thus fixing the position of the phantom in the tank. Then the transducer is mounted on a single unit for moving the transducer. The transducer fits snugly into a slot in a square 1 cm thick horizontal compression plate and can be rotated about a horizontal axis parallel to the scan plane via a screw and spring-loading apparatus. In the case of the Aloka system, the compression plate was stainless steel with horizontal dimensions 17 cm  $\times$  17 cm; in the case of the Siemens system, the compression plate was acrylic and 13 cm  $\times$  13 cm. The oil tank can be rotated by hand about a vertical axis, and that rotational degree of freedom plus the spring-loaded rotation apparatus allows angular alignment of the scan plane relative to the plane of spheres. Finally, linear translations of the tank (and phantom) can be made perpendicular to the plane of spheres. The two rotations plus the linear translation allow alignment of the scan plane on the plane of spheres. B-mode imaging of the spheres facilitates the alignment. In the case of the 1.6 or 2 mm diameter spheres, they may not be detectable on B-mode images; in that case advantage is taken of the known distances between adjacent sphere planes and the micrometer driven linear translation apparatus.

The two elastography systems existing in our ultrasound laboratory were compared using the phantoms. Both systems employed linear arrays at comparable nominal frequency and focus (Siemens Sonoline Antares with a VFX9-4 array and an Aloka SD 2000 with a 7.5 MHz linear array). Precisely controlled axial compression of the phantom is accomplished by stepper motor or micrometer driven translations of the mount for the transducer holder. In the case of the Aloka system, elastograms were computed from images at 3.9 mm of

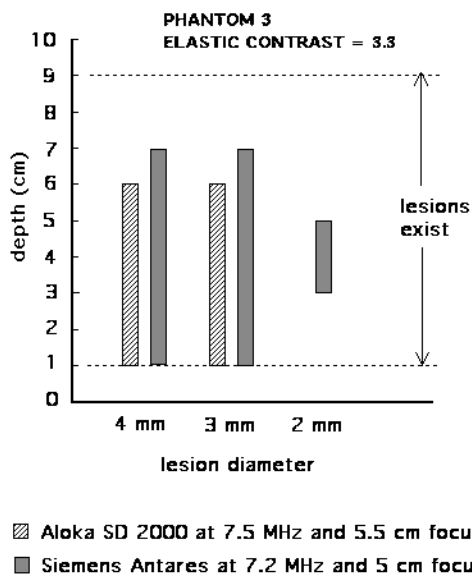


**Figure 7.** Depth ranges in which spherical lesions were detected on elastograms by human observers using phantom 3 with elastic contrast of 3.3. No evidence of 1.6 mm lesions was present for any scanner. Only the Siemens Antares detected 2 mm lesions. Also, the Siemens system allowed detection of 3 and 4 mm lesions to slightly greater depths than the Aloka system.

compression and 4.35 mm of compression. The corresponding compressions in the case of the Siemens system were 3.0 mm and 4.8 mm.

## 6. Results and discussion

Results illustrating use of the phantoms for ultrasound elastography are presented in figures 7–9. Depth ranges in which spheres are detectable on elastograms are shown. Note that the highest nominal frequency available for the Aloka system in our lab is 7.5 MHz, and the closest frequency to that available for the Siemens in our lab is 7.2 MHz; thus, these were the frequencies chosen<sup>2</sup>. Two of the coauthors independently determined all depth ranges in which lesions were detectable. The two observers agreed regarding all results shown in the figures.

The Siemens Antares somewhat outperformed the Aloka system for all three phantoms. However, human observers could not detect the 1.6 mm diameter lesions in any of the phantoms, either on B-mode images or on elastograms; this lack of detection is probably due to the fact that the minimum elevational beam full widths at half maximum (FWHM) were comparable to the sphere diameter with corresponding partial volume effects. For the Siemens system, that FWHM was 1.1 mm, and for the Aloka system, it was 1.5 mm. As expected, detection ranges increased with increasing elastic contrast. Note that higher frequency and broader bandwidth transducers available for the Antares (e.g. VFX13-5) may enhance the range of detectability.

Typical models for the variance time delay and displacement estimation applied to motion tracking (Walker and Trahey 1995, Bilgen and Insana 1997) suggest that estimation error is

<sup>2</sup> The Siemens system in our lab can operate at higher frequencies, but we have not yet investigated lesion detection performance for those.

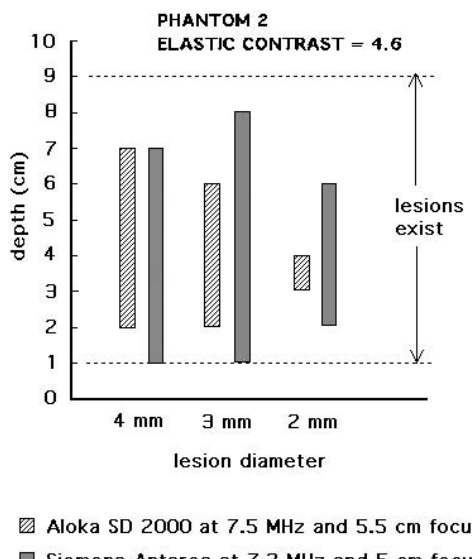


**Figure 8.** Depth ranges in which spherical lesions were detected on elastograms by human observers using phantom 2 with elastic contrast of 4.6. No detection of 1.6 mm lesions occurred. The Aloka SD 2000 system barely detected 2 mm lesions over a 1 cm depth range. The Siemens system somewhat outperformed the Aloka regarding detection of 3 mm lesions, particularly regarding greater depth of detection.

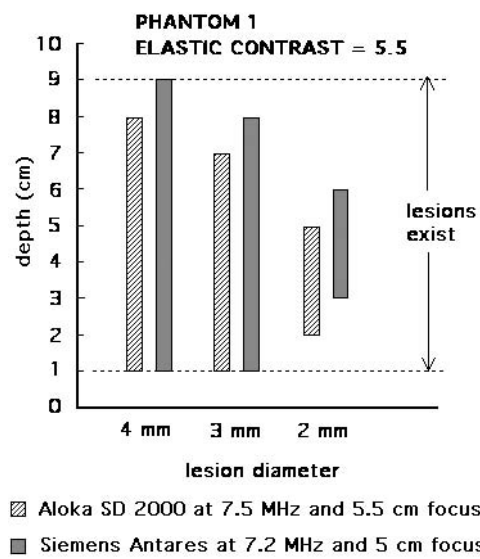


**Figure 9.** Depth ranges in which spherical lesions were detected on elastograms by human observers using phantom 1 with elastic contrast of 5.5. Again, no detection of 1.6 mm lesions occurred for either system. The Siemens and Aloka systems performed comparably for this phantom which has the highest elastic contrast of the three phantoms. The 4 mm lesions were detected by the Siemens system for the entire depth range where lesions existed, and the Aloka detected the 4 mm lesions over the entire depth except for the most distal cm (8 to 9 cm depth).

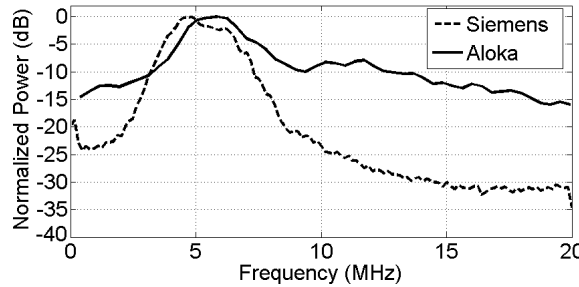


**Figure 10.** Power spectra of the RF data obtained for the Aloka and Antares system. Both spectra are normalized to their maximum values.

reduced as the radiofrequency (RF) echo signal centre frequency, absolute signal bandwidth and electronic signal-to-noise ratio (SNR) increase. Differences in the performance of the two elasticity imaging systems may partly relate to different estimation errors.

The Siemens Antares Axius Direct Ultrasound Research Interface provides digital signals sampled at 40 MHz and encoded in 16 bits whereas the Aloka system uses external digitization of the RF signals with a GAGE digitization board (Gage Applied Technologies, Inc., Lachine, Quebec, Canada) sampling at 50 MHz and 12 bits. The power spectra of the RF echo data obtained from these systems are shown in figure 10. The power spectra were obtained from Phantom 2 using 1 cm long data segments, centred at 5 cm (approximately their focal depths), from 40 independent A-lines. The centre frequency of the Aloka system (5.2 MHz) is slightly greater than for the Antares (5.0 MHz), while the  $-6$  dB bandwidths obtained using a Gaussian fit are slightly higher for the Aloka (3.4 MHz) than for the Antares (3.2 MHz). The Antares system has a significantly higher signal-to-noise ratio (SNR) at 25 dB compared to the Aloka at 10 dB; the lower SNR of the Aloka may result from external digitization of the RF signals from the Aloka. Note also the presence of a second harmonic in the power spectrum obtained from the Aloka suggesting that the lower SNR for the Aloka is not due to lower transmit pressure.

Another factor that could influence strain image performance involves the method of data processing. A 2D block matching algorithm (Zhu and Hall 2002) was used in the case of the Antares whereas a 1D cross-correlation method was used for the Aloka. The 2D block matching algorithm computes the sum-squared difference (SSD) or sum-absolute difference (SAD) between pre- and post-compression RF frames for a rectangular kernel. The kernel size corresponds to approximately 2/3 the length of the axial point spread function (PSF) and about the same width as the lateral PSF. Linear regression with a sliding 1.5 mm window is used to estimate axial strain from these displacement estimates.

In the 1D cross-correlation method differential displacements in localized regions are detected using standard time-delay estimation techniques (Knapp and Carter 1976, Quazi 1981). A window length of 1.5 mm with a 75% overlap is used to obtain the tissue displacements, and then the axial strain is computed using a 5-point linear least-squares fit on the estimates of tissue displacement (Kallel and Ophir 1997). A  $5 \times 5$  median filter was used to reduce strain outliers in the strain image.

## 7. Summary and conclusions

A complete description of the procedure for manufacturing spherical lesion phantoms for elastography with sphere diameters from 1.6 mm through 4 mm has been provided. The

elastic contrasts range from 3.3 through 5.5. Lower elastic contrasts can be produced in the agar/gelatin type phantom by making the dry-weight agar concentration in the spheres closer to that in the background material. Similarly, lower contrasts can be generated in the oil-in-gelatin type phantom by making the spheres from a safflower oil dispersion; the closer the per cent oil in the spheres is to that in the background, the lower the elastic contrast.

It should be noted that the phantoms are durable. About one month after production, bonding between layers of a phantom and between spheres and background is sufficiently firm for at least a 10% compression.

The phantoms brought out differences in performance of the two systems used. A phantom such as described in this work should be useful as a stable performance test tool in labs that are refining hardware and/or software for elastography systems.

### Acknowledgments

Work supported in part by NIH grants R01EB000459, R21EB003853 and R01CA100373.

### References

Bevington P B 1969 *Data Reduction and Error Analysis for the Physical Sciences* (New York: McGraw-Hill) p 72

Bilgen M and Insana M F 1997 Error analysis in acoustic elastography: I. Displacement estimation *J. Acoust. Soc. Am.* **101** 1139–46

Kallel F and Ophir J 1997 A least-squares strain estimator for elastography *Ultrason. Imaging* **19** 195–208

Knapp C H and Carter G C 1976 The generalized correlation method for estimation of time delay *IEEE Trans. Acoust. Speech Signal Process.* **24** 320–7

Kofler J M Jr and Madsen E L 2001 Improved method for determining resolution zones in ultrasound phantoms with spherical simulated lesions *Ultrasound Med. Biol.* **27** 1667–76

Krouskop T A, Wheeler T M, Kallel F, Garra B S and Hall T J 1998 Elastic moduli of breast and prostate tissues under compression *Ultrason. Imaging* **20** 260–74

Madsen E L *et al* 1999 Interlaboratory comparison of ultrasonic backscatter, attenuation and speed measurements *J. Ultrasound Med.* **18** 615–31

Madsen E L, Frank G R, Krouskop T A, Varghese T, Kallel F and Ophir J 2003 Tissue-mimicking oil-in-gelatin dispersions for use in heterogeneous phantoms *Ultrason. Imaging* **25** 17–38

Madsen E L, Hobson M A, Shi H, Varghese T and Frank G R 2005a Tissue-mimicking agar/gelatin materials for use in heterogeneous elastography phantoms *Phys. Med. Biol.* **50** 5597–5618

Madsen E L, Hobson M A, Shi H, Varghese T and Frank G R 2005b Stability of heterogeneous elastography phantoms made from oil dispersions in aqueous gels *Ultrasound Med. Biol.* at press

Quazi A H 1981 An overview of the time delay estimate in active and passive systems for target localization *IEEE Trans. Acoust. Speech. Signal Process.* **29** 527–33

Rice J R, Milbrandt R H, Madsen E L, Frank G R and Boote E J 1998 Anthropomorphic <sup>1</sup>H MRS head phantom *Med. Phys.* **25** 1145–56

Sinkus R, Tanter M, Xydeas T, Catheline S, Bercoff J and Fink M 2005 Viscoelastic shear properties of *in vivo* breast lesions measured by MR elastography *Magn. Reson. Imaging* **23** 159–65 (see figure 5)

Walker W F and Trahey G E 1995 A Fundamental limit on delay estimation using partially correlated speckle signals *IEEE Trans. Ultrason. Ferroelectr. Freq. Control* **42** 301–8

Zhu Y and Hall T J 2002 A modified block matching method for real-time freehand strain imaging *Ultrason. Imaging* **24** 161–76

# Breast Lesions: Evaluation with US Strain Imaging—Clinical Experience of Multiple Observers<sup>1</sup>

Dawn M. Regner, MD  
Gina K. Hesley, MD  
Nicholas J. Hangiandreou, PhD  
Marilyn J. Morton, DO  
Michelle R. Nordland, RTRM  
Duane D. Meixner, RDMS  
Timothy J. Hall, PhD  
Michael A. Farrell, MD  
Jayawant N. Mandrekar, PhD  
W. Scott Harmsen, MS  
J. William Charboneau, MD

**Purpose:**

To prospectively determine the accuracy of using an ultrasonographic (US) strain imaging technique known as lesion size comparison to differentiate benign from malignant breast lesions.

**Materials and Methods:**

Institutional Review Board approval and patient informed consent were obtained for this HIPPA-compliant study. US strain imaging was performed prospectively for 89 breast lesions in 88 patients. Lesions were imaged by using free-hand compression and a real-time strain imaging algorithm. Five observers obtained manual measurements of lesion height, width, and area from B-mode and strain images. By using these size measurements, individual observer and group performances were assessed by using the area under the receiver operating characteristic curve ( $A_z$ ). The performance of a single size parameter versus that of a combination of size parameters was evaluated by using univariate and multivariate logistic regression.

**Results:**

Group  $A_z$  values showed that width ratio and area ratio yielded the best results for differentiating benign and malignant breast lesions, and they were not statistically different from one another ( $P = .499$ ). For the group, the performance of area and width, which was superior to that of height and aspect ratio, was statistically significant for all cases ( $P < .011$ ) except for those that compared area with aspect ratio ( $P = .118$ ). By using a group threshold of 1.04 for width ratio and 1.13 for area ratio, the sensitivity and specificity of the technique were 96% and 21%, respectively, for width and 96% and 24%, respectively, for area. The best observer achieved a sensitivity of 96% and a specificity of 61% by using the area ratio. For all but one observer, combined size parameters did not improve observer performance ( $P > .258$ ). Significant interobserver performance variability was observed ( $P < .001$ ).

**Conclusion:**

Results suggest that US strain imaging has the potential to aid diagnosis of breast lesions. However, manually tracing lesion boundaries for size ratio differentiation in a busy clinical setting did not match the diagnostic performance levels previously reported. Focusing on measurements of lesion width, along with additional observer training or automated processes, may yield a suitable method for routine clinical application.

<sup>1</sup> From the Department of Radiology, Mayo Clinic, 200 First St SW, Rochester, MN 55905. From the 2003 RSNA Annual Meeting. Received July 30, 2004; revision requested October 8; revision received January 21, 2005; accepted February 21; final version accepted, April 1. Supported in part by a grant from Siemens Medical Solutions, Ultrasound Division, Issaquah, Wash. T.J.H. supported by grant DAMD17-00-1-0596 from the U.S. Army Medical Research and Materiel Command.

The observation that benign and malignant breast lesions have inherently different firmness has long been used by clinicians during palpation of the breast; harder and less mobile lesions are considered more likely to be malignant (1). Several different imaging methods, including ultrasonographic (US) strain imaging (also known as US elastography), have been developed to measure the relative stiffness of lesions in contrast to the surrounding tissue (2–17). US strain imaging may allow the differentiation of benign from malignant solid masses on the basis of differences in stiffness.

US strain images are produced by comparing the US echo data obtained prior to and after slight axial compression of the breast. These data are used to determine the tissue displacement at each location in the breast as a result of compression. Strain is computed as the rate of change in axial tissue displacement as a function of depth. Strain images are produced when the relative differences in tissue motion at each location in the breast are calculated and displayed. Harder areas of the breast (ie, areas with less tissue displacement during compression) appear darker on strain images, and softer areas of the breast (ie, areas with more tissue displacement during compression) appear brighter. Preliminary work does not support the use of direct quantification of lesion strain as an accurate means of differentiating benign from malignant solid lesions (6,11,14,17,18).

Peer-reviewed work by Garra et al (6) and others has shown that discrepancies between the size of breast lesions on B-mode and strain images may be a promising way to distinguish benign from malignant lesions; this method is known as the lesion size comparison technique. Researchers have found that malignant lesions tend to be larger on strain images than on corresponding B-mode images, potentially because of the surrounding desmoplastic reaction that accompanies most malignancies (6,11,17,19). Thus, the purpose of our study was to prospectively determine

the accuracy of using a US strain imaging technique known as lesion size comparison to differentiate benign from malignant breast lesions.

### Materials and Methods

Siemens Medical Solutions, Ultrasound Division, Issaquah, Washington, provided equipment and financial support for this study. The authors had control of the data and information submitted for publication.

### Patient Population

Approval for this study was obtained from the Institutional Review Board, and informed consent was obtained from the enrolled patients. The study was compliant with the Health Insurance Portability and Accountability Act. From February 6, 2002, to August 6, 2003, US strain imaging was performed prospectively for 102 consecutive breast masses in 101 patients (mean age, 58 years; median age, 58.5 years; age range, 20–85 years). Candidates were recruited from a clinical pool of patients who were known to have lesions that were visible at US and that warranted biopsy. The first four recruited patients were excluded as training patients, seven recruited patients were excluded because of technical difficulties with radiofrequency echo data transfer, and two patients were excluded because biopsy results showed both benign and malignant histologic features in the same biopsy sample. Thus, 89 lesions in 88 women were included in the final data analysis. Lesion diameters ranged from 0.3 to 3.0 cm, with a mean lesion diameter of 1.3 cm. For 73 of 88 lesions, biopsy was performed after strain imaging on the same day (mean, 41.5 minutes; range, 3–245 minutes). For 12 of 88 lesions, biopsy was performed at a later date (mean, 17 days; range, 1–112 days). For three of 88 lesions, biopsy was performed at a previous date (1, 2, and 6 years previously). For these three lesions, the five observers were blinded to the fact that a previous biopsy had been performed, as well as to the previous biopsy results.

### US Strain Imaging Technique

A mammography technologist with 10 years of experience in breast US imaged all lesions at 7.3 MHz by using a real-time strain imaging algorithm that was developed by Hall et al (17); this algorithm was implemented by using a standard commercial US system (Elegra scanner and 7.5L40 linear array transducer; Siemens Medical Solutions). By using a freehand compression technique, the technologist manually applied slight axial compression to the lesions with the US probe. B-mode and strain images were reconstructed off line by using the same radiofrequency echo data that were acquired during the US examination. Images were displayed in a side-by-side format within the individual frames that were contained within a cine-loop sequence of approximately 100 frames. Off-line processing of the stored radiofrequency data was performed by using custom software which utilized the same algorithm that exists on the US scanner, except a smaller correlation window was used (16 samples instead of 24 samples) resulting in superior strain image spatial resolution. Also, radiofrequency data were stored at a greater frame rate than were those displayed in real time with the US scanner; thus, off-line temporal resolution

Published online

10.1148/radiol.2381041336

**Radiology** 2006; 238:425–437

#### Abbreviation:

$A_z$  = area under the receiver operating characteristic curve

#### Author contributions:

Guarantors of integrity of entire study, D.M.R., G.K.H., N.J.H., M.A.F.; study concepts/study design or data acquisition or data analysis/interpretation, all authors; manuscript drafting or manuscript revision for important intellectual content, all authors; approval of final version of submitted manuscript, all authors; literature research, D.M.R., G.K.H., N.J.H., T.J.H., M.A.F.; clinical studies, D.M.R., M.J.M., M.R.N., D.D.M.; statistical analysis, D.M.R., N.J.H., J.N.M., W.S.H.; and manuscript editing, D.M.R., G.K.H., N.J.H., M.J.M., D.D.M., T.J.H., M.A.F., W.S.H., J.W.C.

**Address correspondence to** D.M.R.  
(e-mail: regner.dawn@mayo.edu).

See Materials and Methods for pertinent disclosures.

was superior to that displayed in real time with the scanner (17).

### B-Mode and Strain Image Evaluation

Five observers (designated as observers A–E) with different characteristics (Table 1) individually produced measurements of lesion size, including height and width, and traced the area of the lesion off line on reconstructed B-mode and corresponding strain images by using a mouse. Observers made their measurements on a single representative image frame that was personally chosen as best (designated as “own image”) from the cine-loop sequence of about 100 frames. At a later date, the measurements, including height, width, and traced area, were repeated by each observer on the unmarked standardized image frames (designated as “reference image”) that were chosen as best by the technologist who performed the examinations (observer D). Prior to obtaining study measurements, all of the observers met two to three times to receive specific training both in choosing the optimal strain image from the cine-loop sequence and in making consistent lesion size measurements. All observers practiced breast lesion measurements on multiple sample B-mode and strain images during these training sessions. All observers were comfortable with the technique at the end of the training sessions. During the study, observers were asked to report any concerns they had regarding difficulties in producing measurements, as well as any anecdotal observations they believed to be important.

### Data and Statistical Analysis

Size ratios were computed for each of the four size parameters (ie, height, width, area, and aspect [width-to-height] ratio) by dividing the strain image measurements by the B-mode image measurements. Ratios were calculated for each individual observer and for the group as a whole. Group ratios were obtained by averaging the individual observer B-mode and strain image measurements and by calculating ratios from these averaged measurements. The own image size ratios were analyzed by using receiver operating characteristic methods for each observer and for the group. Because images from the same patient were used multiple times, the correlated areas under the receiver operating characteristic curve ( $A_z$  values) were compared to determine which size ratio was best suited for differentiating benign from malignant lesions; comparisons between these values were made by using a method proposed by DeLong et al (20). The ratio threshold value that achieved at least 95% sensitivity in differentiating malignant from benign lesions while optimizing specificity was then determined for each individual observer and for the group. This 95% sensitivity threshold is likely the most valuable parameter for breast imaging because the desire is to minimize the chances of missing a malignancy.

Univariate and multivariate logistic regression analyses (21) were performed, and a comparison of the  $c$  statistic values that were generated from these analyses was performed by using

the method proposed by DeLong et al (20) to determine if the combined size parameters were superior to any one size parameter alone in predicting benignity or malignancy. The  $A_z$  value, threshold, and sensitivity and specificity values for own image observer data were compared to see if there was significant interobserver performance variation. Own image and reference image  $A_z$  values for width and area were compared by using the method proposed by DeLong et al (20), and the ranges of own image and reference image sensitivity and specificity were compared in an attempt to isolate the most important sources of any interobserver performance variation. A subset analysis was performed by using receiver operating characteristic methods of only those lesions that were judged by observer A to have well-defined borders on conventional B-mode US images to determine if the performance of the lesion size comparison technique was dependent on the conspicuity of lesion borders at B-mode imaging.

Finally, a comparison was made between the results presented by Hall et al (22) and those obtained in the current study by using the same US strain imaging algorithm and analysis approach. A  $P$  value of less than .05 was considered to indicate a statistically significant difference for all analyses. All of the statistical analyses were performed by using a commercially available software program (SAS, version 8.0; SAS Institute, Cary, NC).

Observers A, B, and C participated in a preliminary study (19) (performed

**Table 1**

#### Observer Characteristics

Observer	Degree	Title	Clinical Experience in Breast US	Experience in US Strain Imaging	Measurement Environment*
A	MD	Radiology resident	1 mo	Yes	Laboratory
B	RDMS	Ultrasonographer	None	Yes	Laboratory
C	MD	Board-certified radiologist	5 yrs	Yes	Clinical
D	RTRM	Breast US technologist	10 yrs	No	Clinical
E	MD	Board-certified radiologist	15 yrs	No	Clinical

\* The laboratory measurement environment refers an environment in which observers made measurements in a laboratory, with fewer distractions and much more time available to dedicate to lesion measurements. The clinical measurement environment refers to a more hectic environment in which observers made measurements under considerable time constraints owing to concomitant clinical duties.

4–6 months earlier) during which measurements were made of the first 50 of 89 lesions that were included in the current study. Although the three observers involved in the preliminary study

remeasured the first 50 lesions for the current study, none of the observers believed that the initial analysis provided any advantage or bias other than increased practice. To support this, an analysis was performed to compare the  $A_z$  values of the first 50 lesions of the current study (ie, those that were previously measured as part of the preliminary study) with those of the last 39 lesions of the current study (ie, those that were not previously measured) for observers A, B, and C.

**Table 2**

**Histologic Characteristics of Breast Lesions**

Characteristic	No. of Lesions
<b>Benign (n = 38)</b>	
Fibroadenoma	16
Fibrocystic change	6
Stromal fibrosis	6
Abscess	2
Intraductal papilloma	2
Fat necrosis	2
Pseudoangiomatous stromal hyperplasia	1
Hematoma	1
Radial scar	1
Complex cyst	1
<b>Malignant (n = 51)</b>	
Invasive ductal carcinoma	39
Invasive lobular carcinoma	6
Mixed ductal and lobular carcinoma	3
Invasive tubular carcinoma	2
Ductal carcinoma in situ	1

shown in Table 3. For four of five observers and for the entire group, width and area ratios yielded the best results (ie, the largest  $A_z$  values) for differentiating benign from malignant breast lesions. Observer E was the exception in that, for this observer, width and aspect ratios yielded the best results. For the entire group, the superior performance of width and area measurements when compared with height and aspect ratio was statistically significant for all cases ( $P \leq .011$ ), except for the comparison of area and aspect ratio, which was not significant ( $P = .118$ ). For the five individual observers, the  $A_z$  values for width and area, when compared with those of height and aspect ratio in every combination, resulted in 13 of 20 comparisons in which width and area yielded significantly better performance ( $P \leq .032$ ). In six of 20 comparisons, width and area were superior to height and aspect ratio, but the differences were not statistically significant ( $P \geq .054$ ). In one of 20 comparisons (ie, for observer E), aspect ratio was superior to area, but the difference was not significant ( $P = .311$ ). Width and area were statistically equivalent to one another

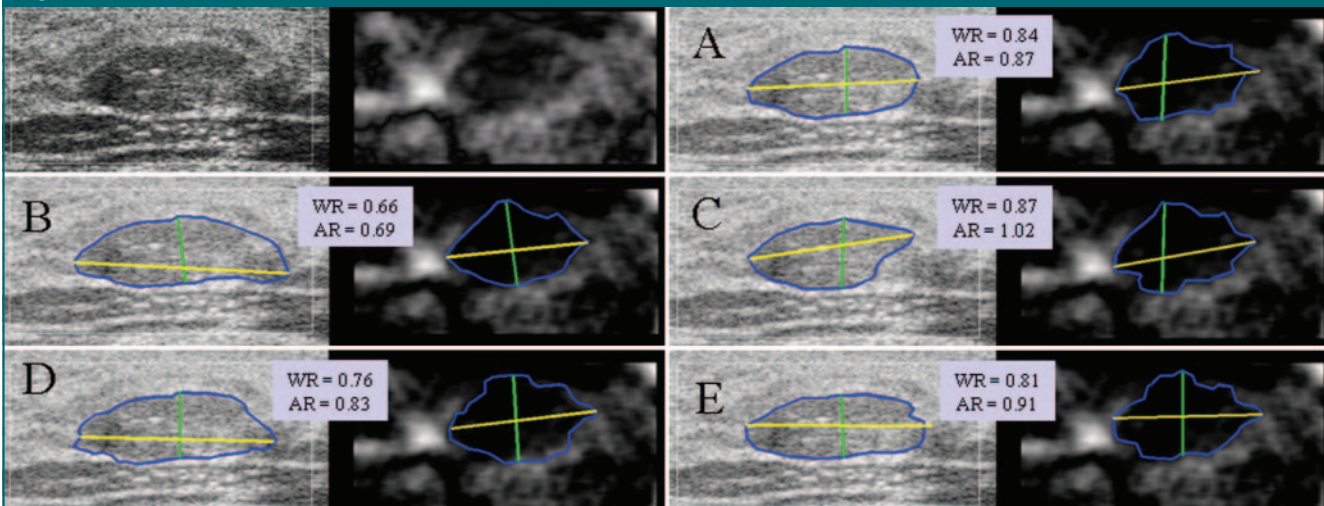
**Results**

All lesions were grouped as benign ( $n = 38$ ) or malignant ( $n = 51$ ) according to surgical or needle biopsy results (Table 2). Figures 1–3 show examples of the appearance of benign and malignant lesions, as well as the size measurements made by each of the observers. Figures 4–9 show additional examples of various benign and malignant lesions that were observed during the study.

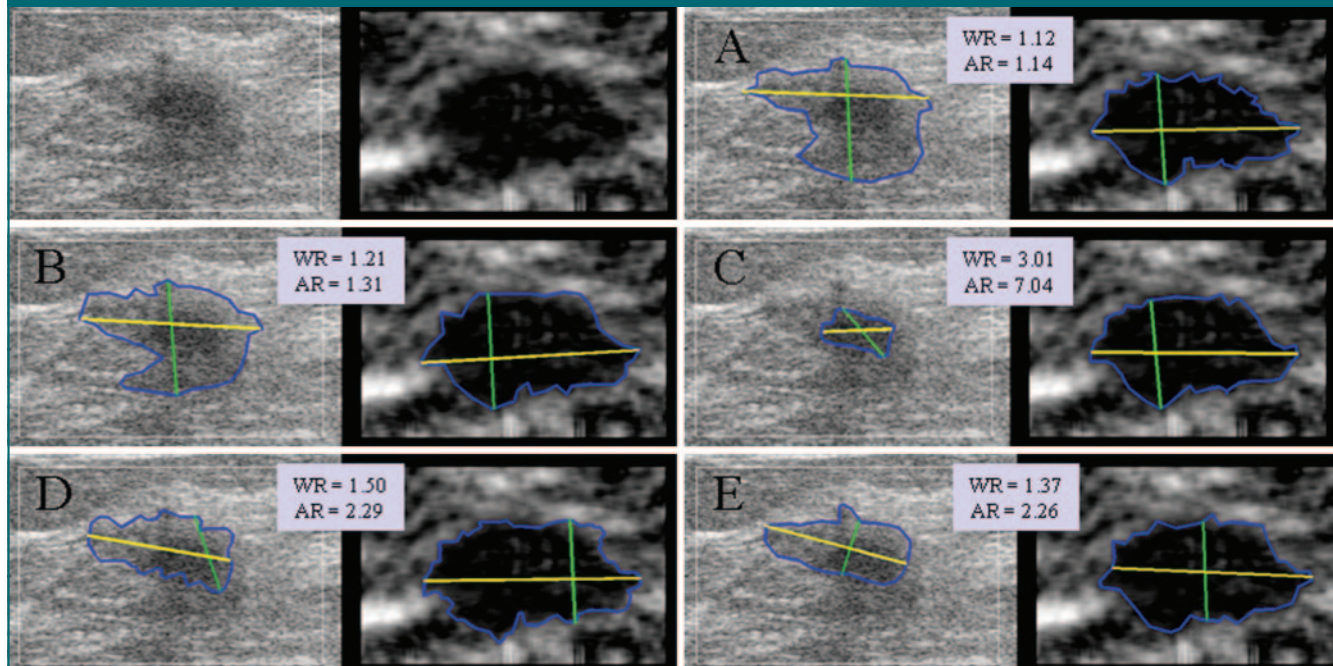
**$A_z$  Value, Threshold, Sensitivity, and Specificity**

Own image  $A_z$  values for the five observers and for the group as a whole are

**Figure 1**



**Figure 1:** Side-by-side paired displays of B-mode (left image of each pair) and strain (right image of each pair) US images of benign fibroadenoma. Unmarked reference images (upper left pair) along with images showing measurements of height (green line), width (yellow line), and traced area (blue line) are displayed for each observer (A–E). The resulting size ratios for width (WR) and area (AR) are noted. By using the group area and width threshold ratios presented in Table 4, strain imaging was used to correctly predict lesion benignity (true-negative finding).

**Figure 2**

**Figure 2:** Side-by-side paired displays of B-mode (left image of each pair) and strain (right image of each pair) US images of invasive ductal carcinoma. Unmarked reference images (upper left pair) along with images showing measurements of height (green line), width (yellow line), and traced area (blue line) are displayed for each observer (A–E). The resulting size ratios for width (WR) and area (AR) are noted. Lesion has somewhat indistinct borders on B-mode images and demonstrates that marked interobserver measurement variability can result with this technique. By using the group width and area threshold ratios (Table 4), strain imaging was used to correctly predict lesion malignancy (true-positive finding).

( $P = .499$  for the group,  $P \geq .421$  for observers A–D, and  $P = .069$  for observer E).

Table 4 shows the own image threshold data that was computed for each observer (designated as “observer threshold”) and for the entire group (designated as “group threshold”) for both width and area ratios. The optimal group ratio threshold was 1.04 for width and 1.13 for area. These thresholds yielded a sensitivity and specificity of 96% and 21%, respectively, for width and of 96% and 24%, respectively, for area. Figures 10 and 11 show individual case-by-case data in graphic format.

To determine if a combination of multiple size parameters was superior to any single size parameter in predicting if a lesion was benign or malignant, univariate and multivariate logistic regression analyses were performed (Table 5). Several size parameter models (ie, single size parameters and combined size parameters) were assessed

on the basis of the  $c$  statistic, which is equivalent to  $A_z$  value (21), and were compared by using the method proposed by DeLong et al (20). Models with a larger  $c$  statistic represent enhanced observer performance in differentiating benign from malignant breast lesions. In Table 5, either traced area or width alone was an important discriminating factor of malignancy for four of five observers by using univariate logistic models. Also in Table 5, only a few combinations of size parameters yielded slightly higher  $A_z$  values than width or area alone; however, for four of five observers, the differences were not statistically significant ( $P \geq .258$ ). Observer E was the exception in that, for two of eight comparisons, a significant advantage was seen when combined parameters were used ( $P \leq .027$ ). Overall, this analysis demonstrates that there is no overall improvement in the discriminating capabilities of multivariate models, as is shown in Table 5.

#### Assessment of Interobserver Variation

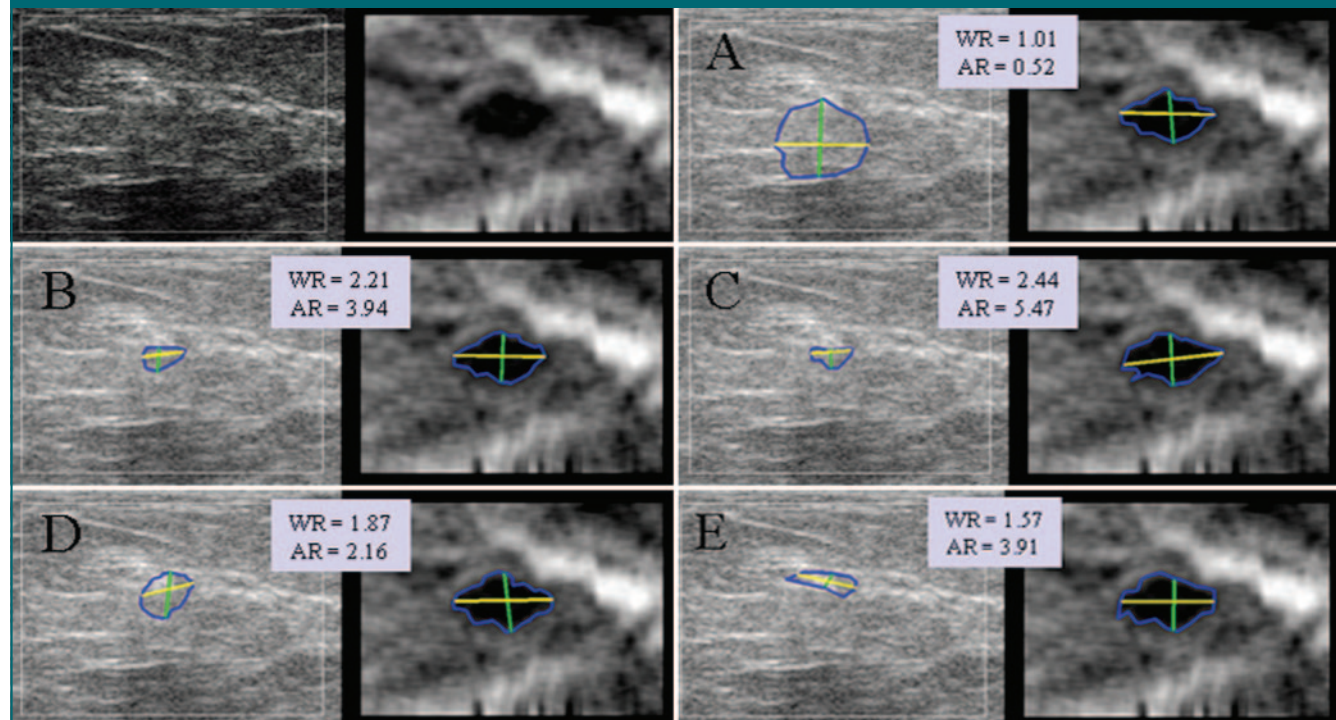
As seen in Table 3, individual observer  $A_z$  values ranged from 0.74 to 0.90 for width ratios and from 0.67 to 0.92 for area ratios. As seen in Table 4, individual observer thresholds for own image measurements ranged from 0.28 to 1.04 for width and from 0.90 to 1.24 for area. Applying the group threshold to each observer’s own image width data resulted in observer sensitivities ranging from 86% to 96% and specificities ranging from 21% to 61%. Applying the group threshold to each observer’s own image area data resulted in observer sensitivities ranging from 82% to 98% and specificities ranging from 16% to 71%. Testing all pairs of individual observers against one another showed some statistically significant differences between observers at the 95% confidence level ( $P < .001$  for the group) (Table 6). Specifically, observer A performed significantly better than all other observers when the area parameter was used ( $P \leq$

.01) and significantly better than all but one other observer when the width parameter was used ( $P \leq .01$  for the remaining observers). Observers B and C

performed significantly better than observer E when the area parameter was used ( $P \leq .01$ ). In addition, observers B and C tended to perform better than

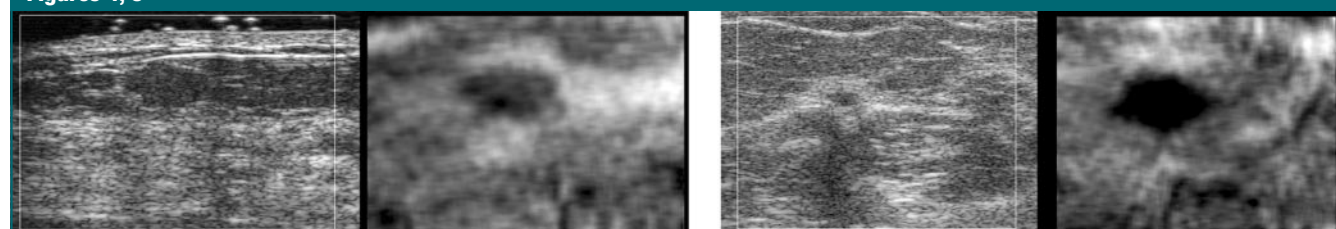
observer D for both width and area and better than observer E for width; this difference, however, was not statistically significant ( $P \geq .07$ ).

**Figure 3**

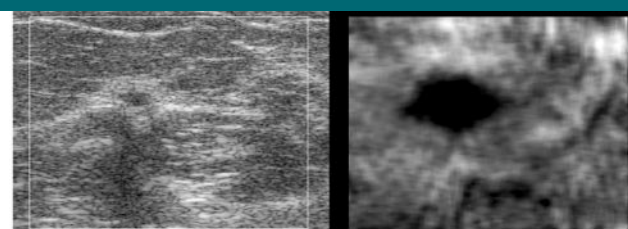


**Figure 3:** Side-by-side paired displays of B-mode (left image of each pair) and strain (right image of each pair) US images of benign fat necrosis. Unmarked reference images (upper left pair) along with images showing measurements of height (green line), width (yellow line), and traced area (blue line) are displayed for each observer (A–E). The resulting size ratios for width (WR) and area (AR) are noted. Images illustrate one of the potential problems with this technique in that, for some lesions, the lesion is difficult, if not impossible, to distinguish from the surrounding breast tissue on B-mode images. This likely makes measurements of lesion size on B-mode images inaccurate, and as shown here, different observers will vary widely in their interpretation of border and size measurements. In this example, only the size ratios for observer A correctly predicted lesion benignity. This lesion also demonstrates how strain imaging can confirm the presence of subtle lesions, which are much more conspicuous at strain imaging.

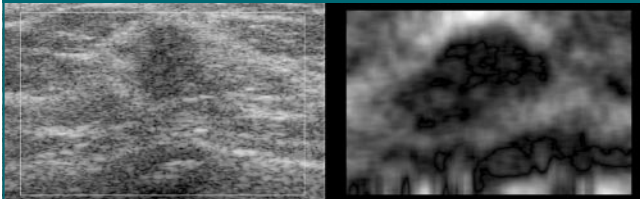
**Figures 4, 5**



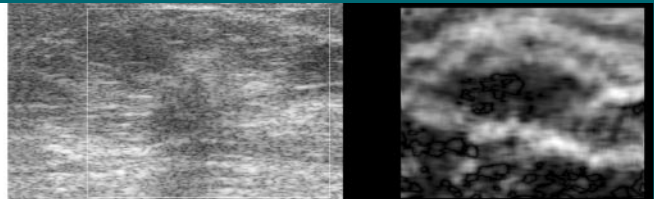
**Figure 4:** Side-by-side paired display of B-mode (left) and strain (right) US images of fibrocystic change. By using the group width and area thresholds presented in Table 4, strain imaging was used to incorrectly predict lesion malignancy (false-positive finding).



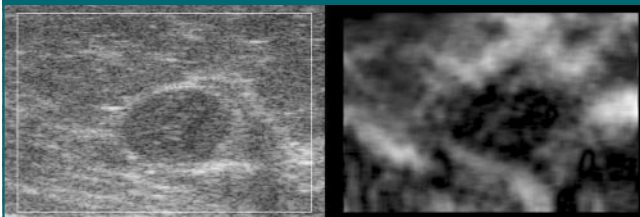
**Figure 5:** Side-by-side paired display of B-mode (left) and strain (right) US images of invasive ductal carcinoma. Lesion appears much bigger on strain image than on corresponding B-mode image. By using the group area and width threshold ratios presented in Table 4, strain imaging was used to correctly predict lesion malignancy (true-positive finding).

**Figures 6, 7**

**Figure 6:** Side-by-side paired display of B-mode (left) and strain (right) US images of invasive ductal carcinoma. By using the group width and area threshold ratios presented in Table 4, strain imaging was used to correctly predict lesion malignancy (true-positive finding).



**Figure 7:** Side-by-side paired display of B-mode (left) and strain (right) US images of invasive lobular carcinoma. By using the group width and area threshold ratios presented in Table 4, strain imaging was used to correctly predict lesion malignancy (true-positive finding).

**Figures 8, 9**

**Figure 8:** Side-by-side paired display of B-mode (left) and strain (right) US images of invasive ductal carcinoma. Lesion width and area are similar on strain and B-mode images. By using the group width and area threshold ratios presented in Table 4, strain imaging was used to incorrectly predict lesion benignity (false-negative finding).

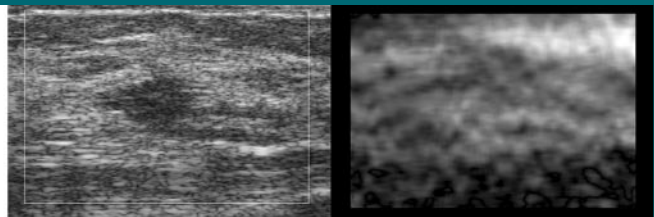


**Figure 9:** Side-by-side paired display of B-mode (left) and strain (right) US images of benign stromal fibrosis in patient with a history of breast cancer. Anecdotally, strain images that show little or no contrast between the lesion and the surrounding breast tissue, as is seen in this patient, seem to be a reliable indicator of benignity.

**Table 3** **$A_z$  Values for Complete Data Set and Subset of Lesions with Well-defined Borders**

Parameter	Complete Data Set for Own Image				Complete Data Set for Reference Image		Well-defined Subset for Own Image*	
	Height	Width	Area	Aspect Ratio	Width	Area	Width	Area
Entire group	0.71	0.85	0.83	0.74	0.77	0.73	0.81	0.81
Observer A	0.72	0.90	0.92	0.72	0.87	0.85	0.90	0.92
Observer B	0.73	0.83	0.82	0.70	0.73	0.72	0.80	0.81
Observer C	0.71	0.79	0.79	0.63 <sup>†</sup>	0.75	0.67	0.76	0.74
Observer D	0.62 <sup>†</sup>	0.75 <sup>†</sup>	0.77	0.68 <sup>†</sup>	0.75	0.77	0.68	0.72
Observer E	0.47 <sup>†</sup>	0.74	0.67	0.74	0.71	0.66	0.75	0.71

Note.—Standard errors for all  $A_z$  values ranged from 0.03 to 0.06.

\* Subset includes data generated for lesions with well-defined borders at B-mode imaging only.

<sup>†</sup> Values were not found to be statistically significant at the 5% level.

**Analysis of Interobserver Variation**

After the US data are acquired, there are at least two potential sources of interobserver variation when the lesion size comparison technique is used—that is, variation in choosing the optimal strain image from the cine-loop se-

quence and variation in measuring the lesion size parameter on the strain and corresponding B-mode images within the chosen frame. To determine which of these sources contributed most to our significant observer variation, all observers made measurements on un-

marked standard images. To remove the potential interobserver variation that is inherent in choosing the image, these unmarked images were chosen by the same technologist who performed the examinations and were designated as the reference images. Applying the

group threshold to each observer's reference image width data resulted in observer sensitivities ranging from 90% to 100% and specificities ranging from 11% to 42% (Table 4). Applying the group threshold to each observer's ref-

erence image area data resulted in observer sensitivities ranging from 90% to 98% and specificities ranging from 16% to 50% (Table 4). For width, individual reference image  $A_z$  values ranged from 0.71 to 0.87 (Table 3), and for area,

individual observer reference image  $A_z$  values ranged from 0.66 to 0.85 (Table 3). By definition, the own image and reference image  $A_z$  values for observer D were equivalent. For the remaining four observers, comparison of own im-

**Table 4****Ratio Thresholds with Sensitivities and Specificities for Each Observer and the Entire Group**

Parameter	Width			Area		
	Ratio Threshold Value	Sensitivity (%)	Specificity (%)	Ratio Threshold Value	Sensitivity (%)	Specificity (%)
<b>Entire group</b>						
Own image						
Group threshold	1.04	96 (87, 100)*	21 (10, 37)*	1.13	96 (87, 100)*	24 (11, 40)*
Reference image						
Group threshold	1.03	96 (87, 100)*	18 (8, 34)*	1.17	96 (87, 100)*	21 (10, 37)*
<b>Observer A</b>						
Own image						
Observer threshold	0.98	96	42	1.01	96	61
Group threshold	1.04	92	61	1.13	88	71
Reference image						
Observer threshold	1.13	96	68	1.05	96	40
Group threshold	1.03	100	42	1.17	90	50
<b>Observer B</b>						
Own image						
Observer threshold	0.90	96	24	0.90	96	22
Group threshold	1.04	86	46	1.13	82	51
Reference image						
Observer threshold	1.01	96	37	1.06	96	18
Group threshold	1.03	94	37	1.17	94	24
<b>Observer C</b>						
Own image						
Observer threshold	1.04	96	29	1.08	96	21
Group threshold	1.04	96	29	1.13	94	21
Reference image						
Observer threshold	0.98	96	16	1.33	96	29
Group threshold	1.03	94	21	1.17	96	16
<b>Observer D</b>						
Own image						
Observer threshold	0.28	96	3	1.24	96	29
Group threshold	1.04	90	21	1.13	98	16
Reference image						
Observer threshold	0.28	96	3	1.24	96	29
Group threshold	1.03	90	16	1.17	98	18
<b>Observer E</b>						
Own image						
Observer threshold	0.97	96	29	0.96	96	18
Group threshold	1.04	88	34	1.13	86	32
Reference image						
Observer threshold	0.96	96	11	1.01	96	13
Group threshold	1.03	90	11	1.17	90	21

Note.—The optimal group and observer ratio thresholds for width and area were determined by obtaining a sensitivity of at least 95% while maximizing specificity for own image and reference image data. The group threshold was then applied to each observer's own image and reference image data to obtain a second set of sensitivities and specificities, which allowed for comparison of individual observer performance.

\* Numbers in parentheses are 95% confidence intervals.

Figures 10, 11

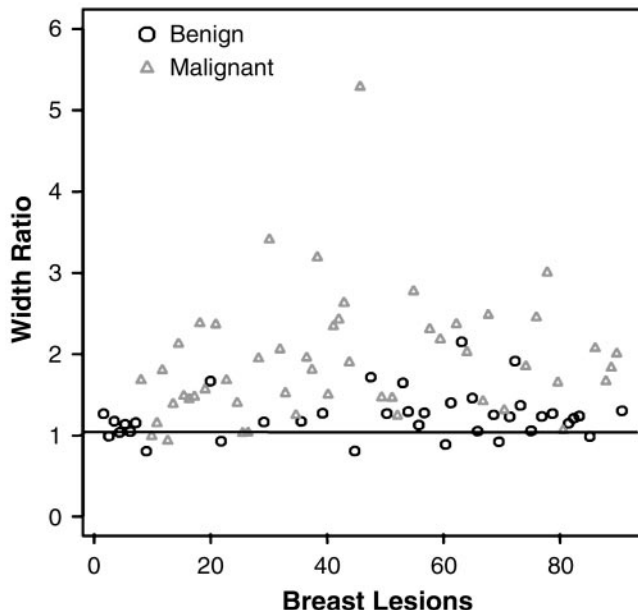


**Figure 10:** Graph of own image group width ratios plotted for each lesion in the study. Horizontal line represents optimal group threshold ratio of 1.04. Above this threshold, malignant lesions were classified as true-positive findings, and below this threshold, benign lesions were classified as true-negative findings. Although malignant lesions tend to have larger width ratios, one can see that there is considerable overlap near the threshold line, which is reflected in low specificity values.

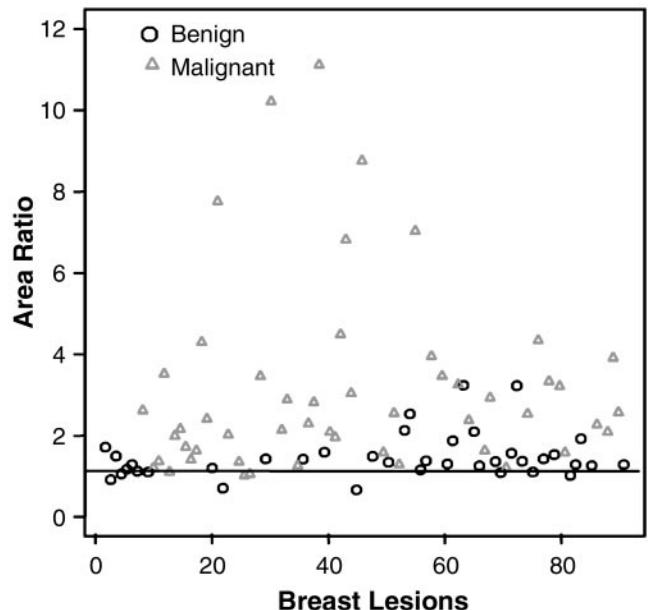


**Figure 11:** Graph of own image group area ratios plotted for each lesion in the study. Horizontal line represents optimal group threshold ratio of 1.13. Above this threshold, malignant lesions were classified as true-positive findings, and below this threshold, benign lesions were classified as true-negative findings. Although malignant lesions tend to have larger area ratios, as is the case with width, one can see that there is considerable overlap near the threshold line, which is reflected in low specificity values.

Table 5

## Univariate and Multivariate Logistic Regression Analyses

Observer	Univariate <i>c</i> Statistic*					Multivariate <i>c</i> Statistic			
	Height	Width	Area	Aspect Ratio		Height and Aspect Ratio	Width and Aspect Ratio	Height and Aspect Ratio	Area and Aspect Ratio
A	0.72	0.90	0.92	0.72		0.90	0.92	0.92	0.92
B	0.73	0.83	0.82	0.70		0.84	0.83	0.84	0.85
C	0.71	0.79	0.79	0.63		0.75	0.79	0.80	0.79
D	0.62	0.75	0.77	0.68		0.70	0.74	0.79	0.78
E	0.47	0.74	0.67	0.74		0.76	0.76	0.78	0.92

Note.—For all *c* statistics, standard errors ranged from 0.03 to 0.06.

\* Univariate *c* statistics are equivalent to  $A_z$  values, which appear in Table 3.

age and reference image  $A_z$  values for width and area demonstrated a statistical reduction in observer performance in only one of eight comparisons ( $P = .025$  for area, observer C). In three other instances, however, marginal  $P$  values were obtained ( $.057 \leq P \leq .084$ ).

## Subset Analysis of Breast Lesions with Well-defined Borders at B-Mode US

During the analysis, several observers reported that, in certain cases, measuring lesions on the conventional B-mode display was particularly difficult (Fig 3). This might lead to a decrease in measurement accuracy and an increase in

interobserver (and possibly intraobserver) variability. Observer A reviewed the cases and determined that a total of 60 of 89 lesions had well-defined borders on B-mode images. A subset analysis was performed for measurements obtained in these 60 lesions (31 malignant and 29 benign). Group  $A_z$  val-

ues for this subset were 0.81 for both width and area (Table 3). These  $A_z$  values were slightly lower than the group  $A_z$  values for the complete data set, which were 0.85 and 0.83 for width and area, respectively (Table 3). In only one case did the subset produce a somewhat superior  $A_z$  value (observer E, area). Also, for the group and for all but one observer, the sensitivity and specificity of width and area ratio thresholds were not substantially improved when only the subset of lesions with well-defined borders at B-mode imaging was considered.

#### Comparison with Previous Results

In a previous study by Hall et al (22), a series of 169 breast lesions were evaluated by using the same strain imaging technique as was used in our study. A single observer who had extensive experience with the lesion size comparison technique picked the optimal strain image from the cine-loop sequence and obtained area measurements. By using area as the size parameter and 1.2 as the optimal area ratio threshold, a sensitivity of 100% and a specificity of 75.4% in characterizing breast lesions were obtained in this series of 169 lesions. When this 1.2 threshold for area ratio was applied to the own image ratio

data obtained in our current study, our group sensitivities and specificities were 94% and 29%, respectively. When the 1.2 threshold for area ratio was applied to the own image ratio data of observer A (our best performer), sensitivity and specificity were 86% and 82%, respectively.

#### Analysis of the First 50 Lesions

To show that the preliminary study did not provide observers A, B, and C with any advantage or bias other than increased practice, an analysis was performed to compare  $A_z$  values of the first 50 lesions of the current study (ie, those that were previously measured as part of the preliminary study) with those of the last 39 lesions of the current study (ie, those that were not previously measured). This analysis showed that, in general, the  $A_z$  values were not significantly different between the first 50 lesions and the last 39 lesions for observers A, B, and C.

#### Observations Reported by Observers

All observers reported that choosing the optimal frame from the cine-loop sequence and making size measurements took much more time than expected and more time than might be available in a typical busy breast imag-

ing practice. Particularly, observers thought that choosing the optimal image was the most time-consuming step. Also, it was a consensus observation that observers A and B had much more time available in a laboratory environment to make measurements than did the other observers, who performed measurements under considerable time constraints during the course of a busy clinical day.

Several important anecdotal observations that were unrelated to lesion size comparison were reported by the observers during the study. The lesion was sometimes much more conspicuous on strain images than on B-mode images, which aided in determining that a lesion was, in fact, real (Fig 3). In many cases, there was little contrast between the breast lesion and surrounding tissue on the strain images, thereby making the lesion inconspicuous. This finding seemed to correlate with benignity (Fig 9). These observations are consistent with those obtained by Garra et al (6). We also observed that repetitive conspicuity of lesions on US strain images throughout the course of the cine-loop sequence was correlated with increased probability of malignancy. Finally, in at least two patients, strain imaging aided in localizing the optimal site of biopsy. For example, in one patient, the initial biopsy passes, which were made by using only the B-mode image as a guide, yielded a suboptimal sample. US strain imaging was subsequently performed on the lesion, and the firmest area of the lesion was identified as superior to the initial biopsy site. Multiple biopsies that were performed through the area that was identified at strain imaging as being the firmest yielded several good core biopsy results that proved to be adequate for histologic diagnosis. These observations suggest that the use of strain imaging with means of interpretation other than the comparison of lesion dimensions may have clinical utility.

**Table 6**

#### Comparison of $A_z$ Values and $P$ Values for Pairs of Observers

Observer	$A_z$ Value*	Observer B	Observer C	Observer D	Observer E	<i>P</i> Value
						Width
A	0.90 (0.04)	.08	.01	<.01	<.001	
B	0.83 (0.03)	...	.39	.24	.08	
C	0.79 (0.04)		...	.58	.32	
D	0.75 (0.05)	...	...	...	.74	
E	0.74 (0.05)	...	...	...	...	
Area						
A	0.92 (0.03)	.01	<.01	.01	<.001	
B	0.82 (0.04)	...	.58	.41	<.01	
C	0.79 (0.04)	...	...	.68	.01	
D	0.77 (0.04)	...	...	...	.07	
E	0.67 (0.05)	...	...	...	...	

Note.—For any given pair, a  $P$  value of less than .05 represents a statistically significant difference in observer performance at the 95% confidence level. The overall  $P$  value for the entire group of observers was less than .001 for both width and area.

\* Numbers in parentheses represent standard errors.

#### Discussion

In our study, low specificity values were obtained when using the lesion size comparison technique along with our

best parameters (ie, width and area) and an optimal ratio threshold to characterize breast lesions. For each observer and for the group as a whole (except for observer E), width and area yielded similar results. A combination of size parameters did not produce better results than either width or area alone. The use of width measurements may be beneficial in a busy breast imaging practice because width is an easier and quicker measurement to obtain than traced area.

One of the main limitations that we found was the statistically significant performance differences between observers. On the basis of  $A_z$  values, differences in performance were most directly related to the amount of time available to make the lesion size measurements (laboratory vs clinical environment) and, to a lesser extent, the amount of prior experience that each observer had with the lesion size comparison technique; differences in performance were not correlated with general clinical breast imaging experience. For example, although no formal time data were collected, all observers agreed that, compared with the other three observers, observers A and B had much more available time in a laboratory setting to make the measurements. This conferred a performance advantage (ie, a larger  $A_z$  value) for observers A and B. This suggests that manually selecting a frame from the cine-loop sequence, tracing the lesion boundaries, and measuring the lesion width and height may require more time than is routinely available in typical clinical practice; this supports the consensus impression that the current technique required too much time. Development of an automated version of the technique that could choose the optimal frame from the cine-loop sequence and make measurements of the lesion border could improve the speed of the technique.

Even though observers D and E have the most clinical breast imaging experience, observers A, B, and C performed better (in some cases significantly better). We believe this is in part because of their prior experience with

and training in the lesion size comparison technique as part of a prior preliminary study. A comparison between  $A_z$  values for the first 50 lesions and those for the second 38 lesions showed that the enhanced performance of observers A, B, and C was not the result of previous experience in specifically measuring the first 50 lesions. Rather, the enhanced performance of observers A, B, and C was a function of increased general experience and practice with the lesion size comparison technique that was derived from the preliminary study. This suggests that even highly experienced mammographers and breast US technologists (eg, observers E and D) who have specific training in the technique will potentially need more extensive training than that which was offered prior to this study, as well as more practice and experience in the current lesion size comparison technique in order to use the technique effectively.

Having proved that significant interobserver variability exists with this technique, an attempt to isolate the main source of this variability was made by comparing the group and observer own image and reference image data. After US data have been acquired, the two potential sources of variability include choosing the optimal frame from the cine-loop sequence and making measurements of the lesion in that chosen frame. If a reduction in the performance range was observed for the reference image data when compared with the wide performance range for the own image data, this would suggest that most of the variation was introduced during the choosing of the optimal frame. Likewise, if no reduction was seen, this would indicate that little or no variation was introduced during the choosing of the frame, and thus, the bulk of variability occurred during measuring. Results showed that there was only a slight decrease in the performance range of reference images (and thus in interobserver variability) compared with the observer performance range of own images (particularly for area) when comparing observer sensitivity and specificity data.

When comparing observer own im-

age  $A_z$  values with reference image  $A_z$  values, a statistically significant reduction in performance occurred for only one of eight comparisons; in three cases, however, the  $P$  values were marginal. This demonstrates that most of the interobserver variability resulted from the measurement of lesion size, although frame selection was still important.

Finally, subjectively, one can see from Figures 2 and 3 that the five different observers sometimes had different interpretations of lesion borders, and thus, different size ratios were obtained. Identifying that the differences in lesion measurement contributed most to observer variability is helpful. It suggests that the most concentrated training for breast imagers who are learning to use the lesion size comparison technique should be on the actual measuring of lesion size on B-mode and strain images. It also suggests that automated border detection and measurement may decrease variability and hopefully lead to higher sensitivity and specificity values.

Several observers reported that some of the lesions were difficult to measure on the B-mode display because of ill-defined borders. This may, in part, be the result of the relatively low-frequency US probe (7.3 MHz) that was used in the study. To determine if B-mode lesion border conspicuity affected the performance of the technique, a subset analysis of only those lesions that had well-defined margins on B-mode images was performed. On the basis of the results of the analysis, which included lower  $A_z$  values for the subset, it appears that the conspicuity of lesions on B-mode images is not a complicating factor when performing these measurements and analysis. This was unexpected because it was believed that lesions with ill-defined borders on B-mode images might have more inaccurate measurements (and thus more inaccurate ratios) than the well-defined lesions owing to the difficulty in perceiving lesion borders. It was postulated that including only those lesions with well-defined borders in the analysis would increase the performance of the

technique. The results, however, are contrary to this postulation.

One potential explanation for this unexpected finding is that most of the ill-defined lesions (20 of the 29 lesions) had malignant histologic characteristics. In looking at these malignant lesions, such lesions tended to be obviously larger on the US strain images than they were on the corresponding B-mode images. Thus, an inaccurate measurement obtained from B-mode images potentially becomes unimportant because the resultant size ratio would still be well above the threshold ratio for determining malignancy, and thus, the technique would still be able to accurately characterize most of these lesions as malignant. Taking these lesions that are accurately characterized by the technique out of the complete data set would actually result in lower  $A_z$  values and no improvement in the sensitivity and specificity values. This analysis may also suggest that the low-frequency US probe that was used in the study probably did not contribute to the low specificity values that were obtained.

In the previous presentation by Hall et al (22), an optimal area ratio threshold of 1.2, a sensitivity of 100%, and a specificity of 75.4% in characterizing breast lesions were obtained in a series of 169 lesions. This threshold is similar to our group area threshold of 1.13, but our group sensitivity was 96% and specificity was only 24%. Also, when the threshold of 1.2 for area ratio was applied to our own image ratio data, our group sensitivities and specificities were 94% and 29%, respectively. Our best performer (observer A) obtained a sensitivity of 96% and a specificity of 61% by using an area ratio threshold of 1.01, which is closer to the sensitivity and specificity values obtained by Hall et al (22).

When using the area threshold of 1.2, however, we found that the sensitivity and specificity for observer A were only 86% and 82%, respectively. This shows that "tuning" a ratio threshold to an individual observer can produce good results but that finding a single generalizable threshold may be diffi-

cult. The differences in our group performance compared with the results of Hall et al are likely related to the fact that, in the study by Hall et al, the results were obtained by a single observer who had both extensive experience with this technique and more time available to make the measurements, which were performed in the laboratory as opposed to a typical busy clinical environment. This conclusion is supported by the fact that the results of observer A, who had prior experience with the technique and who had more available time to make measurements, better approached the results of Hall et al (although not with the same area threshold) than did the results of the group as a whole. Again, this supports the conclusion that more extensive training and experience with the technique are vital to use the lesion size comparison technique in an acceptable way. Most importantly, this suggests that the sensitivity and specificity of the technique are directly related to the time available to perform the measurements and that fitting the technique into a typical busy clinical practice may pose problems.

We identified two main limitations in our study. First, strain images were generated by a single technologist, and thus, variation that was introduced during the acquisition of the strain images was not tested. Second, although all observers agreed that the observers who obtained measurements in the clinical environment had much less time and that the technique took much more time than anticipated, formal time records of how long each observer took to pick the optimal image and to generate the size measurements were not documented. Future studies could address these issues.

In conclusion, US strain imaging has the potential to aid in diagnosis of breast lesions; however, manually traced lesion borders for size ratio differentiation did not result in acceptable performance, though improvements were noted. The main limitations we identified with this technique include low specificity for some observers and marked interobserver variation (mainly in lesion size measurement). The con-

sensus of the participants was that the extensive time required in choosing the optimal frame from the cine-loop sequence and in tracing the lesion boundaries in both B-mode and strain images could make the routine application of this technique in a typical busy clinical breast imaging practice difficult. These findings, however, do not preclude the possibility that alternative approaches to using this general method would be more successful. For example, manual measurements of lesion width alone might be performed in an acceptably short time, and this simpler measurement, coupled with more extensive user training and experience, may result in better observer performance and improved observer agreement. The development of an automated process that could choose the optimal frame from the cine-loop and obtain lesion size measurements might also decrease variability and increase the ease and speed with which the technique can be applied.

## References

1. Anderson WAD. *Pathology*. St Louis, Mo: Mosby, 1953.
2. Lerner RM, Huang SR, Parker KJ. Sonoelasticity images derived from ultrasound signals in mechanically vibrated tissues. *Ultrasound Med Biol* 1990;16:231-239.
3. Ophir J, Cespedes EI, Ponnekanti H, Yazdi Y, Li X. Elastography: a quantitative method for imaging the elasticity of biological tissues. *Ultrason Imaging* 1991;13:111-134.
4. O'Donnell M, Skovoroda A, Shapo B, Emelianov S. Internal displacement and strain imaging using ultrasonic speckle tracking. *IEEE Trans Ultrason Ferroelectr Freq Control* 1994;41:314-325.
5. Skovoroda AR, Emelianov Y, O'Donnell M. Tissue elasticity reconstruction based on ultrasonic displacement and strain images. *IEEE Trans Ultrason Ferroelectr Freq Control* 1995;42:747-765.
6. Garra BS, Cespedes EI, Ophir J, et al. Elastography of breast lesions: initial clinical results. *Radiology* 1997;202:79-86.
7. Ophir J, Kallel F, Varghese T, et al. Elastography: a systems approach. *Int J Imaging Syst Tech* 1997;8:89-103.
8. Chaturvedi P, Insana MF, Hall TJ. 2-D compounding for noise reduction in strain imag-

ing. *IEEE Trans Ultrason Ferroelectr Freq Control* 1998;45:179–191.

9. Fatemi M, Greenleaf JF. Application of radiation force in noncontact measurement of the elastic parameters. *Ultrason Imaging* 1999;21:147–154.
10. Lubinski MA, Emelianov Y, O'Donnell M. Adaptive strain estimation using retrospective processing. *IEEE Trans Ultrason Ferroelectr Freq Control* 1999;46:97–107.
11. Ophir J, Alam S, Garra B, et al. Elastography: ultrasonic estimation and imaging of the elastic properties of tissues. *Proc Inst Mech Eng [H]* 1999;213(3):203–233.
12. Pesavento A, Lorenz A, Ermet H. System for real-time elastography. *Elect Lett* 1999;35: 941–942.
13. Doyley MM, Bamber JC, Fuechsel F, Bush NL. A freehand elastographic imaging approach for clinical breast imaging: system development and performance evaluation. *Ultrasound Med Biol* 2001;27:1347–1357.
14. Hiltawsky KM, Druger M, Starke C, Heuser L, Ermert H, Jensen A. Freehand ultrasound elastography of breast lesions: clinical results. *Ultrasound Med Biol* 2001;27:1461–1469.
15. Nightingale KR, Palmeri ML, Nightingale RW, Trahey GE. On the feasibility of remote palpation using acoustic radiation force. *J Acoust Soc Am* 2001;110:625–634.
16. Varghese T, Zagzebski JA, Lee FT Jr. Elastographic imaging of thermal lesions in the liver *in vivo* following radiofrequency ablation: preliminary results. *Ultrasound Med Biol* 2002;28(11-12):1467–1473.
17. Hall TJ, Zhu Y, Spalding CS. *In vivo* real-time freehand palpation imaging. *Ultrasound Med Biol* 2003;29:427–435.
18. Hangiandreou NJ, Meixner DM, Hesley GK, et al. Ultrasound strain image data obtained in breast masses: preliminary quantitative analysis [abstr]. *Ultrasound Med Biol* 2003; 29:S178.
19. Regner DM, Hesley GK, Hangiandreou NJ, et al. Initial clinical experience with ultrasound strain imaging for the evaluation of breast masses [abstr]. *Radiology* 2003; 229(P):213.
20. DeLong ER, DeLong DM, Clarke-Pearson DL. Comparing the areas under two or more correlated receiver operating characteristic curves: a nonparametric approach. *Biometrics* 1988;44:837–845.
21. Hosmer DW, Lemeshow S. *Applied logistic regression*. New York, NY: Wiley, 2000.
22. Hall TJ, Svensson W, Von Behren P, et al. Lesion size ratio for differentiating breast masses. *IEEE International Ultrasonics Symposium Book of Abstracts*, 2003; 87–88.

# A Novel Performance Descriptor for Ultrasonic Strain Imaging:

## A Preliminary Study

Jingfeng Jiang, Timothy J. Hall and Amy M. Sommer

Department of Medical Physics, University of Wisconsin-Madison  
1300 University Avenue, 1530 MSC,  
Madison, WI 53706, USA

**ABSTRACT:** Ultrasonic strain imaging that utilizes signals from conventional diagnostic ultrasound systems is capable of showing the contrast of tissue elasticity, which provides new diagnostically valuable information. To assess and improve the diagnostic performance of ultrasonic strain imaging, it is essential to have a quantitative measure of image quality. Moreover, it is useful if the image quality measure is simple to interpret and can be used for visual feedback while scanning and as a training tool for operator performance evaluation.

This report describes the development of a novel quantitative method for systematic performance assessment that is based on the combination of measures of the accuracy of motion tracking and consistency among consecutive strain fields. The accuracy of motion tracking assesses the reliability of strain images. The consistency among consecutive strain images assesses the signal quality in strain images. The clinical implications of the proposed method to differentiate ‘good’ or ‘poor’ strain images are discussed. Results of experiments with tissue-mimicking phantoms and *in vivo* breast-tissue data demonstrate that the performance measure is a useful method for automatically rating elasticity image quality.

*Index Terms* — Ultrasonic strain imaging, performance assessment, correlation, elasticity imaging, E-mode imaging, elastography

## I. Introduction

The onset of many cancers is accompanied by changes in tissue macrostructure and microstructure that often result in increased tissue stiffness. Unfortunately, many cancers, despite large differences in stiffness, may or may not differ in x-ray attenuation or acoustic properties compared to their surroundings. As a result, many carcinomas are difficult to visualize with standard imaging techniques. For example, approximately 15% of palpable breast cancers are not detectable with mammography, and this number is likely higher in younger women [1]. Ultrasonic strain imaging (E-mode imaging, elasticity imaging, elastography, etc.) is a technique that emulates manual palpation where tissue is pressed to feel the differences in hardness. Ultrasonic strain imaging has spanned a broad range of applications, including breast tumor detection and differentiation [2, 3], characterization of vascular plaques [4], and assessment of fetal lung maturity [5]. These recent advances suggest that strain imaging provides diagnostically-valuable information that is not otherwise available in standard imaging modalities.

Ultrasonic strain imaging utilizes conventional signals (either radiofrequency or quadrature echo data) from clinical ultrasound scanners acquired before and after deformation is applied and derives ‘relative hardness’ information — local strains from a displacement function that is estimated by comparing the pre- and post-compression echo fields. General steps in ultrasonic strain image formation include deforming the imaged tissue using an external or internal stimulus, measuring tissue response under deformation, and estimating strain from relative tissue motion. Both the complexity and sophistication of ultrasonic strain imaging systems have increased dramatically over the past fifteen years, as summarized in several survey papers [6-10]. Alongside this development there has been a progression in the understanding of strain image quality facilitating the development of predictive theories for the design and enhancement of ultrasonic strain imaging systems. In early work [11-18], attention was focused on estimating lower bounds for displacement estimate error variance, because measuring tissue deformation plays a critical role in strain imaging. A number of authors [11-14] have studied the displacement estimate error variance, usually in a simplified form using the formalism and analysis of time delay estimation (TDE). The general strategy of these approaches

has been to seek a closed-form analytical expression, parameterized in terms of ultrasound system configuration (i.e. bandwidth, center frequency, etc.) and time delay estimation parameters (i.e. window length and window separation). For instance, Carter *et al.* [11] were among the first to establish the relationship between the Cramer-Rao lower bound (CRLB) for TDE variance and signal magnitude-squared coherence (MSC)  $C_{ab}(f)$  between signals  $\mathbf{a}(x)$  and  $\mathbf{b}(x)$ . They demonstrated that the Cramer-Rao lower bound  $\mathbf{s}_{CRLB}$  is a function of  $C_{ab}(f)$  as well as the estimation window length  $T$  in TDE [11],

$$\mathbf{s}_{CRLB}^2 = \left| T \int_{-w}^{\infty} (2\mathbf{p}f^2) \frac{C_{ab}(f)}{1 - C_{ab}(f)} df \right|^{-1} \quad (1)$$

$$C_{ab}(f) = \left| \frac{S_{ab}(f)}{\sqrt{S_{aa}(f)S_{bb}(f)}} \right|^2 \quad (2)$$

where  $S_{ab}(f)$  is the cross-power spectral density,  $S_{aa}(f)$  and  $S_{bb}(f)$  are the respective auto-power spectral densities, and  $f$  is the frequency.

The predicted “jitter error” is the minimum error achievable by any unbiased time delay estimation algorithm including, but not limited to, correlation-based algorithms. Walker and Trahey [12] extended Carter’s theory to include partially de-correlated signals. However, the CRLB is only applicable when the sonographic signal-to-noise ratio (i.e. the SNR in radiofrequency signals) is high (e.g.  $> 30$  dB); otherwise, the Barankin bound or the Ziv-Zakai bound are more appropriate [13, 14].

In ultrasonic strain imaging, axial strain  $\hat{s}$  is often estimated from the difference between two displacement estimates  $\hat{D}_1$  and  $\hat{D}_2$  that are measured by a window length  $Z$  and axially separated by a distance of  $\Delta Z$  as follows [15],

$$\hat{s} = \frac{(\hat{D}_2 - \hat{D}_1)}{\Delta Z} \quad (3)$$

The covariance  $Cov(\hat{D}_1, \hat{D}_2)$  for one-dimensional (1-D) motion tracking can be conservatively approximated by the error variance in displacement estimates  $\mathbf{s}_d^2$  as follows [15],

$$Cov(\hat{D}_1, \hat{D}_2) \leq \mathbf{s}_d^2 \left( 1 - \frac{\Delta Z}{Z} \right) \quad (4)$$

From this result the lower bound on error variance in estimated axial strain can be obtained by assuming  $\mathbf{s}_{\hat{D}_1}^2 \approx \mathbf{s}_{\hat{D}_2}^2 = \mathbf{s}_d^2$  for stationary echo signals [15],

$$\mathbf{s}_s^2 = \frac{\mathbf{s}_{\hat{D}_1}^2 + \mathbf{s}_{\hat{D}_2}^2 - Cov(\hat{D}_1 - \hat{D}_2)}{\Delta Z^2} \geq \frac{2\mathbf{s}_d^2}{Z\Delta Z} \quad (5)$$

Equation (5) demonstrates that the minimum error achievable in axial strain estimates is predictable, once the strain processing parameters, i.e. window length  $Z$  and window separation distance  $\Delta Z$ , are known. Bilgen and Insana [16], among others, have shown that the error variance of axial strain estimates for small strains (e.g. <0.1%) increases monotonically with axial strain. However, it is well recognized that such small axial strains result in low contrast strain images [8]. It is also well understood that severe signal decorrelation occurs with large deformation (e.g. strain > 10%) resulting in ‘poor’ quality strain images [16-18]. There is an intermediate range of deformations from which reasonably high quality strain images can be obtained. The error variance bound alone is insufficient for selecting an ‘optimal’ strain range and that is why the signal-to-noise ratio (SNR), a relative measure, is of greater interest as a general performance measure.

Varghese and Ophir [17] made use of these error variance bounds to estimate elastographic signal-to-noise ratio ( $SNR_e$ ). They defined the elastographic  $SNR_e$  as the ratio of the mean value of the estimated strain  $m$  and the standard deviation of the estimated strain errors  $\mathbf{s}_s$  as follows,

$$SNR_e = \frac{m}{s_s} \quad (6)$$

The behavior of  $SNR_e$  as a function of axial strain is similar to a band-pass filter, therefore the analysis result was called a ‘strain filter’. Potential performance assessed by the strain filter approach offers insight for designing strain-imaging systems, though the strain filter approach may only be applicable to homogeneous regions of tissue being imaged [17]. For example, the effects of modifying several system parameters, such as the center frequency, bandwidth and tissue deformation, on the performance of a strain imaging system can be predicted by the strain filter. In general, high center frequency, broad echo signal bandwidth and moderately small ( $\sim 1\%$ ) strain are preferred for strain imaging. Similar conclusions were drawn by others using a different approach [16, 18-22].

Unfortunately, error variance analysis based on the strain filter approach is inadequate for several reasons. First, to achieve a closed form solution, the variance bounds are often derived with simplifying assumptions which limit applicability. For example, error variance bounds for strain imaging were derived for one-dimensional time delay estimation problems. However, ultrasonic speckle tracking algorithms can be multi-dimensional [23-25] or non-correlation-based [26, 27]. In addition, the effects of smoothness constraints, i.e. motion regularization [26, 28], in displacement estimation are difficult to model statistically. Secondly, variance bounds assume large displacement errors can be detected and corrected so the residual errors in motion tracking are sub-sample ‘jitter errors’. This is a good assumption for some experiments, such as radiation force experiments [29-31], where deformations are small compared to acoustic wavelength. But experiments where axial strain is typically 1—2% commonly involve displacements of more than one wavelength. In addition, displacement estimate error variance bounds obtained with homogeneous and isotropic phantoms provide overly optimistic results for *in vivo* biological tissues because motion in biological tissues is far more complex than that in typical phantoms. Thirdly, error variance bounds are used to place a limit on the expected result in any single observation by an unbiased time delay estimation algorithm. However, in medical image formation, where accuracy in a single

observation is important, variance bounds (descriptions of anticipated image noise) are insufficient to describe the performance for a specific deformation field. In other words, it is also important to have a method that can assess accuracy in each case individually.

Recall that, in ultrasonic strain imaging, the goal of speckle tracking between two radiofrequency (RF) echo fields  $r_A$  and  $r_B$  is to obtain a transformation  $T$  that maximizes the similarity between  $r_A$  and  $T(r_B)$ . Thus, strain image quality can be judged, in part, by assessing the motion tracking accuracy directly, as opposed to statistically. An example of this approach is the ‘trashogram’ [32] which displays the local normalized correlation coefficients between the pre- and post-deformation RF echo fields as a grayscale image. Although this method is attractive due to its simplicity, it can be misleading when displacement errors of an integer wavelength occur. A more comprehensive framework is based on signal coherence between the pre- and motion-compensated post-deformation RF echo signals [33-35]. By comparing the cross-power spectrum between the pre- and motion-compensated post-deformation RF echo signals, Insana, et al., [33, 34] derived the Fourier cross-talk matrix to assess ultrasonic strain imaging systems. Basically, motion tracking can be evaluated in terms of spatial sampling characteristics. The Fourier cross-talk matrix, to some extent, can be regarded as a graphical representation of signal coherence. The diagonal elements of the cross-talk matrix represent the generalized transfer function, describing the strength of every Fourier coefficient representing the signals. The off-diagonal components of the cross-talk matrix represent the degree of aliasing between any two Fourier coefficients. If the pre- and motion-compensated post-deformation RF fields are aligned perfectly, no off-diagonal elements will be observed. When motion tracking errors result in signal misalignment, off-diagonal elements in the cross-talk matrix increase. Although the graphical representation of signal coherence makes this method appealing, this approach is most useful in strain imaging system design and is more difficult to use as a performance tool for strain imaging of biological tissues. The trace of the cross-talk matrix was offered as a summary performance measure, but it is an unbounded quantity that would be difficult to interpret in a clinical setting.

We propose a different approach to the performance assessment problem, one that is heuristic in nature. The two components of our strain imaging performance measure are

an assessment of motion tracking accuracy and consistency among consecutive strain fields. The motion tracking accuracy, measured by the normalized correlation coefficient between reference and motion-compensated target RF echo fields, describes the fidelity of displacement estimates from which the strain images are obtained. The consistency among consecutive strain images, measured by the normalized correlation coefficient between consecutive motion-compensated strain images, relates directly to the signal-to-noise ratio in strain images. In the proposed method, both parameters were estimated by a single scalar metric, the normalized correlation coefficient, and an empirical equation was then used to obtain a single summary measure of the overall quality for strain images. Compared to methods available in the literature, the proposed method has several advantages: (1) no assumptions are needed regarding the signals, underlying motion, or motion tracking algorithms; (2) performance of strain imaging can be assessed for individual cases accurately; (3) the final performance descriptor, a scalar value between zero and one, is quantitative and easy to interpret.

The remainder of this paper is organized as follows. The next section describes performance assessment criteria for ultrasonic strain imaging, as well as implementation details of the proposed algorithm. We then present results of tests of the proposed method with a tissue-mimicking (TM) phantom and *in vivo* breast tissue data including comparisons with ranking of images by human observers, followed by a discussion section and conclusions.

## II. Methods and Materials

It is well accepted that local strains correlate strongly with tissue modulus distribution under certain boundary conditions (e.g. uniaxial compression) [36, 37]. When full knowledge of the ground truth (the modulus distribution and boundary conditions) is available (i.e., a numerically-simulated or tissue-mimicking phantom), a comparison of an estimated strain field to the ideal strain field provides an ideal basis for error analysis. In fact, a number of authors [38] [39] have used this approach to validate new algorithms. Unfortunately, “true” modulus maps are unavailable *a priori* for *in vivo* biological tissues, noting that acoustic scattering and tissue elasticity are uncorrelated [40]. There is a need

for a method that would allow the evaluation of strain image quality when the ground truth is not available.

Two important aspects of ultrasonic strain imaging, namely motion tracking accuracy and consistency among consecutive strain images, were used in several papers [2,32] as measures of strain image quality. Hall *et al.* [2] argued that examining tissue motion through a relatively long ( $>10$  frames) sequence of B-mode images, together with consistency among successive strain images would provide some assessment of confidence in strain image accuracy. Kaluzynski *et al.* [32] used the radiofrequency (RF) signal correlation value of 0.985 as a measure for strain rate imaging and stated that reliable motion tracking would not be guaranteed if the correlation value fell below 0.985. The work presented below combines motion tracking accuracy and the consistency among consecutive strain images to create a performance assessment method that automatically quantifies strain image quality on a normalized scale.

The normalized cross-correlation (NCC) between the two fields is a common measure of their similarity. Since frame-average tissue deformations of 1% strain are easily achieved *in vivo*, and local deformations can approach 5% strain, comparisons are made between a reference field,  $\mathbf{a}_{ij}$ , and the motion-compensated target field,  $T(\mathbf{b}_{ij})$ . Thus, the NCC,  $\mathbf{r}_{ab}$ , can be written as follows [41],

$$\mathbf{r}_{ab} = \frac{\sum_{i=1}^N \sum_{j=1}^M (\mathbf{a}_{ij})(T(\mathbf{b}_{ij}))}{\sqrt{\sum_{i=1}^N \sum_{j=1}^M (\mathbf{a}_{ij})^2} \sqrt{\sum_{i=1}^N \sum_{j=1}^M (T(\mathbf{b}_{ij}))^2}} \quad (7)$$

where N and M are the width and height of the frames of data, respectively.

### A. Motion tracking accuracy

As stated above, a goal of ultrasonic strain imaging is to obtain a transformation T that maximizes the similarity between two radio-frequency (RF) echo fields  $rf_{n-1}$  and  $T(rf_n)$ . Local displacement and strain are estimated from this transformation. Once the local

displacements are known, the target field can be re-sampled, e.g., using a cubic spline interpolation algorithm, to obtain its corresponding motion-compensated target field. Thus, the accuracy of motion tracking can be quantified by the normalized cross correlation,  $\mathbf{r}_{rf}$ , between the reference RF echo field  $rf_{n-1}$  and the motion-compensated target RF echo field,  $T(rf_n)$ .

### *B. Consistency among strain images*

Similarly, the consistency among strain images can be defined by the normalized cross correlation,  $\mathbf{r}_s$ , between the previous strain field  $s_{n-1}$  in a sequence of consecutive fields and the current strain field in the sequence  $s_n$  mapped into the spatial coordinate system of strain field  $s_{n-1}$ .

For small deformations, the strain information in successive images have approximately the same underlying signal (i.e., the tissue modulus distribution), but the signals are corrupted by noise. Belaid *et al.* [42] have shown through simulations that noise in strain fields estimated from radiofrequency (RF) echo signals is Gaussian distributed. Given the assumption that noise in strain images is uncorrelated with its underlying signal, a high correlation between two consecutive, motion-compensated strain images means relatively low noise in both strain images and thereby suggests better strain image quality.

### *C. Empirical Equation*

Correlation among motion-compensated RF echo fields and strain images are both important measures of strain imaging system performance. Combining them to provide a single summary performance measure for the overall quality of ultrasonic strain imaging is a logical approach, and a simple empirical equation for this combination is

$$p = \mathbf{r}_{rf} \mathbf{r}_s \quad (8)$$

where  $p$  is the overall performance. It is worth noting that the summary performance measure  $p$  ranges from zero to one.

#### *D. Implementation*

We implemented the proposed summary performance measure in our existing strain image formation software in MATLAB<sup>®</sup> (Mathworks Inc., Natick, MA), as schematically illustrated in Fig. 1. The proposed method consists of following major steps:

1. Obtain a pair of RF frames (e.g, the (i-1)th and (i)th frame in Fig. 1 where the (i)th frame is the reference frame) and track motion. The displacement field contains both lateral and axial displacement components from the (i)th frame to the (i-1)th frame. Form a strain image in the coordinate system of (i)th RF echo frame (e.g.  $S_i$  in Fig. 1).
2. Use the displacement field obtained in Step 1 to warp the (i)th RF echo frame into the (i-1)th coordinate system and calculate the normalized cross correlation between the (i-1) and motion-compensated (i)th RF echo field to assess the motion tracking accuracy. Note that warping is a process of compensating the motion between the (i)th and the (i-1)th strain frames, as described in Section II-A.
3. Warp the (i)th strain image into the (i-1)th coordinate system and calculate the normalized cross correlation between the (i-1)th and motion-compensated (i)th strain images to estimate the consistency between consecutive strain images. Note that the (i-1)th strain image is formed at the physical grid of the (i-1)th RF echo field.
4. Calculate the summary performance measure (Eqn. 8) and assign this value to the (i)th strain image.
5. Repeat Step 1—4 for each pair of RF echo frames in a sequence.

#### *E. Remarks*

The proposed method performs best in a sequence of strain images where the estimated performance values are slowly varying. The success of ultrasonic strain imaging relies on

the ability to control tissue motion during deformation. For instance, the ideal motion for breast scanning is a nearly uniaxial compression, with minimal out-of-plane motion [2]. To maintain consistency between two successive strain images, the boundary conditions and modulus distribution that is being imaged have to be nearly unaltered during data acquisition. Real-time elasticity imaging systems [2, 25] that provide elasticity images with a frame rate high enough to control the boundary conditions of freehand deformation result in consistently high quality elasticity images. To a first approximation, the elastic moduli of biological tissue are constant for small deformations [43]. Also, with a sufficiently high frame rate between the RF echo frames paired to form strain images, the viscosity of biological tissue may be ignored [44].

There are at least two reasonable approaches to estimating consistency among strain images that relate to the selection of a reference strain image. One may choose the ‘best’ quality strain image among the sequence as the standard for comparison (the ‘reference strain image’ approach). A second approach is to use the adjacent strain image as the standard for comparison. There are several motivations for using the ‘adjacent strain image’ approach over the ‘reference strain image’ approach. First, the selection of the ‘best strain image’ is likely subjective and not fully automated. The ‘adjacent strain image’ approach provides full automation, thereby suggesting an objective assessment. Second, the assumptions that the modulus distribution and boundary conditions are unaltered may be problematic if a single reference strain image in a long sequence of data (typically greater than 60 radiofrequency echo frames) is used. It is easy to argue that these assumptions are valid for adjacent strain images where small deformation increments (1% strain) under similar boundary conditions are applied to the object being imaged.

One drawback of using the ‘adjacent strain image’ approach is that comparison of a high-quality strain image with a low-quality strain image will result in degraded cross correlation. It is possible to re-assign a higher consistency value to the (i)th strain image when it correlates poorly to a low-quality (i-1)th frame, but correlates well with the (i+1)th strain image. The scheme does not work when a reasonably high quality strain image is interleaved between two low quality strain images. Although the ‘reference strain image’ approach might work well in that case, the subjectivity in reference frame

selection, the loss of automation, and the potential for violating the assumption regarding unaltered boundary conditions make that approach significantly less attractive.

### III. Algorithm Evaluation

The proposed method for quantifying strain image quality was tested with RF echo data acquired from a tissue-mimicking (TM) phantom and *in vivo* breast tissue. The first test of the proposed method used a TM phantom with a known elasticity distribution and its corresponding strain image under well controlled imaging conditions. The second test evaluated algorithm performance using *in vivo* breast tissue data acquired with freehand scanning. Image ratings obtained from three human observers were compared with measured performance values to determine whether results from the proposed method match well with human perception.

A real-time strain imaging system [2, 25] based on the Siemens SONOLINE Elegra (Siemens Medical Solutions, Mountain View, CA) with a 7.5 MHz linear array (7.5L40) transmitting 7.2 MHz broadband pulses was used to guide I-Q data acquisition. The strain images used in this study were processed off-line by first converting the I-Q data to RF and then forming strain images using a more numerically demanding algorithm [45] than the real-time algorithm on the Elegra [25]. This motion tracking algorithm is a modified block matching algorithm and consists of the two-dimensional search for equivalent patterns between pre- and post-deformation radiofrequency echo fields delimited by a small two-dimensional kernel. The sum-squared-difference (SSD) is employed to estimate displacement fields. A small two-dimensional non-overlapping kernel  $0.96 \times 0.40$  mm (length by width) was used to track tissue motion. Displacement estimates in a small one-dimensional window were then fitted into a line locally and the slope of this line was assigned to the center of this window as the estimated local strain value. In this study, a relatively large window (2.4 mm) was used to obtain axial strains that were displayed as grayscale images. No additional filtering was applied in this study. The performance assessment algorithm has been integrated into our off-line strain imaging processing program to obtain performance values for all examples shown here.

### *A. Tissue-Mimicking Phantom Experiment*

The tissue-mimicking phantom, shown in Fig. 2, has a uniform background and two spherical inclusions, whose diameters are 2.4mm and 3mm, have similar acoustic properties but are three times stiffer than the background. The inclusions are barely visible in B-mode images. The phantom (Fig. 2) was manufactured as described in [40]. Thirty-one I-Q echo frames of data were recorded while freehand scanning the phantom with the Elegra. The physical size of B-mode images is roughly  $38\text{ mm} \times 40\text{ mm}$  (W x L) and a single transmit focal zone was centered at the depth of 20mm. Note that the reference radiofrequency echo frame was paired with frames with different time delays to obtain the six frame-average strains shown in Fig. 2.

### *B. In vivo Breast Tissue Experiment*

Human subjects who, with informed consent, agreed to participate in elasticity imaging research were scanned at Charing Cross Hospital, (London, UK) and Mayo Clinic (Rochester, MN, United States) using identical Siemens SONOLINE Elegra systems equipped with real-time elasticity imaging software [2], including the linear array ultrasound transducer. Sixty-five frames of RF echo data were acquired from a fibroadenoma and 99 frames of RF echo data were acquired from an invasive ductal carcinoma.

### *C. Human Observer Study*

Three ultrasound physicists who are actively involved in elasticity imaging research participated in this human observer study. The observers learned to rate strain images in an initial training session with 100 strain images (ten consecutive strain images from ten different data sets) that included both benign and malignant solid tumors (five fibroadenoma (FA) and five invasive ductal carcinoma (IDC)). Observers were instructed to rate the quality of strain images using the scale and criteria shown in Table I. During the training session the computer ratings for each of the 100 images were provided as feedback to enable all observers to consistently rate strain image quality.

During the human observer study, 20 different data sets (nine FA, eight IDC, one invasive lobular cancer, one unknown cancer and one fat necrosis) of *in vivo* breast tissue data were used and each set consists of at least 60 consecutive strain images. Observers first viewed the complete sequence of side-by-side B-mode and strain images in each data set and then rated the quality of the pre-determined subset of ten strain images for that data set. Computer ratings of these two hundred strain images were unknown to the observers. By first viewing the complete data set observers learned the typical appearance of the specific lesion in that data set. Scoring ten successive strain frames reduced the number of strain images that must be rated by observers in order to achieve a statistically significant result.

Specific instructions were given to observers on how to determine image quality. The approximate location and contour of the lesion in the sequence of B-mode images was used to set expectations of lesion size and location in strain images. Lesion location in strain images must correspond to that in B-mode, but size and contrast in the two image types can differ significantly. No attempt to compare lesion morphology was suggested to the observers. The observers may try to identify the ‘best’ strain image in a particular sequence, together with adjacent strain images, as the reference image to assess image quality. Note that the reference strain image is not necessary within the span of ten pre-determined strain images. The observers may take complexity of tissue motion into consideration. That is, tissue motion may be visually tracked in a sequence of B-mode images to determine the degree to which RF echo data decorrelates to subjectively assess the complexity in motion tracking. The image formation algorithm and display grayscale mapping was consistent among all data. Also, no ground truth regarding the ‘correct’ strain image is available. Therefore, an apparent lack of detail in an image (e.g., image smoothness or lesion contrast) should not bias the observer toward ‘good’ or ‘bad’ image quality.

The observers were also asked to follow the same procedures and score a continuous sequence of forty strain images acquired from a patient with a fibroadenoma. Note that results of this data set are presented in Figs. 9 and 10, whereas the results from the first 200 strain images are separately presented in Fig. 8. It is also worth noting that all *in vivo*

data presented in this subsection was acquired using the real-time elasticity imaging system described above.

A viewing software program providing strain images displayed side-by-side with their corresponding B-mode images was employed for this study. Observers could view image sequences at eight frames per second, or slower, or could step through images frame by frame. Image rating was performed only when stepping through the sequence frame by frame. All images were displayed on typical flat panel monitors (NEC MultiSync LCD 1860NX) and viewing time was not limited. Note that monitors were set to the same configurations.

#### IV. Results

Representative strain images obtained from the tissue-mimicking phantom experiment are displayed in Figs. 2(a)–(f). The frame-average axial strain varies from 0.3% — 4.5%. In each plot, the size of the echo field was 38mm × 40mm (width × depth). Note that low-frequency banding is apparent in low-strain images (e.g. < 1.0%). This banding is due, in part, to a biased interpolation algorithm used for obtaining sub-sample displacement estimates [46]. One measure of image content is the contrast-to-noise ratio (CNR) defined [47] as

$$CNR = \frac{2(s_t - s_b)^2}{(s_t^2 + s_b^2)} \quad (9)$$

where  $s$  and  $s^2$  denote signals and variances of signals, and subscripts  $b$  and  $t$  represent the background and target, respectively. The estimated CNR for the two spherical targets ( $CNR_{2.4}$  for the 2.4mm sphere;  $CNR_3$  for the 3mm sphere) in strain images together with their estimated performance values (Eqn. 8) are shown in Table 2. The estimated CNR correlates with the performance values obtained by the proposed method.

The NCC among motion-compensated RF echo fields,  $\mathbf{r}_{rf}$ , decreases monotonically with the increasing axial deformation, as shown in Fig. 3(a). Note that, given a long sequence of RF data, different frame-average axial strains can be achieved by pairing the

pre- and post-deformation RF echo frames separated by different time intervals. It is significant to note that the estimated  $\mathbf{r}_{rf}$  will change somewhat if different regions of interest are used. The consistency of estimated strain images,  $\mathbf{r}_s$ , versus axial compressions is displayed in Fig. 3(b). The horizontal banding artifact shown in Fig. 2 is mitigated as the axial deformation increases resulting in strain images with less noise and greater consistency from frame to frame. Thus, the estimated consistency among strain images correlates with the CNR of strain images. The estimated summary performance measure as a function of frame-average strain is shown in Fig. 3(c). The estimated performance is consistent with findings reported by Chaturvedi et al. [23] which showed that strain image quality (the contrast-to-noise ratio) increases with frame-average strain up to about 5% for a tissue-mimicking phantom. The error bars in these plots denote one standard error and were obtained from more than 20 pairs of RF and strain fields.

Representative strain images obtained from *in vivo* breast tissue with different axial deformations are shown in Figs. 4(a)–(d). The frame-average axial strain in these images varies from 0.4% — 3.0%. The strain image contrast increases with deformation and the maximum contrast-to-noise ratio is obtained when the frame-average axial strain reaches about 2%. Summary performance values correlate with strain image CNR as shown in Table 3, and thereby suggest that the estimated performance values are reasonable measures of strain image quality, similar to the results obtained from the TM phantom experiment.

The correlation among motion-compensated RF echo fields,  $\mathbf{r}_{rf}$ , is plotted with respect to different axial deformation in Fig. 5(a) for the same *in vivo* breast tissue data set represented in Fig. 4. Different frame-average axial strains were again achieved by pairing the pre- and post-deformation RF echo frames separated by different time intervals. The error bars in Fig. 5 also denote one standard error and were obtained from more than 30 independent pairs of RF and strain fields. The correlation among motion-compensated RF echo fields decreases much faster with increased axial deformation compared to that found in the tissue mimicking phantom results. This result implies that complex tissue motion is challenging to track with a simple block matching algorithm, whereas motion in the TM phantom is relatively uniform and easy to track even under

large deformation. The normalized correlation coefficient among consecutive motion-compensated strain images versus frame-average axial strain is plotted in Fig. 5(b). The peak correlation coefficient occurs near 1.2% axial strain. The maximum correlation and the strain at which it is found are much lower than that of the TM phantom experiment. In addition, the correlation falls rapidly beyond the peak value. The estimated performance, shown in Fig. 5(c), is low for small axial deformation and reaches its peak when the frame-average strain is about 0.8% to 1.2%.

During freehand scanning, a sinusoidal compress/release cyclic deformation was used and the acquired data typically contained one or more cycles. More details regarding data acquisition can be found in [2]. Unfortunately, freehand scanning sometimes results in non-uniform frame-average strains, as illustrated in Fig. 6(a). Adaptively selecting the RF frame pairs in post-processing [45, 48] to obtain nominally 1 — 1.5% absolute frame-average strain significantly improves the quality of a sequence of strain images, as demonstrated in Fig. 6(b).

Fig. 7(a) is a typical “good” quality strain image of an invasive ductal carcinoma. The normalized cross correlation values for estimating motion tracking accuracy ( $r_{rf}$ ) and strain image consistency ( $r_s$ ) were 0.83 and 0.89, respectively. Thus, this strain image was obtained from reasonably accurate displacement estimation and correlated well with its adjacent strain images. An atypical strain image obtained from this data set is shown in Fig. 7(b). The estimated consistency ( $r_s$ ) was 0.81 and therefore it was fairly consistent with its adjacent strain images. But the estimated motion tracking accuracy  $r_{rf}$  was 0.47 for this particular strain image. The sequence of B-mode images showed high decorrelation for relatively small axial strain suggesting extensive elevation (out of acoustic imaging plane) motion.

Figure 8 shows a plot of the strain image quality rated by human observers (1—10 scale) and the summary performance measure (0—1 scale). Results in Fig. 8 show that the rating by observers was generally well described as a linear function of the summary performance measure ( $r = 0.87$ ). The quality rating by human observers has higher correlation to those by the summary performance measure when the strain image quality is reasonably high. By filtering the data in Fig. 8 to include only those strain images with

a summary performance measure in excess of 0.6 the correlation between human rating and summary performance measure increased to 0.99.

The comparison of average scores of the observers and the summary performance measure based on a sequence of containing 40 consecutive strain images of a fibroadenoma is shown in Fig. 9(a). The frame-average strains are plotted with respect to the frame numbers in Fig. 9(b). All 40 frames of strain data can be seen in Movie 1 (see Fig. 10) provided with this manuscript. Note that computer ratings were rescaled from 1—10 for comparison with human rating (Table 1). Results in Fig. 9(a) suggest that human rating of strain images was well described by the computed performance values through most of the sequence. However, beyond the 26<sup>th</sup> frame there are discrepancies between the human observers and the computed performance measure. Observations from the 27<sup>th</sup> and 28<sup>th</sup> frames of strain data (see Movie 1 in Fig. 10) show that these two strain images were significantly different compared to typical ‘good’ strain images in this sequence, therefore human observers rated these frames low. Adjacent strain image frames were sufficiently similar for the algorithm to rate them reasonably high. In the last ten frames (31—40) of strain data in Movie 1 (see Fig. 10), there was extensive lateral motion, as observed in the B-mode image sequence. Correspondingly, there are signs of motion tracking failure in the strain image sequence and the estimated values of the motion tracking accuracy are relatively low (see Fig. 9(a)). These ten strain images are still fairly consistent with typical ‘good’ strain images in this sequence. It appears that the observers weighted ratings toward consistency of strain images in this particular case (the solid line marked with triangles in Fig. 9(a)). For these few images the observers’ rating scores match better with the measure of consistency among successive strain images than with the overall performance assessment. It is worth noting that there are large discrepancies between the estimated values of motion tracking accuracy (*i.e.*  $r_{rf}$ ) and the human ranked values, particularly from the 20<sup>th</sup> frame to 30<sup>th</sup> frame as shown in Fig. 9(a). As illustrated by Fig. 9(b), the frame-average strains are low (within  $\pm 0.5\%$ ) from the 20<sup>th</sup> frame to the 30<sup>th</sup> frame demonstrating that the motion tracking accuracy is biased toward small deformations.

## V. Discussion

In this study, motion tracking accuracy and similarity of consecutive strain images were shown to contribute to the overall quality of strain images. The implication of Eqn. (8) is that we favor strain images that are consistent with their adjacent peers and also are computed from reliable motion estimates. In addition, the particular combination clearly reflects the following facts. Correlation among consecutive RF echo fields,  $\mathbf{r}_{rf}$ , favors small deformations ( $\text{abs}(\text{strain}) < 0.5\%$ ), as illustrated in Figs. 3(a) and 5(a). At the same time, small deformation often results in noisy strain images (see Figs. 2(a) and 4(a)) for which the correlation between consecutive strain images,  $\mathbf{r}_s$ , is penalized. As a result, the product of  $\mathbf{r}_{rf}$  and  $\mathbf{r}_s$  is low at small deformation. However, under large deformation ( $\text{abs}(\text{strain}) > 10\%$ ), the performance value is also low. Large deformation produces large echo signal decorrelation resulting in low  $\mathbf{r}_{rf}$  and  $\mathbf{r}_s$ . Therefore, there is an intermediate range of deformation for which both  $\mathbf{r}_{rf}$  and  $\mathbf{r}_s$  are reasonably high and good quality strain images can be obtained.

It is interesting to note that pairs of consecutive strain images that are reasonably consistent were found even when echo signals were severely decorrelated suggesting that strain image consistency as a single criterion can be misleading as a measure of image content and quality. Data presented in Fig. 7(b) is an example. On the other hand, using motion tracking accuracy alone to indicate strain image quality could be misleading too. Figs. 3(a) and 5(a) demonstrate that the normalized cross-correlation between a pair of motion-compensated RF echo data is highest for small deformation, but this measure alone is also insufficient to describe the quality of strain images (see Figs. 2(a) and 4(a)). The results presented in Fig. 8 also clearly show that there are large discrepancies between the estimated motion tracking accuracy  $\mathbf{r}_{rf}$  and the visual perception of human observers (see Movie 3 in Fig. 10). In summary, the combination of motion tracking accuracy and consistency between consecutive strain images provides a practical solution to objectively rating strain images, though this combination (*i.e.* Eqn. (8)) is established intuitively, and this approach cannot quantify the true task-dependent psychophysical strain image quality. In other words, this study showed that the combination of motion tracking accuracy and consistency between consecutive strain images is adequate to

assess strain image quality in the absence of ‘ground truth’ by applying the proposed method to *in vivo* tissue data where tissue motion is complex.

Considerably higher summary performance measures were obtained in TM phantom experiments compared to *in vivo* breast tissues. In addition, summary performance measures remained high at large axial strain (e.g. 4.0%) for the TM phantom experiment but decreased significantly beyond about 1.5% frame-average strain for *in vivo* breast tissues. These results suggest that studies involving simulations and phantoms might be overly optimistic for predicting the overall performance of an elasticity imaging system and might be misleading regarding the desirable strain range for image formation. Our algorithm [25] is a modified version of classic block-matching algorithm that assumes rigid body motion. The algorithm does not accurately track large deformation (>10% strain), small scale tissue rotation or shear. Complex tissue motion (e.g. shearing and slipping boundaries in tissue) can cause difficulty in obtaining consistent tissue elasticity images and more robust motion tracking algorithms (e.g. [26, 27, 49]) may be beneficial.

One of the most promising uses of the proposed performance assessment method is to eliminate ‘poor’ quality strain images from a sequence of images. That is, only the strain images that are consistent from frame to frame and obtained through accurate motion tracking would be included for clinical diagnosis. The visual impression of the tissue elasticity is improved by selecting a threshold (0.7 for the sequence containing 40 strain images in Fig 9) and including only those strain images whose summary performance measure exceeds that threshold. An unedited sequence of 40 frames of strain images is available in Movie 1 (see Fig. 10), and the edited version is available in Movie 2 (see Fig. 10). The contour of the *in vivo* fibroadenoma is more consistent throughout the sequence, after ‘low-quality’ strain images are eliminated.

It is also interesting to note that the observers seemed to heavily weight the consistency of consecutive strain images. That may suggest that for an algorithm to match the performance of human observers, motion tracking accuracy and consistency among successive strain images might need to be weighted differently. However, the current study is limited by the small number of data sets (10 human subjects) and the involvement of only three observers. A larger number of *in vivo* data sets and observers are essential to reach such a conclusion with statistical significance.

Alternatively, it is not clear that matching the performance of human observers is a necessary goal. The motivation in this work was to aid the observer in determining which images in a sequence could be trusted as displaying accurate elasticity information. Accuracy in tracking motion and consistency in consecutive strain images suggest that a strain image displays accurate information. The summary performance measure based on these parameters is not dependent on what an observer expects or wants to see.

Clinically, the quality of strain imaging is evaluated in terms of displayed strain images, if human observers (typically radiologists) are involved. That is, the human observer is the final arbiter for an elasticity imaging device whose output is intended for clinical diagnosis. It is well recognized that human perception is a complex mixture of psychology, physiology, and environment. The results shown here demonstrate that the summary performance measure correlates well with assessment by human observers, particularly for ‘high-quality’ strain images. Given that we are most interested in identifying ‘good-quality’ strain images, the proposed method appears very practical.

Besides diagnostics, training clinicians is necessary to promote and improve the use of ultrasonic elasticity imaging. The proposed summary performance measure can help trainees understand the importance of maintaining boundary conditions during patient scanning. For instance, the summary performance measure can provide instant feedback to trainees through a scoring system to help them master boundary condition control and through this improve their elasticity imaging technique and overall image quality.

It is worthwhile to note that the normalized cross correlation is mathematically restricted to stationary random signals. Strain images directly correlate to intrinsic mechanical properties of tissue being imaged and those properties may not be stationary. RF echo frames of data may also be non-stationary due, in part, to diffraction and frequency-dependent attenuation. In this circumstance, using the normalized cross correlation merely measures pattern similarity. Nevertheless, the correlation value, primarily used for estimating the similarity between two different signals, may be satisfactory as long as this metric provides sufficient differentiability between ‘good’ or ‘poor’ performance.

The risk of local recurrence of breast cancer is reduced by removing the tumor and a tumor-negative margin around it. Once a diagnosis of breast cancer has been made, the extent of disease (e.g. lesion boundaries) must be assessed for treatment planning. Preliminary studies [2, 50] have demonstrated that the size of a breast tumor is larger in strain images than shown in B-mode ultrasound images, and it is a reasonable hypothesis that the tumor size in strain images is a more accurate representation of that measured at pathology than that available in B-mode images [2,51]. Although real-time ultrasonic strain imaging systems [2, 52] are essential for manipulation of boundary conditions to achieve ‘good’ quality of strain images, quality fluctuations in strain images still exist, as demonstrated by error bars in Fig. 5(c). Objective elimination of ‘low-quality’ strain images by the proposed summary performance measure makes a sequence of strain images more consistent for tracking lesion boundaries. It is therefore reasonable to hypothesize that elasticity imaging and the proposed summary performance measure will improve treatment planning.

The work reported is only part of the assessment of strain image quality. Other parameters (e.g. resolution) must be incorporated to provide a more comprehensive measure of elasticity image quality. Research is underway to include more attributes of strain imaging systems to provide more comprehensive assessment of ultrasonic strain imaging.

## VI. Conclusions

A quantitative summary performance measure of ultrasonic strain imaging was obtained by combining the measures of motion tracking accuracy and consistency among consecutive strain images. The proposed method can be used to assess the quality of strain images with full automation and the measured performance is consistent with visual perception. The descriptor can be used clinically as a method for objectively deciding what are ‘good’ and ‘better’ strain images and can be used as a training tool providing feedback to the clinician while they scan and learn to obtain high-quality elasticity images. This task is important, because the ‘right answer’ is unknown when heterogeneous tissues are being imaged.

### **Acknowledgements**

We are grateful for the support from the USAMRMC (DAMD17-00-1-0596), the NIH (CA100373), and the University of Wisconsin. We are also grateful to colleagues at the Mayo Clinic in Rochester, MN (especially Nicholas Hangiandreou and Gina Hesley) and the Charing Cross Hospital in London, UK (especially William Svensson) for providing some of the data used in this study.

## Reference

- [1] M. E. Costanza and K.L. Edmiston, "Breast cancer screening: early recognition," *Comprehensive Therapy*, vol. 23, pp. 7-12, Jan. 1997.
- [2] T. J. Hall, Y. Zhu, and C.S. Spalding, "In vivo real-time freehand palpation imaging," *Ultrasound in Med. & Biol.*, vol. 29, pp. 427-35, Mar. 2003.
- [3] B. S. Garra, *et al.*, "Elastography of breast lesions: initial clinical results," *Radiology*, vol. 202, pp. 79-86, Jan. 1997.
- [4] C. L. de Korte, *et al.*, "Intravascular elasticity imaging using ultrasound: feasibility studies in phantoms," *Ultrasound in Med. & Biol.*, vol. 23, pp. 735-746, May 1997.
- [5] R. S. Adler, *et al.*, "Quantitative tissue motion analysis of digitized M-mode images: gestational differences of fetal lung," *Ultrasound in Med. & Biol.*, vol. 16, pp. 561-569, June 1990.
- [6] L. Gao, *et al.*, "Imaging of the elastic properties of tissue--a review," *Ultrasound in Med. & Biol.*, vol. 22, pp. 959-977, Aug. 1996.
- [7] J. Ophir, *et al.*, "Elastography: ultrasonic estimation and imaging of the elastic properties of tissues," *Proc. of the Institution of Mechanical Engineers. Part H - Journal of Engineering in Medicine*, vol. 213, pp. 203-233, Mar. 1999.
- [8] T. J. Hall, "AAPM/RSNA physics tutorial for residents: topics in US: beyond the basics: elasticity imaging with US," *Radiographics*, vol. 23, pp. 1657-1671, Dec. 2003.
- [9] J. F. Greenleaf, M. Fatemi, and M. Insana, "Selected methods for imaging elastic properties of biological tissues," *Annual Review of Biomedical Engineering*, vol. 5, pp. 57-78, 2003.

- [10] K. J. Parker, *et al.*, “Techniques for elastic imaging: a review,” *IEEE Engineering in Medicine and Biology Magazine*, vol. 15, pp. 52-59, June 1996.
- [11] G. C. Carter, “Coherence and time delay estimation: an applied tutorial for research development, test and evaluation engineers,” New York: IEEE Press, 1992, pp. 1-28.
- [12] W. F. Walker and G.E. Trahey, “Fundamental limit on delay estimation using partially correlated speckle signals,” *IEEE Trans. on Ultrason., Ferroelect., and Freq. Contr*, vol. 42, pp. 301-308, Feb. 1995.
- [13] A. J. Weiss and E. Weinstein, “Fundamental limitations in passive time delay estimation – part I: narrow-band systems,” *IEEE Trans. on Acoustics, Speech, and Signal Processing*, vol. 31, pp. 472-486, Feb. 1983.
- [14] E. Weinstein and A.J. Weiss, “Fundamental limitations in passive time delay estimation – part I: wide-band systems,” *IEEE Trans. on Acoustics, Speech, and Signal Processing*, vol. 32, pp. 1064-1078, May. 1984.
- [15] I. Cespedes, M. Insana, and J. Ophir, “Theoretical bounds on strain estimation in elastography,” *IEEE Trans. on Ultrason., Ferroelect., and Freq. Contr*, vol. 42, pp. 969-972, May. 1995.
- [16] M. Bilgen and M.F. Insana, “Error analysis in acoustic elastography. I. Displacement estimation,” *J. Acous. Soc. of Amer.*, vol. 101, pp. 1139-1146, Feb. 1997.
- [17] T. Varghese and J. Ophir, “Theoretical framework for performance characterization of elastography: the strain filter,” *IEEE Trans. on Ultrason., Ferroelect., and Freq. Contr*, vol. 44, pp. 164-172, Jan. 1997.

- [18] M. Bilgen, M. and M.F. Insana, “Error analysis in acoustic elastography. II. Strain estimation and SNR analysis,” *J. Acous. Soc. of Amer.*, vol. 101, pp. 1147-1154, Feb. 1997.
- [19] M. Bilgen, “Dynamics of errors in 3D motion estimation and implications for strain-tensor imaging in acoustic elastography,” *Phys. in Med. & Biol.*, vol. 45, pp. 1565-1578, June 2000.
- [20] J. Meunier and M. Bertrand, “Ultrasonic texture motion analysis: theory and simulation,” *IEEE Trans. on Med. Imaging*, vol. 14, pp. 293-300, June 1995.
- [21] F. Kallel, M. Bertrand, and J. Meunier, “Speckle motion artifact under tissue rotation,” *IEEE Trans. on Ultrason., Ferroelect., and Freq. Contr*, vol. 41, pp. 105-122, Jan. 1994.
- [22] R. L. Maurice and M. Bertrand, “Speckle-motion artifact under tissue shearing,” *IEEE Trans. on Ultrason., Ferroelect., and Freq. Contr*, vol. 46, pp. 584-594, May 1994.
- [23] P. Chaturvedi, M.F. Insana, and T.J. Hall, “2-D companding for noise reduction in strain imaging,” *IEEE Trans. on Ultrason., Ferroelect., and Freq. Contr*, vol. 45, pp. 179-191, Jan. 1998.
- [24] L. N. Bohs, *et al.*, “Speckle tracking for multi-dimensional flow estimation,” *Ultrasonics*, vol. 38, pp. 369-375, Mar. 2000.
- [25] Y. Zhu and T.J. Hall, “A modified block matching method for real-time freehand strain imaging,” *Ultrasonic Imaging*, vol. 24, pp. 161-176, May 2002.
- [26] Y. Zhu, P. Chaturvedi, and M.F. Insana, “Strain imaging with a deformable mesh,” *Ultrasonic Imaging*, vol. 21, pp. 127-146, Mar. 1999.

- [27] F. Yeung, *et al.*, ‘Feature-adaptive motion tracking of ultrasound image sequences using a deformable mesh,’ *IEEE Trans. on Med. Imaging*, vol. 17, pp. 945-956, Dec. 1998.
- [28] C. Pellet-Barakat, *et al.*, ‘Ultrasound elastography based on multiscale estimations of regularized displacement fields,’ *IEEE Trans. on Med. Imaging*, vol. 23, pp. 153-163, Feb. 2004.
- [29] K. Nightingale, *et al.*, ‘Acoustic radiation force impulse imaging: in vivo demonstration of clinical feasibility’, *Ultrasound in Med. & Biol.*, vol. 28, pp. 227-235, Feb. 2002.
- [30] F. Viola and W.F. Walker, ‘Radiation force imaging of viscoelastic properties with reduced artifacts,’ *IEEE Trans. on Ultrason., Ferroelect., and Freq. Contr*, vol. 50, pp. 736-742, June 2003.
- [31] M. Fatemi and J.F. Greenleaf, ‘Ultrasound-stimulated vibro-acoustic spectrography,’ *Science*, vol. 280, pp. 82-85, Apr. 1998.
- [32] K. Kaluzynski, *et al.*, ‘Strain rate imaging using two-dimensional speckle tracking,’ *IEEE Trans. on Ultrason., Ferroelect., and Freq. Contr*, vol. 48, pp. 1111-1123, Apr. 2001.
- [33] M. F. Insana and L.T. Cook, ‘Bio-elasticity imaging: System design,’ in *Proc. of SPIE - Medical Imaging*, 1999, pp. 224-235.
- [34] L. T. Cook, *et al.*, ‘Bioelasticity imaging II: Spatial resolution,’ in *Proc. of SPIE - Medical Imaging*, 2000, pp. 315-324.
- [35] M. F. Insana, M.F., *et al.*, ‘Maximum-likelihood approach to strain imaging using ultrasound,’ *J. Acous. Soc. of Amer.*, vol. 107, pp. 1421-1434, Mar. 2000.

- [36] S. Srinivasan, T. Krouskop, and J. Ophir. “Correlation of elastographic tissue strain images with mechanically scanned modulus images,” in *Proc. of the 2002 IEEE Engineering in Medicine and Biology (BMES / EMBS)*, 2002.
- [37] S. Srinivasan, T. Krouskop, and J. Ophir, “Comparing elastographic strain images with modulus images obtained using nanoindentation: preliminary results using phantoms and tissue samples,” *Ultrasound in Med. & Biol.*, vol. 30, pp. 329-343, Mar. 2004.
- [38] U. Techavipoo and T. Varghese, “Wavelet denoising of displacement estimates in elastography,” *Ultrasound in Med. & Biol.*, vol. 30, pp. 477-491, Apr. 2004.
- [39] F. Kallel and J. Ophir, “A least-squares strain estimator for elastography,” *Ultrasonic Imaging*, vol. 19, pp. 195-208, May 1997.
- [40] T. J. Hall., *et al.*, “Phantom materials for elastography,” *IEEE Trans. on Ultrason., Ferroelect., and Freq. Contr*, vol. 44, pp. 1355-1365, Dec. 1997.
- [41] J. S. Bendat and A.G. Piersol, “Random data: analysis and measurement procedures,” 2nd , rev. and expand ed., New York: Wiley, 1986.
- [42] N. Belaid, *et al.*, “Lesion detection in simulated elastographic and echographic images: a psychophysical study,” *Ultrasound in Med. & Biol.*, vol. 20, pp. 877-91., Sept. 1994.
- [43] Y. C. Fung, “Biomechanics: mechanical properties of living tissues,” 2nd ed., New York: Springer-Verlag, 1993.
- [44] T. A. Krouskop, *et al.*, “Elastic moduli of breast and prostate tissues under compression,” *Ultrasonic Imaging*, vol. 20, pp. 260-74, July 1998.

- [45] T. J. Hall, *et al.*, “Noise reduction strategies in freehand elasticity imaging,” in *2002 IEEE Ultrasonics Symposium*, 2002.
- [46] I. Cespedes, *et al.*, “Methods for estimation of subsample time delays of digitized echo signals,” *Ultrasonic Imaging*, vol. 17, pp. 142-171, Mar. 1995.
- [47] M. Bilgen, “Target detectability in acoustic elastography,” *IEEE Trans. on Ultrason., Ferroelect., and Freq. Contr*, vol. 46, pp. 1128-1133, Sept. 1999.
- [48] M. A Lubinski, S.Y. Emelianov, and M. O'Donnell, “Adaptive strain estimation using retrospective processing,” *IEEE Trans. on Ultrason., Ferroelect., and Freq. Contr*, vol. 46, pp. 97-107, Jan. 1999.
- [49] J. Jiang, “An Offline Motion Tracking Algorithm for Elastic Strain Imaging,” Master thesis, University of Kansas, Lawrence, KS, 2002.
- [50] T. Matsumura, *et al.* “Diagnostic Results for Breast Disease by Real-time Elasticity Imaging System,” in *IEEE Ultrasonic Symposium*. 2004.
- [51] W. Svensson, *et al.* “Elasticity and phahology imaging correlation of breast tumors: initial results,” in the 4<sup>th</sup> International Conference on the Ultrasonic Measurement and Imaging of Tissue Elasticity, Austin, TX, 2005.
- [52] T. Shiina, *et al.* “Clinical assessment of real-time, freehand elasticity imaging system based on the combined autocorrelation method,” in *2003 IEEE Ultrasonic Symposium*, 2003.

**Table 1.** Guidelines for rating strain image quality

Scores	Description
1	strain images that appear noisy and apparently contain no tissue elasticity information
2-3	strain images that have low contrast-to-noise ratios but contain no obvious motion tracking failures; or strain images that contain a little tissue elasticity information and where noise is so distracting that little useful information can be effectively extracted
4	strain images that have some correlation to the reference strain images but noise is apparent; or strain images that are reasonably consistent from frame to frame but have large motion tracking errors which may degrade the ability to extract lesion contours
5	strain images that are reasonably consistent from frame-to-frame and any large motion tracking errors have limited affect on the ability to extract consistent lesion contours
6-7	strain images that are consistent from frame to frame and have no significant motion tracking errors
8-9	strain images that are not only consistent from frame to frame coarsely, but also preserve structural details reasonably well
10	Strain images that consistently preserve structural details at a very fine level

**Table 2.** Comparison of estimated contrast-to-noise ratios to the calculated performance values in a tissue-mimicking phantom

	Fig. 2a	Fig. 2b	Fig. 2c	Fig. 2d	Fig. 2e	Fig. 2f
$\text{CNR}_{2.4}$	1.2	4.1	3.7	5.7	6.9	7.9
$\text{CNR}_3$	3.2	5.4	5.9	8.4	9.3	10.3
Performance value	0.25	0.45	0.65	0.85	0.92	0.93
Frame-average strain	0.30%	0.60%	1.10%	2.00%	3.80%	4.50%

**Table 3.** Comparison of estimated contrast-to-noise ratios to the calculated performance values for an *in vivo* fibroadenoma

	Fig. 4a	Fig. 4b	Fig. 4c	Fig. 4d
CNR	3.4	12.5	13.5	6.5
Performance value	0.4	0.76	0.82	0.62
Frame-average strain	0.40%	1.00%	2.00%	3.00%

### Figure Captions

**Fig. 1.** A schematic illustration of the frame pairing procedure for strain image formation.

**Fig. 2.** B-mode and strain images obtained under different axial compression: (a) 0.3%; (b) 0.6%; (c) 1.1%; (d) 2.0%; (e) 3.8%; (d) 4.5%. The white boxes in the B-mode images define the regions of interest (ROI) from which strain images were estimated.

**Fig. 3.** Estimates of the NCC between pre-deformation and motion-compensated post-deformation (a) RF echo fields, and (b) consecutive strain images and (c) the summary performance values vs. axial deformation using the tissue-mimicking phantom. Error bars denote one standard error.

**Fig. 4.** B-mode and strain images from an *in vivo* breast fibroadenomas at (a) 0.4%, (b) 1%, (c) 2%, and (d) 3% frame-average axial strain. The white boxes in the B-mode images define the regions of interest from which strain images were estimated.

**Fig. 5.** Estimates of normalized cross correlation between pre-deformation and motion-compensated post-deformation (a) RF echo fields, (b) consecutive strain images and (c) performance values vs. axial deformation using data acquired from a palpable *in vivo* breast fibroadenoma. Error bars denote one standard error.

**Fig. 6.** Plots of (a) the frame-average strain obtained with freehand scanning of an *in vivo* breast, and (b) the estimated overall performance values. The solid line represents results obtained by pairing adjacent RF frames of data for calculating local strains. The dashed line represents results obtained by adaptively selecting the RF frame pairs to achieve approximately 1—1.5% frame-average strain.

**Fig. 7.** B-mode and strain images obtained from an *in vivo* invasive ductal carcinoma. Images in (a) show a typical ‘good-quality’ strain image and in (b) a ‘low-quality’ strain image that is consistent with its adjacent strain images and but is not consistent with typical ‘good’ quality strain images in the same sequence. The frame-average strains are

0.92% in (a) and 1.2% in (b), respectively. The estimated summary measures are 0.74 in (a) and 0.38 in (b), respectively.

**Fig. 8.** A plot of comparing the summary performance values and human rating scores for 200 strain images. The solid line represents a linear fit between the summary performance measure and human rating scores.

**Fig. 9.** Plots comparing (a) the summary performance measure and human rating scores from a sequence of 40 consecutive strain images of a palpable *in vivo* fibroadenoma, and (b) the frame-average strains in the same sequence.

**Fig. 10.** A sequence of strain images whose performance scores are plotted in Fig. 8. Movie 1 is the unedited sequence and Movie 2 is the edited sequence where ‘bad’ quality strain images whose estimated performance values are below 0.65 are eliminated. Movie 3 is obtained by filtering strain images whose estimated values of motion tracking accuracy ( $r_{rf}$ ) are below 0.9.

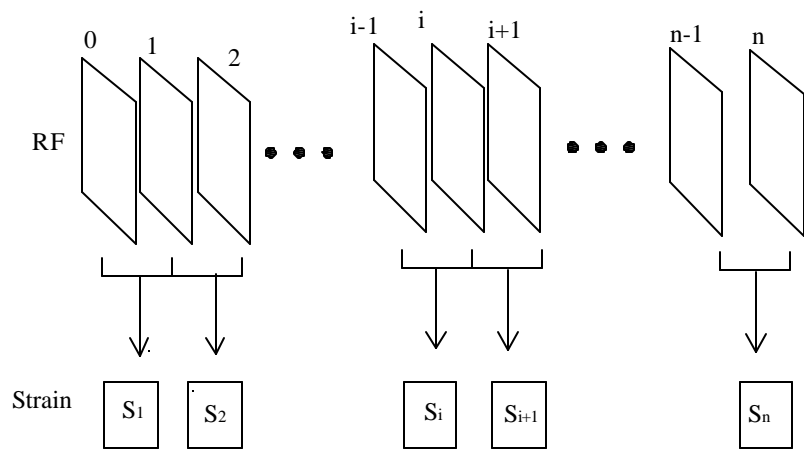


**Fig. 1**

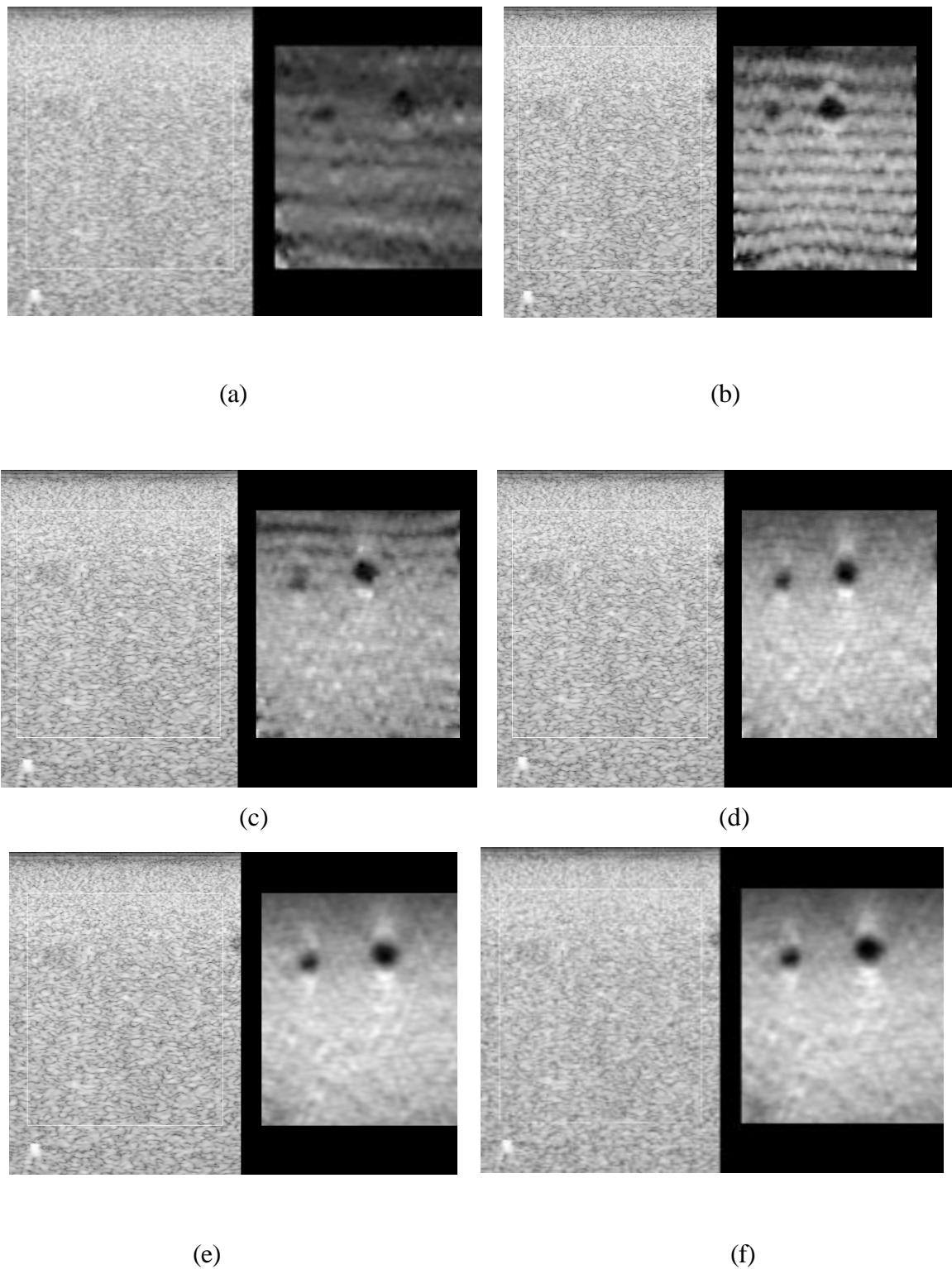
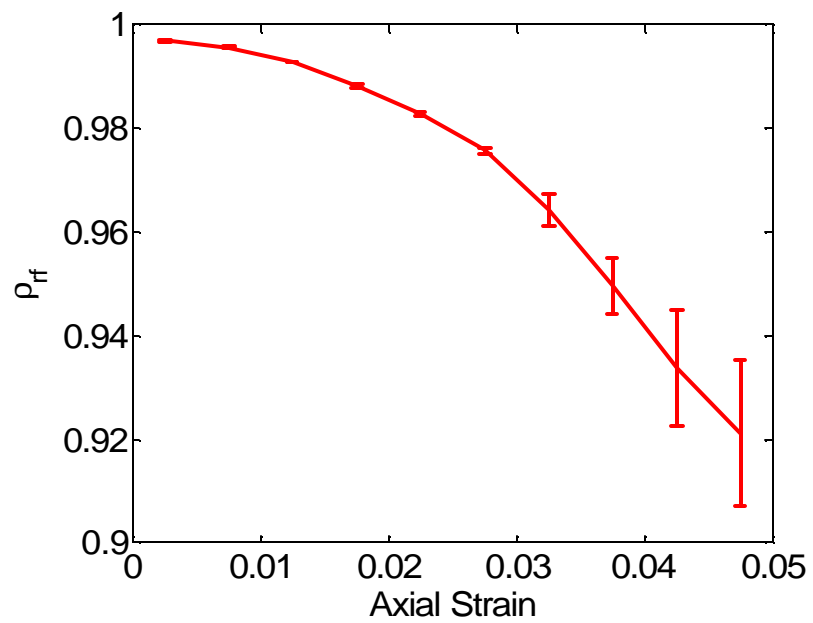
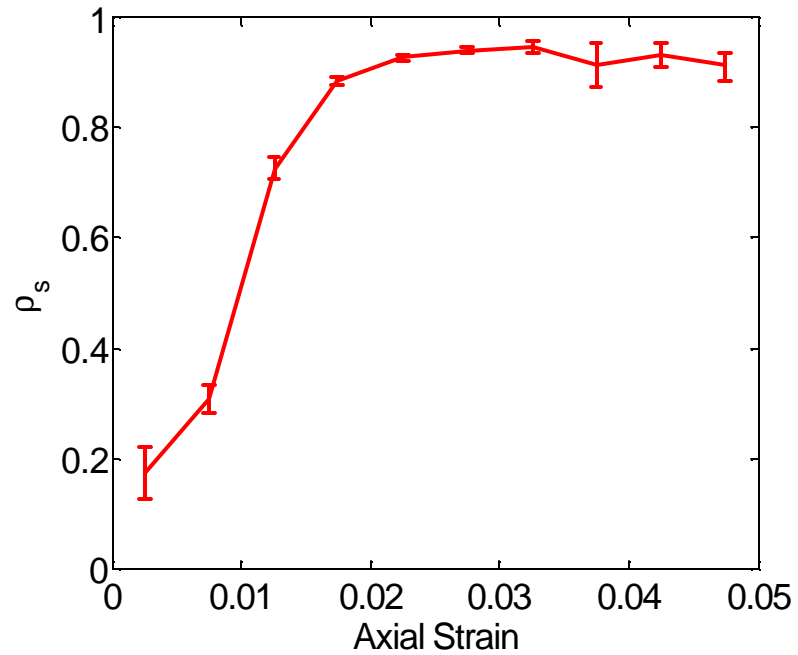


**Fig. 2.**



(a)



(b)

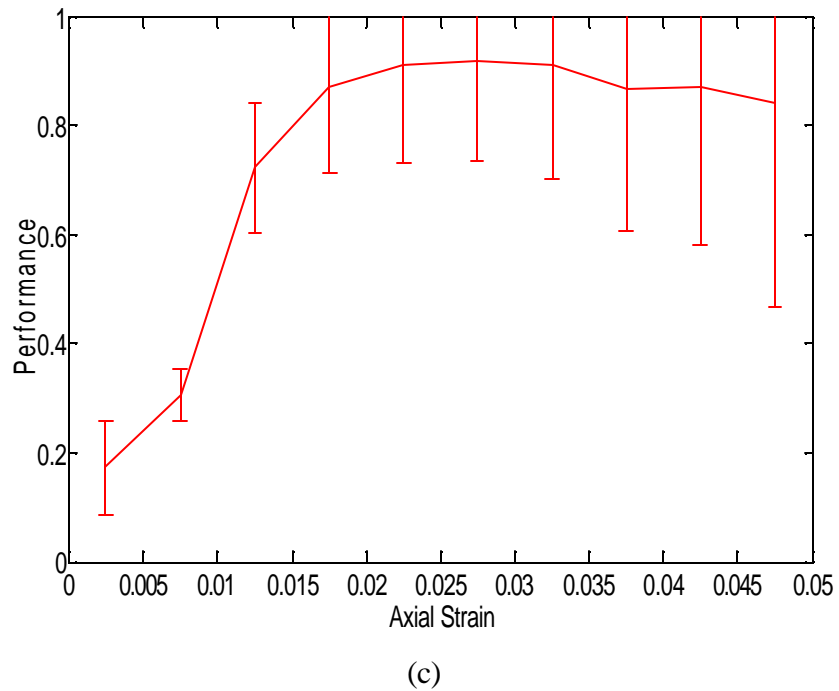


**Fig. 3.**

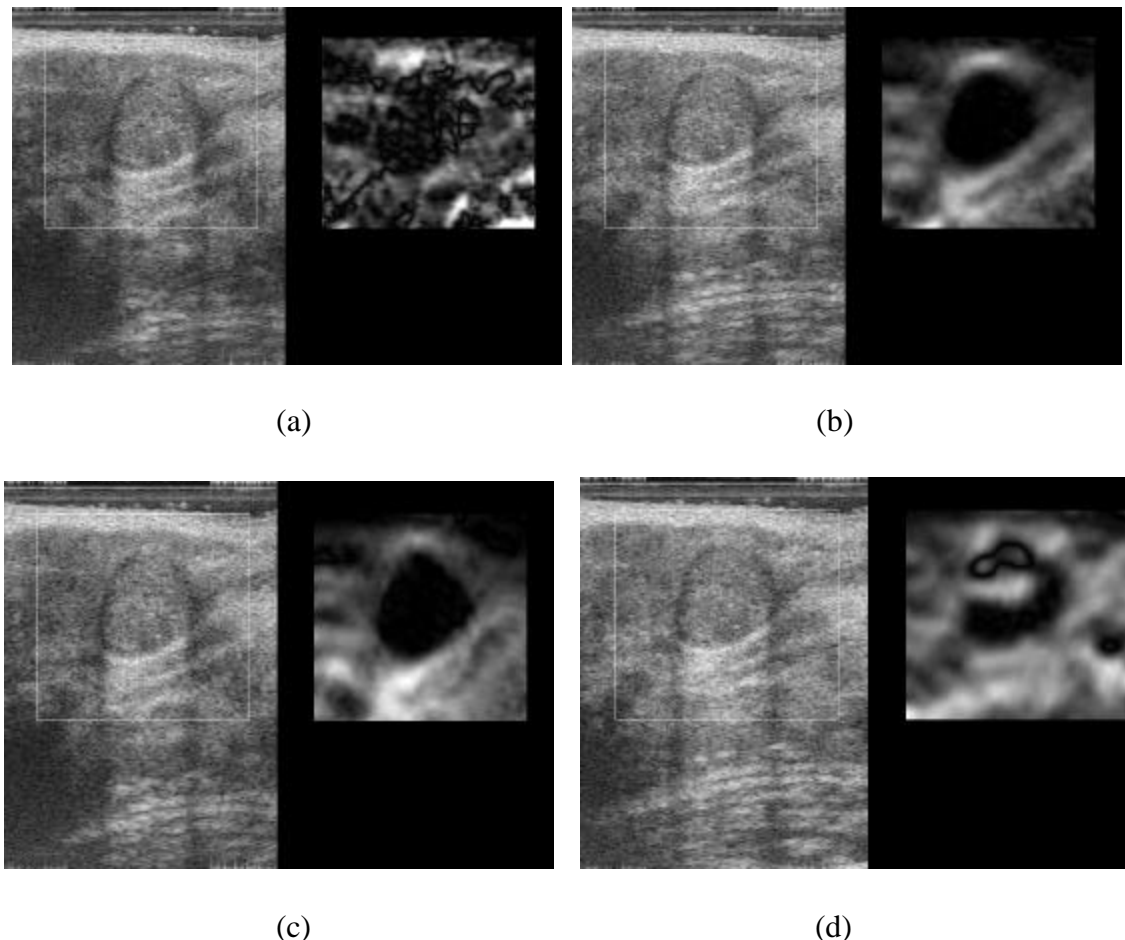
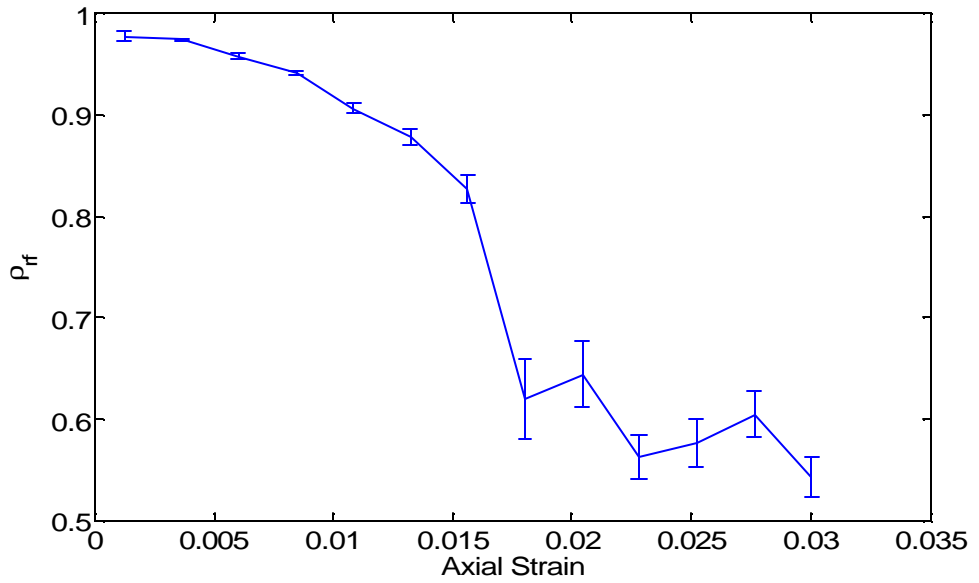
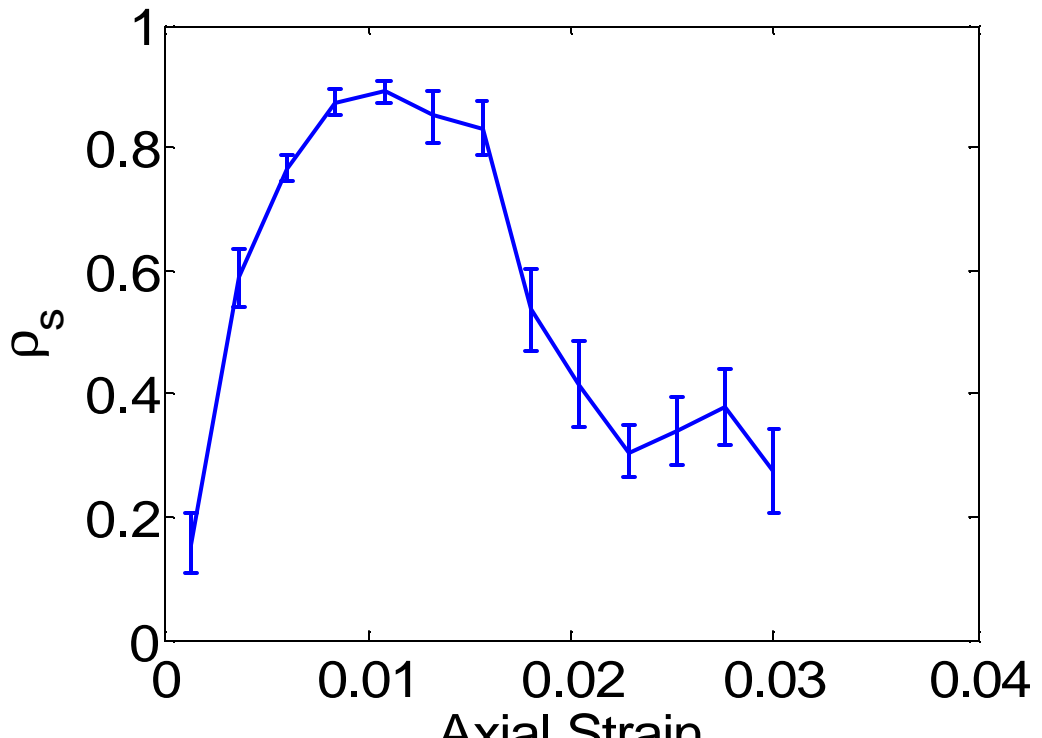


**Fig. 4.**



(a)



(b)

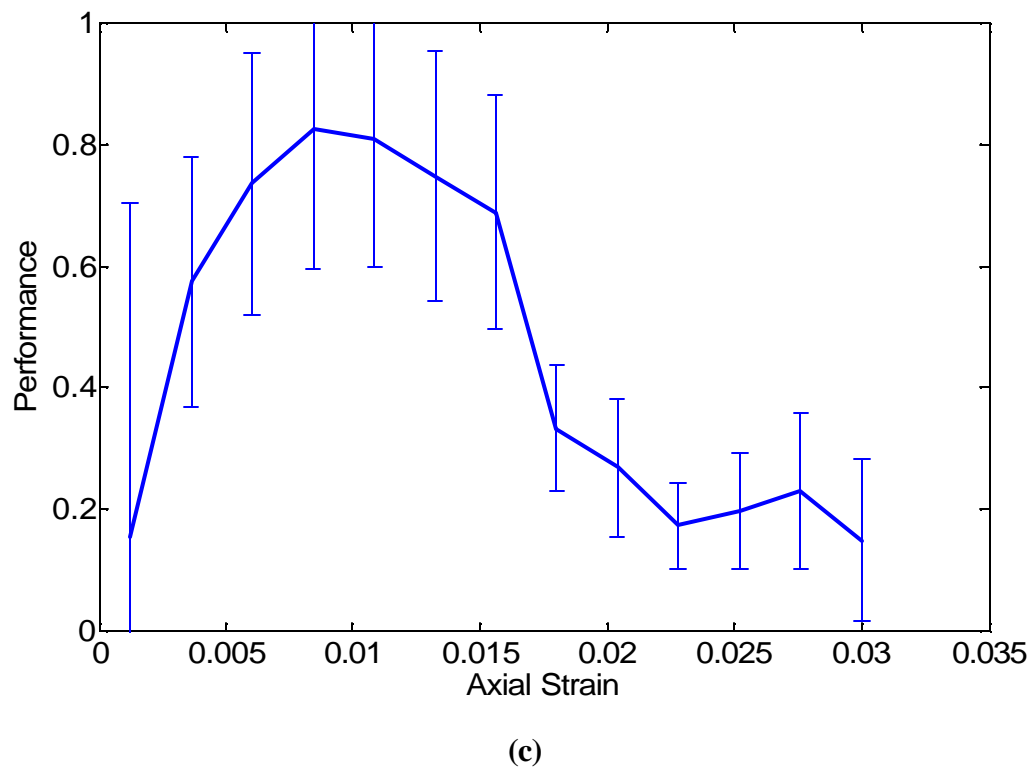
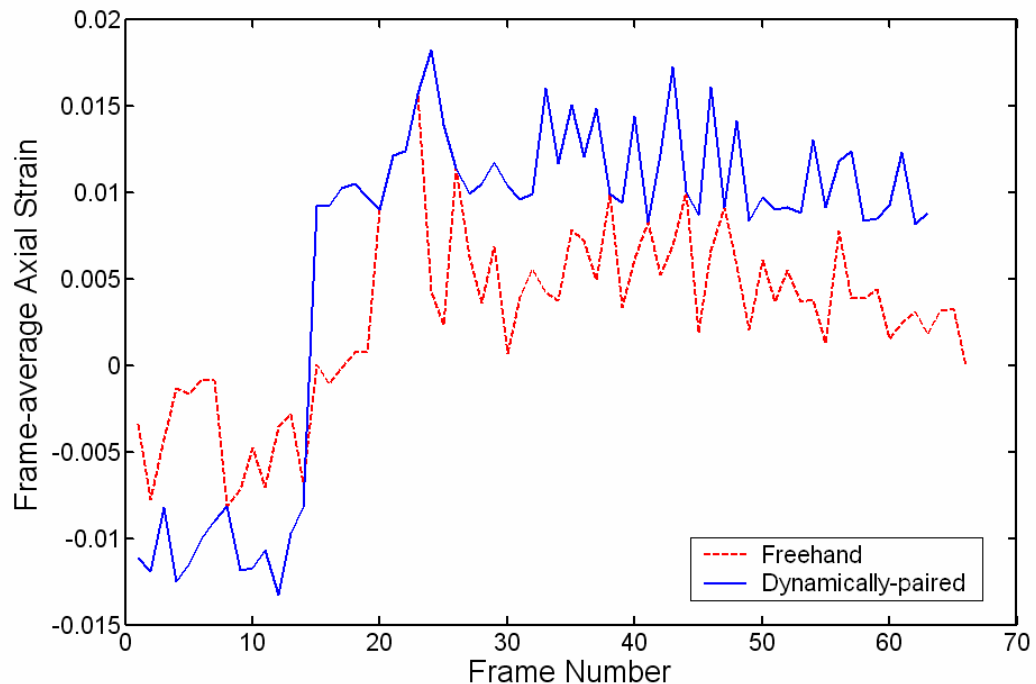
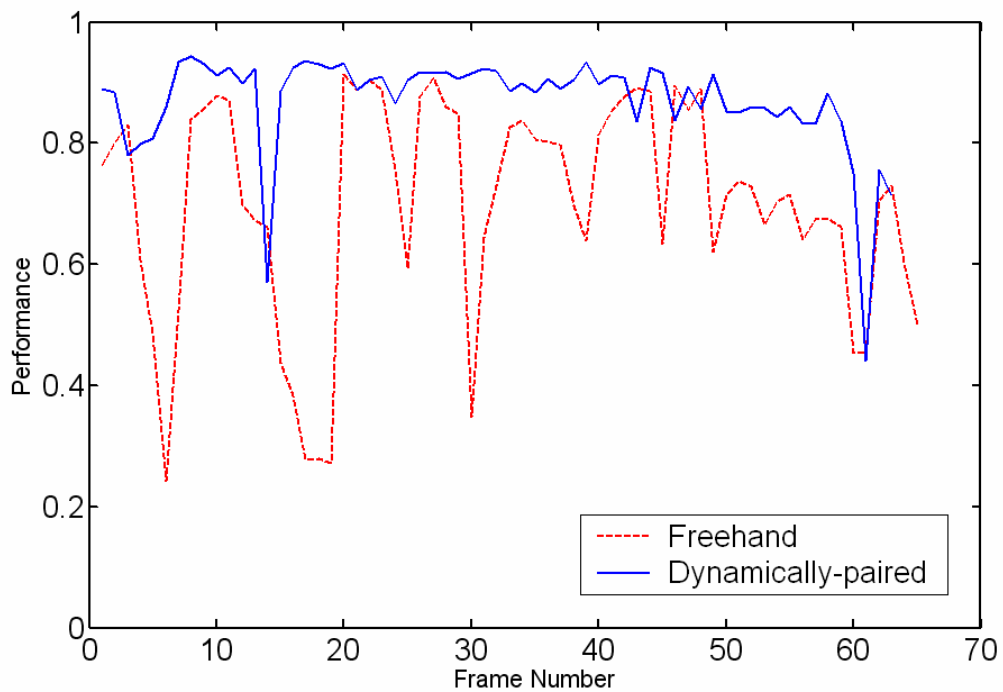


**Fig. 5.**

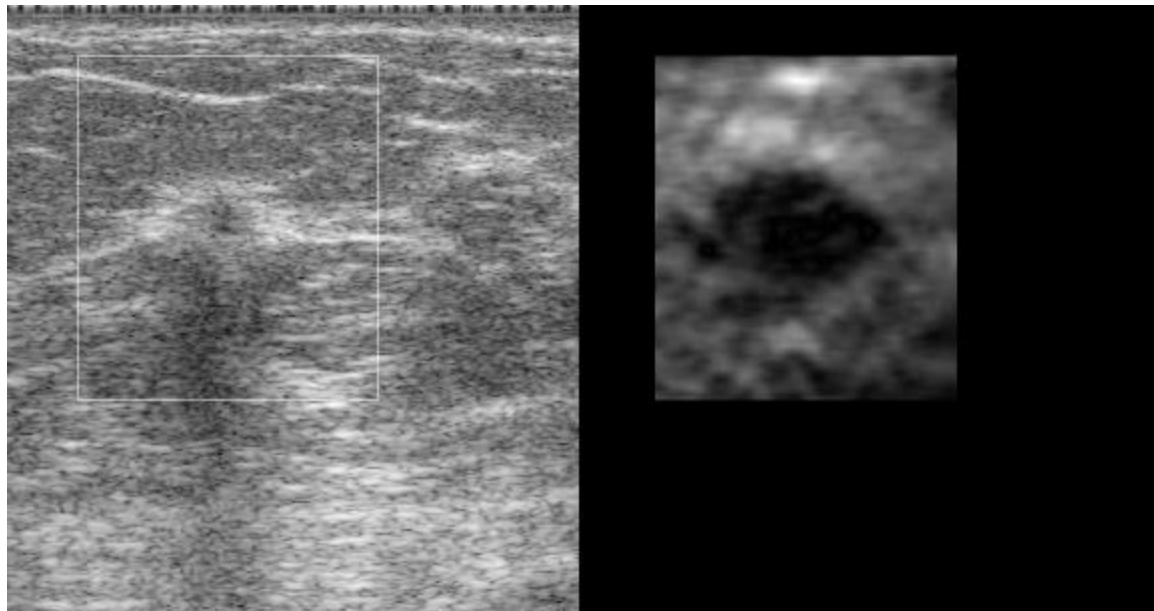


(a)

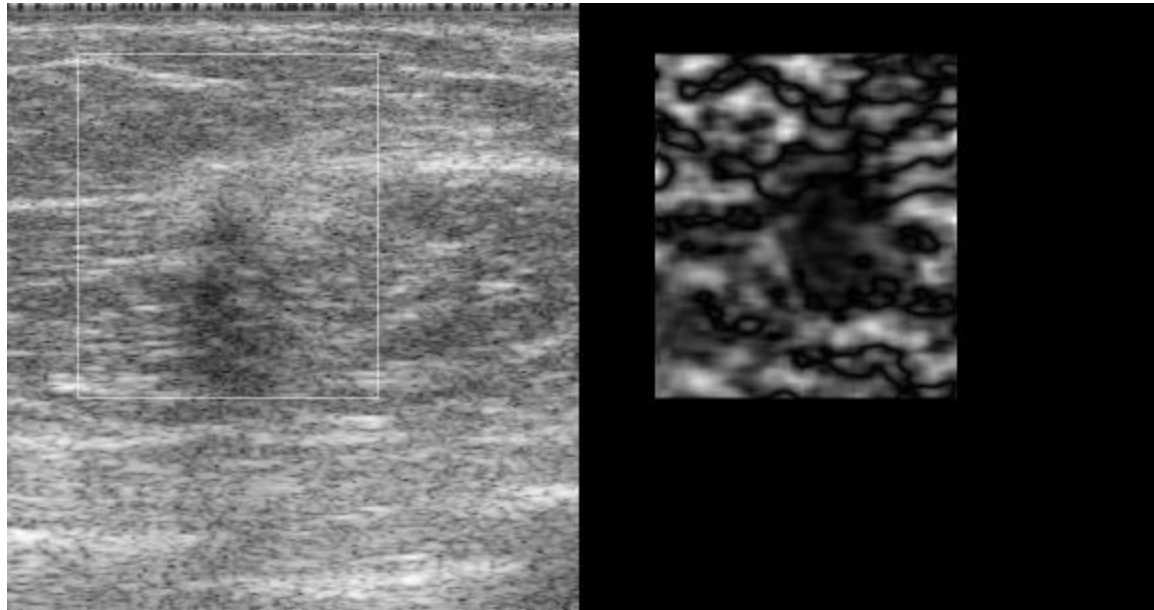


(b)

**Fig. 6.**



(a)



(b)

**Fig. 7.**

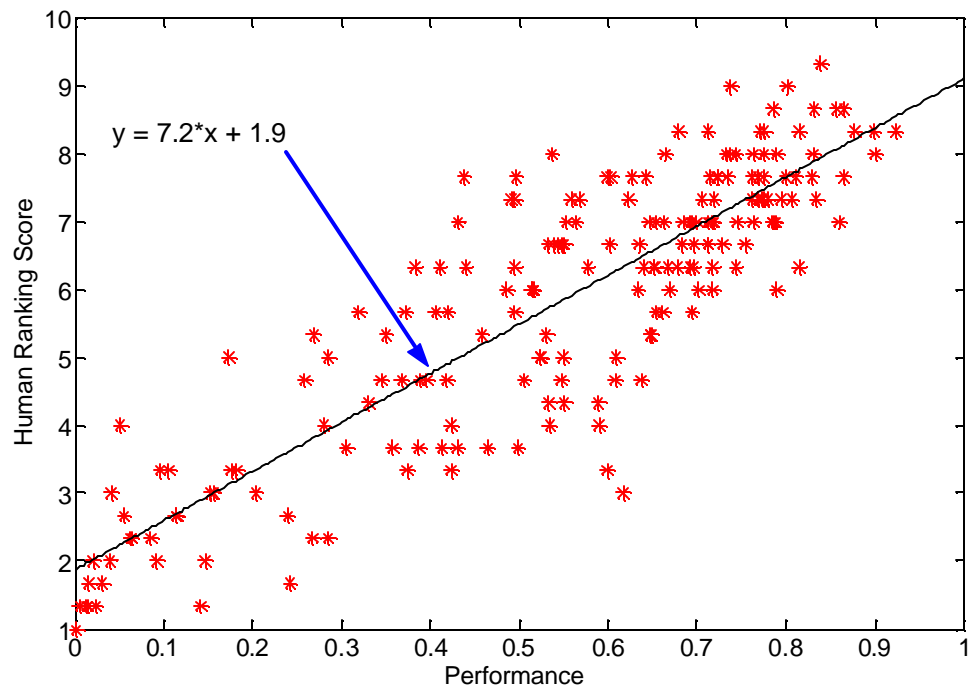
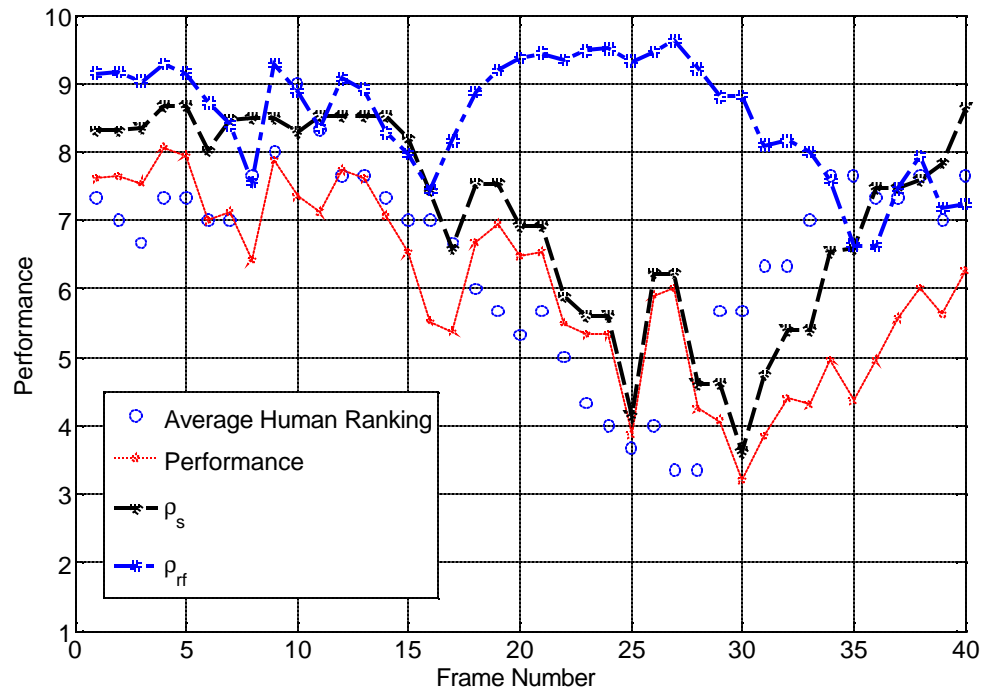
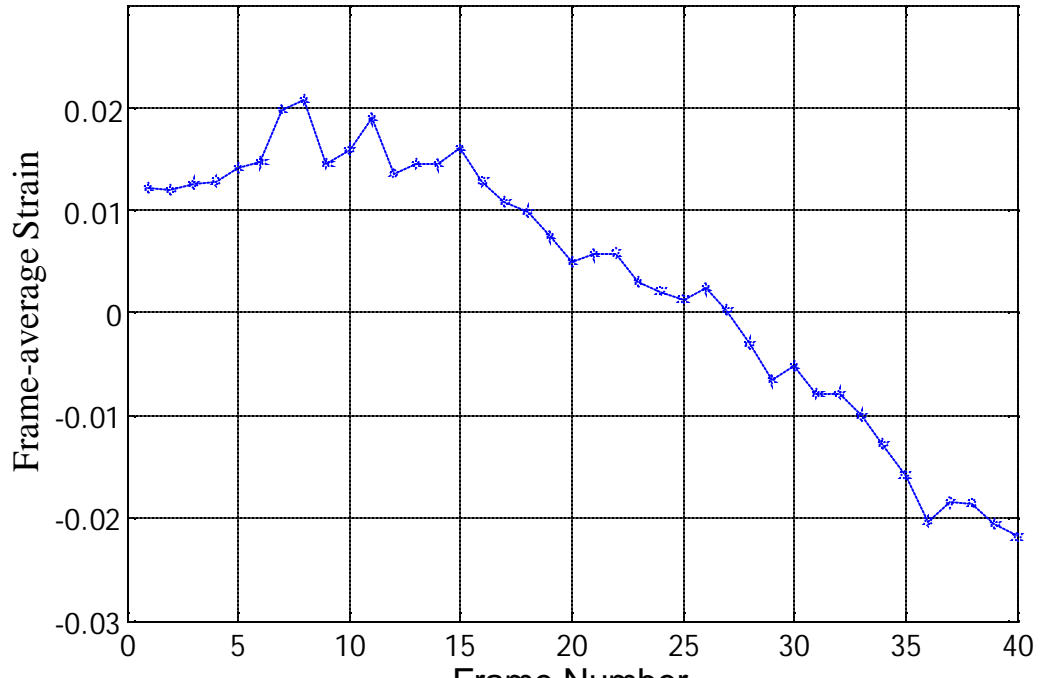


**Fig. 8.**



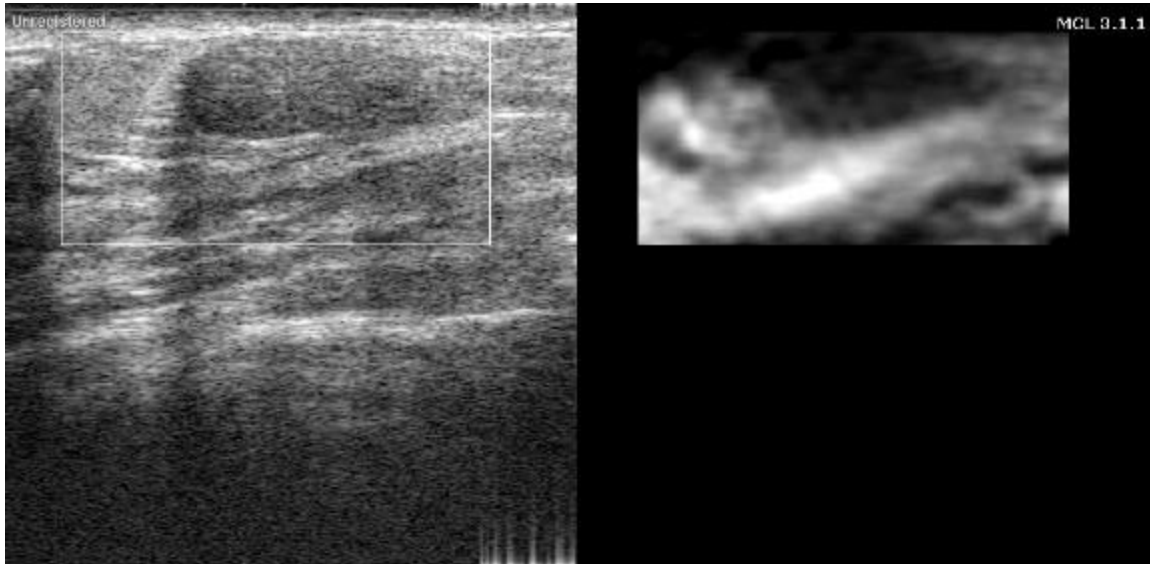
(a)



(b)

**Fig. 9.**

**Movies and animations**: please click on the movie icons to see movie and animations.



**Media-Movie 1**

[File size: 2495 KB; Format: MPEG;  
Resolution: 912 X 480; Duration: 1 second]



**Media-Movie 2**

[File size: 975 KB; Format: MPEG;  
Resolution: 912 X 480; Duration: 0.4 second]



**Media-Movie 3**

[File size: 2495 KB; Format: MPEG;  
Resolution: 912 X 480; Duration: 0.5 second]

**Fig. 10.**

# Using Ultrasound Strain Imaging to Improve the Decision to Biopsy Solid Breast Masses

Original Research

## ABSTRACT

### PURPOSE

To retrospectively determine the accuracy of the ultrasound (US) strain imaging to differentiate benign and malignant breast masses and thereby improve the decision to biopsy solid breast masses.

### MATERIALS AND METHODS

Approval for the study was obtained from the Institutional Review Board and informed consent obtained from patients who participated in image acquisition. Strain imaging was performed on 403 breast masses. Lesions were imaged using free-hand compression and a real-time strain imaging algorithm. The 50 highest quality-malignant and 50 highest-quality benign lesions were selected for a reader study. Three observers blinded to pathologic outcomes first interpreted B-mode images using BI-RADS descriptors and provided a probability of malignancy. Then the readers viewed the strain image appearance and measurements and their updated probability of malignancy. Receiver operating characteristic (ROC) curves were constructed for each observer using probabilities assessed first without and then with strain. The areas under these curves (AUC) as well as sensitivity and specificity at several decision thresholds were calculated and compared. Inter-observer variability was evaluated. We also analyzed whether the correlation between an automated and a subjective quality assessment predicted reader performance.

### RESULTS

Each reader's AUC improved when strain imaging was used to assess the probability of malignancy. The average AUC for all three readers after strain imaging was significantly better than after B-mode alone (0.872 versus 0.902,  $P = 0.012$ ). Using a threshold of 2% probability of malignancy, as a group, specificity with strain improved significantly over B-mode alone (0.140

versus 0.191,  $P < 0.0001$ ) while achieving high sensitivity (0.986 versus 0.993,  $P = 0.32$ ).

Statistically significant inter-observer variability was observed ( $p < 0.001$ ). In addition, the ability to accurately assess strain image quality appeared to correlate with highest observer performance.

## CONCLUSIONS

We find that US strain imaging has the potential to aid in the discrimination of benign and malignant breast masses. However, inter-observer variability and image quality appear to be important considerations in performance optimization.

Key Words: Breast, Breast Neoplasms, Ultrasound

## INTRODUCTION

Breast biopsy, the current method used to distinguish between benign and malignant breast abnormalities on imaging, actually delivers a benign result in over 75% of cases making it the most costly per capita component of a breast cancer screening program.(1) A decade ago, physicians found that imaging features on ultrasound can be used to discriminate benign and malignant solid breast masses in order to decrease biopsy rates.(2) Unfortunately, their successes have not been reliably confirmed and are not widely used. In addition, The Agency for Healthcare Research and Quality (AHRQ) recently stated that current ultrasound performance is insufficiently sensitive or specific to be used in place of breast biopsy for diagnosis of mammographically identified abnormalities.(3) A method to reliably differentiate benign and malignant solid masses on ultrasound would indeed be valuable.

Ultrasound strain imaging (also known as elastography) may aid the differentiation of benign and malignant solid breast masses.(4-19) This research is based on the fact that benign and malignant breast lesions have an inherently different firmness. Strain imaging measures the relative stiffness of lesions compared to surrounding tissue. Stiffer areas, which by definition deform less easily than their surroundings, are encoded as dark while softer areas, which deform more easily than their surroundings, are depicted as light on strain images. Malignant masses typically appear dark and have high contrast with background breast tissue during deformation. Benign masses typically appear lighter and have lower contrast with background tissue with deformation. In addition, malignant lesions tend to be larger on strain images than the corresponding B-mode images which may be caused by the desmoplastic reaction commonly

associated with these tumors.(5-7, 13, 18, 20) Figures MALIGNANT and BENIGN show the appearance of malignant and benign lesions on B-mode and strain images respectively. The appearance of strain images and lesion size discrepancies between B-mode and strain images may be a promising way to distinguish benign from malignant lesions.

In the past, various characteristics of strain imaging (eg. strain to B-mode size ratio) have been used as isolated predictors of benign and malignant breast disease.(5, 6) In contrast, in clinical practice strain imaging is much more likely to be used as an adjunct to ultrasound in lesion evaluation and management. In this experiment we wish to add strain images into a radiologist's cohort of evidence that is used to determine the risk of malignancy. In this manner, we aimed to determine if strain imaging might improve the radiologists risk prediction and management decisions for solid breast masses. Thus, the purpose of our study was to retrospectively determine the accuracy of the ultrasound strain imaging to differentiate benign and malignant breast lesions on ultrasound to thereby improve the decision to biopsy.

## MATERIALS AND METHODS

Siemens Medical Solutions, Ultrasound Division, Issaquah, WA provided equipment and partial financial support for this study. The authors had control of the data and information submitted for publication.

### *Patient Population*

Approval for the study was obtained from the appropriate Institutional Review Board and informed consent obtained from all enrolled patients. Two institutions participated in patient

enrollment and imaging: Charing Cross Hospital in London, England and the Mayo Clinic in Rochester, Minnesota. Eligible patients were those women undergoing sonographically guided percutaneous breast biopsy. We excluded patients who had technically inadequate strain images or who did not undergo biopsy for pathologic outcome. Charing Cross enrolled 259 patients between 2/22/2002 and 4/8/2004 imaging 259 lesions. Eleven lesions were excluded for technical reasons and 11 were excluded because biopsy was not performed. The Mayo Clinic enrolled 156 patients between 2/4/2002 to 5/25/2004 imaging 186 lesions of which 17 lesions were excluded for technical reasons and 3 were excluded because biopsy was not performed. In total, strain imaging was performed prospectively on 445 breast masses of which 42 were discarded based on our exclusion criteria leaving 403 (157 malignant—39.0%; 246 benign—61.0%) lesions as candidates for our reader study.

Pathologic results determined by percutaneous or excisional biopsy were considered our reference standard in this study. Imaging-histologic concordance was documented for each lesion to minimize the chance for sampling error.

#### *Strain Imaging Technique*

The strain imaging technique has been previously published but is repeated here for the convenience of the reader.(18) US strain images are produced by comparing US echo data prior to and after a slight axial deformation of the breast to determine the tissue displacement at each location in the breast as a result of the deformation. Strain is computed as the rate of change in the axial tissue displacement as a function of depth. The strain images are produced when the relative differences in tissue motion at each location in the breast are calculated and displayed.

Lesions were imaged at Mayo Clinic by a mammography technologist with 10 years of experience in breast ultrasound. Lesions were imaged at Charing Cross by a radiologist with 17 years of experience in breast ultrasound. Both sites used the Siemens SONOLINE Elegra (Siemens Medical Solutions, Ultrasound Division, Issaquah WA) employing either the 7.5L40 linear array at **7.2 MHz** or the VFX13-5 multi-row linear array at 10MHz. A real-time strain imaging algorithm developed by Hall, et al. (6), and implemented on a the Siemens Elegra was used to guide strain image acquisition. A free-hand compression technique was used in which slight axial deformation was applied to the lesions manually by the clinician using the US probe. B-mode images and strain images for this study were reconstructed off-line from the same RF echo data acquired during the US examination and were displayed in a side-by-side format with individual frames contained within a cine-loop sequence of approximately 100 frames.

B-mode images were formed off-line from the stored RF by first computing the Hilbert transform of the zero-mean RF A-line. The transformed data was then down-sampled axially to obtain square pixels. The resulting data were displayed with an 8-bit log-compressed colormap where

$$\text{colormap value (i)} = \log_{10}(i*12+1)$$

This algorithm is similar to that used in clinical imaging systems, however, manufacturers are very protective of their unique B-mode image formation algorithms and a great deal of ‘art’ beyond that implemented here provides improvements in B-mode image quality beyond that available in this study. Consequently, the B-mode image quality used in this study is less than that found in state-of-the-art imaging systems.

Strain images were formed off-line from the stored RF data using custom software similar to that described in detail elsewhere.(21, 22) The primary modification to the previously reported strain image formation algorithm is that three frames of RF data are used to form two strain images in the same physical grid, and those two strain images are averaged to obtain lower noise strain images(23), resulting in superior strain image quality compared to that displayed in real-time on the Siemens Elegra. Also, RF data were stored at a greater frame rate than real-time strain image display on the Siemens Elegra (approximately 20 frames per second instead of 8), so the off-line temporal resolution was also superior to that displayed in real-time on the scanner.(6)

#### *Reader Study*

Two parameters were used to select the abnormalities for the reader study: the distribution of pathologic diagnoses and image quality. First, in order to optimally represent the entire pathologic spectrum of solid breast abnormalities seen in clinical breast imaging practice, we determined the distribution of pathologic diagnoses in our collected cases (Table SIMPOP). Next, we selected the 50 highest-quality malignant and the 50 highest-quality benign abnormalities on strain images while preserving this same distribution of pathologic diagnoses in the malignant and benign categories respectively. We also made sure that only one lesion per patient was included in the reader study to preserve independence of cases for statistical analysis.

An objective method of quantifying strain image quality, actually a displacement quality measure (DQM), was developed (22) to rate individual strain images and images sequences. The DQM is obtained by using the measured displacement field to warp the post-deformation radio frequency (RF) echo field, and the strain field, back into the coordinate system of the pre-deformation RF echo field. The correlation between the pre-deformation RF echo field and the

motion-compensated post-deformation RF echo field is an objective measure of the accuracy of displacement estimation. The correlation between consecutive strain images, mapped into the same coordinate system, is an objective measure of the consistency of consecutive strain images. The product of these correlation coefficients is a summary measure of the accuracy and similarity of consecutive strain images. The individual correlation coefficients and their product ranges from 0—1 resulting in a metric that is easily interpreted. Need a sentence here saying “images that fell below a level of XXX were excluded from both the B-mode and strain image loop” (is that right?). Summing the squared product of these correlation coefficients provides a measure of the quality of a strain image sequence. The final DQM used for our analysis was calculated after inferior images had been removed. Although the choice of squaring the product of correlation coefficients is not rigorous and was empirically chosen, the resulting DQM is convenient and correlates well with the visual ranking by researchers actively involved in developing and testing strain imaging systems.(22)

#### *B-mode and Strain Image Evaluation*

Three radiologists were included in this study. All of the radiologists who participated were board certified (by the American Board of Radiology) and fulfilled the MQSA requirements in terms of volume of studies read per year and continuing medical education. All three radiologists are fellowship trained in breast imaging and spend at least 30% of their clinical time in breast imaging practice (years of experience range from 5 to 13 years). The three observers (designated A-C) individually completed a training module containing 56 instructional Power-point® slides and 40 sample cases. The introductory slides provided didactic instruction on: 1) the physics of strain imaging; 2) characteristic appearance of strain imaging in benign and malignant masses; 3) the significance of size ratio differences between B-mode and

strain imaging and 4) methods to evaluate the quality of strain imaging using ten of the 40 sample cases (5 benign, 5 malignant). The additional 30 sample cases contained 14 benign and 16 malignant solid masses shown as unknowns with illustrations of significant findings and relevant measurements available when desired.

Once the training session was complete to the radiologist's satisfaction, test cases were presented in random order. The interface (Figure INTERFACE) first presented the B-mode images as a movie clip which the radiologist assessed with BI-RADS descriptors, BI-RADS categories, and a probability of malignancy. The radiologist also selected a frame from the cine loop on which to make measurements on the B-mode image. The radiologist traced the lesion boundary and measured the largest linear dimension and the largest perpendicular dimension. Strain images were then made available and were presented as side-by-side B-mode and strain images in a movie clip. The radiologist first assessed the quality of the strain images on a 10 point scale. Then they selected a frame on which to trace the lesion boundary and measure the largest linear dimension and the largest perpendicular dimension on the strain image. Note that the frame used for strain image measurements was not necessarily the same as that used for B-mode measurements. The radiologist then viewed the ratio of the lesion area in the strain image to that in the B-mode image prior to re-assessment of the probability of malignancy.

Probability assessment correlations between readers were calculated in a pair-wise fashion. Probability assessments were also used to construct ROC curves to measure performance. The AUC without and with strain imaging were compared. Sensitivity and specificity were measured at a threshold of 2% probability of malignancy without and with strain and were compared. We also compared difference in AUC, sensitivity, and specificity between pairs of readers for B-mode and strain imaging.

Finally, the correlation between the DQM and the radiologists' subjective quality score was calculated. Subset analysis of these correlations was also performed within the malignant and benign cases. In order to determine whether quality influenced overall performance we divided the cases into the 50 best and 50 worst images based on the DQM. We dichotomized image quality at the median, separately for malignant and benign lesions, to ensure roughly equal numbers of "higher quality" and "lower quality" images. For malignant lesions, median image quality was 15, with 30 "higher quality" images being  $\geq 15$ , while for benign lesions, median was 35, with 26 "higher quality" images being  $\geq 35$ .

#### *Data and Statistical Analysis*

All statistical analyses were done using S-PLUS, Version 5.3, MathSoft, Inc, Cambridge, MA. We computed correlation coefficients, separately for each pair of readers, and after averaging across pairs of readers. When averaging across pairs, we used 1000 bootstrap samples to compute the standard errors of the average correlations.(24).

We used the Student's *t* test to compare of data having a normal distribution and the chi-square test to compare proportional data. Standard binormal ROC curve analysis was applied to the probability assessments made by the radiologist without and with strain images.(25) To combine information across readers, we took an average of the AUCs. Point estimates and 95% confidence intervals for AUCs were calculated and compared using tests for paired data (NEED THESE). These analyses were implemented using LABMRMC ([http://www-radiology.uchicago.edu/krl/roc\\_soft.htm](http://www-radiology.uchicago.edu/krl/roc_soft.htm)).

The Fisher's exact test was used to calculate the difference between the sensitivity and specificity without and with strain images at the level of 2% probability of malignancy. To summarize overall sensitivity and specificity, we averaged across readers, with standard errors of

averages accounting for within and across reader correlations in readings. To analyze inter-observer variability for AUC, sensitivity and specificity, we used McNemar's test.

For image quality analysis, we computed correlation coefficients between DQM and subjective quality assessment for each reader, first for all abnormalities then for malignant and benign lesions separately. Finally, we computed the average AUC, combining information across readers, separately for "higher quality" and "lower quality" images. A *p* value of less than 0.05 was considered statistically significant.

## RESULTS

Patients included in the reader study ranged in ages from 19 to 83 years (mean = 48.6; SD = 17.2). This was which was not statistically different (*P* = .92) from the total population of patients from whom the lesions were initially collected (ranging from 13-92 years; mean = 48.7; SD = 17.1). Table SIMPOP illustrates the pathologic diagnoses of all the lesions collected from routine clinical practice compared to the lesions included in the reader study.

### *Correlation of probability assessments*

The correlation between readers' probability assessments based on B-mode imaging ranged from 0.581-0.819 with an average correlation of 0.675. This correlation improved with strain imaging for each reader and on average. (Table IOV1). These correlations were all statistically significant (*P* < .001). In addition, the correlation of the two superior readers (B and C) was statistically significantly better than the correlation of either reader A and B (*P* < .001) and A and C (*P* < .01).(26)

### *ROC Curve Area*

The AUC values for the three radiologists and the group as a whole without and with strain images are shown in Table AUC. While each radiologist improved in the assessment of the risk

of malignancy when strain imaging was available, only Reader 1 demonstrated a statistically significant improvement. The improvement of the average AUC with strain imaging for the group as a whole also was statistically significant ( $P < 0.012$ ). The actual average ROC curves achieved without and with strain imaging are shown in Figure ROC.

#### *Sensitivity and Specificity*

Using probabilities as risk estimates, patients and physicians can decide against biopsy if the chance of malignancy is low. A 2% threshold is commonly used in mammography to forgo biopsy in favor of imaging follow-up.(27-29) Table S&S illustrates the sensitivity and specificity achieved at a 2% probability of malignancy. At this level, strain imaging allowed readers to improve specificity while maintaining sensitivity. If the decision to biopsy was based on this threshold, each reader could have avoided benign biopsies (Reader A = 1, Reader B = 6, Reader C = 11) without missing a breast cancer.

#### *Assessment of Inter-observer Variation*

As seen in Table IOV, individual observer AUC values ranged from 0.779 to 0.923 without and 0.830 to 0.949 with strain imaging. The difference in AUCs for readers A and B were statistically significant for B-mode ( $p=.002$ ) and strain ( $p=.01$ ) as was the difference for readers A and C for B-mode ( $p=.0006$ ) and strain ( $p=.0005$ ). There was no statistically significant difference between the AUCs of Reader B and C. In terms of sensitivity at the 2% threshold level, all readers performed at a high level without a statistically significant difference. Differences in specificity were significant for readers A and B for B-mode ( $p=.043$ ) and strain ( $p=.006$ ), and for readers A and C for B-mode ( $p=.045$ ) and strain (.0001), but not for readers B and C.

#### *Quality measures*

The average DQM was 19.9 (SD = 10.6) for malignant lesions and 35.6 (SD = 16.8) for benign lesions, which represents a statistically significant difference ( $P < .0001$ ). In order to determine if quality influenced performance, we assessed the correlation of the DQM with both the radiologists' subjective quality assessment and performance. Overall, there was a statistically significant correlation between the DQM and the radiologists' quality assessment (Table QUALCORR1). Readers B and C appeared to have superior correlations between their subjective quality scores and the DQM than Reader A which parallels AUC performance. In addition, this correlation appeared to be stronger for benign abnormalities as compared to malignant ones.

In order to determine whether quality influenced overall performance we divided the cases into the 50 best and 50 worst image sequences based on the DQM. Subset analysis of performance for these groups does show that performance was worse in the "lower quality" image sets (in both B-mode and strain) but these differences were not statistically significant (Table QUALCORR2).

Finally, we analyzed whether transducer type made a difference in terms of image quality and radiologist performance. Four cases included in the reader study did not specify the type of transducer used. For the remaining 96 cases, the VFX13-5 transducer demonstrated a statistically significantly better DQM ( $P < .001$ ), average AUC for B-mode ( $P < .05$ ) and average AUC for strain ( $P < .05$ ) as compared to the 7.5L40 transducer (Table TRANSDUCER).

## DISCUSSION

Our research demonstrates that incorporation of strain imaging into the radiologists' prediction that a solid breast mass is malignant can improve specificity without sacrificing sensitivity and elevate the overall AUC. The ability of strain imaging to contribute to accurate

discrimination of benign and malignant solid breast masses which is consistent with foregoing research.(5, 6) But this is the first evidence that strain image quality may influence the performance of radiologists using this data for risk predictions as measured by the area under the ROC curve. In this study, rather than ask the radiologist for their ultimate management decision (which might be determined predominantly by B-mode imaging and a radiologists prior training) we used a probability threshold as a surrogate for the decision to biopsy. The 2% threshold for the decision to biopsy has been well accepted in mammography practice.(27, 28) At this threshold, incorporation of strain imaging into the radiologists' prediction that a solid breast mass is malignant can improve specificity without sacrificing sensitivity.

The performance improvement we see in this study occurs in patients drawn from actual clinical practice. Even though we selected the cases for the reader study based on high quality and enriched our number of malignant cases for our reader study, we kept the proportion of diagnoses within categories (benign, high risk, and malignant) constant. The mean age between all cases and cases in the reader study remained the same. Therefore, we believe our cases are generalizable to routine clinical practice. The fact that we used clinical cases collected from two different institutions reinforces the diversity of our case mix. We believe this is a first step to integrating strain imaging into decision-making in clinical practice which will need to be further studied in a prospective manner.

Interobserver variability is a commonly-cited and important shortcoming for ultrasound imaging in general which we verified and extended to strain imaging in our study. Specifically, two readers performed significantly better than the third on both B-mode and strain imaging interpretation despite similarities between the physicians' training, experience, and accreditation. We found moderate correlation between the probability assessments of each combination of

reader pairs but the correlation between the two superior performers was statistically different than the single reader with inferior performance. Interestingly this correlation measuring reader agreement uniformly improved for each reader with strain imaging. Though the source of this interobserver variability cannot be gleaned from our study due to small sample size, future studies will hopefully determine if it can be overcome with training and experience. In fact, it is important to remember that the radiologists in our study were virtual novices in the application of strain imaging to risk assessment and decision-making. Each reader had only a short introduction to the technique before evaluation of performance commenced. Investigators with vast experience with strain imaging have achieved excellent discrimination between benign and malignant masses with 100% and specificity of 75.4% in a series of 169 lesions.(30)

Our ability to quantify the quality of the strain image enriches our data analysis. By using the DQM measurement we were able to remove images where lateral and/or out of plane motion degraded the image. In this way, we were able to present the radiologist with the highest quality images that best capture axial deformation for our reader study. Using this new parameter influenced our study in several ways. First, there were more benign lesions in the total number of cases collected (61%) as compared to the reader study (50%). Therefore, there were more high quality images within the benign group to choose from. That is why the DQM of the benign masses was statistically significantly better than the malignant lesions in our reader study. Second, using the DQM measurement to remove images that were suboptimal from both the B-mode and the strain image cine loop may have degraded the B-mode image enough to influence B-mode performance. While this technique is necessary to keep the B-mode and strain images in sync, it likely explains why the performance of B-mode discrimination between malignant and benign masses degraded in parallel with DQM. Specifically, as overall DQM decreases, more

images are excluded from the B-mode and strain cine loop, making the lesion “jump” due to missing images. Further optimization of the strain quality and its implications on B-mode will be important in the future.

There was a somewhat poor correlation of radiologist assessed image quality to the DQM. Only Reader C’s quality assessments correlated with the DQM to a statistically significant degree for all lesions. In addition, the correlation between the radiologists’ quality assessment and the DQM appeared to be much better for benign masses than for malignant ones. In fact, Readers B and C, the superior performers, showed a moderate and statistically significant correlation between quality assessments and DQM in benign cases, while no radiologist achieved a significant correlation with DQM for malignant masses. It is possible that radiologists judge benign strain images as higher quality because they appear similar to the B-mode images while strain images of malignant masses are extremely different in terms of contrast and lesion size. While this is only a possible explanation, it is indirect evidence that these readers have a somewhat limited understanding of the strain images. Other investigators more experienced with the strain imaging technique have demonstrated a high correlation between subjective quality assessments and the DQM ( $r = 0.87$ ).<sup>(30)</sup> It is possible that with continued training and experience, radiologist performance may improve to these levels, but further study with larger patient and reader populations is necessary to confidently assert the strength and nature of the relationship between quality and performance.

Overall, we did discover that ability of radiologists to recognize the quality of images can predict performance, Average AUC was better in the lower-quality images as compared to the higher quality images though this did not reach statistical significance. Interestingly, average performance improved to almost exactly the same degree with strain images over B-mode in the

50 higher-quality and 50 lower-quality images. Therefore, quality may affect overall AUC but may not preclude strain imaging from improving upon this baseline level of performance.

We were surprised to find that the transducer type made a difference in the radiologists' ability to discriminate between benign and malignant masses. It is possible that this phenomenon relates to the fact that the 7.5L-40 was used earlier in data collection and the imagers collecting data were still learning how to acquire high quality strain data. It is also possible that differences in resolution may account for these differences. Unfortunately, due to small sample size, further subset analysis is not possible. This finding does warrant further study.

Our results mirror the work of other investigators in several ways. We find that strain imaging is able to differentiate between benign and malignant masses and radiologists can assess the features of strain imaging such as contrast and size differential. The novel discoveries of this research include the fact that integration of strain characteristics actually can improve radiologist decision-making. Radiologists use image features and experience to make a decision to biopsy solid breast masses on ultrasound. Unfortunately, imaging features such as lesion shape, margins, echogenicity and posterior acoustic features between malignant and benign masses overlap and sometimes simply reiterate similar characteristics on mammography. Perhaps the fact that strain imaging provides an entirely different feature that can be weighed independently in these judgments explains why this technique can improve the performance of radiologists already diligently weighing conventional imaging features (as encoded in the BI-RADS lexicon). Minimizing benign breast biopsies is a goal that has been cited as important despite the inability of any imaging modality alone to achieve it. In our study, strain imaging added patients to those that might not be biopsied based on a 2% threshold for biopsy, an accepted level based on

mammography. This improvement in specificity came without a cost in sensitivity which is valuable.

There are limitations to our study. First, our study is a retrospective analysis with three radiologists and a limited number of patients potentially limiting the ability to generalize our results to prospectively assessed imaging features and strain images over a diverse group of radiologists and patients. In addition, our retrospective design probably allowed radiologists more time to assess findings without and with strain imaging than would be available in actual clinical practice. Previous investigators have demonstrated that evaluations of strain image analysis done in the “laboratory” may confer performance advantages over those done in a busy clinical environment.(18) Only a prospective evaluation of these techniques on actual clinical patients will resolve this question. Second, it is important to emphasize that our study cases were selected based on quality. This fact limits the ability to generalize our results to other practices where a full range of quality was present. It will be important in future studies to determine the quality that must be achieved before using strain imaging data for clinical decisions.

In conclusion, we find that ultrasound strain imaging has potential to aid radiologists in the differentiation of malignant and benign solid breast masses and, therefore, has the potential to improve the decision to perform breast biopsy. Such decisions have a high impact on the efficacy of breast cancer screening programs in terms of cost and quality. Our work also demonstrates that further research will be important to understand how image quality and interobserver variability attenuate the contribution of strain imaging to performance. This work also demonstrates the need for improvements in strain image quality and better tools to aid radiologists in interpreting strain images. Prospective trials are now necessary to confirm that strain imaging is a promising tool for radiologists in the accurate diagnosis of breast cancer.

Table SIMPOP. Pathologic diagnoses

Diagnosis	All cases		Study cases	
	#	%	#	%
<b>Benign (total)</b>	246	0.61	50	0.5
Fibroadenoma	132	32.8%	27	27.0%
Complex cyst	24	6.0%	5	5.0%
Normal tissue	19	4.7%	2	2.0%
Fibrocystic chang	13	3.2%	3	3.0%
Stromal fibrosis	13	3.2%	3	3.0%
Fat necrosis/scar	8	2.0%	2	2.0%
Inflammation	8	2.0%	2	2.0%
Intraductal papilloma	6	1.5%	1	1.0%
Lymph node (benign)	6	1.5%	1	1.0%
Abcess	3	0.7%	1	1.0%
Phylloides	3	0.7%	1	1.0%
Lipoma	3	0.7%	1	1.0%
Duct ectasia	3	0.7%	1	1.0%
Ductal hyperplasia	1	0.2%	0	0.0%
Hematoma	1	0.2%	0	0.0%
Galactocele	1	0.2%	0	0.0%
Hamartoma	1	0.2%	0	0.0%
Tubular adenoma	1	0.2%	0	0.0%
<b>High risk lesions (total)</b>	3	0.007	1	0.01
ADH	1	0.2	1	1.0
LCIS	2	0.5	0	0.0
<b>Malignant (total)</b>	154	0.382	49	0.49
IDC	133	33.0%	42	41.2%
ILC	12	3.0%	3	2.9%
Mixed	4	1.0%	2	2.0%
DCIS	5	1.2%	2	2.0%
	403	100.0%	100	100.0%

Table AUC. ROC Areas

	B-mode	95% CI	B-mode & Strain	95% CI	P-value
Reader 1	0.779	.691, .867	0.830	.752, .908	0.011
Reader 2	0.916	.859, .972	0.929	.878, .980	0.51
Reader 3	0.923	.872, .974	0.949	.912, .986	0.11
Average	0.872	.837, .907	0.903	.870, .936	0.021

Table S&S. Sensitivity and specificity

	Sensitivity					Specificity				
	B-mode	95% CI	Strain	95% CI	P	B-mode	95% CI	Strain	95% CI	P
Reader 1	50/50	.929, 1.0	50/50	.929, 1.0	1.0	2/50	.005, .137	3/50	.013, .165	1.0
Reader 2	48/50	.862 , .995	49/50	.894, .999	1.0	10/50	.100, .337	16/50	.195, .467	.07
Reader 3	50/50	.929, 1.0	50/50	.929, 1.0	1.0	9/50	.086, .314	20/50	.264, .548	<.001
Average	148/150	.968, 1.00	149/150	.980, 1.00	1.0	21/150	.081, .199	39/150	.124, .258	<.001

Table IOV1. Correlation of reader's probability assessments

	Correlation (Std Err)			
	B Mode	95% CI	Strain	95% CI
Reader1/Reader2	0.581	.477, .684	0.614	.498, .730
Reader1/Reader3	0.625	.486, .764	0.708	.569, .847
Reader2/Reader3	0.819	.705, .932	0.834	.724, .944
Average	0.675	.582, .767	0.718	.645, .791

Table QUALCORR1. Correlation between radiologist assessed quality and DQM

	All		Malignant		Benign	
	Correlation	P-value	Correlation	P-value	Correlation	P-value
Reader 1	0.07	0.49	0.17	0.24	-0.06	0.69
Reader 2	0.15	0.13	-0.10	0.50	0.41	0.002
Reader 3	0.30	0.002	0.09	0.54	0.47	0.0005
Average	0.26	0.01	0.05	0.73	0.42	0.003

Table QUALCORR2. Association between quality and average performance

	AUC higher- quality	95% CI	AUC lower- quality	95% CI	P-value
B-mode	.900	.841, .959	.823	.733, .913	.15
Strain	.932	.887, .977	.857	.776, .937	.11

Table TRANSDUCER. Association between quality and average performance

	# cases	DQM	Average AUC
7.5L40 (7.2 MHz)	25	18	.860
VFX13-5 (10 MHz)	71	31	.917
unknown	4	22	NA

Figure INTERFACE

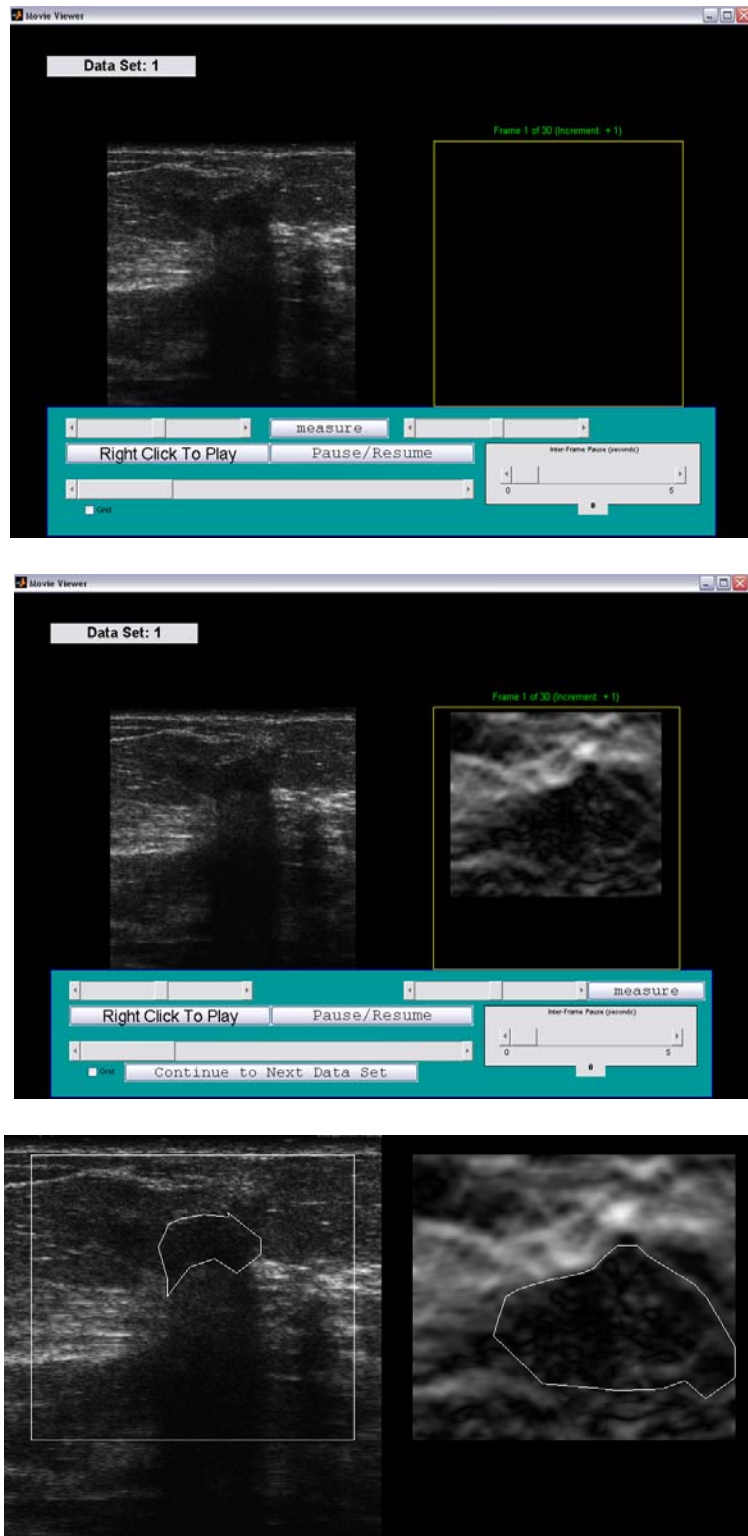


Figure MALIGex

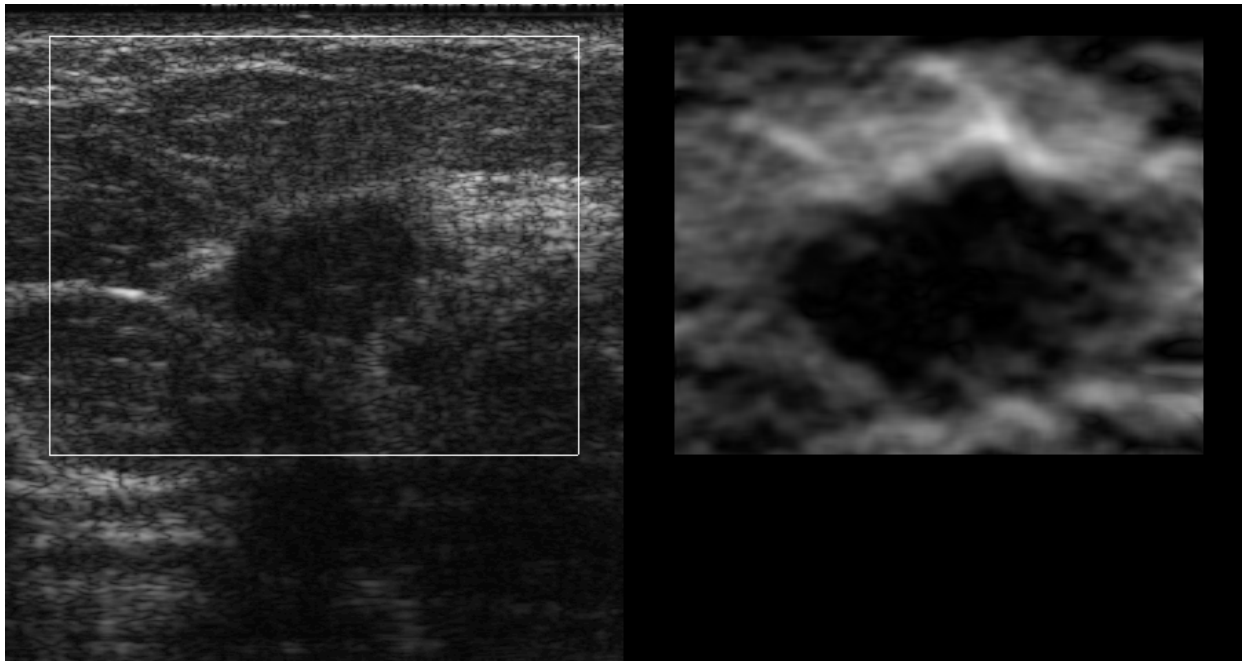


Figure BENIGNex

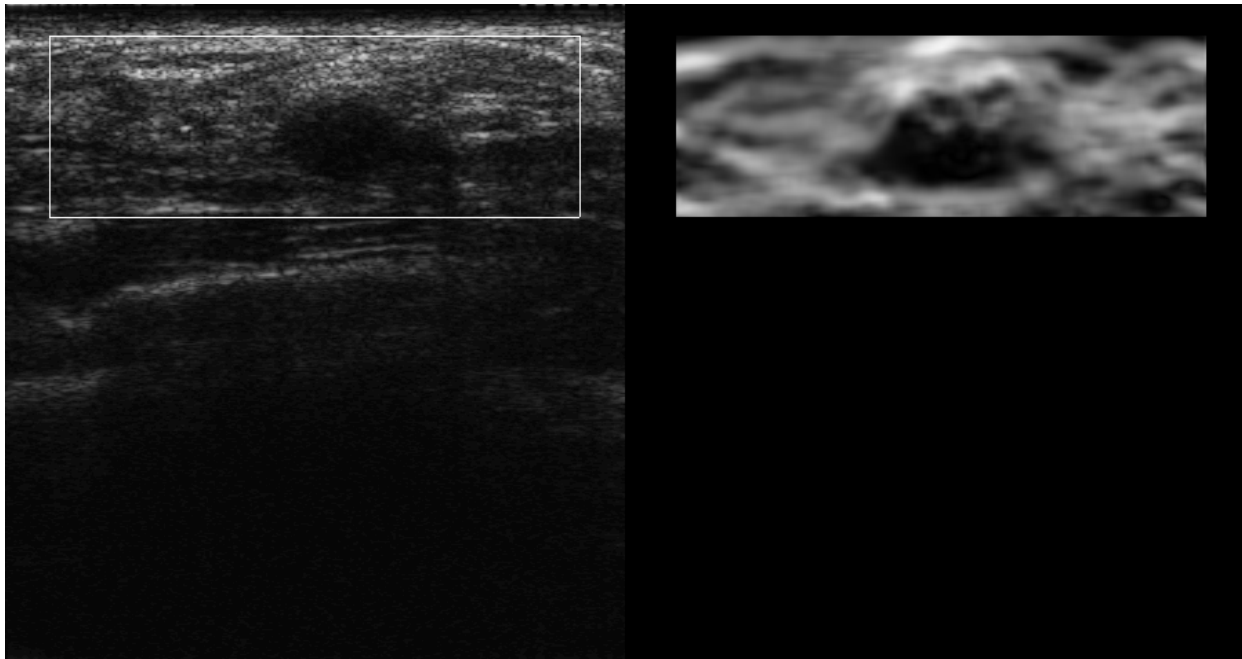


Figure ROC

Will contain 4 ROC curves (1 for each reader and then an average comparing B-mode and strain)

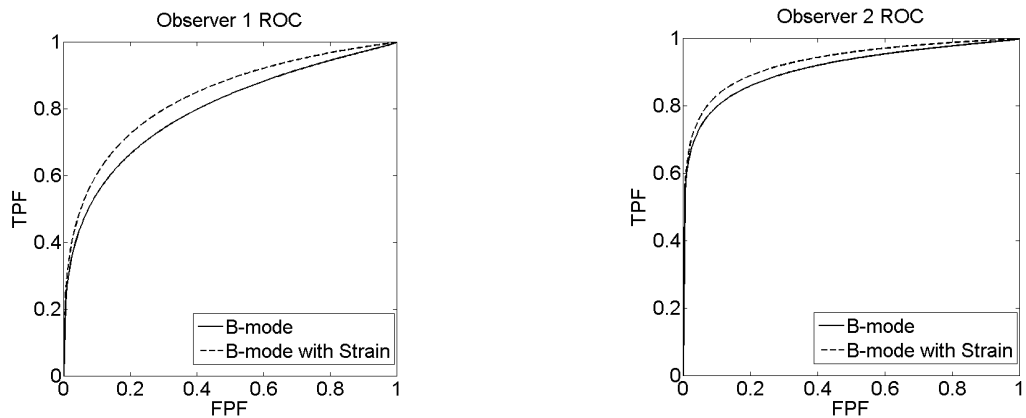


Figure 1

Figure 2

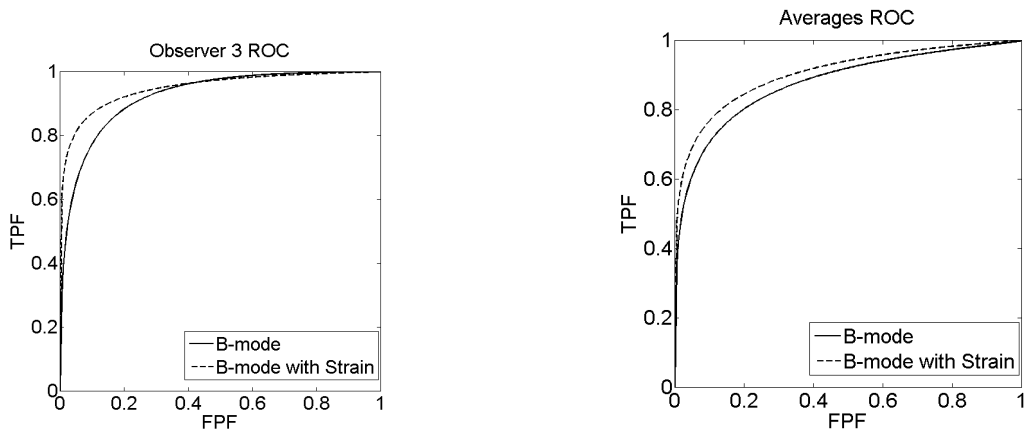


Figure 3

Figure 4

## Legends

**Figure INTERFACE.** Example of the side-by-side display of the B-mode ultrasound image (left image) and ultrasound strain image (right image) of a benign/malignant abnormality as presented in the reader study.

**Figure MALIGex.** Ultrasound B-mode and strain image of an invasive ductal carcinoma.

**Figure BENIGNex.** Ultrasound B-mode and strain image of benign fibroadenoma

**Figure ROC.** Graphic representation of the Average ROC curves.

List of analysis (must include in M&M, results, and discussion)

Comparison of study patients and overall population (table)

Correlation of readers' probability assessments (table IOV1)

AUC areas (table AUC)

Sensitivity and specificity (table S&S)

Comparing readers AUC, sens, and spec (text)—now it is table IOV2

Correlation of each reader with DQM (table QUALCORR 1)

Correlation of Bad and Good images with performance (table QUALCORR 2)

Differential performance between transducers (TRANSDUCER)

1. Poplack SP, Carney PA, Weiss JE, Titus-Ernstoff L, Goodrich ME, Tosteson AN. Screening mammography: costs and use of screening-related services. *Radiology* 2005; 234:79-85.
2. Stavros AT, Thickman D, Rapp CL, Dennis MA, Parker SH, Sisney GA. Solid breast nodules: use of sonography to distinguish between benign and malignant lesions.[see comment]. *Radiology* 1995; 196:123-134.
3. Bruening W, Launders J, Pinkney N, Kostinsky H, Schoelles K, Turkelson C. Effectiveness of Noninvasive Diagnostic Tests for Breast Abnormalities. Comparative Effectiveness Review No. 2. (Prepared by ECRI Evidence-based Practice Center under Contract No. 290-02-0019.) Rockville, MD: Agency for Healthcare Research and Quality, February 2006.
4. Doyley MM, Bamber JC, Fuechsel F, Bush NL. A freehand elastographic imaging approach for clinical breast imaging: system development and performance evaluation. *Ultrasound Med Biol* 2001; 27:1347-1357.
5. Garra BS, Cespedes EI, Ophir J, et al. Elastography of breast lesions: initial clinical results. *Radiology* 1997; 202:79-86.
6. Hall TJ, Zhu Y, Spalding CS. In vivo real-time freehand palpation imaging. *Ultrasound Med Biol* 2003; 29:427-435.
7. Hiltawsky KM, Kruger M, Starke C, Heuser L, Ermert H, Jensen A. Freehand ultrasound elastography of breast lesions: clinical results. *Ultrasound Med Biol* 2001; 27:1461-1469.
8. Insana MF, Pellet-Barakat C, Sridhar M, Lindfors KK. Viscoelastic imaging of breast tumor microenvironment with ultrasound. *J Mammary Gland Biol Neoplasia* 2004; 9:393-404.
9. Lerner RM, Huang SR, Parker KJ. "Sonoelasticity" images derived from ultrasound signals in mechanically vibrated tissues. *Ultrasound Med Biol* 1990; 16:231-239.
10. Lubinski MA, Emelianov Y, O'Donnell M. Adaptive strain estimation using retrospective processing. *IEEE Trans Ultrason Ferroelectr Freq Control* 1999; 46:97-107.
11. Nightingale KR, Palmeri ML, Nightingale RW, Trahey GE. On the feasibility of remote palpation using acoustic radiation force. *J Acoust Soc Am* 2001; 110:625-634.
12. O'Donnell M, Skovoroda A, Shapo B, Emelianov S. Internal displacement and strain imaging using ultrasonic speckle tracking. *IEEE Trans Ultrason Ferroelectr Freq Control* 1994; 41:314-325.
13. Ophir J, Alam SK, Garra B, et al. Elastography: ultrasonic estimation and imaging of the elastic properties of tissues. *Proc Inst Mech Eng [H]* 1999; 213:203-233.
14. Ophir J, Cespedes I, Ponnekanti H, Yazdi Y, Li X. Elastography: a quantitative method for imaging the elasticity of biological tissues. *Ultrason Imaging* 1991; 13:111-134.
15. Ophir J, Kallel F, Varghese T. Elastography: a systems approach. *Int J Imaging Syst Tech* 1997; 8:89-103.
16. Pesavento A, Lorenz A, Ermet H. System for real-time elastography. *Elect Lett* 1999; 35:941-942.
17. Regner DM, Hesley GK, Hangiandreou NJ. Initial clinical experience with ultrasound strain imaging for the evaluation of breast masses [abstr]. *Radiology* 2003; 229P:213.
18. Regner DM, Hesley GK, Hangiandreou NJ, et al. Breast lesions: evaluation with US strain imaging--clinical experience of multiple observers. *Radiology* 2006; 238:425-437.

19. Skovoroda A, Emelianov S, O'Donnell M. Tissue elasticity reconstruction based on ultrasonic displacement and strain images. *IEEE Trans Ultrason Ferroelectr Freq Control* 1995; 42:747-765.
20. Hangiandreou NJ, Meixner DM, Hesley GK. Ultrasound strain image data obtained in breast masses: preliminary quantitative analysis [abstr]. *Ultrasound Med Biol* 2003; 29:S178.
21. Zhu Y, Hall TJ. A modified block matching method for real-time freehand strain imaging. *Ultrason Imaging* 2002; 24:161-176.
22. Jiang J, Hall T, Sommer A. Simultaneous performance assessment and image formation: A novel method for performance validation of ultrasonic strain imaging. submitted to *IEEE Trans Med Imag* 2006.
23. Jiang J, Hall T, Sommer A. A novel performance descriptor for ultrasonic strain imaging: A preliminary study. accepted in *IEEE Trans Ultrason, Ferroelec, Freq Contr (UFFC)* 2005.
24. Efron B, Tibshirani R. Bootstrap methods for standard errors, confidence intervals, and other measures of statistical accuracy. *Statistical Science* 1986; 1.
25. Metz CE, Herman BA, Roe CA. Statistical comparison of two ROC-curve estimates obtained from partially-paired datasets. *Med Decis Making* 1998; 18:110-121.
26. Olkin I, Finn J. Testing Correlated Correlations. *Psychological Bulletin* 1990; 108:330-333.
27. Sickles EA. Periodic mammographic follow-up of probably benign lesions: results in 3,184 consecutive cases. *Radiology* 1991; 179:463-468.
28. Varas X, Leborgne JH, Leborgne F, Mezzera J, Jaumandreu S, Leborgne F. Revisiting the mammographic follow-up of BI-RADS category 3 lesions. *AJR Am J Roentgenol* 2002; 179:691-695.
29. Vizcaino I, Gadea L, Andreo L, et al. Short-term follow-up results in 795 nonpalpable probably benign lesions detected at screening mammography. *Radiology* 2001; 219:475-483.
30. Hall TJ, Svensson W, Von Behren P. Lesion size ratio for differentiating breast masses. *IEEE International Ultrasonics Symposium Book of Abstracts* 2003:87-88.

# IN VIVO RESULTS OF REAL-TIME FREEHAND ELASTICITY IMAGING

Timothy J. Hall, Yanning Zhu, Candace S. Spalding, and Larry T. Cook

Department of Radiology, University of Kansas Medical Center

3901 Rainbow Boulevard, Kansas City, KS 66160-7234

**Abstract**— We are developing a system for real-time estimation and display of tissue elastic properties using a clinical ultrasonic imaging system. Our hypothesis is that real-time feedback of elasticity images is essential in obtaining high-quality data. Extensive experience with laboratory fixtures and off-line processing of elasticity data showed that problems occurring in data acquisition often resulted in poor elasticity image quality. Our experience with real-time freehand elasticity imaging shows that images with high contrast-to-noise can be obtained. Results in volunteer patients have shown that high quality elasticity images are easily obtained *in vivo* in breast and thyroid pathologies. The key element to successful scanning is real-time visual feedback which guides the patient positioning and compression direction. Results show that individual images of axial strain in tissues can be quite misleading and that a ‘movie loop’ of strain images provides significantly more information adding to intuition.

## I. INTRODUCTION

The potential for improving the qualitative nature of palpation by imaging quantitative measures of tissue viscoelasticity has generated a great deal of research and commercial interest world-wide. Our initial efforts focused on modelling displacement and strain, developing algorithms for displacement and strain estimation, and testing those techniques in phantoms and *in vitro* kidneys (see, for example, [1–5]). Significant effort was expended on developing high-order motion estimators for tracking fine-scale motion. However, little

We are grateful for the financial support of USAMRAA DAMD17-00-1-0596 and NSF BES-9708221 and technical support from Siemens Medical Systems Ultrasound Group. The U.S. Army Medical Research Acquisition Activity, 820 Chandler Street, Fort Detrick MD 21702-5014 is the awarding and administering acquisition office for DAMD17-00-1-0596. The information reported here does not necessarily reflect the position or policy of the U.S. Government, and no official endorsement should be inferred.

data were available to investigate the need or utility of the high-order motion estimation techniques for *in vivo* imaging of tissues. The most useful report [6] used relatively crude data acquisition hardware and simple motion tracking software, but this effort clearly demonstrated that strain imaging has merit in breast lesion discrimination.

Our efforts in this study focus on the development of algorithms with the potential for performing strain imaging at substantially real-time frame rates, and implementing and testing those algorithms on a state-of-the-art ultrasound imaging system. Our results demonstrate the value in real-time side-by-side display of B-mode and strain images for guiding data acquisition and data interpretation. Comparisons among different lesion types studied *in vivo* show a significant difference in strain images for cysts, fibroadenoma, and carcinoma.

The report by Garra, et al., [6] described a set of criteria applied to evaluate strain imaging compared to normal B-mode imaging. Among those criteria were lesion visibility, relative brightness, lesion margin regularity, lesion margin definition, lesion size (lateral and axial), B-mode image measurements relative to strain image and pathology measurements. Among their findings, they noted that all benign lesions have about the same width on B-mode and strain images, but the height measurement could not be trusted due to axial blurring in image formation. Fibroadenomas typically were non-uniform in stiffness; cancers were uniformly stiffer than their surroundings in all but one case.

Our results are generally consistent with those found by Garra, et al., but the differences in carcinoma size in B-mode and strain images is greater and all lesions found in sonography or mammography, whether palpable or not, were visible with our techniques. Some of our findings help to understand the shortcomings of

the results reported by Garra and provide even more evidence for the utility of this technique for the discrimination of carcinomas from benign conditions.

## II. MATERIALS AND METHODS

### *Strain Image Formation*

A 2-D block matching algorithm, based on the sum-squared difference (SSD) algorithm, is used for motion tracking in our implementation. With this method, motion is tracked by searching for a kernel of data from the pre-compression rf echo data in a search region of the post-compression rf echo field. The kernel size was selected to approximate the 2-D pulse-echo ultrasound point spread function for the system employed (Siemens SONOLINE Elegra with 7.5L40 and VFX13-5 linear arrays). Data were processed on the Image Processor subsystem of the Elegra. This subsystem hosts two Texas Instruments TMS320C80 processors. The SSD algorithm exceeds the computational capacity of the Image Processor subsystem. To reduce the computational load, an adaptive search strategy was developed which reduces the size of the required search region in performing the SSD block matching. The resulting algorithm displays streaming B-mode and strain images side-by-side at about eight frames per second and stores the full sequence of I-Q echo data at full bus speed for on-line post-processing.

Echo data obtained while scanning phantoms with motorized and freehand compression result in equivalent strain image contrast and resolution when the average strain in the image is the same for the two methods. Displacement variance is slightly higher for freehand compression, and the frame-to-frame strain is not constant, but this is a small penalty for the ease of freehand scanning. In fact, small (e.g., 2.4mm diameter) spherical targets are considerably easier to locate and scan with freehand compared to motorized compression.

### *Patient Scanning*

All patients provided informed consent consistent with the protocol approved by the Human Subjects Committee (Institutional Review Board) at Kansas University Medical Center. Patient scans were performed in a manner consistent with a normal breast ultrasound exam; the breast was scanned with the patient (typically) in the supine position with her arm behind her head. When the breast lesion was located,

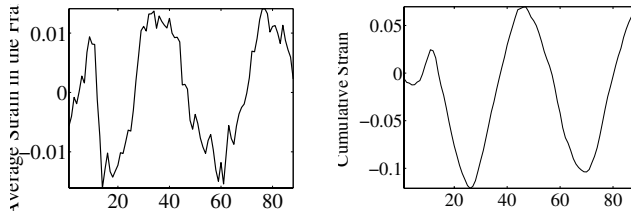
the transducer was pressed toward the chest wall at a steady rate in an effort to achieve about 1–1.5% compression frame-to-frame. In some cases, for example when scanning lateral lesions in large (D-cup) breasts, the patient was rolled slightly to her contralateral side so that gravity would flatten the breast tissue in the region to be scanned. Using this scanning technique, no patient has experienced any discomfort in our procedures.

The scanning procedure began, following lesion localization, by repeating the compress/release cycle for relatively large (>10%) compression while watching the B-mode image. The compression technique was adjusted, by changing the compression direction or patient position, until there was nearly uniaxial compression with minimal elevation motion. With this achieved, the strain imaging software was enabled to evaluate the quality of the sequence of strain images. If a large sequence (<30 frames) of strain images had good image quality (relatively high contrast-to-noise ratio) and high frame-to-frame similarity, the data acquisition was frozen, the image sequence stored, and select images recorded on-line. If the compression was too slow resulting in low frame-average strain, the inter-frame skip was adjusted to increase the strain between frame pairs used in displacement and strain estimation, as suggested by Lubinski, et al., [7]. A representative result for a 3mm cyst is shown in figure 1.

A similar scanning technique was used to acquire data from several thyroids. The scanning technique began by viewing the thyroid in a B-mode image during compress/release cycles to determine the preferred probe position and compression direction. The goal for the average strain between adjacent frames and the total cumulative strain are the same as before. We have much less experience with Palpation Imaging of the thyroid (compared with breast), however, figure 2 proves that high quality strain images can be obtained.

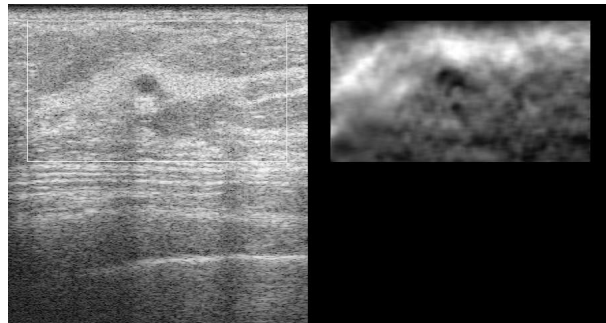
## III. RESULTS

One of the most promising uses of this technology is differentiation among breast lesions. To date we have successfully scanned 42 breast patients. Among these patients we have acquired data from 25 cysts, 18 fibroadenomas, and six carcinomas. Each of these lesion types has a distinctive behavior in its strain image under cyclic compression. Cysts have well-defined



(a) Average strain.

(b) Cumulative strain.



(c) B-mode and strain images as displayed on the Elegra for frame 40 in the sequence.

Fig. 1. Data obtained by freehand scanning of a breast cyst *in vivo*. The average strain per frame (a) suggests nearly ideal compression rate in this case. The adjacent frames were used in analyzing this sequence of data. The cumulative strain in the sequence (b) demonstrates that about a 18% compression range was achieved in this study. A B-mode and strain image pair obtained from this sequence is shown in (c).

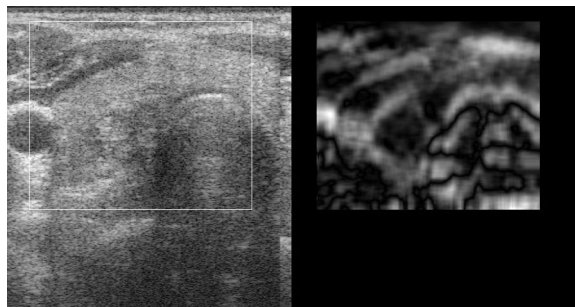


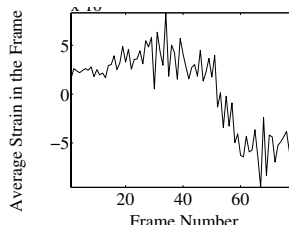
Fig. 2. A B-mode and strain image pair obtained by freehand scanning of a thyroid *in vivo*. A small benign lesion is seen in the lower corner of the thyroid.

boundaries at the top and sides, but sometimes show a very soft bottom layer. That layer might be due to a sediment inside the cystic fluid. The interior echoes within the cysts rapidly decorrelate with com-

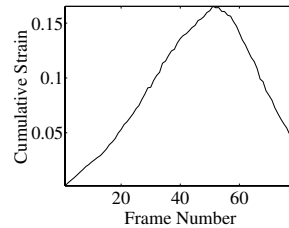
pression. Overall a cyst can be either relatively stiff, as if it were a distended balloon, or relatively soft. Fibroadenomas also (typically) have well-defined boundaries and often have relatively homogeneous interior stiffness. However, some fibroadenomas have heterogeneous strain patterns. All fibroadenomas are more comparable in stiffness to the surrounding tissues than carcinomas. Indeed, fibroadenomas appear to have a nonlinear stress-strain relationship relative to their surroundings as illustrated in figure 3. All carcinomas studied so far were invasive ductal carcinomas that were easily diagnosed from mammogram and sonogram results.

In an effort to compare lesion size in the two imaging modalities, we transferred the data to an off-line computer for further analysis. We reprocessed the strain images using the exact algorithm implemented on the Elegra. Movie loops of the side-by-side B-mode and strain image pairs (avi files) were created to view the motion of the lesion in the B-mode image and the resulting strain image. A representative frame was selected that showed the "typical" strain image for that lesion, and the B-mode image was displayed allowing the lesion border to be traced. The lesion width (and height) were estimated as the maximum dimension parallel (and perpendicular) to the acoustic beam. The tracing and measurement process was then repeated with the strain image from that same frame. Example images for a fibroadenoma and a carcinoma are shown in figure 4.

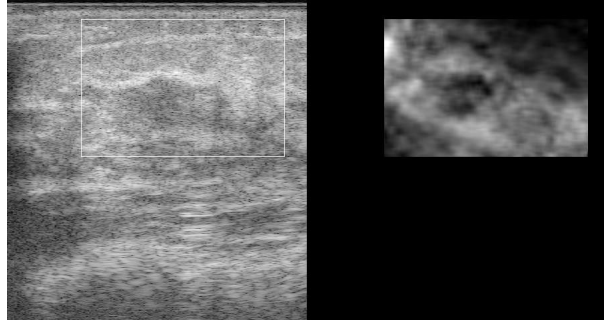
It is intriguing to examine the relative size of these lesions comparing their width, height, and area as measured in B-mode and strain images. Garra, et al., suggested that the width of a carcinoma in a strain image is typically larger than that measured in a B-mode image. Our results support that observation, and apparently extend its diagnostic utility. Figure 5(a) shows plots of the width and height of these three lesion types as measured in B-mode and strain images. Figure 5(b) shows plots of a similar comparison of the total area of the lesion in the two imaging modes. Our results show that the width and height of benign lesions tend to be about the same size in B-mode and strain images and carcinomas are larger in strain images than B-mode, but the separation between benign and carcinoma is much larger when we use the lesion area.



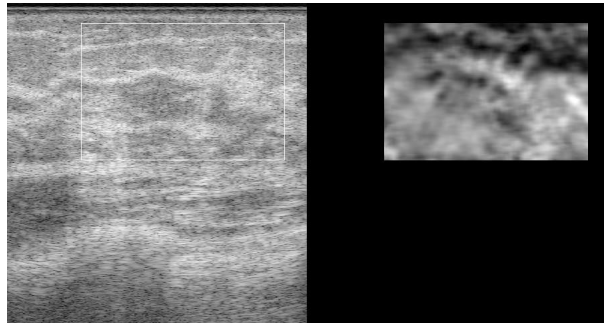
(a) Average strain.



(b) Cumulative strain.



(c) B-mode and strain images for frame 38. A similar image is found at frame 53.

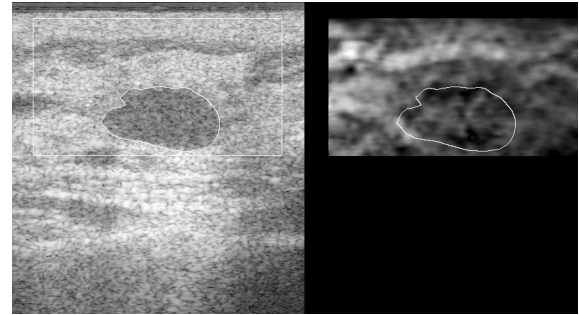


(d) B-mode and strain images for frame 8. A similar image is found at frame 72.

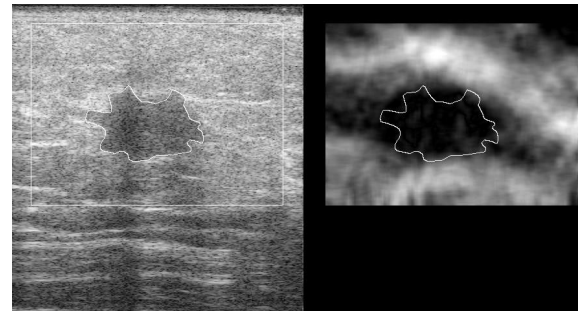
Fig. 3. Data obtained by freehand scanning of a fibroadenoma *in vivo*. The average strain per frame (a) suggests a slow compression rate in this case. The inter-frame skip was increased to pair every fourth frame in analyzing this sequence of data. The cumulative strain in the sequence (b) demonstrates that about a 20% compression range was achieved in this study.

#### IV. DISCUSSION

Real-time display of side-by-side B-mode and strain images is essential for guiding the manipulation of boundary conditions for the mechanics experiment that



(a) B-mode and strain images of a fibroadenoma.

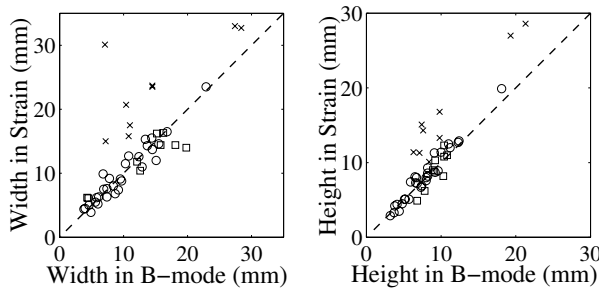


(b) B-mode and strain images of an invasive ductal carcinoma.

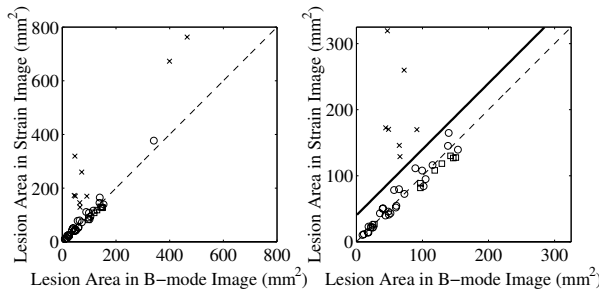
Fig. 4. B-mode and strain images of lesions with their perimeter traced in the B-mode image, and that tracing also appearing in the strain image for comparison.

is strain imaging. The real-time feedback to the hand-eye coordination systems allows the sonographer to manipulate the compression direction, force, and rate to obtain high-quality sequences of strain images. The system involves no addition fixtures or remote data acquisition or signal processing hardware. It is fully integrated into the Elegra system.

Our results show significantly different strain image sequences for each lesion type studied. Although the range of lesion types does not include all those found in breasts, they do include the vast majority of types. It was found that to appreciate the differences among lesion types, and to determine the “typical” strain image for a given lesion, it was necessary to observe a sequence of B-mode and strain images displayed side-by-side. With that sequence, a very reproducible determination of the lesion boundary could be obtained. Measurements of lesion dimension were then made



(a) Plots of the lesion linear dimension.



(b) Plots of lesion area. All lesions are included in left plot. Only those smaller than about 1cm dia are shown in plot on the right.

Fig. 5. Plots comparing the size of a lesion traced in the B-mode image versus the same lesion traced in a representative strain image for cysts ( $\circ$ ), fibroadenomas ( $\square$ ), and invasive ductal carcinomas ( $\times$ ). The dashed line in each image represents equal size measurement in both images. The solid straight line (lower right plot) suggests that a simple linear discriminant would completely separate carcinomas from benign lesions based on lesion.

and the results for lesion width are consistent with those reported by Garra, et al. That report stated a lack of confidence in their measurements of lesion height. Our results with cylindrical and spherical targets in phantoms show that we can accurately measure lesion dimension in both height and width, and therefore we use lesion area as the criterion for comparing lesion size in B-mode and strain images.

The smoothly varying strain contrast appears to be unique to fibroadenomas so far in our experience. Smoothly varying contrast suggests that the stress-strain relationship for the fibroadenoma does not parallel that of the surrounding tissue. Fibroadenomas that vary in strain contrast appear dark (stiffer) at low precompression and lose contrast (become relatively

softer) at higher precompression. This suggests that the stress-strain relationship for the surrounding tissue is likely more nonlinear than that of the fibroadenoma.

The sequence of B-mode and strain image pairs allows the sonographer to select images representative of the “typical” strain image for a lesion. This ability, along with better determination of lesion boundary available by viewing a sequence of images, has likely improved the ability to measure true lesion size in strain imaging compared with the results reported by Garra, et al.

## V. CONCLUSIONS

A new system for real-time imaging of tissue strain in vivo using freehand scanning is described and some of the results obtained with this system are reported. The new system provides real-time feedback allowing the user to manipulate the conditions of tissue compression resulting in the ability to successfully scan all patients for which the technique was attempted. The strain images for various lesion types are unique, and the relative size of the lesions appears to be a strong candidate for discriminating benign from cancerous lesions. However, further testing will be needed to support this observation.

## REFERENCES

- [1] P. Chaturvedi, M. F. Insana, and T. J. Hall, “2-D companding for noise reduction in strain imaging,” *IEEE Trans Ultrason, Ferroelec, Freq Cont*, vol. 45, no. 1, pp. 179–191, 1998.
- [2] P. Chaturvedi, M. F. Insana, and T. J. Hall, “Testing the limitations of 2-D companding for strain imaging using phantoms,” *IEEE Trans Ultrason, Ferroelec, Freq Cont*, vol. 45, no. 4, pp. 1022–1031, 1998.
- [3] T. J. Hall, M. Bilgen, M. F. Insana, and T. A. Krouskop, “Phantom materials for elastography,” *IEEE Trans Ultrason, Ferroelec, Freq Cont*, vol. 44, no. 6, pp. 1355–1365, 1997.
- [4] M. F. Insana, P. Chaturvedi, T. J. Hall, and M. Bilgen, “3-D companding using linear arrays for improved strain imaging,” *Proc IEEE Ultrason Symp*, vol. 97CH36118, pp. 1435–1438, 1997.
- [5] Y. Zhu, P. Chaturvedi, and M. Insana, “Strain imaging with a deformable mesh,” *Ultrasonic Imaging*, vol. 21, pp. 127–146, 1998.
- [6] B. S. Garra, I. Céspedes, J. Ophir, S. R. Spratt, R. A. Zuurbier, C. M. Magnant, and M. F. Pennanen, “Elastography of the breast: Initial clinical results,” *Radiology*, vol. 202, pp. 79–86, 1997.
- [7] M. A. Lubinski, S. Y. Emelianov, and M. O’Donnell, “Adaptive strain estimation using retrospective processing,” *IEEE Trans Ultrason, Ferroelec, Freq Cont*, vol. 46, no. 1, pp. 97–107, 1999.

# IN VIVO REAL-TIME FREEHAND ELASTICITY IMAGING

*Timothy J. Hall, Yanning Zhu, Candace S. Spalding, and Larry T. Cook*

Department of Radiology, University of Kansas Medical Center  
3901 Rainbow Boulevard, Kansas City, KS 66160-7234

## ABSTRACT

We are developing a system for real-time estimation and display of tissue elastic properties using a clinical ultrasonic imaging system. Results in phantoms are in excellent agreement with that predicted with finite element analysis. Results in volunteer patients have shown that high quality elasticity images are easily obtained *in vivo* in breast and thyroid pathologies. The key element to successful scanning is real-time visual feedback which guides the patient positioning and compression direction. Results show that the frame-to-frame changes in strain image contrast appear to be unique to specific lesion types. In addition, the size of a lesion displayed in a strain image, relative to that in a standard B-mode image, is about the same for benign lesions but the size is considerably larger for malignant lesions. The observations will likely significantly improve the discrimination of radiologically indeterminant lesions.

## 1. INTRODUCTION

The potential for improving the qualitative nature of palpation by imaging quantitative measures of tissue viscoelasticity has generated a great deal of research and commercial interest world-wide. Our initial efforts focused on modelling displacement and strain, developing algorithms for displacement and strain estimation, and testing those techniques in phantoms and *in vitro* kidneys (see, for example, [1-5]). Significant effort was expended on developing high-order motion estimators for tracking fine-scale motion. However, little data were available to investigate the need or utility of the high-order motion estimation techniques for *in vivo* imaging of tissues. The most useful report [6] used relatively crude data acquisition hardware and simple motion tracking software, but this effort clearly demonstrated that strain imaging has merit in breast lesion discrimination.

---

We are grateful for the financial support of USAMRAA DAMD17-00-1-0596 and NSF BES-9708221 and technical support from Siemens Medical Systems Ultrasound Group. The U.S. Army Medical Research Acquisition Activity, 820 Chandler Street, Fort Detrick MD 21702-5014 is the awarding and administering acquisition office for DAMD17-00-1-0596. The information reported here does not necessarily reflect the position or policy of the U.S. Government, and no official endorsement should be inferred.

Our recent efforts focus on the development of algorithms with the potential for performing strain imaging at substantially real-time frame rates, and implementing and testing those algorithms on a state-of-the-art ultrasound imaging system. Our results demonstrate the value in real-time side-by-side display of B-mode and strain images for guiding data acquisition and data interpretation. Comparisons among different lesion types studied *in vivo* show a significant difference in strain images for cysts, fibroadenoma, and carcinoma.

The report by Garra, et al., [6] described a set of criteria applied to evaluate strain imaging compared to normal B-mode imaging. Among those criteria were lesion visibility, relative brightness, lesion margin regularity, lesion margin definition, lesion size (lateral and axial), B-mode image measurements relative to strain image and pathology measurements. Among their findings, they noted that all benign lesions have about the same width on B-mode and strain images, but their height measurement could not be trusted due to axial blurring in image formation. Fibroadenomas typically were non-uniform in stiffness; cancers were uniformly stiffer than their surroundings in all but one case.

Our results are generally consistent with those found by Garra, et al., but the differences in carcinoma size in B-mode and strain images is greater and all lesions found in sonography or mammography, whether palpable or not, were visible with our techniques. Viewing the sequence of images, available from our techniques, helps to understand the shortcomings of the results reported by Garra and provides even more evidence for the utility of this technique for the discrimination of carcinomas from benign conditions.

## 2. MATERIALS AND METHODS

### 2.1. Strain Image Formation

A 2-D block matching algorithm, based on the sum-squared difference (SSD) algorithm, is used for motion tracking in our implementation. With this method, motion is tracked by searching for a kernel of data from the pre-compression rf echo data in a search region of the post-compression rf echo field. The kernel size was selected to approximate the

2-D pulse-echo ultrasound point spread function for the system employed (Siemens SONOLINE Elegra with 7.5L40 and VFX13-5 linear arrays). Data were processed on the Image Processor subsystem of the Elegra. This subsystem hosts two Texas Instruments TMS320C80 processors. The SSD algorithm exceeds the computational capacity of the Image Processor subsystem. To reduce the computational load, an adaptive search strategy was developed which reduces the size of the required search region in performing the SSD block matching. The resulting algorithm displays streaming B-mode and strain images side-by-side at about eight frames per second and stores the full sequence of I-Q echo data at full bus speed for on-line post-processing.

Echo data obtained while scanning phantoms with motorized and freehand compression result in equivalent strain image contrast and resolution when the average strain in the image is the same for the two methods. Displacement estimation error variance for freehand compression is also about the same as with motorized compression, but the frame-to-frame strain is not constant. This is a small penalty for the ease of freehand scanning. In fact, small (e.g., 2.4mm diameter) spherical targets are considerably easier to locate and scan with freehand compared to motorized compression.

## 2.2. Patient Scanning

All patients provided informed consent consistent with the protocol approved by the Human Subjects Committee (Institutional Review Board) at Kansas University Medical Center. Patient scans were performed in a manner consistent with a normal breast ultrasound exam; the breast was scanned with the patient (typically) in the supine position with her arm behind her head. When the breast lesion was located, the transducer was pressed toward the chest wall at a steady rate in an effort to achieve about 1–1.5% compression frame-to-frame. In some cases, for example when scanning lateral lesions in large (D-cup) breasts, the patient was rolled slightly to her contralateral side so that gravity would flatten the breast tissue in the region to be scanned. Using this scanning technique, no patient has experienced any discomfort in our procedures.

The scanning procedure began, following lesion localization, by repeating the compress/release cycle for relatively large ( $>10\%$ ) compression while watching the B-mode image. The compression technique was adjusted, by changing the compression direction or patient position, until there was nearly uniaxial compression with minimal elevation motion. With this achieved, the strain imaging software was enabled to evaluate the quality of the sequence of strain images. If a large sequence ( $<30$  frames) of strain images had good image quality (relatively high contrast-to-noise ratio) and high frame-to-frame similarity, the data acquisition was frozen, the image sequence stored, and select images

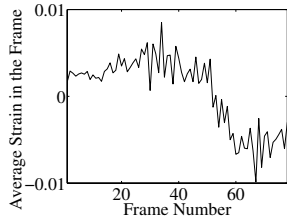
recorded on-line. If the compression was too slow resulting in low frame-average strain, the inter-frame skip was adjusted to increase the strain between frame pairs used in displacement and strain estimation, as suggested by Lubinski, et al., [7].

## 3. RESULTS

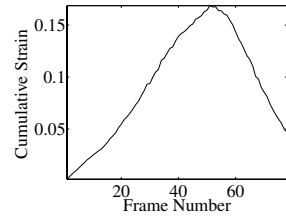
One of the most promising uses of this technology is differentiation among breast lesions. To date we have successfully scanned 42 breast patients. Among these patients we have acquired data from 25 cysts, 18 fibroadenomas, and six carcinomas. Each of these lesion types has a distinctive behavior in its strain image under cyclic compression. Cysts have well-defined boundaries at the top and sides, but sometimes show a very soft bottom layer. That layer might be due to a sediment inside the cystic fluid. The interior echoes within the cysts rapidly decorrelate with compression. Overall a cyst can be either relatively stiff, as if it were a distended balloon, or relatively soft. Fibroadenomas also (typically) have well-defined boundaries and often have relatively homogeneous interior stiffness. However, some fibroadenomas have heterogeneous strain patterns. All fibroadenomas are more comparable in stiffness to the surrounding tissues than carcinomas. Indeed, fibroadenomas appear to have a nonlinear stress-strain relationship relative to their surroundings as illustrated in figure 1. All carcinomas studied so far were invasive ductal carcinomas that were easily diagnosed from mammogram and sonogram results.

In an effort to compare lesion size in the two imaging modalities, we transferred the data to an off-line computer for further analysis. We reprocessed the strain images using the exact algorithm implemented on the Elegra. Movie loops of the side-by-side B-mode and strain image pairs (avi files) were created to view the motion of the lesion in the B-mode image and the resulting strain image. A representative frame was selected that showed the “typical” strain image for that lesion, and the B-mode image was displayed allowing the lesion border to be traced. The lesion width (and height) were estimated as the maximum dimension perpendicular (and parallel) to the acoustic beam. The tracing and measurement process was then repeated with the strain image from that same frame. Example images for a fibroadenoma and a carcinoma are shown in figure 2.

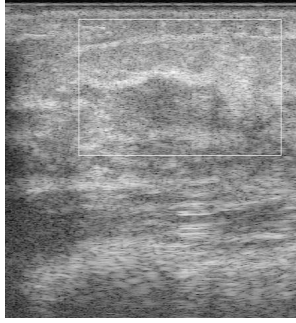
It is intriguing to examine the relative size of these lesions comparing their width, height, and area as measured in B-mode and strain images. Garra, et al., suggested that the width of a carcinoma in a strain image is typically larger than that measured in a B-mode image. Our results support that observation, and apparently extend its diagnostic utility. Figure 3 shows plots of the total area of three lesion types as measured in B-mode and strain images. Our results show



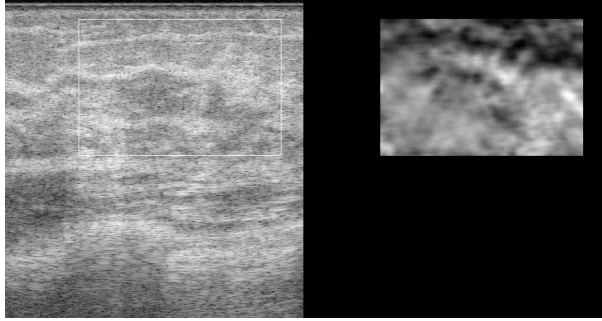
(a) Average strain.



(b) Cumulative strain.



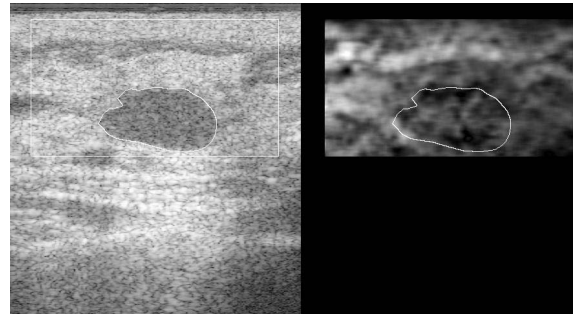
(c) B-mode and strain images for frame 44. A similar image is found at frame 59.



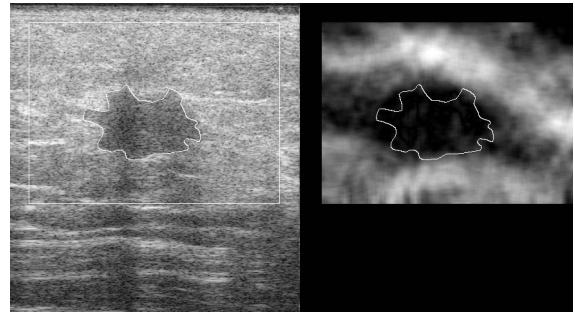
(d) B-mode and strain images for frame 17. A similar image is found at frame 77.

**Fig. 1.** Data obtained by freehand scanning of a fibroadenoma *in vivo*. The average strain per frame (a) suggests a slow compression rate in this case. The inter-frame skip was increased to pair every fourth frame in analyzing this sequence of data. The cumulative strain in the sequence (b) demonstrates that about a 20% compression range was achieved in this study.

that the size of benign lesions tend to be about the same size in B-mode and strain images and carcinomas are larger in strain images than B-mode, but the separation between benign and carcinoma is much larger when we use the lesion area.



(a) B-mode and strain images of a fibroadenoma.



(b) B-mode and strain images of an invasive ductal carcinoma.

**Fig. 2.** B-mode and strain images of lesions with their perimeter traced in the B-mode image, and that tracing also appearing in the strain image for comparison.

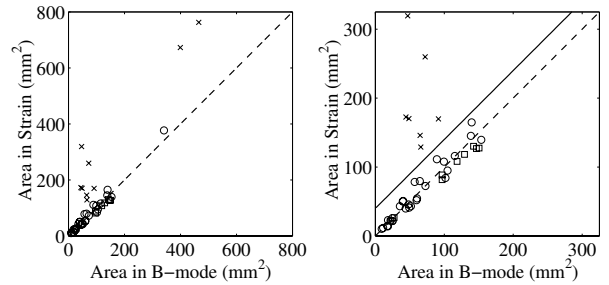


**Fig. 3.** Plots comparing the size of a lesion traced in the B-mode image versus the same lesion traced in a representative strain image for cysts (○), fibroadenomas (□), and invasive ductal carcinomas (x). All lesions are included in left plot. Only those smaller than about 1cm dia are shown in plot on the right. The dashed line in each image represents equal size measurement in both images. The solid straight line (right plot) suggests that a simple linear discriminant would completely separate carcinomas from benign lesions based on lesion area.

#### 4. DISCUSSION

Real-time display of side-by-side B-mode and strain images is essential for guiding the manipulation of boundary conditions for the mechanics experiment that is strain imaging. The real-time feedback to the hand-eye coordination systems allows the sonographer to manipulate the compression direction, force, and rate to obtain high-quality sequences of strain images. The system involves no addition fixtures or remote data acquisition or signal processing hardware. It is fully integrated into the Elegra system.

Our results show significantly different strain image sequences for each lesion type studied. Although the range of lesion types does not include all those found in breasts, they do include the vast majority of types. It was found that to appreciate the differences among lesion types, and to determine the “typical” strain image for a given lesion, it was necessary to observe a sequence of B-mode and strain images displayed side-by-side. With that sequence, a very reproducible determination of the lesion boundary could be obtained. Measurements of lesion dimension were then made and the results for lesion width are consistent with those reported by Garra, et al. That report stated a lack of confidence in their measurements of lesion height. Our results with cylindrical and spherical targets in phantoms show that we can accurately measure lesion dimension in both height and width, and therefore we use lesion area as the criterion for comparing lesion size in B-mode and strain images.

The smoothly varying strain contrast appears to be unique to fibroadenomas so far in our experience. Smoothly varying contrast suggests that the stress-strain relationship for the fibroadenoma does not parallel that of the surrounding tissue. Fibroadenomas that vary in strain contrast appear dark (stiffer) at low pre-compression and lose contrast (become relatively softer) at higher pre-compression. This suggests that the stress-strain relationship for the surrounding tissue is likely more nonlinear than that of the fibroadenoma.

The sequence of B-mode and strain image pairs allows the sonographer to select images representative of the “typical” strain image for a lesion. This ability, along with better determination of lesion boundary available by viewing a sequence of images, has likely improved the ability to measure true lesion size in strain imaging compared with the results reported by Garra, et al.

This new imaging modality is based on a standard clinical ultrasound imaging system and is simply an added software program. It could run on any system with the appropriate architecture and sufficient computational capacity. This is particularly exciting because that would allow this technology to propagate inexpensively to existing systems. In addition, because it is based on standard clinical ultrasound, it can be safely used serially on young or pregnant

women. Further, since ultrasound systems are portable and relatively inexpensive, this technology can easily propagate to medically-under server areas.

#### 5. CONCLUSIONS

A new system for real-time imaging of tissue strain in vivo using freehand scanning is described and some of the results obtained with this system are reported. The new system provides real-time feedback allowing the user to manipulate the conditions of tissue compression resulting in the ability to successfully scan all patients for which the technique was attempted. The strain images for various lesion types are unique, and the relative size of the lesions appears to be a strong candidate for discriminating benign from cancerous lesions. However, further testing will be needed to support this observation.

#### 6. REFERENCES

- [1] Pawan Chaturvedi, Michael F. Insana, and Timothy J. Hall, “2-D companding for noise reduction in strain imaging,” *IEEE Trans Ultrason, Ferroelec, Freq Cont*, vol. 45, no. 1, pp. 179–191, 1998.
- [2] Pawan Chaturvedi, Michael F. Insana, and Timothy J. Hall, “Testing the limitations of 2-D companding for strain imaging using phantoms,” *IEEE Trans Ultrason, Ferroelec, Freq Cont*, vol. 45, no. 4, pp. 1022–1031, 1998.
- [3] Timothy J. Hall, Mehmet Bilgen, Michael F. Insana, and Thomas A. Krouskop, “Phantom materials for elastography,” *IEEE Trans Ultrason, Ferroelec, Freq Cont*, vol. 44, no. 6, pp. 1355–1365, 1997.
- [4] Michael F. Insana, Pawan Chaturvedi, Timothy J. Hall, and Mehmet Bilgen, “3-D companding using linear arrays for improved strain imaging,” *Proc IEEE Ultrason Symp*, vol. 97CH36118, pp. 1435–1438, 1997.
- [5] Yanning Zhu, P. Chaturvedi, and M.F. Insana, “Strain imaging with a deformable mesh,” *Ultrasonic Imaging*, vol. 21, pp. 127–146, 1998.
- [6] Brian S. Garra, Ignacio Céspedes, J. Ophir, Stephen R. Spratt, R. A. Zuurbier, C. M. Magnant, and M. F. Pennanen, “Elastography of the breast: Initial clinical results,” *Radiology*, vol. 202, pp. 79–86, 1997.
- [7] Mark A. Lubinski, Stanislav Y. Emelianov, and Matthew O’Donnell, “Adaptive strain estimation using retrospective processing,” *IEEE Trans Ultrason, Ferroelec, Freq Cont*, vol. 46, no. 1, pp. 97–107, 1999.

# NOISE REDUCTION STRATEGIES IN FREEHAND ELASTICITY IMAGING

Timothy J. Hall, Jingfeng Jiang, Yanning Zhu, Larry T. Cook  
Department of Radiology, University of Kansas Medical Center  
3901 Rainbow Boulevard, Kansas City, KS 66160-7234

**Abstract**— We are developing a clinical ultrasonic imaging system for real-time estimation and display of tissue elastic properties. We have demonstrated that real-time feedback of elasticity images is essential for obtaining high-quality data (consecutive images with high spatial coherence). The key element to successful scanning is real-time visual feedback which guides the patient positioning and compression direction. Our data have clearly demonstrated nonlinearity in the strain properties of different tissue types. We have also demonstrated that a comparison of the area of a breast lesion observed in strain images versus B-mode images is a sensitive criterion for differentiating malignant from benign tumors. Frame-to-frame variability in strain images somewhat degrades the ability to observe these phenomena. Three strategies for reducing frame-to-frame strain image noise are described. The combination of these post-processing strategies provides a significant improvement in the quality of long sequences of strain images.

## I. INTRODUCTION

We are implementing and testing real-time mechanical strain imaging integrated into a clinical ultrasound imaging system (Elegra, Siemens Medical Solutions) [1]. Our work was motivated by promising *in vivo* results reported by Garra et al. [2]. In that report they described data acquisition based on a modified mammography system. The use of that system limited the areas of the breast from which they could acquire data.

We are grateful for the financial support of USAMRAA DAMD17-00-1-0596 and technical support from Siemens Medical Systems Ultrasound Group. The U.S. Army Medical Research Acquisition Activity, 820 Chandler Street, Fort Detrick MD 21702-5014 is the awarding and administering acquisition office for DAMD17-00-1-0596. The information reported here does not necessarily reflect the position or policy of the U.S. Government, and no official endorsement should be inferred.

Freehand scanning has been the dominant method of clinical sonography for many years. So, freehand scanning will likely more quickly gain clinical acceptance of elasticity imaging if it can be performed efficiently. We have argued that real-time feedback to the hand-eye coordination system allows constant manipulation of the boundary conditions of deformation and allows the observer to know when high quality strain image data are acquired. The small delay between acquiring successive frames (tens of milliseconds) and the relatively slow deformation rate (cyclic freehand deformation at about 1 Hz) likely results in primarily an elastic response in tissue (minimal viscous effect) [3].

*In vivo* elasticity images of breast lesions obtained with our system have high contrast-to-noise ratios. In fact, relatively long sequences (30 sequential frames or more) of high quality strain images are normally obtained in clinical trials. An example image from a breast tumor is shown in Fig. 1. Using our system we have demonstrated that broadenomas often have a surface pressure-dependent strain image contrast [1]. The strain image contrast for a broadenoma is generally highest with the least surface pressure and contrast decreases as the pressure is increased. In addition, the relative size of a lesion in B-mode versus strain images is a sensitive criterion for differentiating malignant from benign lesions [1, 2]. A plot of lesion area measured in B-mode images versus lesion area in the corresponding strain images (Fig. 2) illustrates this performance.

Viewing strain image sequences allows visualization of strain image noise that is not apparent in single strain images. Given that pressure dependent strain image contrast and the relative lesion size comparison are useful criteria for differentiating breast lesions, reducing that frame-to-frame variability in strain estimates will improve the ability to visualize that varying contrast and better determine lesion boundaries.

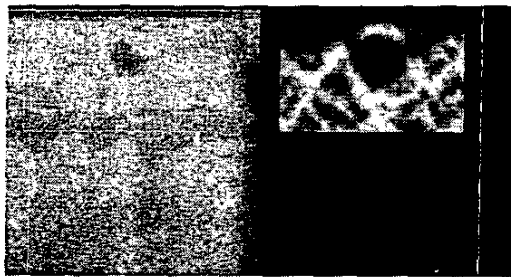


Fig. 1. A B-mode and strain image pair obtained by freehand scanning of a breast carcinoma *in vivo*.

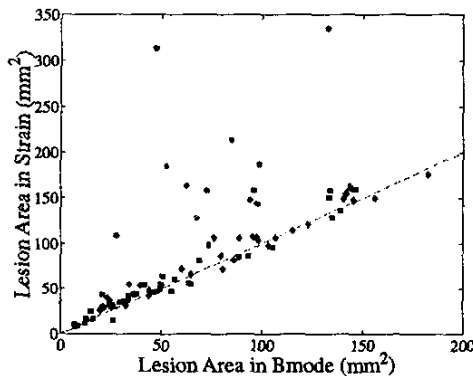


Fig. 2. A comparison of lesion area for carcinomas (circles), cysts (squares) and fibroadenomas (diamonds).

Strategies for reducing that frame-to-frame variability in local strain estimates is the subject of this report. The goal is to reduce noise while maintaining spatial resolution. An additional goal is to obtain reduction in strain image noise with minimal incremental computational load such that the technique can be implemented in on-line processing for clinical trials. Several possible approaches are suggested, and results of implementing those approaches are encouraging.

## II. MATERIALS AND METHODS

### Strain Image Formation

A 2-D block matching algorithm, based on the sum-squared difference (SSD) algorithm, is used for motion tracking in our implementation. The kernel size was selected to approximate the 2-D pulse-echo ultrasound point spread function for the system employed (Siemens SONOLINE Elegra with 7.5L40 and VFX13-5 linear arrays). Data were processed on the

image processor subsystem of the Elegra. The algorithm displays streaming B-mode and strain images side-by-side at about seven frames per second and stores the full sequence of I-Q echo data for on-line post-processing.

### Patient Scanning

All patients provided informed consent consistent with the protocol approved by the Human Subjects Committee (Institutional Review Board) at Kansas University Medical Center. Patient scans were performed in a manner consistent with a normal breast ultrasound exam; the breast was scanned with the patient (typically) in the supine position with her arm behind her head. When the breast lesion was located, the transducer was pressed toward the chest wall at a steady rate in an effort to achieve about 0.5–1.2% compression frame-to-frame while repeating the compress/release cycle for relatively large (>10%) compression. The compression technique was adjusted, by changing the compression direction or patient position, until there was nearly uniaxial compression with minimal elevation motion. Real-time B-mode and strain image display allowed visualization of the data quality. Using this scanning technique, no patient has experienced any discomfort in our procedures.

## III. SOURCES OF NOISE AND STRATEGIES FOR IMPROVED RESULTS

### Small Deformation—Low Average Strain

The strain image contrast-to-noise ratio increases as the applied (uniaxial) strain increases for frame-average strains up to about 5% (see, for example [4]). Freehand deformation sometimes results in nonuniform frame-to-frame average strain. The pairing of rf echo frames of data in post-processing can be adjusted to select appropriate frame pairs to obtain, nominally, 1–1.5% frame-average strain [5]. A representative result for a *in vivo* breast fibroadenoma is shown in figure 3.

### Large Displacement Errors

Regardless of the average applied strain, the motion tracking algorithm, and whether that strain was applied with freehand scanning or motorized deformation, displacement estimation errors sometime occur. When

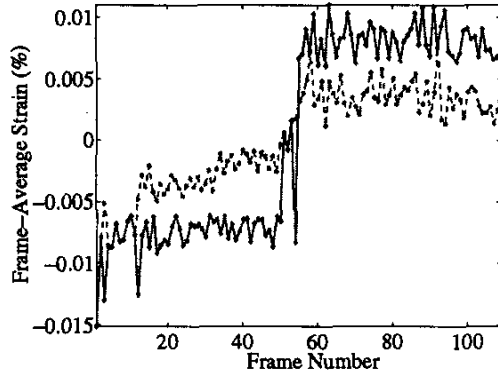


Fig. 3. The frame-to-frame strain obtained by freehand scanning of a breast *in vivo* and pairing adjacent frames (dashed) or dynamically adjusting the frame pairing in post-processing (solid) for strain estimation.

using a very small 2-D kernel to track motion, relatively large errors are easily detected. A statistical argument and a moving linear regression can be used to detect displacement estimates that are so different from their neighbors that they are very unlikely to be correct. For example, if we know that adjacent displacement estimates differences of one sample imply a local strain of 7%, and the frame-average strain is only about 1%, then adjacent displacement estimate differences of more than one sample are extremely unlikely. We can use linear regression to estimate the local displacement and compare each estimate to the local regression fit. If the difference between the individual estimate and the regression value is more than some threshold, for example one sample, that estimate is judged to be in error and is replaced by the regression value. This approach is very effective at detecting and removing large displacement errors prior to estimating local strain. An example of this technique applied to *in vivo* breast data is shown in Fig. 4.

It is straightforward to extend this approach and fit local displacement estimates to a small (planar) surface to detect and exclude large errors. The advantage of using a surface fit is that it minimizes local axial shear. The size of the surface, as with the linear regression window, is a tradeoff between tracking true displacements (resolution) with small surfaces and rejecting consecutive displacement errors (noise reduction) with a longer window. A 2 mm  $\times$  2 mm surface provides subjectively satisfactory results.

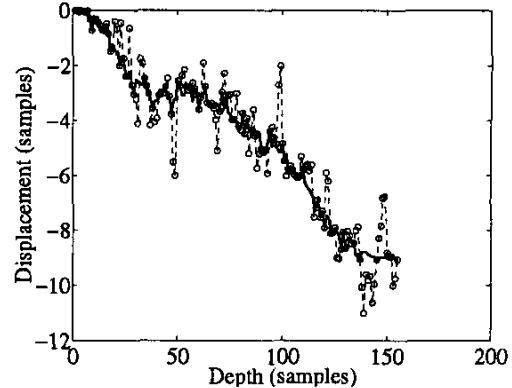


Fig. 4. Displacement estimates resulting from 2-D block matching (dashed) and moving linear regression (solid) for those results as a function of depth for one line of data.

#### Complex Motion

Correlation search techniques for motion tracking, such as that employed for our real-time strain imaging, work well when the deformation is small and the motion is relatively simple [6]. When the motion is relatively large ( $>5\%$  strain) or includes obvious shear the performance of correlation search techniques degrades. Under these conditions higher order motion models typically improve motion tracking performance but at higher computational load [7].

In these techniques, a cost function is defined that minimizes the constraints used to model the motion. The basic approach assumes that the brightness of each point in the image remains constant from one frame of data to the next. A brightness constraint,  $E_b$ , is then used to estimate the deformation field that describes the transformation from one frame of data to the next. That general concept was adapted to rf echo samples, instead of B-mode pixel brightness in our previous work [8]. Our current approach uses the sum squared difference between pre- and warped post-compression echo fields as the brightness constraint. A smoothness constraint,  $E_s$ , is added to the cost function to place a penalty on large deviations from average local motion. Numerous approaches to create smoothness constraints have been reported. One of the earliest smoothness constraints was reported by Horn [9].

From our previous work using similar techniques [8] we recognized the importance of the constraint function in the overall performance of this approach. We

are investigating the use of strain energy as a smoothness constraint function, as suggested by Bajscy [10]. The resulting cost function is

$$C = \iint_{\Omega} (\gamma E_b + E_s) dx dy \quad (1)$$

where  $\gamma$  is an adaptively chosen scale factor. Example images of the same data with and without these noise reduction strategies are shown in Figs. 5 and 6.

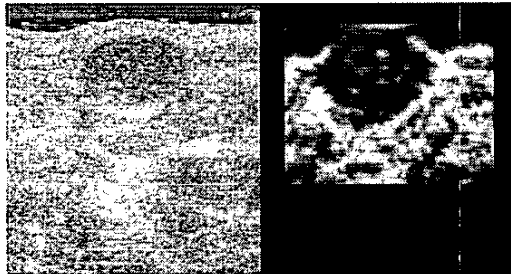


Fig. 5. A B-mode and strain image pair without noise reduction.

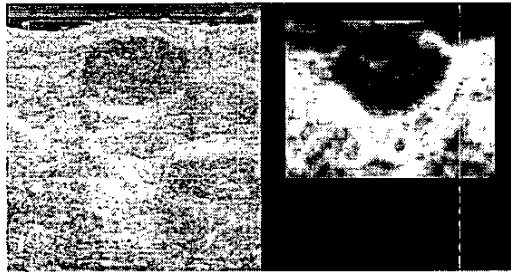


Fig. 6. A B-mode and strain image pair with all three noise reduction strategies.

#### IV. DISCUSSION

Real-time display of side-by-side B-mode and strain images is essential for guiding the manipulation of boundary conditions for the mechanics experiment that is strain imaging. The real-time feedback to the hand-eye coordination systems allows the sonographer to manipulate the compression direction, force, and rate to obtain high-quality sequences of strain images. The system involves no remote data acquisition or display, and no additional signal processing hardware. It is fully integrated into the Elegra system.

The sequence of B-mode and strain image pairs allows the sonographer to select images representative

of the "typical" strain image for a lesion. This ability, along with better determination of lesion boundary available by viewing a sequence of images, has likely improved the ability to measure true lesion size in strain imaging compared with the results reported by Garra, et al.

Deformable model approaches are iterative and require an initial displacement field approximation. When that approximation has large errors, accurate displacement estimates are influenced by the presence of local displacement errors. By first using the above techniques to minimize local displacement errors, we start the deformable model iteration with a reasonable approximation to the true displacement field. The result is a significant reduction in frame-to-frame variability in strain images and improved detection of lesion boundaries and contrast changes.

#### V. CONCLUSIONS

Strategies for reducing strain image noise in a sequence of strain images are described. Tests of these strategies on breast data acquired *in vivo* demonstrate improvements in the image sequence. In combination these strategies provides significant improvements in the visual interpretation of a sequence of strain images.

#### REFERENCES

- [1] T. J. Hall, Y. Zhu, and C. S. Spalding, "In vivo real-time free-hand palpation imaging," *Ultrasound Med Biol*, p. accepted for publication, 2002.
- [2] B. S. Garra, I. Céspedes, J. Ophir, S. R. Spratt, R. A. Zurbier, C. M. Magnant, and M. F. Pennanen *Radiology*, vol. 202, pp. 79–86, 1997.
- [3] T. A. Krouskop, W. TM, F. Kallel, B. S. Garra, and T. J. Hall *Ultrasonic Imaging*, vol. 20, pp. 260–274, 1998.
- [4] P. Chaturvedi, M. F. Insana, and T. J. Hall *IEEE Trans Ultrason, Ferroelec, Freq Cont*, vol. 45, no. 4, pp. 1022–1031, 1998.
- [5] M. A. Lubinski, S. Y. Emelianov, and M. O'Donnell *IEEE Trans Ultrason, Ferroelec, Freq Cont*, vol. 46, no. 1, pp. 97–107, 1999.
- [6] G. E. Trahey, J. W. Allison, and O. T. von Ramm *IEEE Trans Biomed Eng*, vol. BME-34, pp. 965–967, 1987.
- [7] G. E. Mailloux, A. Bleau, M. Bertrand, and R. Petitclerc *IEEE Trans Biomed Eng*, vol. BME-34, pp. 356–364, 1987.
- [8] Y. Zhu, P. Chaturvedi, and M. Insana *Ultrasonic Imaging*, vol. 21, pp. 127–146, 1998.
- [9] B. K. Horn, *Robot Vision*. Cambridge, MA: MIT Press, 1986.
- [10] R. Bajscy and S. Kovacic *Computer vision, graphics and image processing*, vol. 46, pp. 1–21, 1989.

# LESION SIZE RATIO FOR DIFFERENTIATING BREAST MASSES

Timothy Hall<sup>1</sup>, William Svensson<sup>2</sup>, Pat Von Behren<sup>3</sup>, Yanning Zhu<sup>4</sup>,  
Joe Malin<sup>4</sup>, Candace Spalding<sup>4</sup>, Alissa Connors<sup>2</sup>, Dupinder Chopra<sup>2</sup> and Carol Lowery<sup>3</sup>

<sup>1</sup>Medical Physics Department, University of Wisconsin, Madison, WI, USA 53706

<sup>2</sup>Charing Cross Hospital (Hammersmith Hospitals Trust),

Imperial College School of Medicine, London, UK

<sup>3</sup>Siemens Medical Solutions Ultrasound Group, Issaquah, WA, USA

<sup>4</sup>Radiology Department, University of Kansas Medical Center, Kansas City, KS, USA

**Abstract**— We are developing a clinical ultrasonic imaging system for real-time estimation and display of tissue elastic properties. We have demonstrated that real-time feedback of elasticity images is essential for obtaining high-quality data (consecutive images with high spatial coherence). The key element to successful scanning is real-time visual feedback which guides the patient positioning and compression direction. One of our findings, consistent with previous reports, is that benign breast masses are typically about the same size in B-mode and mechanical strain images. However, invasive cancers tend to be significantly larger in strain images than in B-mode images. In this work we continue testing that hypothesis with an increasingly large data set with greater diversity of breast mass types. Results from a single-observer ROC study demonstrate that the lesion size ratio is a useful criterion for classifying benign versus malignant breast masses.

## I. INTRODUCTION

We are implementing and testing real-time mechanical strain imaging integrated into a clinical ultrasound imaging system (SONOLINE Elegra, Siemens Medical Solutions) [1]. Our work was motivated by promising *in vivo* results first reported in the peer-reviewed literature by Garra et al. [2]. In that report they described data acquisition based on a modified mammography system. The use of that system limited the areas of the breast from which they could acquire data and typically only acquired a few frames of echo fields per patient.

Freehand scanning has been the dominant method of clinical sonography for many years. So, freehand scanning will likely more quickly gain clinical acceptance

of elasticity imaging if it can be performed efficiently. We have argued that real-time feedback to the hand-eye coordination system allows constant manipulation of the boundary conditions of deformation and allows the observer to know when high quality strain image data are acquired. The small delay between acquiring successive frames (tens of milliseconds) and the relatively slow deformation rate (cyclic freehand deformation at about 1 Hz) likely results in a mostly elastic response in tissue (minimal viscous effect) [3]. *In vivo* elasticity images of breast lesions obtained with our system have high contrast-to-noise ratios. In fact, relatively long sequences (30 sequential frames or more) of high quality strain images are normally obtained in clinical trials.

Our preliminary tests of this imaging system [1] included a relatively small subject population and scanning was performed by only one sonographer. Results of measurements with five observers making lesion size measurements on that data were very encouraging and suggested nearly perfect separation of benign and malignant lesions. Those results are overly optimistic because of correlation among the data (multiple lesions in the same patients were included), the limited variety of lesion types included (only invasive ductal carcinoma, fibroadenoma and cyst), and the small patient population.

The focus of this study is to further test the hypothesis that the ratio of lesion sizes (strain measurement divided by B-mode measurement) can accurately classify breast masses as benign or malignant. This study includes only uncorrelated data from the previous study (one lesion, and one image sequence, per patient). It also includes data acquired at an additional institution with multiple people performing the ultra-

sound scanning. The subject population is considerably larger and there is a wider variety of lesion types included. It is more limited that the previous study in that only one observer performed the measurements.

Results demonstrate that the lesion size ratio is a sensitive criterion for classifying breast masses. This study also demonstrates that these measurements can be repeated at other institutions, suggesting that the technique and measurements are robust.

## II. MATERIALS AND METHODS

### *Strain Image Formation*

Data were acquired with the Siemens SONOLINE Elegra using either the 7.5L40 or VFX13-5 linear arrays. A 2-D block matching algorithm is used for motion tracking in our implementation [4]. The algorithm displays streaming B-mode and strain images side-by-side at about seven frames per second to ensure acquisition of high-quality data for strain image formation. Data were processed off-line using a more computationally intensive algorithm than currently programmed on the Elegra.

### *Patient Scanning*

Patients were referred to sonography with either a palpable breast lump or indeterminate mammogram, or as follow-up from a previous sonogram. All patients provided informed consent consistent with the protocol approved by the Institutional Review Board at Kansas University Medical Center or the Charing Cross Hospital. Patient scans were performed in a manner consistent with a normal breast ultrasound exam; the breast was scanned with the patient (typically) in the supine position with her arm behind her head. When the breast lesion was located, the transducer was pressed toward the chest wall at a steady rate in an effort to achieve about 0.5–1.2% compression frame-to-frame while repeating the compress/release cycle for relatively large (>10%) compression. The compression technique was adjusted, by changing the compression direction or patient position, until there was nearly uniaxial compression with minimal elevation motion. Real-time B-mode and strain image display allowed visualization of the data quality. Using this scanning technique, no patient has experienced any discomfort in our procedures.

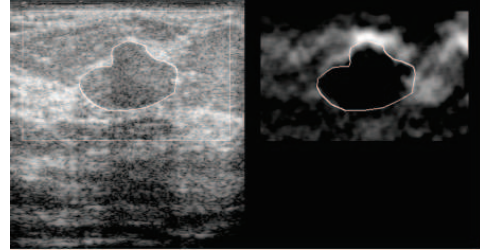


Fig. 1. A B-mode and strain image pair obtained by freehand scanning of an in vivo breast fibroadenoma.

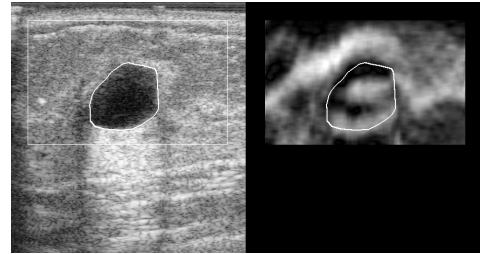


Fig. 2. Freehand strain imaging of an in vivo breast cyst.

To date over 250 lesions have been scanned. The average patient age in this group is about 43yrs old. All lesions included in this study were either biopsied or surgically excised for identification. Example images from in vivo breast masses are shown in Figs. 1, 2 and 3. In those figures the lesion is traced in the B-mode image and that tracing is also displayed in the strain image.

The relatively large lesion size displayed in strain images of invasive ductal carcinomas, compared to the size displayed in the corresponding B-mode image, suggests that a comparison of these sizes is most effective when the breast mass is relatively small in both image modalities. This difficulty is illustrated in Fig. 4.

Other significant difficulties with in vivo elasticity

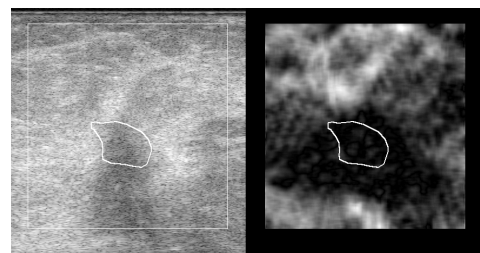


Fig. 3. Freehand strain imaging of an in vivo invasive ductal carcinoma.

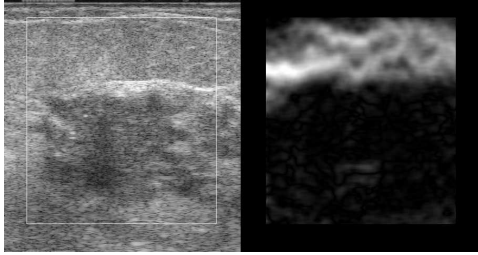


Fig. 4. Freehand strain imaging of a relatively large invasive ductal carcinoma.

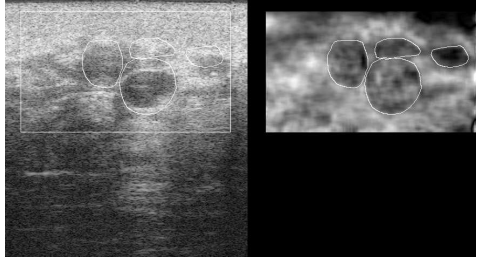


Fig. 5. Freehand strain imaging of an in vivo breast cyst cluster.

imaging occur when multiple closely spaced lesion are imaged, as shown in Fig. 5. In these situations, the boundary conditions for motion of the individual lesions is affected by the motion of the other neighboring lesions. Motion can be quite complex, or the cluster of lesions can behave as a single large object. In either case, the strain image can be more difficult to interpret. In early clinical trials we are avoiding these cases to focus effort on lesions that are separated by at least twice their major dimension from any other nearby lesion.

Eliminating lesion clusters, as shown in Fig. 5, multiple views of the same lesion, multiple lesions in the same patient, lesions that were not biopsied, etc. we have 169 unique data sets. Among these are 43 cancers (38 invasive ductal carcinoma, 1 ductal carcinoma in situ, 2 mucinous carcinoma, 1 invasive lobular carcinoma, 1 invasive apocrine carcinoma) and 126 benign lesions (69 fibroadenoma, 40 cyst, 5 lymph nodes, 4 inflammation, 2 ductal ectasia, 6 other benign conditions).

Using our system we have demonstrated that fibroadenomas often have a surface pressure-dependent strain image contrast [1]. The strain image contrast for a fibroadenoma is generally highest with the least surface pressure and contrast decreases as the pressure is increased. Fibroadenomas tend to be imaged at their largest size when data are acquired with minimal sur-

face pressure. The nonlinear stress-strain relationship of many fibroadenomas, compared to their surrounding tissue, results in the apparent size of those lesion getting smaller as the surface pressure is increased. Therefore, lesion size measurements are generally made with the lowest pre-compression (largest lesion size) for which consistent strain images are obtained.

### III. RESULTS

Plots of lesion size ratio (strain/B-mode) versus lesion area measured in the corresponding B-mode image are shown in Figs. 6 and 7. The red line in those figures represents the lowest possible linear threshold to separate all cancers in this data set from most benign lesions. Lesions with an area ratio larger than the threshold value are likely cancer; those below the threshold are very likely benign and could potentially avoid being biopsied. ROC analysis for the continuous lesion area ratio data results in  $A_z = 0.930 \pm 0.019$ .

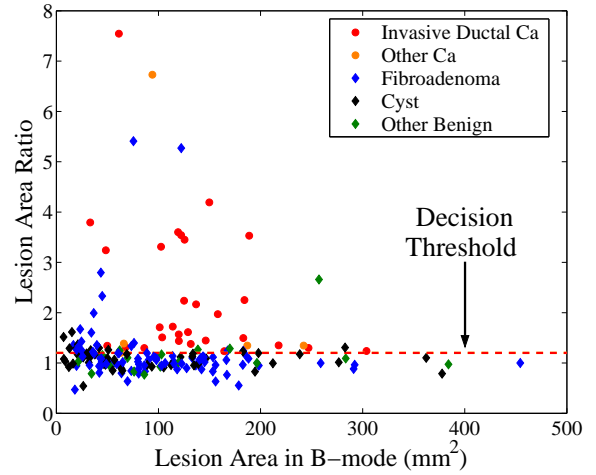


Fig. 6. A comparison of lesion area for breast carcinomas and benign breast masses.

### IV. DISCUSSION

The ability to accurately and reproducibly determine the boundary of breast masses is greatly increased when the observer is provided with a movie clip of the ultrasound scan instead of a single frame B-mode image. Viewing that relative motion is also very helpful in interpreting strain images of in vivo breast masses.

The performance of this single criterion for classifying breast masses is impressive when compared to the set of criteria proposed by Stavros et al. [5]. Given the relatively young average age of this patient group,

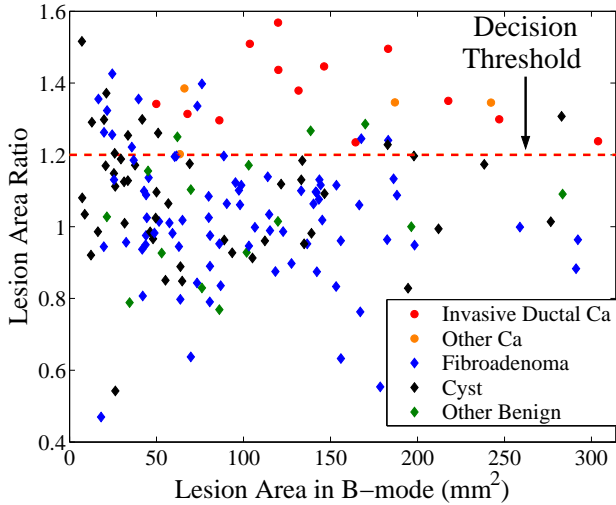


Fig. 7. A comparison of lesion area for a variety of in vivo breast masses. This is a subset of the data shown in Fig. 6 with the axes scaled to highlight lesions below 1cm in effective diameter.

TABLE I  
RESULTS OF SETTING A LINEAR DECISION THRESHOLD TO  
SEPARATE ALL CANCERS FROM MOST BENIGN BREAST  
MASSSES, AS SHOWN IN FIGS. 6 AND 7. B-MODE SONOGRAPHY  
DATA ARE FROM [5], AND FIRST-SCREEN MAMMOGRAPHY  
DATA ARE FROM [6].

Criterion	Area Ratio	B-mode Sono	1 <sup>st</sup> -Screen Mammo
Sensitivity	100%	98.4%	69%
Specificity	75.4%	67.8%	94%
PPV	56.9%	38%	8.6%
NPV	100%	100%	99.7%

this approach holds great promise for diagnosing breast masses in young women. Women under 50 years of age often have mammographically-dense breasts that significantly reduce the ability to confidently identify small breast abnormalities.

The performance of the lesion area ratio as a diagnostic criterion in broad range of breast mass types is encouraging. This study was sufficiently large to include less common types of cancers such as mucinous and apocrine carcinomas. All cancer types, including ductal carcinoma in situ, were found to have increased stiffness in the area outside that seen in the corresponding B-mode image. This phenomenon was expected for invasive ductal carcinoma where collagen, fibrin

and elastin infiltrate the normal tissue surrounding the lesion. The source of this increased area of stiffness in these other types of cancers is not yet understood.

## V. CONCLUSIONS

The ratio of the lesion area seen in strain images to that seen in the corresponding B-mode images appears to be a very useful criterion for separating malignant from benign breast masses. This parameter integrated into a broader set of criteria, such as that proposed by Stavros, et al. [5] would likely further improve the diagnostic accuracy of breast sonography.

## VI. ACKNOWLEDGEMENTS

We are grateful for the financial support of US-AMRMC DAMD17-00-1-0596 and technical support from Siemens Medical Systems Ultrasound Group. The U.S. Army Medical Research Acquisition Activity, 820 Chandler Street, Fort Detrick MD 21702-5014 is the awarding and administering acquisition office for DAMD17-00-1-0596. The information reported here does not necessarily reflect the position or policy of the U.S. Government, and no official endorsement should be inferred.

## REFERENCES

- [1] T. J. Hall, Y. Zhu, and C. S. Spalding, "In vivo real-time free-hand palpation imaging," *Ultrasound Med Biol*, vol. 29, no. 3, pp. 427–435, 2002.
- [2] B. S. Garra, I. Céspedes, J. Ophir, S. R. Spratt, R. A. Zuurbier, C. M. Magnant, and M. F. Pennanen, "Elastography of the breast: Initial clinical results," *Radiology*, vol. 202, pp. 79–86, 1997.
- [3] T. A. Krouskop, W. TM, F. Kallel, B. S. Garra, and T. J. Hall, "The elastic moduli of breast and prostate tissues under compression," *Ultrasonic Imaging*, vol. 20, pp. 260–274, 1998.
- [4] Y. Zhu, M. F. Insana, P. Chaturvedi, T. J. Hall, L. T. Cook, J. M. Gauch, and H. A. Khant, "Deformable mesh algorithm for strain imaging with complex tissue deformation," in *IEEE Ultrason. Symp. Proc.*, vol. 24, pp. 100–108, 2002.
- [5] A. T. Stavros, D. Thickman, C. L. Rapp, M. A. Dennis, S. H. Parker, and G. A. Sisney, "Solid breast nodules: Use of sonography to distinguish between benign and malignant lesions," *vol. 196*, pp. 123–134, 1995.
- [6] C. J. Baines, A. B. Miller, C. Wall, D. V. McFarlane, I. S. Simor, R. Jong, B. J. Shapiro, L. Audet, M. Petitclerc, D. Ouimet-Olvia, J. Ladouceur, G. Herbert, T. Minuk, G. Hardy, and H. K. Standing, "Sensitivity and specificity of first screen mammography in the Canadian National Breast Screening Study: A preliminary report from five centers," *Radiology*, vol. 160, pp. 295–298, 1986.

# MOTION TRACKING FOR PALPATION IMAGING

*Timothy J. Hall and Jingfeng Jiang*

University of Wisconsin  
Medical Physics Department  
1300 University Avenue, Madison, WI 53706 USA

## ABSTRACT

We are developing a method for imaging the elastic properties of tissue using unmodified clinical equipment and techniques that are similar to standard clinical exams. Our work with *in vivo* data from human subjects suggests that elasticity imaging provides new diagnostically significant information. For example, we can observe a nonlinear stress-strain relationship among tissues. Both the accuracy and variance of the displacement estimates must be understood to verify that observation. A significant body of work in algorithm development, computer simulation and phantom experiments precedes this effort. Much of that work addressed the variance in 1-D displacement estimates. The displacement estimate variance for a two-dimensional (2-D) search with a 2-D data kernel can be adequately studied using simulated echo data. The accuracy of displacement estimates when the true displacement is unknown, as with biological tissue experiments, is more difficult to mimic and is studied using data acquired from *in vivo* breast imaging. Methods to reduce displacement estimate variance and verify displacement estimate accuracy are presented.

## 1. INTRODUCTION

Many diseases cause changes to the tissue macrostructure and microstructure that result in increased tissue stiffness. This fact is the basis of the ubiquitous use of palpation. Elasticity imaging with ultrasound is under rapid development as a quantitative surrogate for manual palpation. Numerous research groups around the world are investigating techniques and fundamental limits on performance as well as creating specific implementations. Several literature reviews are available that highlight prior work. [1, 2]

Elasticity imaging is performed using phase-sensitive echo signals (either radio frequency or quadrature data) as maps of anatomy and those signals are tracked as the anatomy is deformed. Thus, displacement (or time delay) estimates from a motion tracking algorithm are the fundamental data

---

We gratefully acknowledge the financial support from CDMRP DAMD17-00-1-0596 and the University of Wisconsin, as well as the technical support from Siemens Ultrasound.

available for elasticity imaging. The variance of these displacement estimates have been studied by several groups (see, for example, [3]). The typical assumption in these approaches to variance estimation is that the displacement estimator is unbiased and that any large errors (wavelength or larger) can easily be detected and corrected. This is a good assumption for some experiments, such as radiation force experiments where deformations are small compared to the acoustic wavelength. Also, most of the previous studies of displacement variance incorporated 1-D motion tracking (again appropriate for the very small deformations induced with radiation force).

Our group implemented a block matching algorithm for high-speed elasticity imaging [4] on a Siemens SONOLINE Elegra and have been testing that implementation since early 2001. [5] The system provides real-time side by side B-mode images (about 20 frames/sec) synchronized with mechanical strain images (about 7 frames/sec). That frame rate provides sufficient feedback to the eye-brain system to control the boundary conditions of the deformation to always obtain high-quality elasticity imaging data with free-hand scanning. The preliminary results of clinical trials in breast imaging with this system [5, 6], which currently include over 300 subjects, suggest that elasticity imaging provides diagnostically-useful information that is not otherwise available. Specifically, the ratio of the lesion size in a strain image to the lesion size in the corresponding B-mode image is a sensitive criterion for differentiating benign from malignant lesions. In addition, we have observed that the elasticity image contrast of many fibroadenomas decreases as the deformation surface pressure increases. This observation is consistent with dynamic mechanical studies of *in vitro* breast tissue samples that demonstrated nonlinear stress-strain relationships for most breast tissues.

From our *in vivo* work it is clear that long sequences, instead of single images, of combined B-mode and elasticity images aid in interpreting tissue elasticity. These sequences of images help to interpret the true boundaries of lesions in both the B-mode and elasticity image. (B-mode lesion boundary definition can be particularly difficult.) Efforts are underway to improve the elasticity image quality to increase

the ability to define lesion boundaries in elasticity images and to improve the confidence in observations of changing lesion contrast. Parallel efforts involve improving the motion tracking error detection and correction algorithms, to reduce the displacement estimate error variance (in the absence of large errors) and to develop methods to judge the accuracy of the displacement estimates. This report will provide an overview of these efforts.

## 2. METHODS

Previous work has demonstrated that tracking motion in 1-D is insufficient when using ‘quasi-static compression’ elasticity imaging. One approach is to use 2-D ‘speckle tracking’ to warp one data field to approximately compensate for motion prior to 1-D cross correlation [7], however, this approach is very numerically intensive. In addition, 1-D cross correlation requires relatively long observation windows to obtain low variance in displacement estimate errors, and these long windows lead to poor spatial resolution. An alternative is to simply perform high-quality 2-D ‘speckle tracking’ (block matching) using 2-D data kernels (templates). The additional information included in the multiple lines of a 2-D template allows the use of relatively short data segments (compared to 1-D cross correlation). We are investigating the statistics of tracking motion in 2-D using 2-D data kernels. These techniques can be directly extended to 3-D at a significant computational cost.

With quasi-static compression elasticity imaging, strain image signal to noise ratio is highest when the deformation induces about 1–1.5% axial strain. Strain significantly less than 1% results in low contrast and increases the significance of sub-sample displacement interpolation noise. Strains significantly larger than 1.5%, in tissue, results in complex motion that is difficult to track. (Axial strain as large as 4–5% is relatively easy to track in homogeneous phantoms with simple block matching algorithms.) Consider the example of breast ultrasound imaging where the typical depth of a region of interest is 4cm. With 1% axial strain the average displacement a maximum depth is about 0.4mm. Using a 10MHz transducer, typical of current breast ultrasound, the displacement corresponds to approximately 2.5 wavelengths. Note also that an image usually has contrast, and this implies that the local strain exceeds 1.5% and often approaches 3–4%. Excessive noise in strain images results when the algorithm fails to track these large local strains. Thus, it is not the average strain that sets the criterion for motion tracking, but the maximum strain.

We are investigating several approaches to detect and correct large motion tracking errors, reduce the error variance in the absence of large errors, and develop criteria for judging the accuracy of motion tracking when the true underlying motion cannot be predicted. This discussion will

be limited to measures of displacement estimate error variance and to motion-compensated echo signal coherence.

### 2.1. Displacement estimate error variance

The variance in displacement estimate errors was computed using simulated data. Incompressibility was assumed and affine deformations included plane strain, and strain combined with axial shear. Simulations were performed under each condition using a set of 30 rf echo field pairs (pre- and post-deformation) and kernel widths ranging from one A-line to about 4mm wide and lengths from about 150 $\mu$ m to about 2.5mm. Each field contained at least 1000 non-overlapping displacement estimates. Displacement estimates were computed with the sum squared difference approach and those estimates were compared to the known deformation to calculate the displacement estimate error variance.

### 2.2. Displacement estimate accuracy

Signal coherence is well recognized as a limiting parameter in displacement (and time-delay) estimation. It has also been shown to be a central issue in elasticity imaging system design—motion tracking algorithms are designed to maximize the similarity between pre- and post-deformation echo signals.

We propose using signal coherence as one measure of motion tracking accuracy. This is most significant for the task of motion tracking in tissue where the true displacement is not known and (due to a lack of sufficient information) cannot be computed from first principles.

The typical approach for judging the accuracy of 1-D cross correlation is to simply estimate the correlation coefficient between the pre- and motion-compensated post-deformation echo signals. When computed for each estimate in an echo field and displayed as an image, this approach results in the ‘trashogram’ [8]. Although this approach is attractive due to its simplicity, high correlation can result from displacements that are in error by an integer wavelength. In addition, accurate displacements can be obtained when correlation is relatively low. Therefore, in addition to testing coherence for the motion-compensated rf echo fields, we also compute the coherence of consecutive, motion-compensated, strain fields. (Note that axial strain is estimated from the axial derivative of the displacement field.)

Signal coherence  $\gamma_{xy}(f)$  measures the similarity, in spatial frequency, of two fields,  $x(t)$  and  $y(t)$ , as follows:

$$\gamma_{xy}(f_1, f_2) = \frac{S_{xy}(f_1, f_2)}{\sqrt{S_{xx}(f_1, f_2)S_{yy}(f_1, f_2)}} \quad (1)$$

where  $S_{xx}(f_1, f_2)$  and  $S_{yy}(f_1, f_2)$  are the auto-power spectral densities of  $x(t)$  and  $y(t)$ , respectively, and  $S_{xy}(f_1, f_2)$

is their cross power spectral density. The magnitude squared coherence (MSC),  $C_{xy}(f_1, f_2) = |\gamma_{xy}(f_1, f_2)|^2$  is the frequency indexed correlation coefficient. The normalized correlation coefficient is obtained by integrating the MSC over frequency. Examples of the MSC for simulated data are shown in Fig. 1.

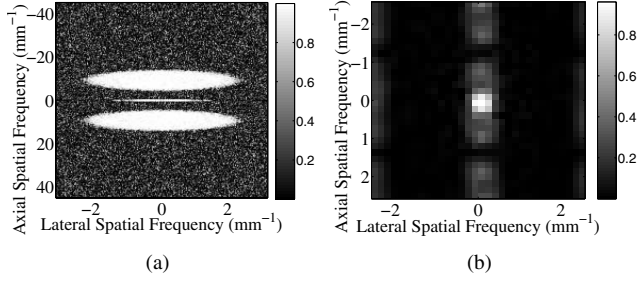


**Fig. 1.** MSC for simulated echo fields [(a) is bandpass rf data, (b) is the corresponding baseband strain image data] with motion compensated using known (input) deformation.

### 3. RESULTS

#### 3.1. Block-matching kernel size

Typical 1-D cross correlation methods employ relatively long data segments (often 3mm or more) for correlations analysis. Figure 2 illustrates the problem of echo signal decorrelation within the data segment for a 3mm window with 1.5% strain in a phantom. The post-deformation waveform is shifted to match the time delay near the center of the analysis window. That shift is seen to be incorrect near the ends of the data segment due to deformation of the phantom, and that resulted in a correlation coefficient of only 0.91. A significant advantage of using shorter data segments is the lack of significant decorrelation within the analysis window. However, short data segments introduce ambiguity in time delay estimates, particularly when tracking motion that exceeds a wavelength. An alternative to using a single long data segment (a 1-D kernel) for motion tracking is to use multiple short segments (a 2-D kernel). Even if adjacent lines of data are highly correlated, multiple lines of data provide additional electronic noise immunity as well as providing some new information.

Figure 3 illustrates the dependence of the displacement estimate error variance on kernel size. The surface plot in (a) illustrates the typical finding of other studies involving 1-D cross correlation—that the variance decreases with increasing window length. The variance is also shown to decrease with increasing kernel width in this case. However, as noted above, strain within the analysis window limits the optimal window length, as seen in (b). With 3% uniaxial strain, the variance increases rapidly for a 1-D kernel longer

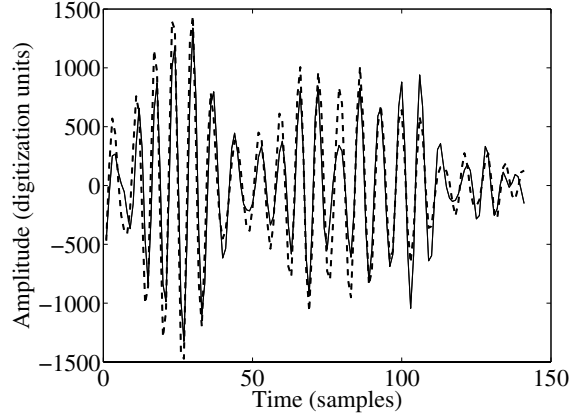


**Fig. 2.** Echo signal decorrelation within the analysis window for 1.5% uniaxial strain.

than about 1mm. Again, increasing the width of the kernel rapidly reduces variance for any given kernel length. The situation becomes far more complicated when axial shear is combined with strain, as seen in (c). Small local shear is unavoidable in complex media with heterogeneous elastic moduli, such as breast tissue. The kernel size used in our current real-time implementation is approximately 1mm wide and 220 $\mu$ m long. Clearly, from these surface plots, lower variance estimates can be obtained with longer kernels, but increasing the kernel width is not likely to significantly reduce variance. Figure 4 provides an example of palpation imaging with a longer kernel. The reduced variance in displacement estimates allowed the linear regression window (used for gradient estimation) to be reduced for an improved (apparent) axial resolution.

#### 3.2. Magnitude-squared coherence

Although a somewhat larger kernel and shorter linear regression window resulted in an apparent improvement in the spatial resolution, it is not clear that the displacement estimates are more accurate and the strain image is higher quality. We are investigating measures of similarity between motion compensated rf echo fields paired for strain image formation and between consecutive strain fields presented in a sequence of strain images. Although it is difficult to see in the grayscale plots in Fig. 5, the MSC is higher throughout the frequency spectrum with the larger kernel and shorter linear regression window (b). This suggests that increasing the kernel size and decreasing the linear regression window somewhat improved motion tracking accuracy.

### 4. DISCUSSION

The surface plots of displacement estimate variance demonstrate that the optimal kernel size is dependent on the defor-

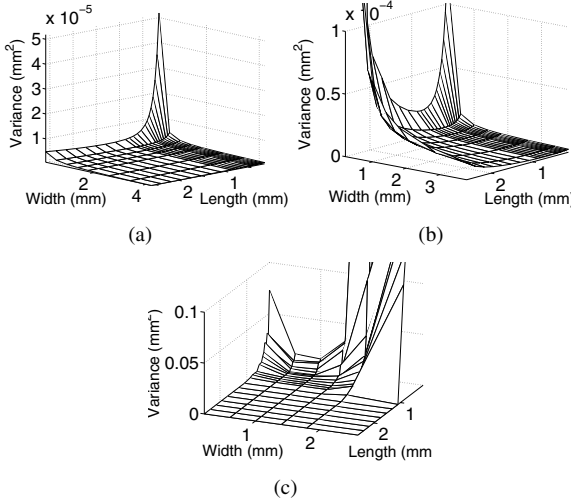


**Fig. 3.** Displacement estimate error variance using the SSD algorithm and varying kernel size. In (a) the simulation involved only 1% plane strain. In (b) plane strain was 3%. In (c) 1% strain was combined with 1° axial shear.

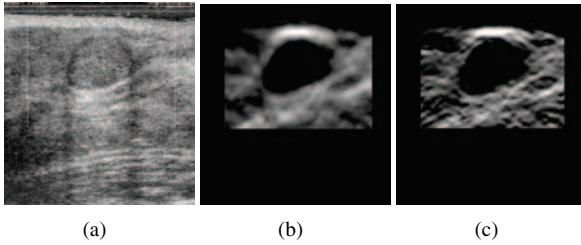


**Fig. 4.** B-mode (a) and strain images of a fibroadenoma obtained with a small (b) and larger (c) block matching kernel.

mation being tracked. Small strain and no shear are accurately estimated with very large 2-D kernels. As the strain increases the maximum window length for high-quality displacements estimates is reduced. In addition, only a small amount of axial shear greatly increases displacement estimate error variance and reduces the maximum kernel width for which low variance displacement estimates are obtained.

Although the MSC is an attractive measure of motion tracking accuracy, it is not the perfect single criterion. Two images of equal brightness and no contrast have very high coherence, but convey very little information. Other image quality parameters are still needed to judge which ‘system’ is best.

## 5. REFERENCES

[1] T. J. Hall, “AAPM/RSNA physics tutorial for residents: Topics in us: Beyond the basics: Elasticity imaging with us,” *Radiographics*, vol. 6, pp. 1657–1671, 2003.

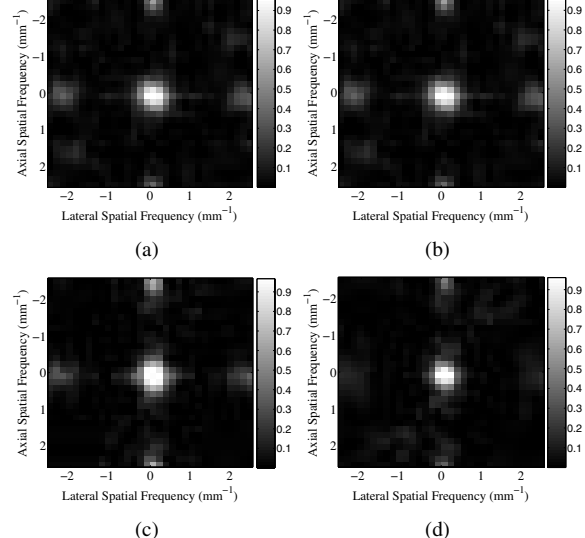


**Fig. 5.** Magnitude-squared coherence among consecutive strain images obtained with a larger (a,b) and small (c,d) block matching kernel and long (a,c) and short (b,d) linear regression windows.

[2] J. Ophir and S. K. A. et al., “Elastography: Ultrasonic estimation and imaging of the elastic properties of tissues,” *Proc Inst Mech Eng*, vol. 213, no. 3, pp. 203–233, 1999.

[3] F. Viola and W. F. Walker, “A comparison of the performance of time-delay estimators in medical ultrasound,” *IEEE Trans Ultrason, Ferroelec, Freq Cont*, vol. 50, no. 4, pp. 392–401, 2003.

[4] Y. Zhu and T. J. Hall, “A modified block matching method for real-time freehand strain imaging,” *Ultrasonic Imaging*, vol. 24, no. 3, pp. 161–176, 2002.

[5] T. J. Hall, Y. Zhu, and C. S. Spalding, “In vivo real-time freehand palpation imaging,” *Ultrasound Med Biol*, vol. 29, no. 3, pp. 427–435, 2002.

[6] T. J. Hall, W. Svensson, and P. V. B. et al., “Lesion size ratio for differentiating breast masses,” in *Proc. 2003 IEEE Ultrasonics Symposium*, 2003.

[7] P. Chaturvedi, M. F. Insana, and T. J. Hall, “Testing the limitations of 2-D companding for strain imaging using phantoms,” *IEEE Trans Ultrason, Ferroelec, Freq Cont*, vol. 45, no. 4, pp. 1022–1031, 1998.

[8] K. Kaluzynski, X. Chen, S. Y. Emelianov, A. R. Skovoroda, and M. O’Donnell, “Strain rate imaging using two-dimensional speckle tracking,” *IEEE Trans Ultrason, Ferroelec, Freq Cont*, vol. 48, no. 4, pp. 1111–1123, 2001.

# Computational Aspects of Young's Modulus Reconstruction from Ultrasonic Freehand Scanning

Jingfeng Jiang and Timothy J. Hall

Department of Medical Physics  
University of Wisconsin-Madison

1300 University Avenue, Wisconsin 53706, USA

**Abstract**— In this paper, we report a method for absolute Young's modulus reconstruction under freehand scanning. The absolute modulus, an intrinsic tissue property, can be used to quantitatively monitor pathological evolution of certain diseases and to evaluate therapeutic treatments. This method could iteratively assess the absolute tissue modulus distribution by simultaneously measuring the surface pressure and tissue deformation. This method could also be used to obtain pressure-sensitive tissue elasticity through a sequence of phase sensitive (either radiofrequency or quadrature) echo signals to study tissue nonlinearity. Since the proposed method uses clinical equipment and procedures that are similar to the standard clinical exams, this approach is likely to gain significant clinical impact if successful.

Numerical simulations and a phantom experiment are reported here as preliminary studies with emphasis on computational aspects. The results show that the modulus distribution can be accurately reconstructed, though work in hardware and algorithm development needs to continue prior to clinical trials.

**Keywords-** ultrasonic strain imaging, modulus reconstruction, inverse problems.

## I. INTRODUCTION

The onset of many cancers is accompanied by changes in tissue macrostructure and microstructure that often result in an increase in stiffness. Ultrasonic strain imaging techniques that estimate relative 'stiffness' of soft tissues using conventional ultrasound scanners are under rapid development [1]. Specifically, a real-time ultrasonic strain imaging system [2] has demonstrated a sufficient frame rate to allow the human eye-brain system to control data acquisition boundary conditions and produce a long sequence of high quality strain images.

For single lesions isolated in relatively uniform healthy tissue, strain images have been proven to be good approximations of expected tissue elasticity maps [1]. However, multiple closely-spaced lesions increase the difficulty of interpreting strain images (e.g. Fig. 1b), as shown in a numerical phantom in Fig. 1a. A similar situation can happen to *in vivo* breast scanning, as shown in Fig. 1(c).

More importantly, the absolute modulus, an intrinsic parameter that directly links to tissue changes, can be used to

quantitatively monitor the pathological evolution and therapeutic treatments of certain diseases.

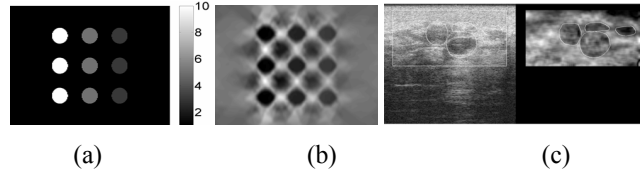


**Figure 1** A relatively simple modulus distribution (a) and the complicated axial strain pattern (b) of a numerical phantom. B-mode and strain images (c) of a cluster of *in vivo* breast cysts. Note that the axial direction is parallel to the ultrasound beam.

We, among others, have found that the outcome of modulus reconstruction is inherently limited by the accuracy of motion estimation. Efforts to improve motion tracking algorithms and reduce displacement estimate variance are underway. Parallel efforts that are essential components of modulus imaging under freehand scanning also involve comprehensive assessment of strain image quality. However, this report will focus on the methodology for modulus reconstruction.

## II. METHOD

Formally, the elasticity reconstruction problem can be considered as follows: given the displacement field  $u(x, y)$  in a medium  $\Omega$  that is governed by certain constitutive equations, determine elasticity parameters of the governing constitutive equations of the domain  $\Omega$ . If we assume tissue to be linear elastic, isotropic, and incompressible, the inverse problem is then simplified to the Young's (shear) modulus reconstruction. The governing equation for elastic modulus reconstruction can be recast as follow [3],

$$-\partial_i p + \partial_j (\mu \partial_i u_j) + \partial_j (\mu \partial_j u_i) = 0 \quad (1)$$

where  $p$  is the hydrostatic part of the stress,  $\mu$  is the shear modulus, and  $u$  is the displacement field as a function of spatial coordinates. Rewriting Eq. (1) in terms of strain and eliminating  $p$ , we obtain [4],

$$(\partial_{yy} - \partial_{xx})(\epsilon_{xy}\mu) + 2\partial_{xy}(\epsilon_{xx}\mu) = 0 \quad (2)$$

We gratefully acknowledge the financial support from DAMD17-00-1-0596, NIH-1R01CA100373-01 and the University of Wisconsin, as well as the technical support from Siemens Medical Solution USA, Inc.

where  $\varepsilon_{xy}$  and  $\varepsilon_{xx}$  are the shear and axial strain, respectively.

Note that  $\partial_j = \partial/\partial x_j$  and  $\partial_{ij} = \partial^2/\partial x_i \partial x_j$  in shorthand notation.

Several methods have been proposed to reconstruct the modulus distribution based on either the estimated strain fields or the intermediate results – displacement estimates. These methods can be classified into two main categories. In the first category (e.g. [3]), the displacement or strain estimates are obtained through motion tracking from the pre- and post-deformed phase-sensitive echo signals (either radio frequency or quadrature data) and then Eq. (1) or its equivalent (for instance, Eq. (2)) is solved by a numerical method (for instance, finite element method) with known boundary conditions. On the other hand, methods in the second category (e.g. [5]) recast the modulus reconstruction problem as a nonlinear optimization problem. This approach seeks a modulus distribution that iteratively minimizes a cost function (e.g. the difference between the measured and predicted displacement fields of the proposed elastic distribution). From our previous work, it seems that iterative reconstruction methods are more robust to noise.

#### A. Formulation

The proposed method is a combination of Kallel and Bertrand's approach [5] and the Zhu, et al., approach [6]. Basically, we use the Zhu, et al., method to obtain an initial solution of the modulus reconstruction problem and then iteratively vary the predicted modulus distribution to minimize the cost function (see Eq. (3)) using the Newton-Raphson method in conjunction with Tikhonov regularization.

In Kallel and Bertrand's method the cost function is defined as the difference between the measured axial displacement estimates  $U$  and predicted axial displacement solution  $T(E)$  of the elastic medium under certain boundary conditions [5],

$$\hat{E} = \arg \min \left\{ \frac{1}{2} \|T(E) - U\|^2 \right\} \quad (3)$$

The cost function could be expanded to incorporate the measured surface force  $F$ ,

$$\hat{E} = \arg \min \left\{ \frac{1}{2} \left( \|T(E) - U\|^2 + \|T_f(E) - F\|^2 \right) \right\} \quad (4)$$

where  $T_f(E)$  is the predicted force boundary condition of the elastic medium.

Eq (3) is linearized and then the Newton-Raphson method in conjunction with the Tikhonov regularization technique was used to minimize the cost function iteratively. The incremental update of the modulus distribution at iteration  $k$  is [5]:

$$\{\Delta \hat{E}_k\} = [S_k^T W_k S_k + \gamma_k Q_k]^{-1} \{S_k^T W_k \Delta U_k\} \quad (5)$$

$$S_k = -[K]^{-1} \left[ \frac{\partial U}{\partial E_k} \right] \{U\} \quad (6)$$

where  $[K]$  is the global stiffness matrix in the finite element model,  $\gamma$  is a regularization parameter, and  $Q$  and  $W$  are both positive definite square matrices that are used to introduce additional constraints. Interested readers are referred to [5] for details. The criteria for convergence of the iterative procedure can be set with pre-determined thresholds  $\varepsilon_1$  and  $\varepsilon_2$  as follows,

$$\Delta \hat{E}_k < \varepsilon_1 \text{ and/or } \hat{D} < \varepsilon_2 \quad (7)$$

Nonlinear optimization could be successfully approximated by a linearization process, given an initial guess that is sufficiently close to the true solution. However, it is generally difficult to establish such initial guesses. It is worth noting that strain images may be misleading in constructing such initial estimates, as shown in Fig. 1.

On the other hand, the Zhu, et al., approach is a direct inversion of the finite element method for rectilinear elements. This approach can be extended to other isoparametric elements to fit curved geometries better. This approach rewrites the global stiffness matrix so that a linear algebraic system, where the modulus distribution is unknown, can be solved explicitly [6].

$$KU = F \Leftrightarrow DE = F \quad (8)$$

where  $E$  is a vector that represents the unknown modulus distribution, and  $D$  is a re-assembled matrix and a function of displacement estimates. It is worth noting that  $D$  may be an over-determined matrix and its inversion could be ill-posed due to errors in displacement estimates. In conjunction with the measured surface force distribution, the Zhu, et al., method could give a good approximation of the true modulus distribution.

#### B. A Special Accommodation for Freehand Scanning

An additional difficulty posed by freehand scanning is that the reference coordinate system for motion tracking is mobile. The contact surface between the ultrasound transducer and the tissues that are being imaged is typically the reference coordinate system for motion tracking, as shown in Fig. 2. However, FEA simulation programs usually use a fixed coordinate that is independent of the physical model. Consequently, a conversion is needed to resolve this inconsistency. By assuming a free-sliding condition in  $x$  direction (see Fig. 2) at the top and bottom surfaces, a simple conversion consists of two steps as follows:

According to the basic force equilibrium for the deformed ROI, as shown in Fig. 2, the surface pressure acquired from an integrated pressure sensor array should equal the reaction forces on the bottom of ROI, except that the directions are opposite.

The displacement around the top of ROI can be measured by 'speckle tracking' algorithms [2] and then prescribed for the FEA mesh to establish displacement boundary conditions. (Note that the displacement around the bottom of ROI has already been enforced by the imposed reaction force from the previous step.)

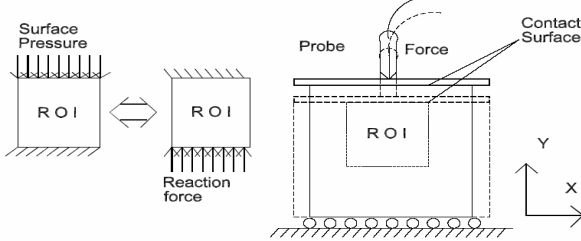


**Figure 2.** Illustration of tissue deformation under ultrasonic freehand scanning

### C. Key Features of the Proposed System

Our proposed absolute ultrasonic modulus imaging system includes a clinical ultrasound scanner as a platform for data acquisition, a compression plate mounted to the ultrasound transducer array with a pressure sensor array on that plate, and an Intel-based workstation for image formation and display.

A device of measuring surface force is necessary for the reconstruction of the absolute modulus distribution. Otherwise, only relative stiffness is assessed. More importantly, the absence of surface pressure information may lead to a nonunique solution for modulus reconstruction [3]. Barbone and Bamber [3] also showed that the solution for modulus reconstruction using Eq. (1) or (2) is well posed if the object that is being imaged is under pure axial compression in the absence of shear stress. In fact, the deformation of a tissue-mimicking phantom with freehand scanning, as illustrated in Fig. 3, may approximate uniaxial compression. Therefore, adding the ability to acquire surface pressure could lead to a well-posed inverse problem. Unfortunately, real clinical procedures with human anatomical structures (e.g. female breasts) may violate this assumption. The consequence and severity of this violation will be investigated with tissue-mimicking anthropomorphic phantoms.

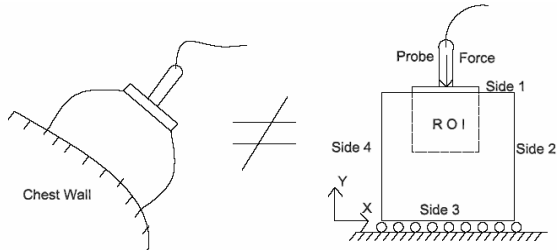


**Figure 3.** Boundary conditions for freehand scanning of a breast and a tissue-mimicking phantom

The procedures of the proposed method are summarized in Fig. 4.

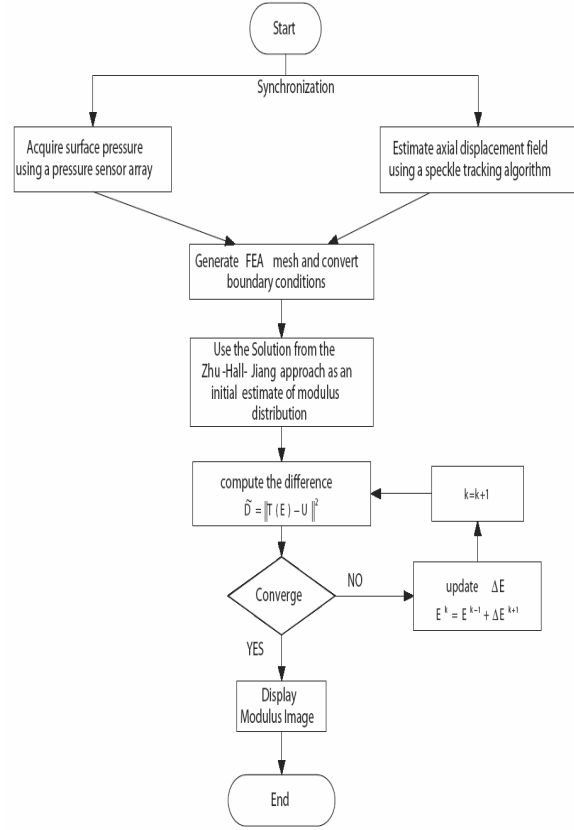


**Figure 4.** Flow-chart of the proposed reconstruction algorithm.

### III. NUMERICAL SIMULATIONS AND PHANTOM EXPERIMENTS

We simulated a two-dimensional object under plain stress conditions with dimension of  $20 \times 20$  (width  $\times$  height in millimeters). The modulus distribution is shown in Fig. 5(a) where the background was 15kPa that approximates normal glandular breast tissue. An 8mm diameter target whose stiffness is 45kPa is embedded into the object. The object is meshed coarsely with 4-node elements as shown in Fig. 5(b) and the ideal forward solution can be obtained, as well as the force boundary conditions.

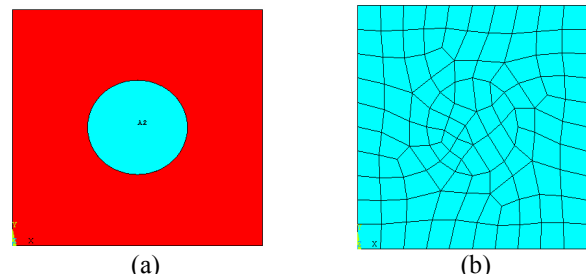


**Figure 5.** Elasticity Map (a) and Mesh (b) generated using ANSYS (Ansys Inc., Pittsburgh, PA)

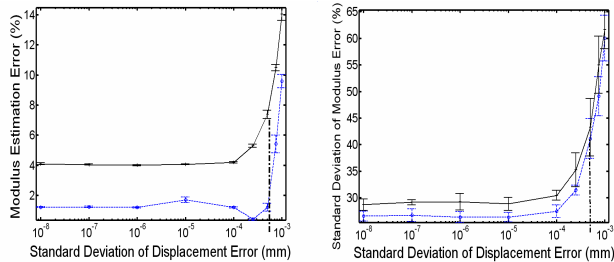
Usually measured displacement and surface pressure are contaminated with errors (noise). The significance of

uncertainties in displacement estimates and force measurements was investigated assuming a zero mean Gaussian process to model the estimation errors and added to the ideal solution to simulate different noise levels.

RF data were acquired from a gelatin tissue-mimicking phantom under freehand scanning and used to validate the proposed method. In the tissue-mimicking phantom, the background and a spherical inclusion have similar acoustic properties, whereas the spherical inclusion is three times stiffer than the background. The FEA solution for the predicted force (with 10% noise added) was used in the reconstruction process. The inclusions can be barely seen in the B-scan images (Figs. 7(a)) demonstrating that scattering and stiffness are uncorrelated properties [7].

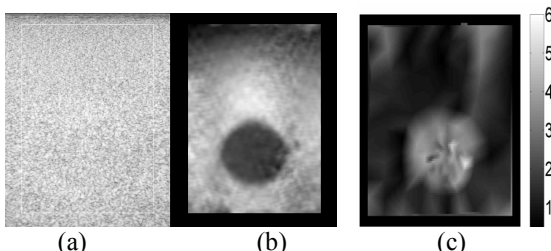
#### IV. RESULTS

Fig. 6 illustrates that uncertainties both in displacement estimates and surface force measurements degrade the performance of the proposed method. Ten realizations of displacement and force distributions were generated for each predetermined level of noise. However, it is easy to conclude that the proposed method is more sensitive to noise in displacement estimates than to noise in force measurements.



**Figure 6.** Plots of the statistical analysis of modulus reconstruction errors. The dashed and solid lines denote noise-free and 10% of error in surface pressure acquisition, respectively. The vertical lines represent displacement estimation variance of our current speckle tracking algorithm.

Fig. 7 shows that the modulus distribution of the tissue-mimicking phantom under freehand scanning can be accurately reconstructed, but the size of the target is overestimated by about 15%.



**Figure 7** B-mode (a), strain (b) and modulus (c) images of the tissue-mimicking phantom. Note that the unit used in modulus image is 10kPa.

#### V. DISCUSSIONS AND CONCLUSIONS

The conversion of the reference coordinate system enables the modulus reconstruction along a sequence of acquired data. It will likely be able to provide more consistent modulus assessment and be used to study tissue nonlinearity under typical clinical setting.

Adding an array for acquiring surfacing pressure not only makes reconstruction of absolute moduli possible, it also offers the possibility of recasting the cost function in optimization.

Many simplifications needed for the analysis, including the coordinate system conversion and uniqueness of the inversion, are built on the assumption of uniaxial compression. However, it is almost impossible to maintain uniaxial compression of human organs. Therefore, the limits of these simplifications will be further studied with anthropomorphic tissue-mimicking phantoms and in vivo tissues.

A 10% error in surface force measurement is a conservative estimate of currently available techniques. However, reducing errors in ultrasonic speckle tracking has greater significance in modulus reconstruction.

Since we chose a gradient-based optimization algorithm to reconstruct Young's modulus, a large discontinuity (three to one contrast in Fig. 7) in the elasticity map may pose difficulties in recovering the boundary between the soft background and hard inclusion. Ideally, a discretization of the elastic medium with high order finite elements can preserve the discontinuity.

The results suggest that the absolute elastic moduli of in vivo tissue can be assessed with minor modification to current standard clinical sonography systems with freehand scanning. Uncertainty in displacement estimates has more influence on modulus reconstruction statistics compared to uncertainty in the force distribution.

#### REFERENCES

- [1] T. J. Hall, "AAPM/RSNA physics tutorial for residents: Topics in US: beyond the basics: Elasticity imaging with US," *Radiographics*, vol. 6, pp. 1657-1671, 2003.
- [2] T. J. Hall, Y. Zhu and C. S. Spalding, "In vivo real-time freehand palpation imaging", *Ultrasound Med. Biol.*, vol. 29, pp. 427-35, 2003.
- [3] P. E. Barbone and J. C. Bamber, "Quantitative elasticity imaging: what can and cannot be inferred from strain images," *Phys. Med. Biol.*, Vol. 47, pp. 2147-64.
- [4] A. R. Skovoroda, S. Y. Emelianov, and M. O'Donnell, "Tissue Elasticity reconstruction based on ultrasonic displacement and strain images," *IEEE Trans. Ultrason., Ferroelect., Freq., Contr.*, vol.42 pp. 747-65, 1995.
- [5] F. Kallel and M. Bertrand, "Tissue elasticity reconstruction using linear perturbation method," *IEEE Trans. on Med. Imaging*, vol. 15, pp. 299-313, 1996.
- [6] Y. Zhu, T. J. Hall and J. Jiang, "A Finite Element Approach for Young's Modulus Reconstruction," *IEEE Trans Med Imaging*, vol. 22, pp. 890-901, 2003.
- [7] T. J. Hall, M. Bilgen, M. F. Insana, and T. Krouskop, "Phantom Materials for Elastography," *IEEE Trans. Ultrason., Ferroelect., Freq., Contr.*, vol.44, pp. 1355-1365, November, 1997.

# Parametric Imaging Using A Clinical Scanner

James A. Zagzebski, Anthony Gerig, Quan Chen, Haifeng Tu, Wu Liu, Tomy Varghese, and Tim Hall

Department of Medical Physics,  
University of Wisconsin-Madison  
Madison, WI, USA

**Abstract**— Ultrasonic scatterer size estimation and imaging has proven to be both feasible and useful for monitoring, diagnosis, and study of disease. We are implementing scatterer size imaging and attenuation coefficient imaging on a clinical scanner equipped with a research interface. The interface provides radio frequency echo data over the image of a sample, which are then analyzed offline. Echo data from a reference phantom, acquired using the same transducer and scanner settings used in acquisition from the sample, accounts for system dependencies on the data. Backscatter coefficient and attenuation coefficients are estimated for small regions. Scatterer size images are generated by performing a modified least squares fit of the backscatter estimate to a theoretical model, which relates backscatter to scatterer size. Tests in well-characterized phantoms have demonstrated the accuracy of the method have revealed limitations. Ultrasonic scatterer size estimates generally have large variances due to the inherent noise of the spectral estimates used to calculate size. Compounding partially correlated size estimates associated with the same tissue, but produced with data acquired from different angles of incidence, is an effective way to reduce the variance without making dramatic sacrifices in spatial resolution. Initial compound acquisitions on the clinical system have been done using manually generated scripts supported by the research interface. Results confirm theoretical expectations of the improvement in signal to noise ratio of scatterer size estimations with selected compounding parameters. Additional parameters, including the attenuation coefficient may also be derived.

**Keywords**-Backscatter; Scatterer size; Ultrasound Attenuation; Parametric Imaging; Compound Imaging

## I. INTRODUCTION

Ultrasonic scatterer size estimation and imaging has proven to be both feasible and useful for monitoring, diagnosis, and study of disease. The techniques combine physically based analytical models for ultrasound scattering with backscatter measurements from tissues. For example, Hall et al., [1] measured glomerular diameters and found good correlation with histology; Garra et al., [2] reported glomerular sizes and scatterer spacing were useful for detecting diffuse kidney disease. Oelze et al., [3] demonstrated that scatterer size measurements and images can differentiate between breast carcinoma and fibroadenomas in an animal tumor model. Sommer et al., [4] showed that narrow bandwidth B-mode images exhibit frequency dependent contrast between liver masses and liver parenchyma, suggesting that scatterer size images may be useful in this organ as well.

We are implementing scatterer size imaging and attenuation coefficient imaging on a clinical scanner equipped with a research interface. The interface provides radio frequency echo data from a region in a sample; currently data are analyzed offline. Echo data from a reference phantom, acquired using the same transducer and scanner settings used in acquisition from the sample, accounts for system dependencies on the data.

This work was supported in part by NIH Grants 1 R21 EB002722 and T32CA09236.

Backscatter coefficient and attenuation coefficients are estimated for small regions. Scatterer size images are generated by performing a modified least squares fit of the backscatter estimate to a theoretical model, which relates backscatter to scatterer size. Attenuation is measured by fitting narrow band,  $\log(\text{signal intensity})$  vs. depth data to a straight line. Extensive tests in well-characterized phantoms have demonstrated the accuracy of the method, as well as revealed limitations.

## II. METHODS

A “reference phantom” data reduction technique [5] is used to determine backscatter coefficients vs. frequency,  $BSC(\omega)$  and attenuation coefficients vs. frequency  $\alpha(\omega)$ , of regions within the sample; RF Echo data are acquired from the sample ( $S_s(\omega)$ ) and from a calibrated reference ( $S_r(\omega)$ ); The ratio of the data from the sample and from the reference effectively eliminates system dependencies on the echo data.

The general approach is to plot  $\log(S_s(\omega)/S_r(\omega))^2$  vs. depth. Our analysis shows that this ratio may be expressed as:

$$\frac{|S_s(\omega)|^2}{|S_r(\omega)|^2} = \frac{BSC_s(\omega)}{BSC_r(\omega)} \exp[-4z(\alpha_s(\omega) - \alpha_r(\omega))]$$

The slope is related to the difference between  $\alpha(\omega)$  of the reference and of the sample. The attenuation coefficient of the reference is known; therefore, the slope yields the attenuation of the sample. The zero depth intercept yields the ratio of the backscatter coefficient,  $BSC(\omega)$  of the sample to that of the reference. Since the latter is known,  $BSC(\omega)$  of the sample is thus determined. Although this example is for a uniform sample, the calculation may also be done over a region starting at some depth in the sample. The attenuation coefficient can readily be determined using this approach. However, for deeper structures, it is necessary to correct for attenuation of overlying tissues to get the BSC of the region of interest. Similarly, attenuation estimations can be limited by a similar problem, namely, attenuation values can be incorrect if the BSC isn’t uniform with depth and isn’t properly corrected for.

Size estimation is accomplished by performing a modified least squares fit between the measured backscatter coefficient from a tissue segment and a theoretical backscatter coefficient, which is dependent upon tissue/scattering properties including

size. The scatter size,  $a$ , corresponds to the value that minimizes the following expression.

$$\hat{a} = \arg \min \frac{1}{n} \sum_{\omega_{\min}}^{\omega_{\max}} [\psi(\omega, a) - \bar{\psi}(a)]^2$$

where

$$\psi(\omega, a) = \log(BSC_s(\omega)) - \log(BSC_t(\omega, a))$$

and  $BSC_t(\omega, a)$  is a model backscatter coefficient dependent on scatterer size. The summation is over the usable bandwidth of the backscatter coefficient measurement. Unlike the standard least squares fitting technique, this method is insensitive to differences between measured and theoretical values by a multiplicative constant, and therefore requires no knowledge of tissue scattering strength for accurate size estimation.

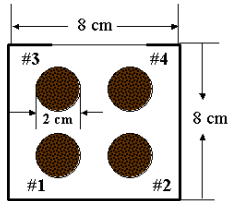


Figure 1 Scatterer size phantom. Target 1 has scatterers whose average radius is 167  $\mu\text{m}$ . Scatterers in target 2 have a 116  $\mu\text{m}$  radius; those in target 3 have a 52  $\mu\text{m}$  radius; and those in target 4 have an average 26  $\mu\text{m}$  in radius.

Initial tests of the scatterer size imaging method were done using an Acuson 128XP10 scanner and V4 transducer. We used a special purpose phantom consisting of polystyrene bead scatterers in a gel background (figure 1). The attenuation coefficient of the contents of the phantom was 0.5 dB/cm-MHz. The background material in the phantom had beads having a mean diameter of 199  $\mu\text{m}$ . Four cylinders, each with a diameter of 2 cm have a different mean scatterer diameter, ranging from 335  $\mu\text{m}$  (#1), 232  $\mu\text{m}$  (#2), 103  $\mu\text{m}$  (#3) and 51  $\mu\text{m}$  (#4).

The scanner was set to image at a center frequency of 2.5 MHz. The 6 dB bandwidth was 40%. RF data were digitized using a Gage Applied Science 12100 A/D board for offline processing. Scan lines were divided into 4 ms  $\times$  ~2 mm pixel elements and spectra were averaged from multiple images in parallel planes to reduce noise.

A typical scatterer size image is shown in figure 2. The color bar is the scatterer radius, estimated from the algorithm and displayed in the image. There is good agreement between image data and the actual scatterer sizes.

Ultrasonic scatterer size estimates generally have large variances due to the inherent noise of the spectral estimates used to calculate size. A number of groups have analyzed the statistical uncertainty of these estimates, including our own. [6] Our analysis and experiments show that size estimate precision is a function of: gate length, frequency bandwidth,

wavenumber, and number of RF echo signal A-lines used. The image in Figure 2 was obtained by averaging data over several parallel planes, which would only be possible if there was translational symmetry in the target.

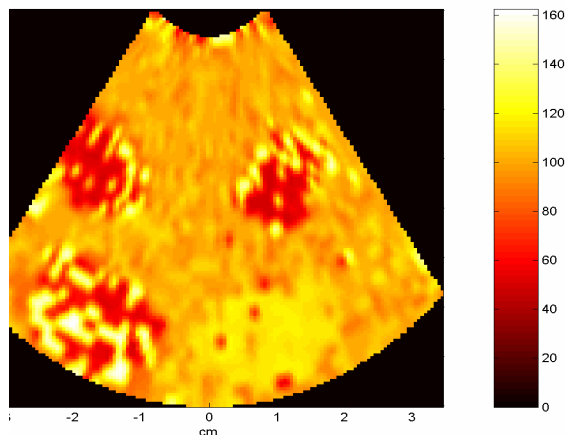


Figure 2 Image of the scatterer size phantom. The scale depicts scatterer radii in micrometers. Seen are target 1 (lower left, 167  $\mu\text{m}$  radius), target 2 (lower right, 116  $\mu\text{m}$  radius), target 3 (upper left, 52  $\mu\text{m}$ ), and target 4 (upper right, 26  $\mu\text{m}$  radius). The background has 100  $\mu\text{m}$  radius scatterers.

### III. SPATIAL COMPOUNDING

One method that can be used to reduce the severity of this problem is to spatially compound partially correlated results which are associated with the same tissue, but which are produced with data that is taken from different angles of incidence. [8] The application of spatial compounding to B-mode imaging has been investigated extensively, and has yielded excellent results. [9] As a result, many modern clinical scanners include a compounding option to reduce speckle and provide the additional benefit of improved specular reflector imaging. Recent work done by our group has been devoted to adapting the spatial compounding technique for use in elastography and parametric imaging that involves spectral analysis, such as scatterer size and attenuation imaging. For the case of parametric imaging, either the necessary spectral estimates can be compounded before parameter estimation, or parametric estimates can be generated for each angle of incidence and then averaged.

Our initial tests to determine the effect of spatial compounding on parametric images used a phased array transducer translated over the scanning window of the scatterer size phantom of figure 1. A 3.5 MHz probe and an Aloka scanner were used. The signal format of the transducer consists of 121 A-lines arranged over a 90° sector, with 0.75° increments between A-lines. To simulate the effects of angular data acquisition of RF echo signals, the phased array transducer was linearly translated over the sample using a precision linear stage, so that each location in the sample was scanned from multiple angles (Fig. 3). The distance between acquisitions was 1/2 mm. The echo data in these RF sets were then rearranged into angled RF data frames, as indicated in the lower part of

Fig 3. Each of these regrouped RF frames was analyzed separately to generate a scatterer size image at each angle.

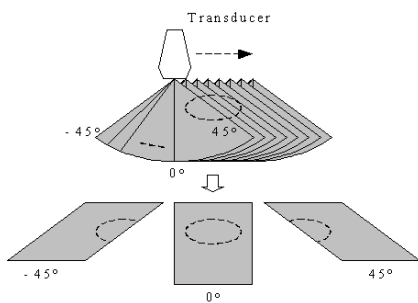


Figure 3 Acquiring compound data using a phased array scanner. Data were then regrouped into angled RF frames (lower part of diagram).

The image pair in Fig 4 illustrates the results of spatial compounding for the scatterer size phantom. The size estimates were done using a 3.5 MHz transducer. Image quality is significantly improved with compounding (right side) vs. no compounding (left side). Note all four targets are seen in the image on the right.

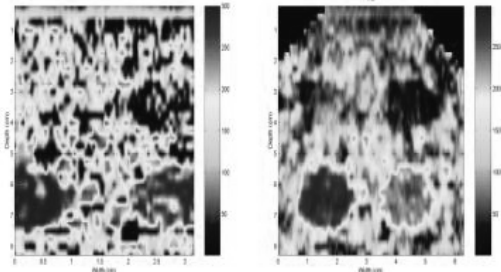


Figure 4 Non-compounded scatterer size image (left) and compounded image (right) of the scatterer size phantom.

The standard deviation of the scatterer sizes displayed for target “1” (mean diameter = 325 mm) is shown in Fig 5 for different degrees of compounding, achieved by increasing the maximum angle over which size data were compounded at each location. The S.D. decreases with number of lines compounded, as expected. Notice that one can skip some beam lines without significant loss of compounding effect. Evidently, the data for beam lines that are only slightly angled from one another are highly correlated for this phased array transducer. [7]

#### IV. ATTENUATION IMAGING

Another important acoustic parameter in clinical ultrasound imaging is the attenuation coefficient. Currently, clinicians recognize and use attenuation in making a diagnosis; however, measures are qualitative rather than quantitative. For example, when describing clinical signs based on attenuation, users employ statements such as “the mass exhibits shadowing” or “the mass exhibits good through transmission.” Our goals are

to incorporate methods for determining attenuation locally, and in the form of images, into ultrasound machines.

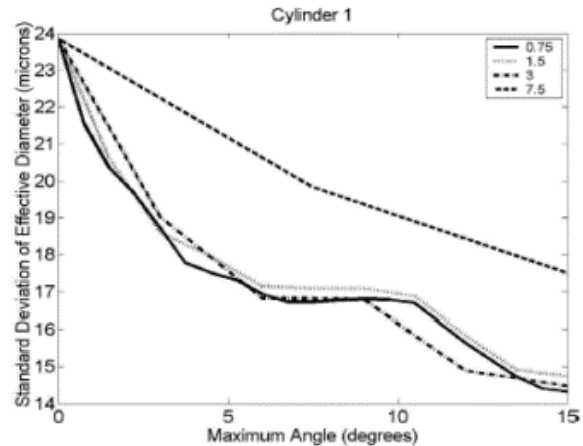


Figure 5 Standard deviation of scatterer size measures for cylinder 1 in the scatterer size phantom, vs. the maximum compounding angle. Results are shown for 4 angular increments between beam lines, ranging from 0.75° (using all beams) to 7.5°.

Attenuation may be measured locally using the reference phantom method, as described above. When applied to a small region, statistical fluctuations of echo signal data affect the estimates. Our analysis shows that  $\sigma_\alpha$ , the standard deviation of an attenuation estimate, is given approximately by the following expression:

$$\sigma = \frac{7.52k\sqrt{N+N'}}{\sqrt{nZ}\sqrt{NN'}}$$

where  $k$  is the inverse of the signal-to-noise ratio,  $N$  and  $N'$  are the number of independent beam lines over which echo data are analyzed for the estimate from the sample and reference phantom,  $n$  is the number of independent estimates of  $(S_s(\omega)/S_r(\omega))^2$  and  $Z$  is the length of the analysis region.

Our approach is to use both spatial and frequency compounding to compute attenuation locally and to form attenuation images. [10,11] Spatial compounding is done analogously to that described for scatterer size images. Frequency compounding assumes the attenuation over a limited frequency range varies linear with frequency,  $f$ .  $\beta = \alpha/f$ , then becomes a useful attenuation metric, where  $\alpha$  is the attenuation at frequency  $f$ . The  $\beta$  estimates from different frequencies can be compounded.

Attenuation imaging has been implemented on a Siemens Antares machine equipped with an Ultrasound Research Interface (URI). In the present implementation, raw, RF data are saved and stored for off-line analysis. Users select a region of interest, number of frames of echo data to acquire, and the acquisition file name by way of front panel controls. Other scanner parameters, such as gain, transmit focus conditions, center frequency, and certain pre-processing settings are set in the usual way. A front panel control initiates the RF

acquisition sequence, storing echo data to a file on the Antares computer system. The file is downloaded to a Windows machine, where the data analysis routines are run.

The Antares machine allows beam steered B-mode acquisitions, where a trackball is used to steer the parallel ultrasound beam lines from the linear array into different angles. This feature was used to acquire RF data from an attenuation phantom, consisting of cylindrical inclusions whose attenuation coefficient was 0.78 dB/cm-MHz, within a uniform background where the attenuation was 0.49 dB/cm-MHz. These values had been obtained using lab apparatus applied to test samples of the materials manufactured when the phantom was poured.

A URI script was written that utilized trackball generated angular increments to shift the beam direction by approximately 2 degrees, from  $-9.5^\circ$  to  $+11.5^\circ$ . At each location, a frame of RF echo data was acquired. The offline analysis consisted of producing  $\beta=\alpha/f$  images at each acquisition angle, then compounding the resultant images. A VFX13-4 linear array transducer was used.

Fig. 6 presents a gray scale image (top) and an attenuation image of a region in the attenuation-contrast phantom containing a 1-cm diameter inclusion. Slight shadowing can be noted distal to the inclusion in the top image. The inclusion is clearly seen in the lower, attenuation vs. frequency slope image. The depicted value for the attenuation coefficient in the inclusion is approximately 0.7 dB/cm-MHz, closely matching the results obtained from test samples.

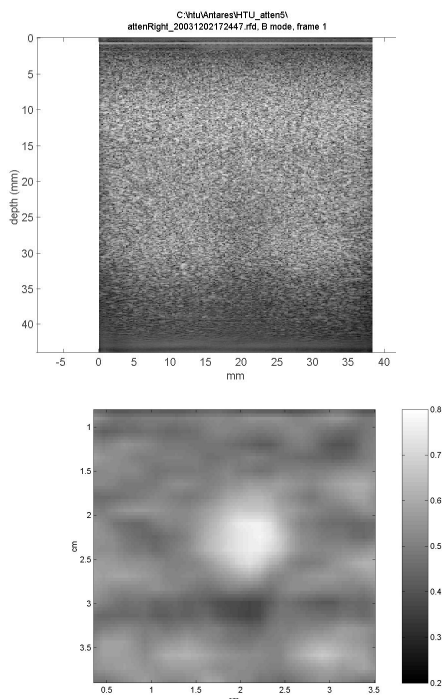


Figure 6 B-mode (top) and attenuation image of a 1-cm diameter inclusion (0.8 dB/cm-MHz) in a uniform background.

## V. CONCLUSIONS

In this paper, we describe methods for acquiring both scatterer size images and attenuation images, and we report quantitative tests of the methods. Compounding scatterer size estimates following RF echo data acquisition from the same location but different beam angles can substantially improve statistical uncertainty in scatterer size images. Results confirm theoretical expectations of the improvement in signal to noise ratio of scatterer size estimations with selected compounding parameters. Both spatial and frequency compounding improve local attenuation estimations, and facilitate the generation of coarse attenuation images.

## REFERENCES

- [1] Hall, T, Insana, M, Harrison, and Cox, G, Ultrasonic measurement of glomerular diameters in normal adult humans, UMB 22: 987-997, 1996.
- [2] Garra, B, Insana, M, Sesterhenn, Hall, T, Wagner, R, Rotellar, Winchester, and Zeman, Quantitative detection of parenchymal structural change in diffuse renal disease, Invest. Radiology 29: 134-140, 1994.
- [3] Oelze, M, O'Brien, W, Blue, and Zachary, J, Differentiation and characterization of rat mammary fibroadenomas and 4T1 mouse carcinomas, IEEE Trans Med Imaging: 23 (6): 764-771, 2004
- [4] Sommer, FG, Olcott, and Tai, Liver tumors: utility of characterization at dual-frequency ultrasound, Radiology 211: 629-636, 1999.
- [5] Yao, L, Zagzebski, J, and Madsen, E, Backscatter coefficient measurements using a reference phantom to extract depth dependent instrumentation factors, Ultrasound Imaging 12: 58-70, 1990.
- [6] Gerig, A, Zagzebski, J, and Varghese, T, Statistics of ultrasonic scatterer size estimation with a reference phantom, JASA 113: 3430-3441, 2003.
- [7] Gerig, A, Varghese, T, and Zagzebski, J, Improved parametric imaging of scatterer size estimates using angular compounding, IEEE Trans. UFFC 51: 708-715, 2004.
- [8] Wagner RF, Insana, M, Brown, D, Statistical properties of radio frequency and envelope detected signals with applications to medical ultrasound, J Optical Soc Am: A Optics and Image Science 4: 910-922, 1987.
- [9] Entrekkin, R, Porter, A, Sillesen, H, et al, Real time spatial compound imaging: application to breast, vascular, and musculoskeletal ultrasound, Seminars in Ultrasound, CT, and MRI 22: 50-64, 2002.
- [10] Tu, H, Varghese, T, Madsen, E, et al, Ultrasound attenuation imaging using compound acquisition and processing, Ultrasound Imaging 25: 245-261, 2003.
- [11] Trahey, G, Allison, J, Smits, S, and von Ramm, O, A quantitative approach to speckle reduction via frequency compounding, Ultrasonic Imaging 8: 151-164, 1986.